

# P-T-t-d constraints on the Late Variscan evolution of the Eastern Pyrenees

Carmen María Aguilar Gil

**ADVERTIMENT**. La consulta d'aquesta tesi queda condicionada a l'acceptació de les següents condicions d'ús: La difusió d'aquesta tesi per mitjà del servei TDX (**www.tdx.cat**) i a través del Dipòsit Digital de la UB (**diposit.ub.edu**) ha estat autoritzada pels titulars dels drets de propietat intel·lectual únicament per a usos privats emmarcats en activitats d'investigació i docència. No s'autoritza la seva reproducció amb finalitats de lucre ni la seva difusió i posada a disposició des d'un lloc aliè al servei TDX ni al Dipòsit Digital de la UB. No s'autoritza la presentació del seu contingut en una finestra o marc aliè a TDX o al Dipòsit Digital de la UB (framing). Aquesta reserva de drets afecta tant al resum de presentació de la tesi com als seus continguts. En la utilització o cita de parts de la tesi és obligat indicar el nom de la persona autora.

**ADVERTENCIA**. La consulta de esta tesis queda condicionada a la aceptación de las siguientes condiciones de uso: La difusión de esta tesis por medio del servicio TDR (**www.tdx.cat**) y a través del Repositorio Digital de la UB (**diposit.ub.edu**) ha sido autorizada por los titulares de los derechos de propiedad intelectual únicamente para usos privados enmarcados en actividades de investigación y docencia. No se autoriza su reproducción con finalidades de lucro ni su difusión y puesta a disposición desde un sitio ajeno al servicio TDR o al Repositorio Digital de la UB. No se autoriza la presentación de su contenido en una ventana o marco ajeno a TDR o al Repositorio Digital de la UB (framing). Esta reserva de derechos afecta tanto al resumen de presentación de la tesis como a sus contenidos. En la utilización o cita de partes de la tesis es obligado indicar el nombre de la persona autora.

**WARNING**. On having consulted this thesis you're accepting the following use conditions: Spreading this thesis by the TDX (**www.tdx.cat**) service and by the UB Digital Repository (**diposit.ub.edu**) has been authorized by the titular of the intellectual property rights only for private uses placed in investigation and teaching activities. Reproduction with lucrative aims is not authorized nor its spreading and availability from a site foreign to the TDX service or to the UB Digital Repository. Introducing its content in a window or frame foreign to the TDX service or to the UB Digital Repository is not authorized (framing). Those rights affect to the presentation summary of the thesis as well as to its contents. In the using or citation of parts of the thesis it's obliged to indicate the name of the author.

Universitat de Barcelona

**Facultat de Geologia**
**Departament de Geoquímica, Petrologia i Prospecció Geològica**
**Programa de Doctorat "Ciències de la Terra"**
**Universitat de Barcelona**

# *P-T-t-d constraints on the Late Variscan evolution of the Eastern Pyrenees*

A Thesis submitted by

**Carmen María Aguilar Gil**

PhD thesis supervised by

**Dr. Montserrat Liesa Torre-Marín**
Departament de Geoquímica, Petrologia i Prospecció Geològica
Facultat de Geologia
Universitat de Barcelona

**Dr. Marina Navidad Fernández de la Cruz**
**Dr. Pedro Castiñeiras García**
Departamento de Petrología y Geoquímica
Facultad de Ciencias Geológicas
Universidad Complutense de Madrid

**2013**

Universitat de Barcelona

**Facultat de Geologia**
**Departament de Geoquímica, Petrologia i Prospecció Geològica**
**Programa de Doctorat "Ciències de la Terra"**
**Universitat de Barcelona**

# *P-T-t-d constraints on the Late Variscan evolution of the Eastern Pyrenees*

Memoria de tesis doctoral presentada por Carmen María Aguilar Gil para optar al grado de Doctora en Geología. La tesis doctoral se ha realizado en el marco del Programa de Doctorat de Ciències de la Terra (2008-2013) bajo la supervisión de los doctores Montserrat Liesa Torre-Marín, Marina Navidad Fernández de la Cruz y Pedro Castiñeiras García.

**Carmen María Aguilar Gil**

Directores de la Tesis doctoral

**Dra. Montserrat Liesa Torre-Marín**

**Dra. Marina Navidad Fernández de la Cruz** **Dr. Pedro Castiñeiras García**

**2013**

A mis abuelas y
a mis padres

# AGRADECIMIENTOS

Esta Tesis no se habría llevado acabo sin la ayuda de mis directores: Dra. Montserrat Liesa, Dr. Pedro Castiñeiras y Dra. Marina Navidad. A todos ellos, les estoy enormemente agradecida por permitirme formar parte de su grupo de investigación, por haber confiado en mi para llevar a acabo este trabajo y sobre todo, por enseñarme todo lo que saben.

Esta Tesis doctoral ha sido financiada por los proyectos de investigación CGL2007-66857-C02-02 y CGL2010-21298, y por la beca FPI (BES-2008-001841) financiada por el Ministerio de Ciencias e Inovación (MICINN). Durante esta Tesis doctoral se han realizado tres estancias breves de varios meses de duración. Las estancias realizadas en Stanford University, California (EEUU) durante el 2010 y en Université de Strasbourg (Francia) durante el 2012 han sido financiadas por MICINN. La tercera estancia realizada en el Center for Lithospheric Research, Czech Geological Survey (Praga) en el 2013 ha sido financiada por el proyecto CGL2010-21298.

También estoy agradecida a Dr. Josep María Casas y a Dr. Josep Anton Muñoz por sus interminables comentarios y revisiones sobre la tectónica de la zona de estudio, la cual ha formado parte de mi tesis. Furthermore, I would also want to thank professors Pavla Stípská and Karel Schulmann, from the University of Strasbourg and the Czech Geological Survey, for their great help and patience, for sharing with me their knowledge and for their warm welcome during two of my stages.

Esta Tesis tampoco habría sido posible sin el gran apoyo técnico de:

Jordi Illa, por recordarme siempre y en todo momento que las muestras deben ir en la Litoteca.

Fadoua Zoura, por su gran compañía en esa litoteca tan oscura y fría.

Vicenç Planella, por ayudarme a serrar sin previo aviso esas rocas tan complejas como son las migmatitas.

Dolors Barsó y Montserrat Sibila, por su ayuda y su confianza.

Xavier Llovet, Eva Prats, Anna María Domínguez, Javier García Veigas, Aránzazu Villuendas y Elisenda Seguí del Centre Científic i Tecnològic (CCiT) de la Universitat de Barcelona, por esas largas horas en la microsonda y por sus asesoramientos e innumerables visitas en el microscopio electrónico de barrido (SEM) y en la

fluorescencia de RX.

In addition, I am especially grateful to Joe Wooden, Jorge Vazquez and Brad Ito of the SUMAC staff at Stanford University for the close supervision of zircon-mount preparations and imaging, zircon analyses and instrument tuning.

Esta Tesis se ha llevado acabo en el Departament de Geoquímica, Petrologia i Prospecció Geològica de la Universitat de Barcelona, donde he podido compartir buenos momento con todos y cada uno de ellos.

A Jordi Báguena, por gestionar todos mis gastos con esa simpatía que le caracteriza tanto, y a Montserrat Errea, por estar siempre de mi parte cuando Jordi hace de las suyas.

A Meritxell Aulinas, Gemma Alías, Juan Diego Martín, Josep Anton Moreno, Telm Bover, Elisabet Playà, Ramón Salas, Albert Permanyer, Anna Travé y a todos aquellos que forman parte del departamento GPPG, por su ayuda científica y sobre todo, por estar siempre y en todo momento disponibles ante cualquier duda.

A mis compañeros (Vinyet Baqués, Irene Cantarero, Ramón Mercedes, Sergi Valenzuela, Guillem Gisbert, Mar Moragas, Àlex Sendrós, Agustín Hernández, Flavia Bazzocchi, Sara Chiostergi, Eduard Albert, Ander Guinea, Emili Carrillo, Consuelo Navarro, Yael Díaz), a los que aún siguen y a los que se fueron, por sus risas, gran apoyo y numerosos comentarios.

A Vinyet Baqués, Sara Martínez, Marta Llario e Irene Cantarero por aguantarme y escucharme en mis momentos bajos, por su gran apoyo y paciencia y sobre todo, por dejarme formar parte de sus vidas.

A mis grandes amigos, Modesto Berbel, Alejandra Fernández, Mayte Pedrosa, Arantxa Antelo, Olalla López y Ana Campos, por estar siempre a mi lado después de tanto tiempo y por su gran apoyo, aunque sea desde la distancia.

Finalmente, y lo más importante, a todos los miembros mi familia, que no son pocos. En especial, a mis padres, por su apoyo incondicional y por estar ahí en todo momento.

MUCHAS GRACIAS, MOLTES GRÀCIES, THANKS SO MUCH

# CONTENTS

**AGRADECIMIENTOS** ..... vii

**ABSTRACT** ..... 1

**1. INTRODUCTION** ..... 5

1.1. Motivation, objectives and structure of this thesis ..... 5

1.2. Geological background ..... 7

**2. GEOLOGICAL SETTING AND PREVIOUS STUDIES** ..... 13

**3. STRUCTURAL EVOLUTION** ..... 17

**4. PETROGRAPHY, MINERAL CHEMISTRY AND WHOLE-ROCK COMPOSITION** ..... 23

4.1. Analytical procedures and abbreviations ..... 23

4.2. Petrography and deformation-crystallization relationships ..... 24

4.2.1. The Upper series ..... 24

4.2.2. The Intermediate series not affected by the Ceret gabbro-diorite contact aureole ..... 26

4.2.3. The Intermediate series affected by the Ceret gabbro-diorite contact aureole ..... 27

- Patchy migmatites ..... 29
- Stromatic migmatites ..... 31
- Schollen migmatites ..... 31
- Melanosome residuum ..... 33

4.2.4. The Lower series ..... 37

4.2.5. Late-Variscan igneous rocks ..... 37

4.3. Mineral chemistry ..... 39

4.3.1. The Upper series ..... 40

4.3.2. The Intermediate series not affected by the Ceret gabbro-diorite contact aureole ..... 40

4.3.3. The Intermediate series affected by the Ceret gabbro-diorite contact aureole ..... 41

4.3.4. The Lower series ..... 45

4.4. Whole-rock composition ..... 48

**5. MINERAL EQUILIBRIA MODELING** ..... 53

5.1. Calculation methods ..... 53

5.2. Assessing *P*–*T* conditions in the MnNCKFMASTHO system ..... 54

5.2.1. The Upper series: pseudosection for sample 187 ..... 56

5.2.2. The Intermediate series not affected by the Ceret gabbro-diorite contact aureole: pseudosection for sample 4.12b ..... 58

5.2.3. The Intermediate series affected by the Ceret gabbro-diorite contact aureole: pseudosection for sample 459 ..... 60

5.2.4. The Lower series: pseudosection for sample 515 ..... 62

**6. FORWARD MODELING OF CONTACT METAMORPHIC MIGMATITES** ..... 65

6.1. Calculation methods ..... 66

6.2. Closed mineral equilibria modeling in the NCKFMASHTO system ..... 68

6.2.1. Patch migmatites: pseudosection for sample 526 ..... 68

6.2.2. Stromatic migmatites: pseudosection for sample 529 ..... 71

6.2.3. Schollen migmatites: pseudosection for sample 459 ..... 74

6.2.4. Residuum melanosome migmatites: pseudosection for sample 462 ..... 76

6.2.5. Average *P*–*T* conditions of last equilibration ..... 78

6.3. Modeling of open-system processes ..... 81

6.3.1. A single melting event with variable fluid content ..... 82

6.3.2. Multiple melt loss–rehydration events ..... 86

- Comparison between modeled and analyzed rock compositions ..... 89

**7. ZIRCON U–PB GEOCHRONOLOGY** ..... 95

7.1. Methodology ..... 96

7.1.1. Sample preparation ..... 96

7.1.2. Analytical Methods ..... 96

7.2. Zircon description ..... 97

7.2.1. Migmatites from the Lower series ..... 99

7.2.2. Sant Llorenç–La Jonquera tonalite and Ceret stock gabbro ..... 100

7.2.3. Migmatites from the Intermediate series affected by the Ceret gabbro-diorite contact aureole ..... 101

7.3. Zircon U–Pb dating ..... 101

7.3.1. Migmatites from the Lower series ..... 101

7.3.2. Sant Llorenç–La Jonquera tonalite and Ceret stock gabbro ..... 104

7.3.3. Migmatites from the Intermediate series affected by the Ceret gabbro-diorite contact aureole ..... 107

7.4. Zircon U, Th, Hf and REE composition ..... 107

7.4.1. Migmatites from the Lower series ..... 107

7.4.2. Sant Llorenç–La Jonquera tonalite and Ceret stock gabbro ..... 111

**8. DISCUSSION** ..... 115

8.1. Metamorphism-deformation-magmatism relationships ..... 115

8.2. Interpretations of the different types of migmatites affected by the Ceret contact aureole ..... 117

8.3. *P–T–d* evolution ..... 119

8.3.1. Prograde paths, peak conditions and early retrogression are not shared ..... 119

8.3.2. Implications from the *P–T–d* paths ..... 121

8.4. High-temperature metamorphic processes in the migmatites ..... 123

8.5. Timing of the Variscan thermal evolution in the Eastern Pyrenees ..... 125

8.6. Comparison of thermal events with neighboring areas of the Variscan belt ..... 127

8.6.1. Thermal events in the Pyrenean segment of the Variscan belt ..... 127

8.6.2. Thermal events in the Variscan segment of Montagne Noire (SE France) and the Catalan Costal Ranges (NE Iberia) ..... 128

8.6.3. Time-space configuration of the Variscan belt in NE Iberia (Pyrenees–Catalan Coastal Ranges) and SE France (Montagne Noire) ..... 128

8.6.4. Correlation with the autochthonous and allochthonous domains of Central and Southeastern Variscan segments of Europe....132

8.7. Tectonic implications of the Eastern Pyrenees P–T–d–t evolution....135

**9. CONCLUSIONS**....141

**REFERENCES**....145

**APPENDIX: MINERAL CHEMISTRY**....161

**LIST OF FIGURE CAPTIONS**....201

**LIST OF TABLE CAPTIONS**....211

# ABSTRACT

Structural, petrological and microstructural studies were combined with pseudosection modeling in the Roc de Frausa Massif (Eastern Pyrenees) affected by Variscan deformation and metamorphism. The massif is constituted by Upper Proterozoic–Lower Cambrian series subdivided in an Upper, Intermediate and Lower series separated by gneiss sheets. It represents a mid-crustal section of the Variscan orogen intruded by a calc-alcaline pluton and a gabbro-diorite stock at different levels. Structural analysis across the massif reveals two folding phases (D1 and D2). D1 is marked by tight to isoclinal small-scale folds and a sub-horizontal foliation (S1). D2 structures are tight upright folds facing to the NW with steep NE–SW axial planes. They heterogeneously rework S1 foliation and in the high-grade metamorphic domains a sub-vertical S2 foliation almost transposes it. Calc-alkaline granitoids intruded interkinematically and hornblende gabbros and diorites of the mafic complexes were coeval with the D2 event. The area is affected by a late subvertical F3 folding phase, characterized by NW–SE folds compatible with steep dextral shear zones. The D3 shear zones retrograde the pre-Variscan rocks and the Variscan intrusives to greenschist facies. N and S of the studied area F3 folds involve Mesozoic rocks, and therefore it can be attributed to the Alpine orogeny.

In the andalusite–sillimanite micaschists of the Upper series, andalusite porphyroblasts with S1 inclusion trails and later sillimanite in the S1 pressure shadows indicate heating from 580 °C to 640 °C in the S1 fabric. Cordierite that includes the previous assemblage and does not exhibit pressure shadows points to isothermal decompression from 3.4 kbar to 2.6 kbar. The Intermediate series are dominated by sillimanite schists with sillimanite–biotite–muscovite in the S1 fabric overgrown by cordierite and K-feldspar without any pressure shadows. These assemblages point to decompression from at least 5 kbar to 3 kbar at 640–660 °C. The intermediate series are locally intruded by a gabbro-dioritic stock that produced a narrow contact aureole and widespread migmatization. In the inner aureole and xenoliths, four types of migmatites have been characterized, with different textures, mineral assemblages, mineral chemistry and whole-rock compositions. In the migmatites, the S1 foliation is defined by the assemblage biotite–sillimanite–K-feldspar–garnet. Garnet has inclusions of

sillimanite and biotite parallel to S1 at the rim. This assemblage and microstructure, together with garnet zoning is compatible with heating within the S1 fabric near the pressure peak at 7 kbar to 730 °C. The F2 folds with subvertical melt-filled S2 foliation were overgrown by cordierite indicating mainly syn-D2 decompression to 4.5 kbar. In order to explain the different whole-rock and mineral compositions and the preservation of mineral assemblages of migmatitic rocks, a $T$–$M(H_2O)$ pseudosection was constructed at 5.5 kbar with the composition of a hypothetical protolith averaged from non-migmatitic neighboring rocks. The fluids released by the crystallizing gabbro-diorite would infiltrate the metasediments at 790 °C and be incorporated into the melt. The mineral assemblages of the different migmatitic types can be reproduced but they would not be preserved on cooling if the system remained closed for melt. Therefore, a series of $T$–$M(H_2O)$ alternating with $T$–$X_{\text{melt loss}}$ diagrams was constructed at 5.5 kbar. Each melting episode represents different volumes of melt produced and expelled along the supersolidus history of the rock, preserving the observed mineral assemblages. This process leads to a reduction of the volume of the rock up to 48 mol.% through melt producing processes and a global amount of melt produces of around 60 mol.%. Therefore, a model sequence of $H_2O$-fluxed melting alternating with melt extraction episodes can explain the preserved high-grade mineral assemblages. The Lower series is dominated by fold-structured migmatites with biotite–cordierite composite S1-S2 biotite-bearing fabric with relict garnet embedded in plagioclase, thus precluding deciphering the early metamorphic evolution. Cordierite overgrowing both S1 and S2 fabric points to late equilibration at 3 kbar and 700 °C.

The early metamorphic history associated with the S1 fabric is interpreted as a result of lower crustal horizontal flow and could be related to moderate crustal thickening. D2 event is characterized by a pressure decrease. Therefore, decompression can be explained by a syn-convergent and highly heterogeneous exhumation of the metamorphic complex during crustal-scale doming during the last stages of the Variscan evolution.

New U–Pb SHRIMP-RG dating of zircon from the plutonic rocks and migmatites was carried out. A thermal episode occurred in the interval 320–315 Ma coeval with the main deformation event (D1) as registered in the migmatites from the Lower series. A

tonalite, from the calc-alkaline granitoid suite, intruded into the upper crustal levels between 314–311 Ma. The gabbro-diorite stock was emplaced at middle levels of the series in two magmatic pulses at 312 and 307 Ma, as suggested by cathodoluminescence, transmitted light microscope and trace element chemistry of zircon.

This thermal event recorded in the Eastern Pyrenees can be correlated with the neighboring areas from NE Iberia (Pyrenees–Catalan Coastal Ranges) and SE France (Montagne Noire), and with further areas from the Iberian Massif and the Central and Southwestern Europe. The correlation suggests a NW–SE trending zonation with the more internal zones of the orogen located to the northeast and the more external ones to the Western Pyrenees and the Southwestern Catalan Coastal Ranges.

**Keywords:** Eastern Pyrenees, Variscan orogen, HT–LP metamorphism, structural geology, petrography, thermal modeling, THERMOCALC, U–Pb Zircon dating

# INTRODUCTION

## 1.1. Motivation, objectives and structure of this thesis

Understanding the processes that take place in the building of orogenic systems, from the thickening stage to the orogenic collapse requires a multidisciplinary approach from the fields of metamorphic and igneous petrology, structural geology, geochemistry, geochronology and thermal modeling. The study of reequilibration processes in metamorphic rocks can give information on the history of the orogenic belt and on the processes taking place in the continental crust. These processes are best studied in the middle crust where there is strong interaction between metamorphic rocks, fluids and melts, thus modifying the rheology of the crust. Fluids released either by dehydration reactions, dehydration-melting reactions or by crystallization of igneous bodies enhance the velocity of reactions. Hence, rocks become sensitive records of microstructural information. Tracking the reactions and their interplay with the structural fabrics allow unraveling the relative history of the orogen. However, the precise ages of these processes can be obtained with methods such as U–Pb zircon dating. Zircon registers crystallization of both the first melts formed and the batholitic scale granitoids. Precise information on these subjects allows construction of geodynamic models of orogenic belts.

In addition, middle crustal rocks and mostly migmatites constitute natural laboratories to keep track of the processes leading to the differentiation of the crust. Theoretical models have been carried out since the beginning of this century (e.g., White & Powell, 2002) but few studies combine geochemical and petrographic studies with thermal modeling approaches (e.g., Hasalová *et al*., 2008). The *P*–*T* paths can be deciphered for a set of individual samples with different bulk and mineral compositions but sharing a common history. These paths can be compared with mineral equilibria modeling to shed light on the processes of fluid flow and/or melt

migration out or into the rock system, i.e., on the open- or closed-system behavior. It can also help to understand why granulite facies terranes are preserved, estimate the volume of melt loss in a specific system and, eventually relate granulite facies metamorphism with upper crustal granitoids.

Prime areas to study these subjects are ancient orogens where erosion or subsequent mountain building processes have exposed old continental crust. One of these areas is the Variscan basement of the Pyrenees since medium- to high-grade rocks and migmatites crop out associated to mostly granodioritic and mafic igneous bodies. The Variscan basement of the Pyrenees is a well-known area on low-pressure–high-temperature (LP–HT) metamorphism since the pioneer work of Zwart (1962, 1963). In these works, this author also established the basis for the relations between metamorphic crystallization and deformation that have been taken as a reference since then (Spry, 1969; Vernon, 1976; Bell & Rubenach, 1983; Paschier & Trouw, 1996). From the 1960 through 1990 a number of studies were carried out and a great amount of geological data was collected. These three decades of studies ended up with highly contradictory interpretations of the geodynamic evolution of the Variscan basement. Contrastingly, during the last 20 years, only a few studies have been fulfilled on the metamorphism of the Variscan basement of the Pyrenees, and nowadays, new techniques and methodologies must be incorporated. All these new approaches and data constitute a challenge and have motivated the realization of this PhD thesis. Therefore, the present thesis provides the first integrated structural, petrological and geochronological study in medium- to high-grade metamorphic rocks and in associated igneous rocks of the Variscan segment of the Pyrenees.

In summary, this study intends to:

(a) provide up-to-date information on the *P*–*T*–*d* conditions of the high-temperature Variscan events in a selected area of the Eastern Pyrenees,

(b) gain insight into the knowledge of high-temperature metamorphic processes occurring in the migmatites,

(c) contribute to the understanding of the thermal evolution and determine the absolute timing of the crustal melting; and

(d) integrate this information with the structural framework to constrain the geodynamic processes that took place during the waning stages of the Variscan orogeny.

The structural history is related to the crystallization of the main metamorphic minerals, and especially garnet and cordierite porphyroblasts, in order to assess the prograde and retrograde character of each metamorphic fabric (see **Chapter 4**). Mineral equilibria modeling is further used together with classical petrological studies to decipher the *P*–*T*–*d* evolution of the different parts of the metasedimentary series (see **Chapter 5**). On the other hand, forward modeling is performed to discuss possible processes that may have operated in the migmatites. The obtained models will shed light on the open- or closed-system behavior of these rocks and on the preservation of granulite facies terranes (see **Chapter 6**). It is worth noting that in Chapter 5 petrological modeling has been carried out in the Mn-NCKFMASHTO system, whereas in Chapter 6 it has been done in the NCKFMASHTO. The reason is that when dealing with medium-grade metamorphic rocks, working in systems with Mn is preferable and when working with migmatites (Chapter 6), the system NCKFMASHTO is also appropriate. Notwithstanding, in order to compare the results of both systems two pseudosections have been calculated for sample (459) (see figures 5.4 and 6.7). In addition, U–Pb zircon dating using sensitive high-resolution ion microprobe-reverse geometry (SHRIMP-RG) is carried out in Variscan migmatites together with dating of Late-Variscan plutonic rocks emplaced in different crustal levels to constraint the timing of the Variscan thermal evolution (see **Chapter 7**). A combination of microstructural, thermobarometric and geochronological studies will allow the identification of well-constrained *P*–*T*–*t*–*d* paths, which are finally discussed (see **Chapters 8 & 9**) to clarify the tectonothermal processes in the hot lower and middle orogenic crust of the Variscan basement of the Pyrenees.

## 1.2. Background

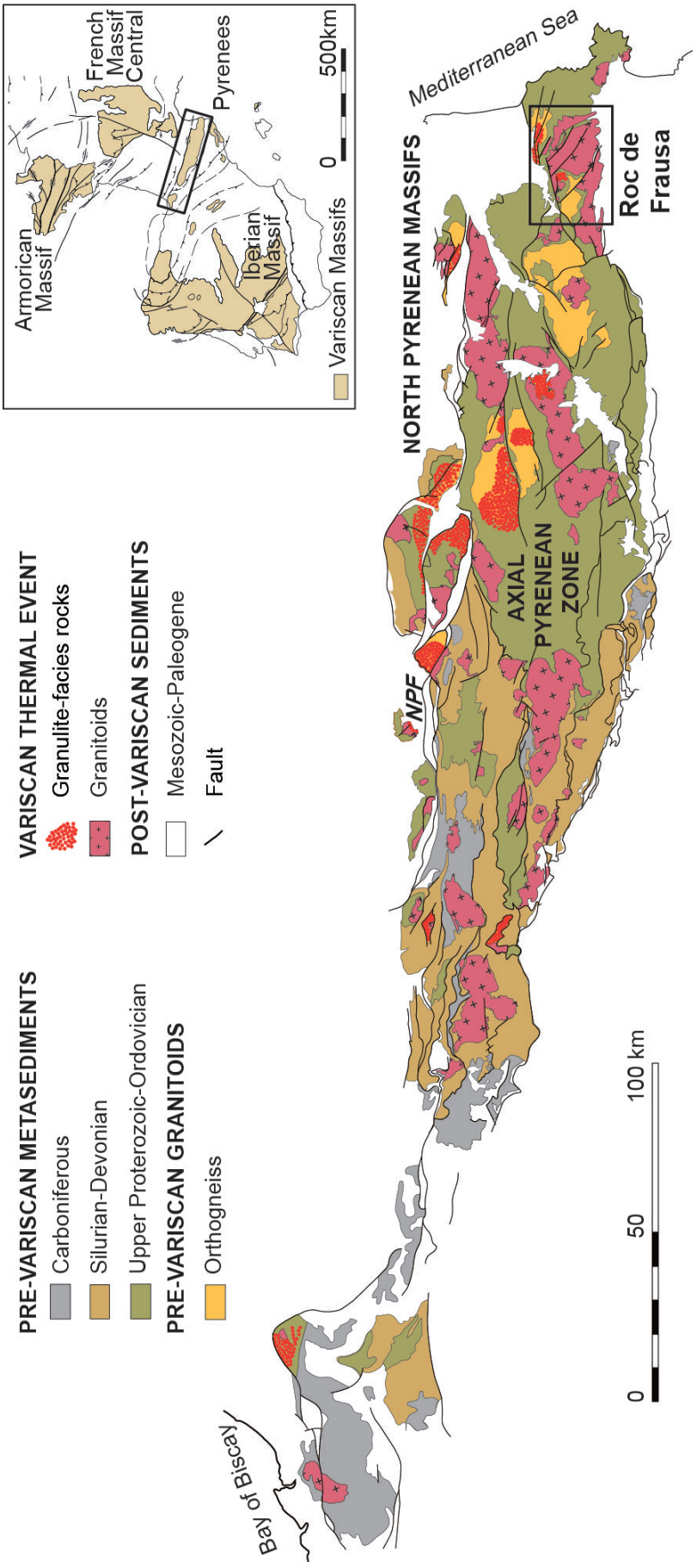
In the Variscan context, the Pyrenees are a fragment of the external zones of the Southwestern European Variscan belt (Matte, 1986). During the Alpine orogeny pre-Variscan and Variscan rocks were involved in the lower thrust sheets. Thus, at present in the Central Pyrenees two zones can be distinguished: the North Pyrenean

Zone and the Axial Zone (Fig. 1.1). They display an approximately East-West antiformal shape parallel to the Alpine trend of the chain. Three types of rocks predominate: a mainly metasedimentary Pre-Variscan sequence of Upper Proterozoic to Carboniferous age, gneiss sheets which mostly represent Ordovician granitic intrusions interbedded in the sequence and late-Variscan calc-alkaline granitoids. Along the Central and Western parts of the Axial Zone, the Variscan basement consists of predominantly upper crustal rocks (Silurian to Carboniferous) at a low-metamorphic grade, whereas towards the Eastern Axial Zone, deep-seated rocks (Upper Proterozoic to Ordovician) in upper amphibolite to granulite facies become more abundant.

From the 1960s through the 1990s, many works were carried out in the Variscan basement of the Pyrenees. In the Central Pyrenees, Zwart and collaborators from dutch universities mapped most of the massifs and studied their stratigraphy, structure and metamorphism. In contrast, the French and Spanish schools mostly worked in the Eastern and Northern Pyrenean massifs.

Since the early work of Zwart (1962, 1963), the Variscan Pyrenees have been known as a classical example of LP–HT metamorphism (e.g., Miyashiro, 1973; Wickham, 1987) documented by a continuous metamorphic sequence, divided in a series of zones: chlorite-muscovite, biotite, andalusite-cordierite, sillimanite and, at the highest grade, migmatites (Guitard, 1970; Zwart, 1979; Guitard *et al*., 1995). At the deepest tectonic levels, close to (or in) the anatectic domains, abundant dykes, stocks and small plutons of peraluminous leucogranites occur. Field relations of the migmatitic rocks suggest that these peraluminous leucogranites crystallized from a parent magma generated by partial melting of metasedimentary rocks and orthogneisses similar to those cropping out in the anatectic domains (Autran *et al.,* 1970; Wickham, 1987; Vilà *et al*., 2005). At mid crustal levels, the presence of stocks and enclaves of mafic rock-types (mainly hornblende gabbros and diorites) gives evidence that mantle-derived magmas played a significant role in providing heat and/or mass input (Wickham & Oxburgh, 1986, 1987; Roberts *et al*., 2000). At higher

**Figure 1.1** Geological map of the Axial Pyrenean Zone and North Pyrenean Zone with the location of granulite facies rocks (the area studied is outlined). The upper right inset displays the general location of the Pyrenees within the European Variscides.


Armorican Massif
French Massif Central
Pyrenees
Iberian Massif
Variscan Massifs
0
500km
Mediterranean Sea
NORTH PYRENEAN MASSIFS
Roc de Frausa
NPF
AXIAL PYRENEAN ZONE
Bay of Biscay
0
50
100 km
PRE-VARISCAN METASEDIMENTS
Carboniferous
Silurian-Devonian
Upper Proterozoic-Ordovician
PRE-VARISCAN GRANITOIDS
Orthogneiss
VARISCAN THERMAL EVENT
Granulite-facies rocks
Granitoids
POST-VARISCAN SEDIMENTS
Mesozoic-Paleogene
Fault

crustal levels and in the 312–301 Ma time span, large Variscan calc-alkaline granitoids were emplaced as plutonic complexes surrounded by well-developed contact aureoles overprinting low-grade regional metamorphism (Debon *et al*., 1995).

Variscan deformation is polyphasic. In the upper structural levels, the main deformation phase is characterized by folds associated to thrust systems and to a poorly developed cleavage. In the lower structural levels, isoclinal folds are formed with a pervasive axial plane foliation transposing the previous structures. The attitude of the main foliation varies according to the structural level. In the upper one it is subvertical, whereas in the lower one it has a flat-lying attitude. This feature is remarkable in the Central Pyrenees and led several authors (mostly Zwart and the Leiden University group, see Zwart (1979) for a synthesis) to distinguish between two structural domains, the suprastructure corresponding to low-grade metamorphic rocks and the infrastructure corresponding to medium- to high-grade metamorphic rocks.

The high-grade metamorphic domain is constituted by broad antiforms with a domal shape, with gneisses or migmatites cropping out in their central part. They have been interpreted either as the result of gravity overturns (Soula *et al*., 1986a), as doming related to a Late Carboniferous transpressional event (e.g., Carreras & Capellà, 1994; Gleizes *et al.,* 1998; Druguet, 2001; Román-Berdiel *et al.,* 2004; Vilà *et al.,* 2007) or as fold interference between late folding phases. The exceptional LP–HT metamorphism and associated granite magmatism were accordingly explained either as a result of generalized rifting associated with the emplacement of a thick basaltic sill at mid crustal depths (Wickham & Oxburgh, 1986) or as a slab breakoff related to the ingress of hot asthenospheric mantle at a shallow level that triggered syn-collisional partial melting in both the mantle and overlying crust (Vilà *et al*., 2007). Petrological studies also emphasize that the crust was only moderately thickened (Azambre & Guitard, 2001) and that the cooling was almost isobaric, which may be indicative for a major heat source located at depth (Vilà *et al*., 2007).

An exceptionally high metamorphic field gradient (70–40 °C/km) resulted in dominantly LP–HT metamorphism (e.g., Gibson & Bickle, 1994) and a sub-horizontal fabric of the high-grade infrastructure. This led to a number of authors to propose a

model of lithosphere-scale extension associated with elevated heat flux (Wickham & Oxburgh, 1986; Wickham, 1987; van den Eeckhout & Zwart, 1988; Vissers, 1992).

Such conflicting interpretations in the tectonic style and in the causes of metamorphism are due to the fact that few petrological studies have been performed together with detailed structural investigations. Structural studies are generally carried out in low-grade metamorphic rocks, whereas petrological studies are done in medium- to high-grade rocks, arriving to different conclusions about the timing of the events. For instance, several structural studies carried out in the infrastructure emphasize the synchronous structural evolution of high-grade rocks and magmatism (Druguet & Hutton, 1998), whereas other researches in suprastructural levels suggest diachronous regional deformation and magma emplacement (Gleizes *et al*., 1998). Generally, an integrated study of the structure and metamorphism in areas where a complete section crops out from the suprastructure to the infrastructure would help to understand if there is a different timing of events in different crustal levels or if, as suggested by Denèle *et al.* (2009), there is a mechanical decoupling between the infrastructure and the suprastructure during the main compressive phase.

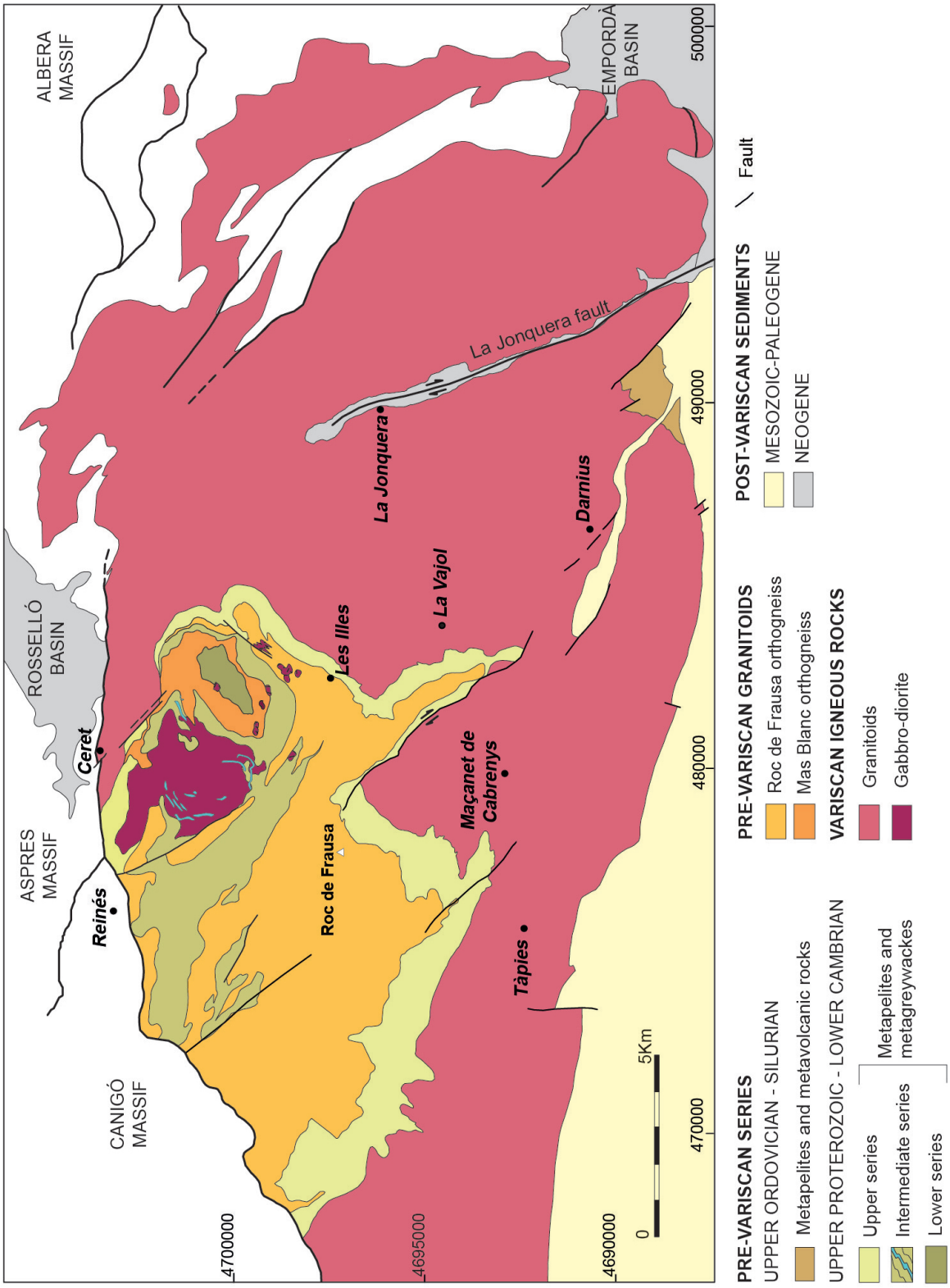
# CHAPTER 2

## GEOLOGICAL SETTING AND PREVIOUS STUDIES

The study area is the Roc de Frausa Massif located at the Eastern Pyrenees, where the deepest pre-Variscan stratigraphic and structural levels crop out (see Fig. 1.1). The massif is formed by pre-Variscan sedimentary and igneous rocks that were deformed and metamorphosed during the Variscan orogeny and intruded by a late-Variscan calc-alkaline plutonic suite and by subordinate mafic rocks (Fig. 2.1). Both the metamorphic massif and the igneous rocks form a distinctive geological ensemble together with the easternmost Albera Massif, and they are separated from the neighboring pre-Variscan areas to the N–NW (namely Aspres and Canigó massifs) by Alpine faults or are unconformably overlain by uppermost Cretaceous sediments to the S.

The metasedimentary sequence is dominated by Upper Proterozoic to Lower Cambrian metapelites and metagreywackes (Castiñeiras *et al.,* 2008a). Sporadically interbedded in these series, there are layers of varied lithologies: amphibolites, metatuffs, marbles, calc-silicate rocks, quartzites and black pelites, making up a lithologically complex unit (Fig. 2.2). Two sheet-like orthogneiss bodies divide the metasedimentary succession into an Upper, an Intermediate and a Lower series (Fig. 2.1 & 2.2). These orthogneisses, namely the Mas Blanc and the Roc de Frausa gneisses (Autran & Guitard, 1969), correspond to pre-Variscan granites intruded at 560 ± 7 and 476 ± 5 Ma, respectively (Castiñeiras *et al*., 2008a).

The metasedimentary sequence preserves a continuous LP–HT prograde metamorphism. The intensity of metamorphism increases from the amphibolite facies in the Upper series to the lower granulite facies in the Lower series (Liesa & Carreras, 1989). These authors defined three metamorphic zones for the low- to medium-grade metamorphic rocks: a narrow andalusite zone, a sillimanite zone and a wide cordierite–K-feldspar zone. In the latter zone, peak metamorphic conditions


ALBERA MASSIF
ROSSELLÓ BASIN
EMPORDÀ BASIN
ASPRES MASSIF
CANIGÓ MASSIF
Ceret
Reinés
Roc de Frausa
Les Illes
La Jonquera
La Vajol
Darnius
Maçanet de Cabrenys
Tàpies
La Jonquera fault
4700000
4695000
4690000
470000
480000
490000
500000
0
5Km
PRE-VARISCAN SERIES
UPPER ORDOVICIAN - SILURIAN
Metapelites and metavolcanic rocks
UPPER PROTEROZOIC - LOWER CAMBRIAN
Upper series
Intermediate series
Lower series
Metapelites and metagreywackes
PRE-VARISCAN GRANITOIDS
Roc de Frausa orthogneiss
Mas Blanc orthogneiss
VARISCAN IGNEOUS ROCKS
Granitoids
Gabbro-diorite
POST-VARISCAN SEDIMENTS
MESOZOIC-PALEOGENE
NEOGENE
Fault

determined from Fe/Mg partitioning indicated values of about 650 °C and 3–3.5 kbar at $P_{H2O}=P_{tot}$ according to the Holdaway & Lee (1977) petrogenetic grid.

The late-Variscan calc-alkaline Sant Llorenç–La Jonquera plutonic complex and the Ceret stock are emplaced in separated levels of the series (Liesa & Carreras, 1989). Both intrusions have contrasting geochemical characteristics and belong to two genetically distinct igneous suites produced in different levels of the lithosphere (Vilà *et al.,* 2005). The late-Variscan calc-alkaline Sant Llorenç–La Jonquera tonalite to granite suite is a sheet-like intrusion (150 $km^2$) emplaced on top of the Upper Proterozoic-Lower Cambrian sequence and below the Upper Ordovician-Silurian rocks of the Montroig Mountain southeast from the Roc de Frausa Massif (Fig. 2.1 & 2.2). It has sharp contacts with the country rocks and includes scarce xenoliths near the borders of the intrusion. A contact metamorphic aureole (approximately 500 meters wide) develops around it, and andalusite-cordierite hornfelses are found. For this pluton, early dating attempts using the Rb–Sr method have yielded an emplacement age of 282 ± 5 Ma (Cocherie, 1984) and more recent U–Pb zircon data have given 295 ± 7 Ma (Maurel, 2003). However, these ages are younger than other intrusion ages obtained in adjacent plutons of the Pyrenees (314–301 Ma). The Ceret stock is the most prominent of a series of small (10 $km^2$) gabbro-diorite bodies intruded into the Intermediate series. It is formed by a main body and by metric satellite intrusions scattered inside the country rock, within a radius of 2 km, and a narrow contact aureole is developed around it. These complex spatial relations between the stock and the host rock make it difficult to map the contacts and suggest strong interaction between them. In addition, marble and pelitic xenoliths are abundant inside the main igneous body. Marbles form continuous hectometric layers that define a round-shape geometry underlining the main structural trends of the areas where it crops out (Fig. 2.1). Pelitic xenoliths consist of rounded to irregular-shaped bodies of centimetric to decametric size. Both xenoliths and pelitic rocks from the inner aureole are migmatitic. Migmatites show highly variable textures at the meso- and micro-scale. In order to refer to individual rock types, the current thesis employs the migmatite terminology of Sawyer (2008), based on their macro- to

**Figure 2.1.** Geological sketch map of the Roc de Frausa Massif and Sant Llorenç–La Jonquera plutonic complex, modified from Liesa (1994).

microscopic appearance. In these rocks, only a contact-metamorphic climax is distinguished, overprinting previous regional metamorphism. Thermometry for the composition of coexisting garnet and retrograde biotite indicated equilibration at about 650–700 °C (Liesa & Carreras, 1989). Thus, the contact metamorphism at deep levels constituted the latest and highest temperature stage of the Variscan metamorphic evolution (Liesa, 1994).

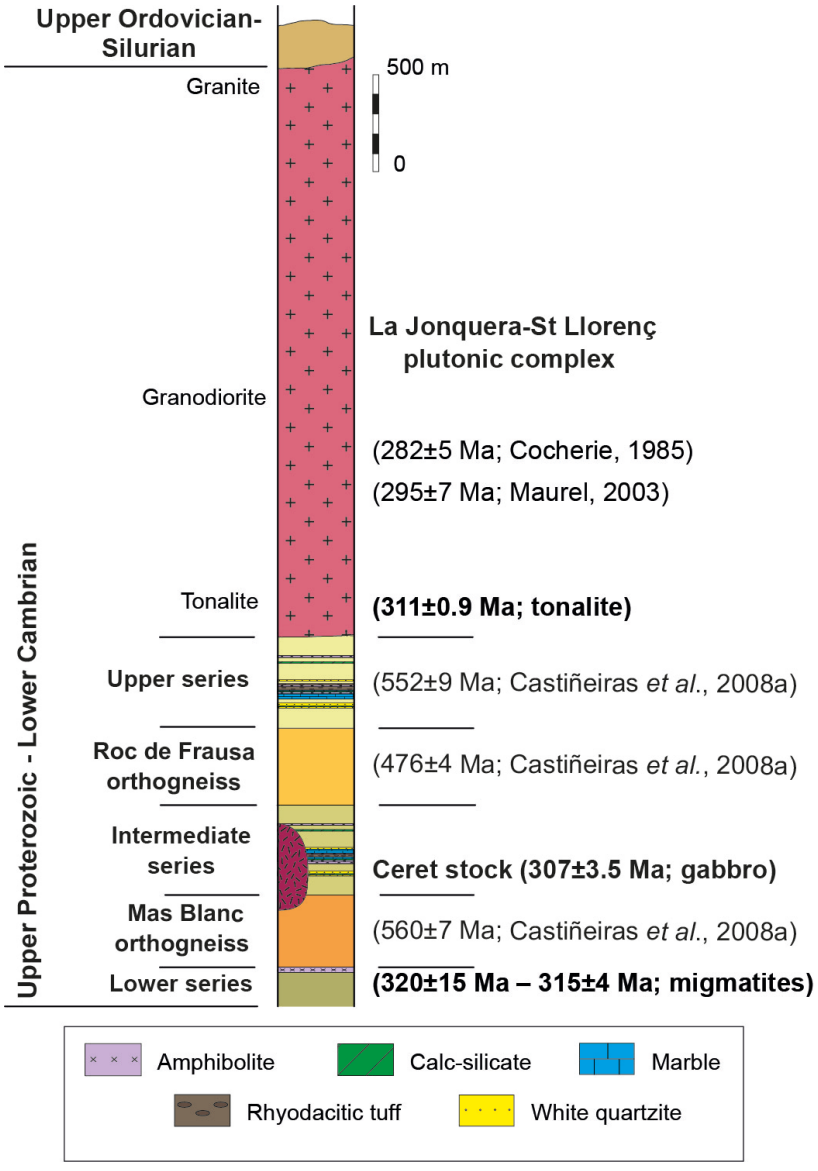


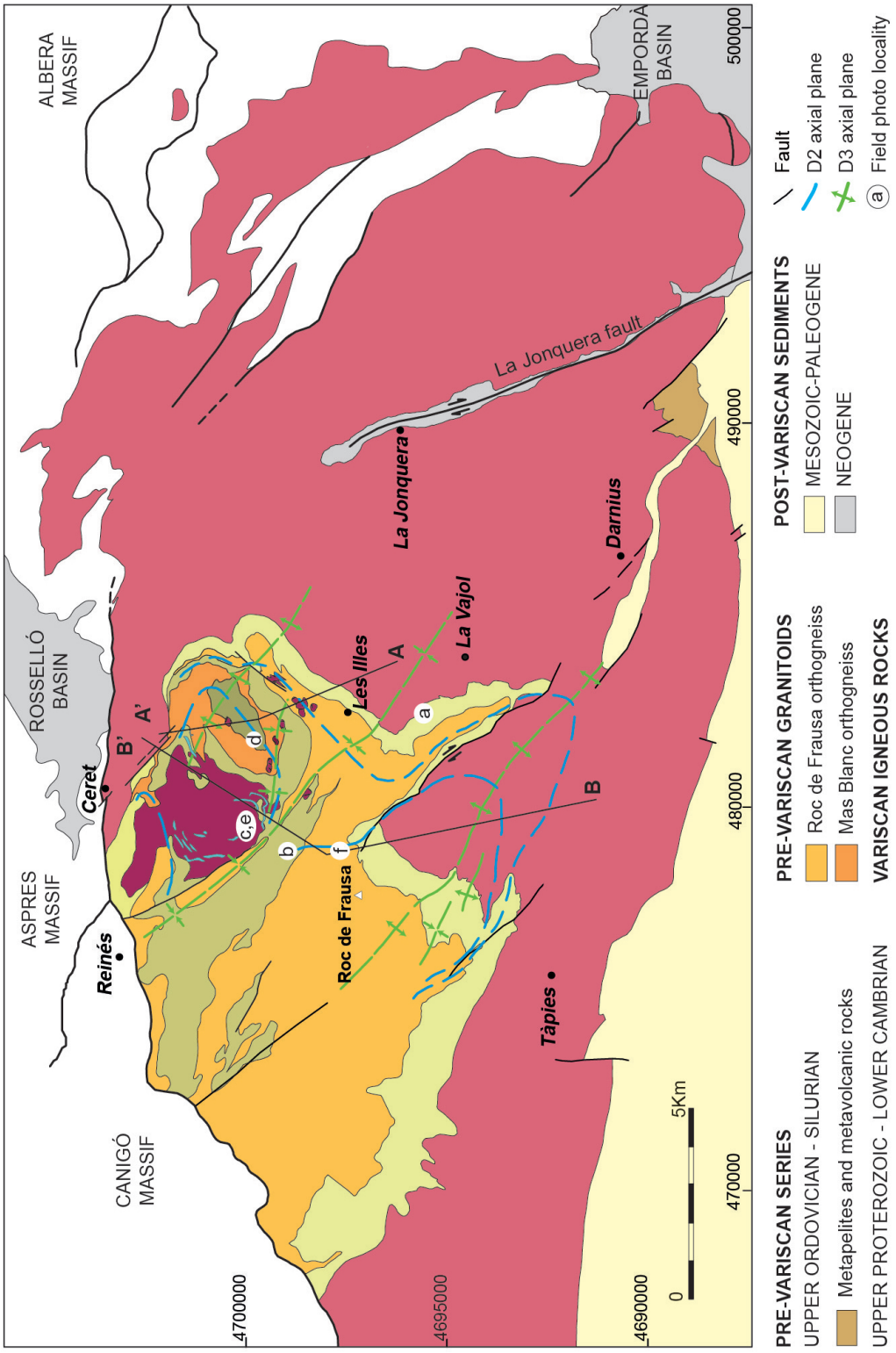

**Figure 2.2.** Synthetic stratigraphic column of Roc de Frausa Massif indicating the intrusion level of the Sant Llorenç–La Jonquera plutonic complex and the Ceret gabbro-diorite, modified from Liesa (1994). New U–Pb zircon dating obtained by Aguilar *et al.* (in review) in bold.

# CHAPTER 3

## STRUCTURAL EVOLUTION

According to previous studies carried out in the Roc de Frausa Massif (Autran & Guitard, 1969; Estévez, 1973; Geyssant *et al*., 1978; Liesa & Carreras, 1989), several deformation events affecting the pre-Variscan rocks can be distinguished. Although these authors do not agree on the number of phases, they all describe an early phase generating a main foliation formed in metamorphic conditions and late folding phases. According to Liesa & Carreras (1989), two Variscan folding phases (D1 and D2) followed by two late folding phases (D3 and D4) affected the regional foliation (S2), which was produced during the initial stages of Variscan metamorphism. The S2 foliation was produced during deformation event D2 and folded a previous foliation S1 parallel to the original bedding. Nevertheless, as no other structures associated to S1 have been found, in this thesis, S1 has been interpreted as the original bedding of the massif and called S0 and metamorphic minerals crystallizing parallel to S0 have been interpreted as mimicking S0. In consequence, D2, D3 and D4 events have been renumbered as D1, D2 and D3, which are described in this thesis (see Figs. 3.1–3.3). This reinterpretation makes the classification of structural events more consistent with the deformation events observed in the neighboring areas (e.g., Albera Massif; Vilà *et al.,* 2005 and Cap de Creus Massif; Druguet, 2001).

S1 is ubiquitous throughout the massif and is the main D1 structure. No major structures associated to the development of this foliation have been recognized, though at outcrop and microscopic scale S1 is an axial plane foliation of intrafolial folds involving both S0 and a foliation parallel to it (Figs. 3.2a & b). At map scale, the main foliation (S1) is parallel to the contacts between the different lithologies within the metasedimentary layers and the orthogneiss units forming characteristic map scale compositional layering.


ALBERA MASSIF
ROSSELLÓ BASIN
EMPORDÀ BASIN
ASPRES MASSIF
CANIGÓ MASSIF
Ceret
Reinés
Roc de Frausa
Les Illes
La Jonquera
La Vajol
Darnius
Tàpies
La Jonquera fault
A
A'
B
B'
a
b
c,e
d
f
4700000
4695000
4690000
470000
480000
490000
500000
0
5Km
PRE-VARISCAN SERIES
UPPER ORDOVICIAN - SILURIAN
Metapelites and metavolcanic rocks
UPPER PROTEROZOIC - LOWER CAMBRIAN
Upper series
Intermediate series
Lower series
Metapelites and metagreywackes
PRE-VARISCAN GRANITOIDS
Roc de Frausa orthogneiss
Mas Blanc orthogneiss
VARISCAN IGNEOUS ROCKS
Granitoids
Gabbro-diorite
POST-VARISCAN SEDIMENTS
MESOZOIC-PALEOGENE
NEOGENE
Fault
D2 axial plane
D3 axial plane
ⓐ Field photo locality

D2 structures mostly correspond to cartographic scale upright and close to tight folds best visible in the eastern part of the massif (Fig. 3.1). In medium-grade metamorphic domains no foliation associated to F2 folds develop, whereas in high-grade domains, the S1 foliation is strongly folded at all scales and transposed by S2 foliation (Fig. 3.2c & d). The axial surfaces of the F2 folds show modified and variable orientation as a result of the F3 refolding. Their present strike varies from WNW–ESE to NE–SW (Fig. 3.1). Unfolding of the F3 folds would result into the NE–SW trending F2 folds facing to the NW (Fig. 3.3–A-A´). In the structurally deeper domains, S2 foliation strikes NE–SW with a steep dip.

The geometry of the D2 structures are best evidenced in a NW–SE cross-section and in the associated stereoplots (Fig. 3.3–A-A´). The two maxima of the foliation show the two flanks of the F2 upright folds, a steep one dipping to the NW and a shallower one dipping to the SE. The poles of the foliation are dispersed along NW–SE great to small circles, thus indicating that they are folded by a subsequent deformation phase. Fold axes of the minor folds are contained in the D2 axial planes as a result of the superposition with the F1 folds.

The gabbro-diorite stock evidences a preferred orientation of the magmatic fabric parallel to S2 (Fig. 3.2e). In contrast, the magmatic fabric of the tonalite-granite intrusion, emplaced on top of the Upper series, tends to parallelize to S1; regardless that, at small scale the contact of the intrusive rocks crosscuts the S1 fabric (Liesa, 1994). The attitude of the magmatic fabric of the tonalite-granite intrusion fits with the laccolithic shape of the body postdating S1 that would be approximately subhorizontal at the time the intrusion took place. These facts, together with the map pattern of the intrusive rocks, indicate that the F2 folds deform the tonalite-granite laccolith, but are coeval with the intrusion of the gabbro-diorite at deeper levels. These field chronological relationships are consistent with zircon U–Pb geochronology that yield an older age for the tonalite-granite (314–311 Ma) with respect to that of the gabbro-diorite (312–307 Ma) (Aguilar *et al*., in review), thereby constraining the timing of the D1 and the D2 events.

**Figure 3.1.** Geological sketch map of the Roc de Frausa Massif and Sant Llorenç–La Jonquera plutonic complex, modified from Liesa (1994). Location of field photographs and the position of the structural profile are indicated.

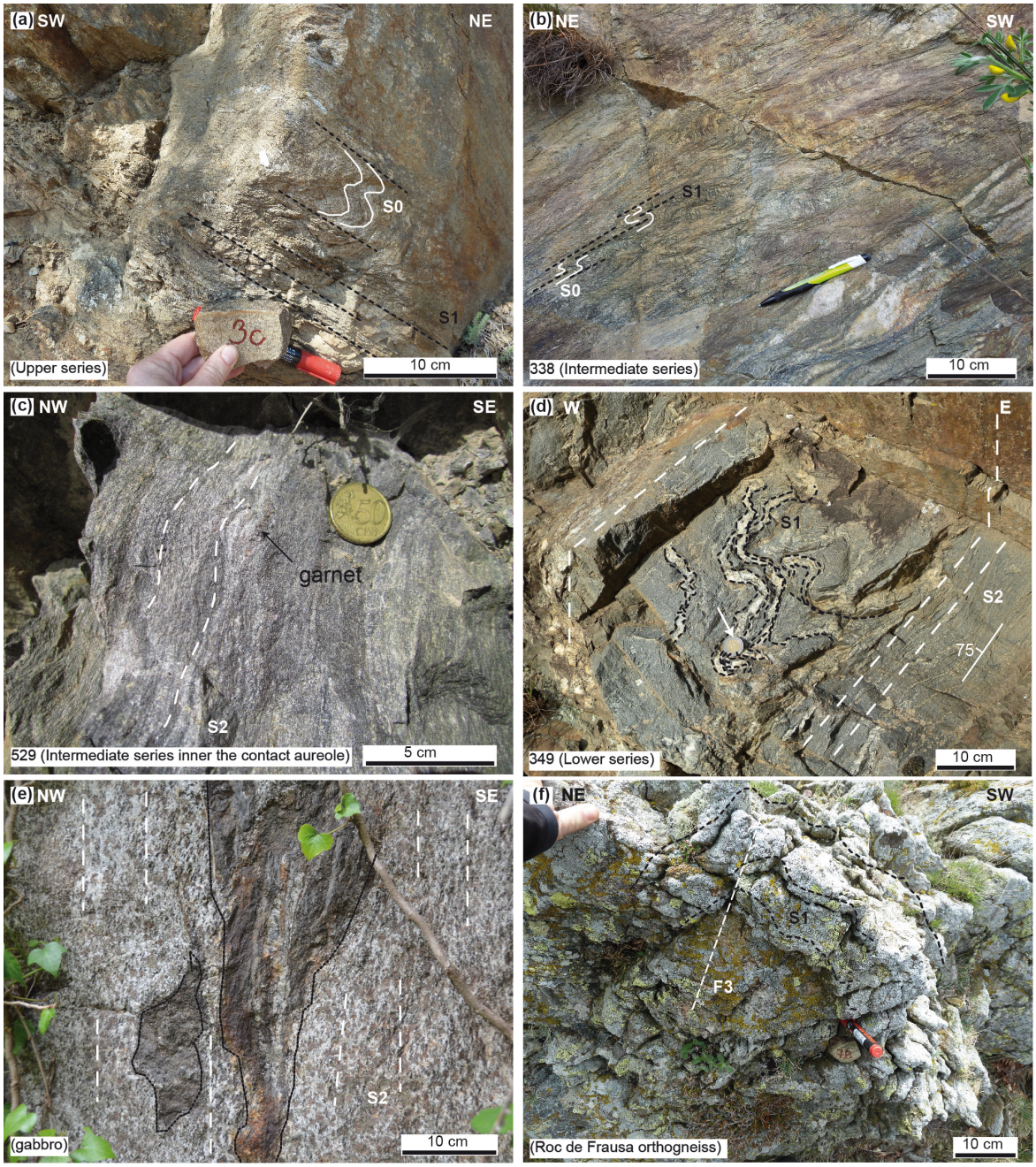



**Figure 3.2.** Structural relationships of the Roc de Frausa Massif: (a) subvertical folded relics of S0 in andalusite–sillimanite micaschists exhibiting S1 cleavage; (b) folded relics of S0 in sillimanite schists from the Intermediate series not affected by the Ceret gabbro-diorite contact aureole; (c) stromatic migmatites around the Ceret gabbro-diorite contact aureole with leucosomes parallel to S2; (d) F2 folds of leucosomes and S2 axial-plane cleavage in migmatites from the Lower series; (e) S2 foliation in the Ceret gabbro-diorite and migmatitic enclaves (highlighted by a dotted black line); and (f) Open F3 folds in the Roc de Frausa orthogneiss affecting S1 foliation. Location in Figure 3.1.

The D3 structures are characterized by WNW–ESE trending folds (Fig. 3.1) facing to the SW (Fig. 3.2f), which are clearly visible in a NNW–SSE cross-section and in the associated stereoplots (Fig. 3.3–B-B´). The poles of the S1 foliation are dispersed along N–S to NE–SW trending great circles with two maxima of the foliation drawing the two dipping flanks of the regional F3 folds. Their intersection defines an eastward plunging F3 fold axis, consistent with the minor fold axes measured in the field. All through the massif, the F3 folds have a fairly constant dip of the axial planes towards the NE, thus indicating that they constitute the last deformation phase in the studied area.

Shear zones with a mean strike and dip direction of 118/57NE occur parallel to the axial planes of the F3 folds (Fig. 3.3–B-B'). Shear zones affect both the metamorphic rocks and the granitoids and are associated with a pervasive retrograde foliation at greenschist facies conditions. Geometric relationships between the F3 folds and the shear zones suggest that they both are the result of the same deformation event. The D3 shear zones affecting the metamorphic rocks continue into the granitoids and structurally upwards they grade into the damaged zones of faults affecting the upper part of the granitic laccolith and the Paleocene rocks above. This would suggest an Alpine age for the shear zones and would be consistent with the post-Variscan age (from 100 Ma to 40 Ma, Maurel, 2003) of the shear zones dated at the eastern end of the massif (El Portús) using the Ar–Ar method. Interference of the F2 with the F3 folds and related shear zones define the main cartographic pattern of the Roc de Frausa Massif as well as its present antiformal geometry. This antiform is also depicted by the Mesozoic and Paleocene rocks preserved at both sides of the massif (Fontboté *et al*., 1986; Casas & Torrades, 2008) suggesting an Alpine age for the D3 structures

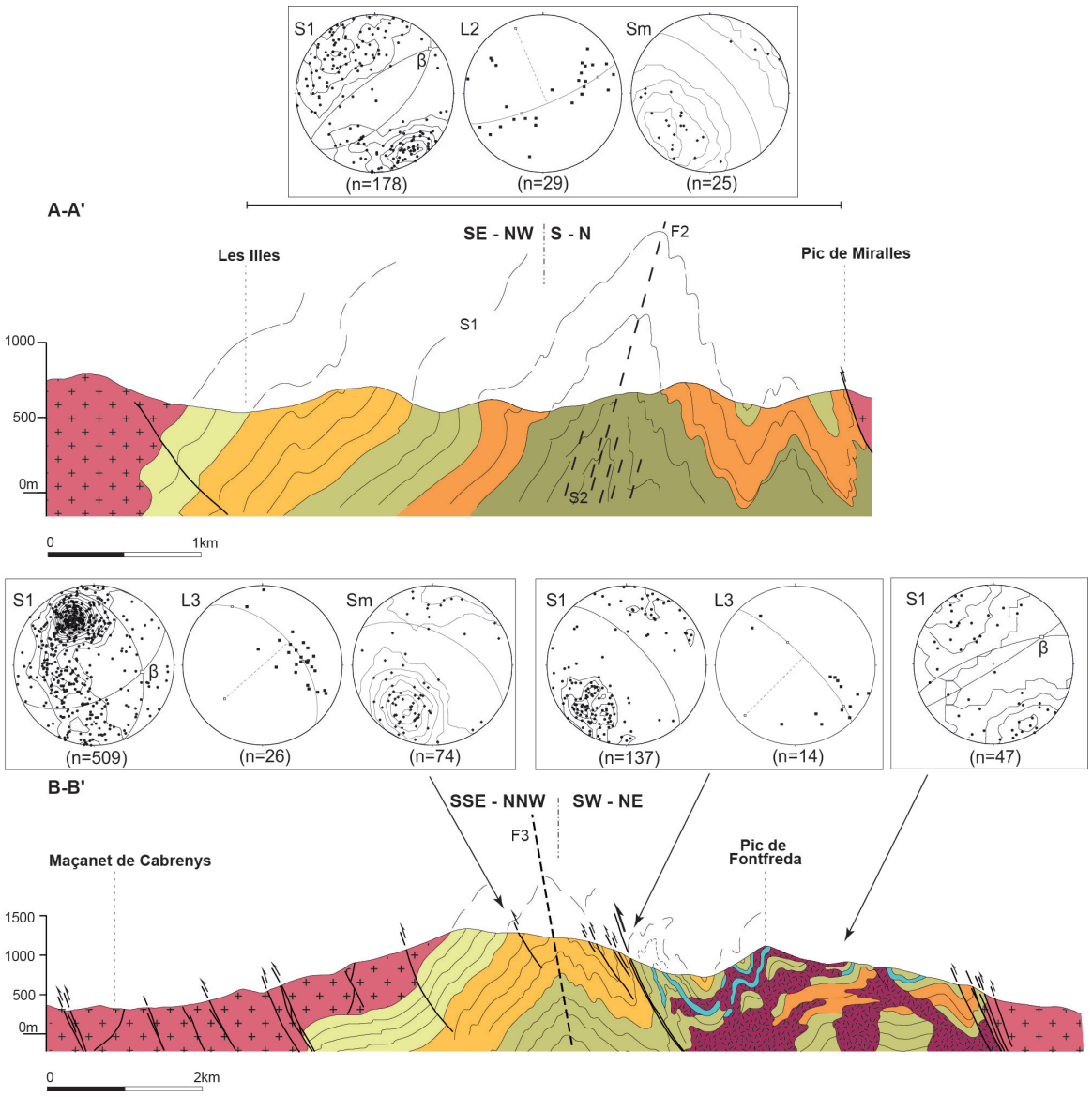



**Figure 3.3.** Cross-sections and lower hemispheric stereoplots showing the main structural relationships between the different rock units (legend as in Figure 3.1 and location of the cross-sections in Figure 3.1. L*: fold axes of the corresponding deformation events. Sm: milonitic foliation. Modified from Liesa & Carreras (1989).

# CHAPTER 4

## PETROGRAPHY, MINERAL CHEMISTRY AND WHOLE-ROCK COMPOSITION

In order to link deformation events with metamorphic assemblages, we performed a detailed petrological and meso- to microscopic structural analysis of metasedimentary rocks and migmatites. These rocks cover the three different levels (the Upper, Intermediate and Lower series) over significant thickness (~15km) of the orogenic Variscan crust in the Eastern Pyrenees.

### 4.1. Analytical procedures and abbreviations

Petrographic and meso- to microstructural studies were performed using a Zeiss Axiophot plane polarized transmitted light microscope equipped with a SONY camera and a Leica MS5 binocular microscope equipped with a Leica DFC 420 camera at the Departament de Petrologia, Geoquímica i Prospecció Geològica of the University of Barcelona. Both microscopes are connected to a computer with a program to capture the macro- to microscope images. Petrography and deformation-crystallization relationships are documented in figures 4.2–4.10.

Minerals were analyzed using the Cameca SX-50 electron microprobe with wavelength-dispersive spectrometer at the Centres Científics i Tecnològics (CCiT) of the University of Barcelona in point beam mode at 15nA and 20kV, with 10 μm beam diameter. Mineral chemistry is shown in figures 4.11–4.14 and representative mineral analyses are summarized in tables 4.1–4.3. Mineral abbreviations used are mu, muscovite; q, quartz; g, garnet; st, staurolite; opx, orthopyroxene; bi, biotite; ky, kyanite; sill, sillimanite; and, andalusite; cd, cordierite; pl, plagioclase; ksp, K-feldspar; liq, granitic liquid; ilm, ilmenite; mt, magnetite; sp, spinel; ru, rutile; alm = Fe / (Ca + Fe + Mg + Mn), prp = Mg / (Ca + Fe + Mg + Mn), grs = Ca / (Ca + Fe + Mg + Mn), sps =

Mn / (Ca + Fe + Mg + Mn), $X_{Fe}$ = Fe / (Fe + Mg), an = Ca / (Ca + Na + K), ab = Na / (Ca + Na + K), or = K / (Ca + Na + K).

Whole-rock major-element analyses were carried out on the X-ray fluorescence spectrometry at the Centres Científics i Tecnològics (CCiT) of the University of Barcelona. The equipment used was a sequential X-ray spectrometer by dispersion of wave length (WDXRF) Model Philips PW2400. Whole-rock compositions are shown in figures 4.14–4.16 and representative whole-rock chemical analyses are given for metasedimentary rocks and migmatites of different crustal levels of the massif in Table 4.4.

## 4.2. Petrography and deformation-crystallization relationships

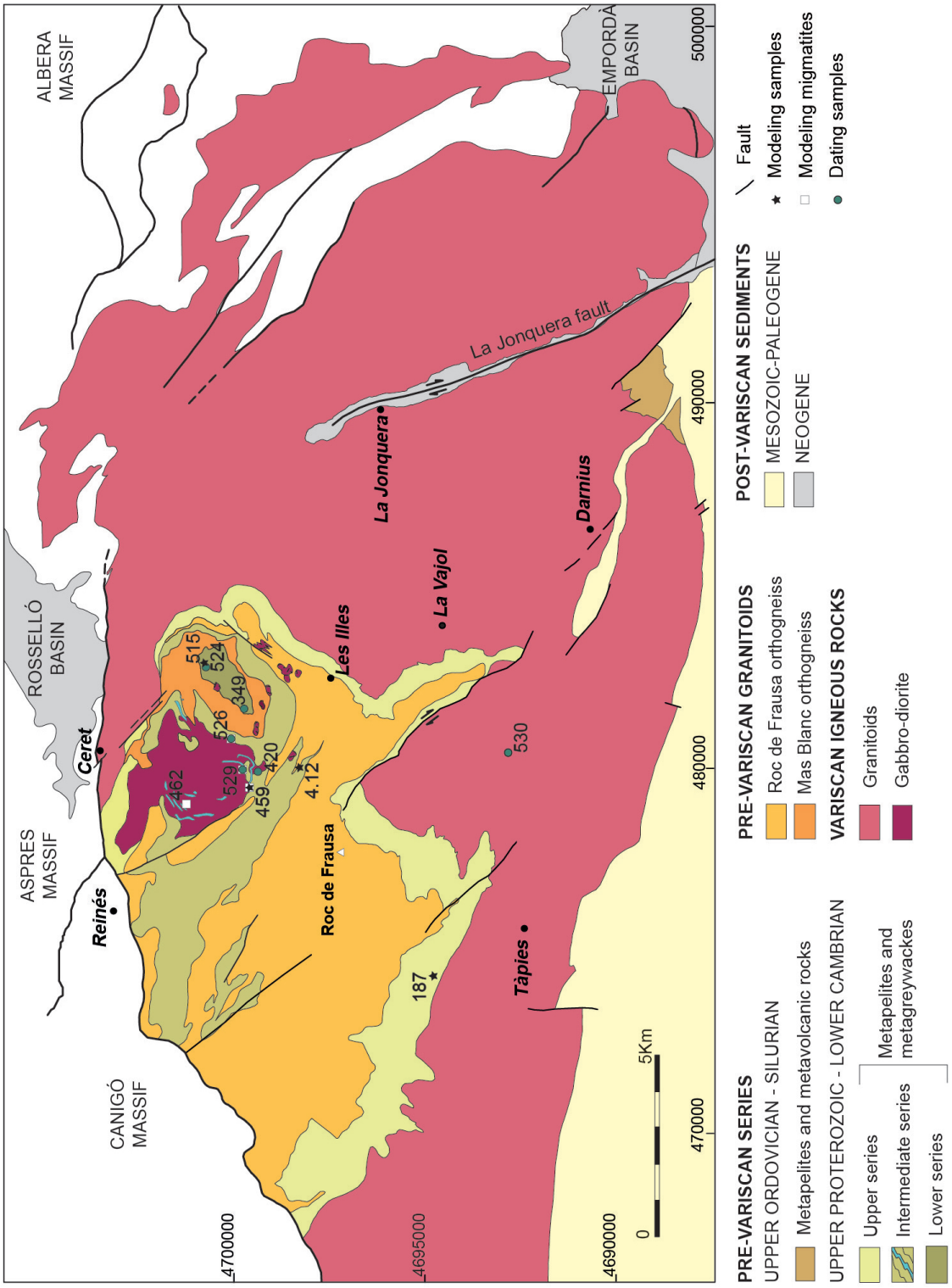
Petrographic and meso- to microstructural studies were carried out in metasedimentary rocks and migmatites of different structural levels of the Roc de Frausa Massif (Fig. 4.1), from which a few were selected for mineral chemical and whole-rock analysis (see section 4.3 and 4.4). In addition, tonalite and gabbro will be also described in this section.

To establish the relative timing between structures and metamorphism, the logic of relationships between multiple foliation development and porphyroblast and mineral growth is adopted (see for example Bell & Welch, 2002). Thin sections were cut perpendicular to the fold axis and intersection lineations of superimposed the S1 and the S2 foliations.

### 4.2.1. The Upper series

Andalusite–sillimanite micaschists are the dominant lithology. They are fine-grained (<0.5 mm) with alternating recrystallized plagioclase–quartz-rich and mica–sillimanite-rich layers, defining the main S1 foliation or mimicking S0 fabric. The characteristic mineral assemblage is muscovite, biotite, andalusite, fibrolitic

**Figure 4.1.** Geological sketch map of the Roc de Frausa Massif and Sant Llorenç–La Jonquera plutonic complex with the location of representative samples used in this thesis. Modified from Liesa (1994).


ALBERA MASSIF
ROSSELLÓ BASIN
EMPORDÀ BASIN
ASPRES MASSIF
CANIGÓ MASSIF
Ceret
Reinés
Les Illes
La Jonquera
La Vajol
Darnius
Roc de Frausa
Tàpies
La Jonquera fault
462
529
526
515
524
349
459
420
4.12
530
187
500000
490000
480000
470000
4700000
4695000
4690000
0
5Km
PRE-VARISCAN SERIES
UPPER ORDOVICIAN - SILURIAN
Metapelites and metavolcanic rocks
UPPER PROTEROZOIC - LOWER CAMBRIAN
Upper series
Intermediate series
Lower series
Metapelites and metagreywackes
PRE-VARISCAN GRANITOIDS
Roc de Frausa orthogneiss
Mas Blanc orthogneiss
VARISCAN IGNEOUS ROCKS
Granitoids
Gabbro-diorite
POST-VARISCAN SEDIMENTS
MESOZOIC-PALEOGENE
NEOGENE
Fault
Modeling samples
Modeling migmatites
Dating samples

sillimanite, cordierite, plagioclase and quartz. Accessory minerals are ilmenite, zircon and monazite.

Andalusite forms subidiomorphic porphyroblasts (up to 0.5 mm) that contain oriented inclusion trails of ilmenite parallel or oblique to the external S1 foliation. It is wrapped by micas and sillimanite parallel to the main S1 foliation, locally forming S1 pressure shadows (Fig. 4.2a). Cordierite forms poikiloblasts (>0.5 mm) that enclose the previous mineral assemblages and do not reveal pressure shadows (Fig. 4.2b). Globally, the microstructural relations suggest that andalusite preceded sillimanite in the S1 fabric, and cordierite was formed after the D1 deformation event. Muscovite and biotite are stable throughout the whole deformational history (Fig. 4.3a).

### 4.2.2. The Intermediate series not affected by the Ceret gabbro-diorite contact aureole

Fine to medium grained sillimanite schists are the dominant lithology. They are compositionally banded rocks with alternating millimetre-scale quartzo-feldspathic and muscovite–biotite–sillimanite-rich layers. These layers are defining either the main S1 foliation or the composite S1/S0 fabric (Fig. 4.2c). Minor proportions of cordierite and K-feldspar may be present. Accessory minerals are ilmenite, zircon, xenotime and monazite.

Cordierite is present both in the quartzo-feldspathic layers and in the melanocratic layers. Similarly to the Upper series micaschists, it includes the minerals forming the S1 and does not display pressure shadows (Fig. 4.2d). Muscovite is typically ragged and replaced by fibrolitic sillimanite. However, some muscovite contains sillimanite folded by F2 folds, and it is therefore interpreted as post-tectonic. Microstructural relations suggest that sillimanite is stable in the S1 foliation, and cordierite grows after the D1 deformation event. Muscovite and biotite are stable throughout the whole deformational history (Fig. 4.3b).

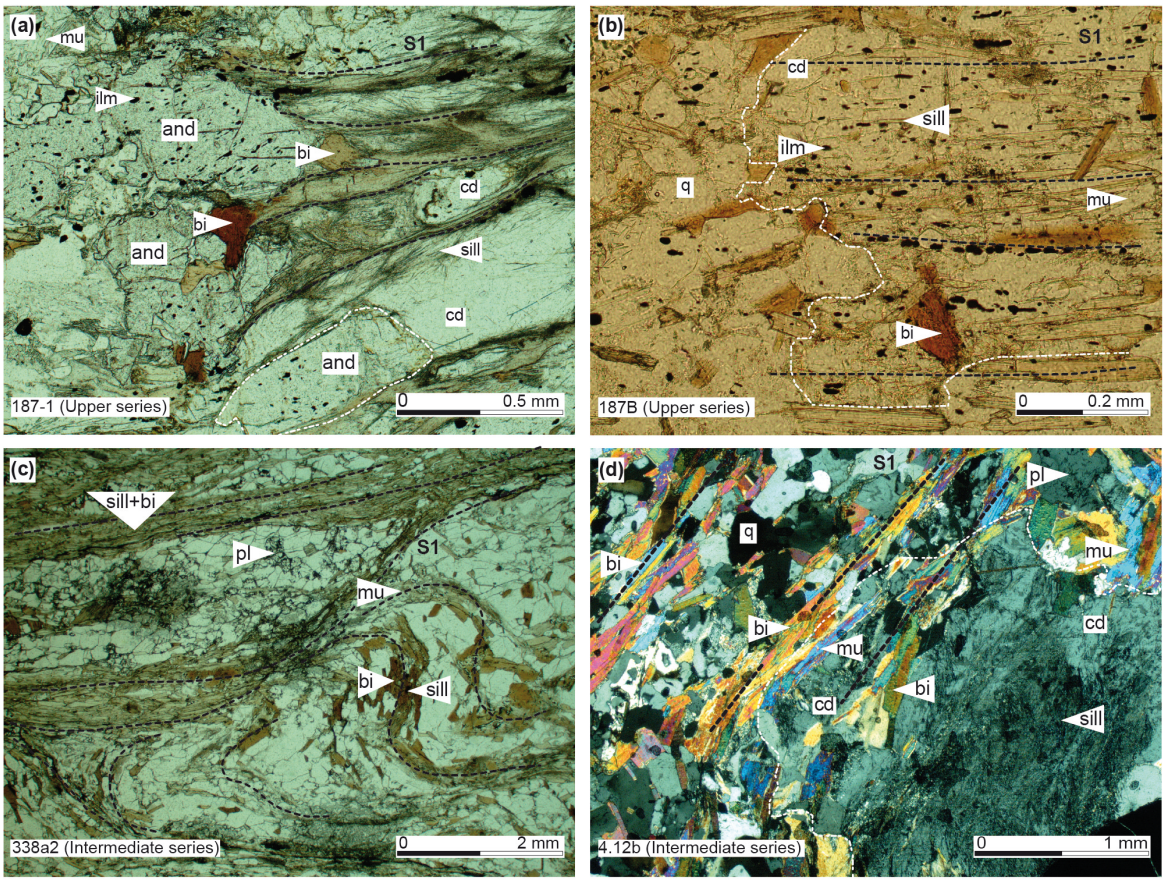
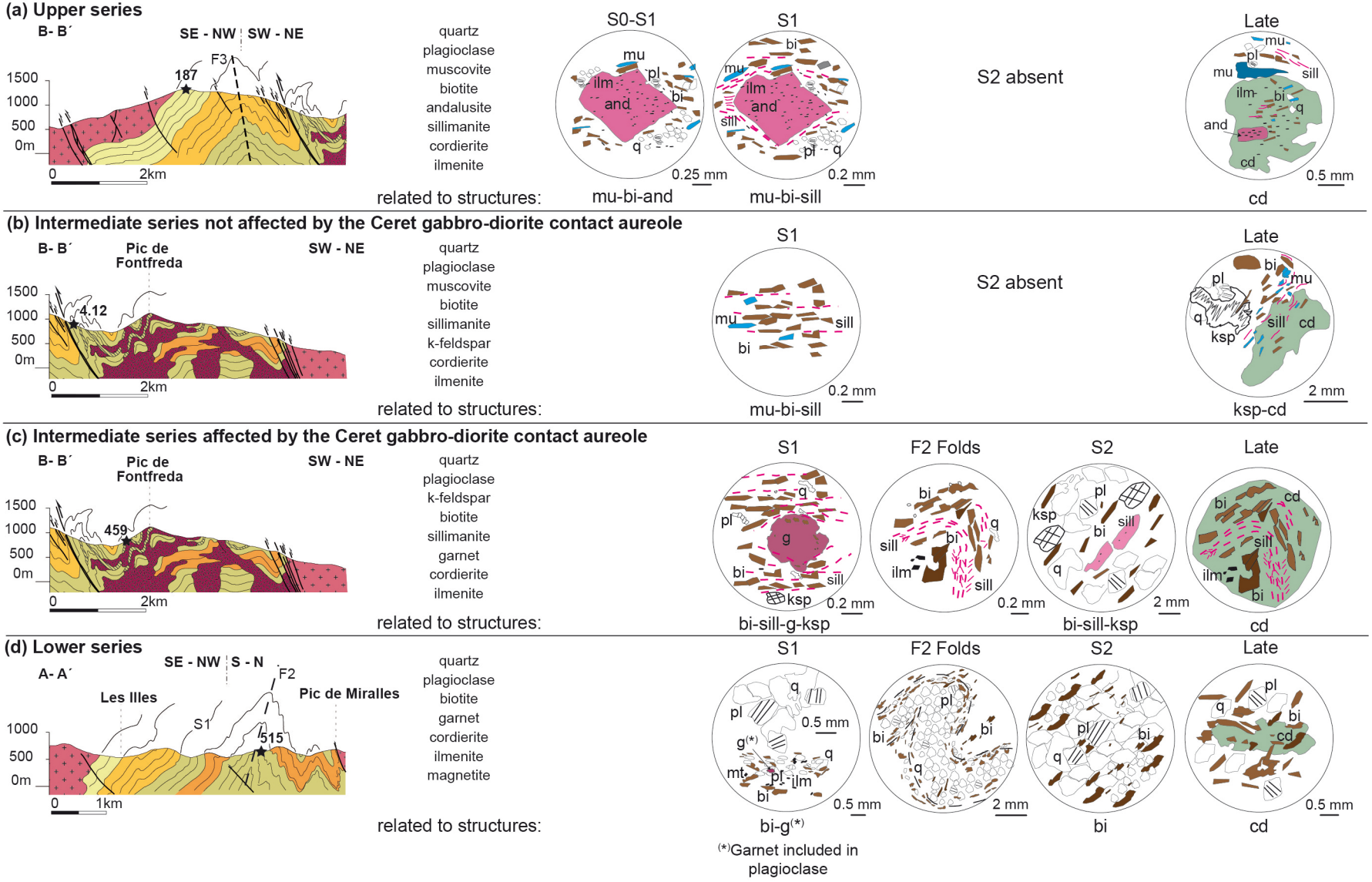



**Figure 4.2.** Microstructural relationshisps of the Upper series (a–b) and the Intermediate series not affected by the Ceret contact aureole (c–d). (a) Andalusite porphyroblasts wrapped by S1 foliation, defined by muscovite, biotite and sillimanite with well-developed S1 pressure shadows; (b) poikiloblastic cordierite (outlined by white dashed lines) including a straight S1 internal foliation without pressure shadow; (c) S0 folded relics within S1 intrafoliation; and (d) cordierite poikiloblast (outlined by white dashed lines) contains straight trails of muscovite, biotite and sillimanite, continuous with external S1 foliation. No pressure shadows are formed around cordierite.

### 4.2.3. The Intermediate series affected by the Ceret gabbro-diorite contact aureole

Pelitic migmatites are the major rock types in the inner aureole and xenoliths of the Ceret gabbro-diorite stock. Migmatites are texturally highly variable at meso- to micro-scale. In order to refer to individual rock types, the current thesis employs the migmatite terminology of Sawyer (2008), based on their macro- to microscopic appearance. In the inner aureole, they range from patch to stromatic and schollen types. Inside the gabbro-diorite, xenoliths are constituted by schollen and residuum melanosome dominated migmatites. They are composed of varying proportions of


(a) Upper series
B- B´
SE - NW
SW - NE
F3
187
1500
1000
500
0m
0
2km
quartz
plagioclase
muscovite
biotite
andalusite
sillimanite
cordierite
ilmenite
S0-S1
S1
Late
mu
pl
ilm
and
bi
q
sill
cd
0.25 mm
0.2 mm
0.5 mm
S2 absent
related to structures:
mu-bi-and
mu-bi-sill
cd
(b) Intermediate series not affected by the Ceret gabbro-diorite contact aureole
B- B´
Pic de Fontfreda
SW - NE
4.12
1500
1000
500
0m
0
2km
quartz
plagioclase
muscovite
biotite
sillimanite
k-feldspar
cordierite
ilmenite
S1
Late
mu
sill
bi
pl
q
ksp
cd
0.2 mm
2 mm
S2 absent
related to structures:
mu-bi-sill
ksp-cd
(c) Intermediate series affected by the Ceret gabbro-diorite contact aureole
B- B´
Pic de Fontfreda
SW - NE
459
1500
1000
500
0m
0
2km
quartz
plagioclase
k-feldspar
biotite
sillimanite
garnet
cordierite
ilmenite
S1
F2 Folds
S2
Late
g
pl
bi
sill
ksp
q
ilm
cd
0.2 mm
2 mm
related to structures:
bi-sill-g-ksp
bi-sill-ksp
cd
(d) Lower series
A- A´
SE - NW
S - N
F2
Les Illes
Pic de Miralles
S1
515
1000
500
0m
0
1km
quartz
plagioclase
biotite
garnet
cordierite
ilmenite
magnetite
S1
F2 Folds
S2
Late
pl
q
g(*)
mt
ilm
bi
0.5 mm
2 mm
related to structures:
bi-g(*)
bi
cd
(*)Garnet included in plagioclase

biotite, both fibrolitic and prismatic sillimanite, garnet, cordierite, plagioclase, quartz and K-feldspar. Sillimanite and/or K-feldspar are absent in stromatites and residuum melanosomes. Paleosomes generally contain biotite, sillimanite and cordierite and leucosomes are dominated by quartz, plagioclase, K-feldspar and garnet. The accessory minerals are ilmenite, pyrite, apatite, zircon, monazite, and locally green or brown spinel included in cordierite or prismatic sillimanite and corundum included in sillimanite. Sericite, pinnite and muscovite are present as retrograde minerals, associated to the last deformation event (D3; not shown in the figures).

- ***Patch migmatites***

Patch migmatites are composed by fine-grained paleosomes with small patches of coarse-grained leucosomes (Fig. 4.4a). The paleosomes are formed by alternating xenoblastic quartz and plagioclase layers with fibrolite-biotite-rich layers, with grano-nematoblastic textures. The scarce lenses of leucosomes are composed of coarse-grained quartz, biotite and feldspars, with a granoblastic to granular texture. Garnet and cordierite occur as porphyroblasts in the paleosome and prismatic sillimanite is absent. Accessory minerals are ilmenite, pyrite, apatite, zircon and monazite.

Patch migmatites are well-foliated rocks preserving two deformation events: D1 and D2 (Fig. 4.8a). S1 foliation is defined by alternating quartz–plagioclase-rich and biotite–sillimanite (fibrolite)-rich layers. S1 is folded by D2 deformation event and locally, an axial plane foliation S2 develops. The small patches of quartz, plagioclase and K-feldspar-rich leucosomes are oriented parallel to S2 foliation (Fig. 4.4b). Garnet porphyroblasts (up to 4.5 mm) have inclusion trails of fibrolite, biotite and ilmenite near the rim and oriented parallel to S1 fabric (Fig. 4.4c). We interpret that garnet grew over the S1 fabric in the presence of sillimanite and biotite (Fig. 4.4d). Cordierite poikiloblasts enclose all minerals of the assemblage and it grows either parallel to the flanks of the folded S1 foliation or to the S2 fabric (Fig. 4.4e). Therefore, it is interpreted as growing late- to post-D2 event.

**Figure 4.3.** Schematic blastesis-deformation relationships of metapelites and migmatites from the different crustal levels of the Roc de Frausa Massif.

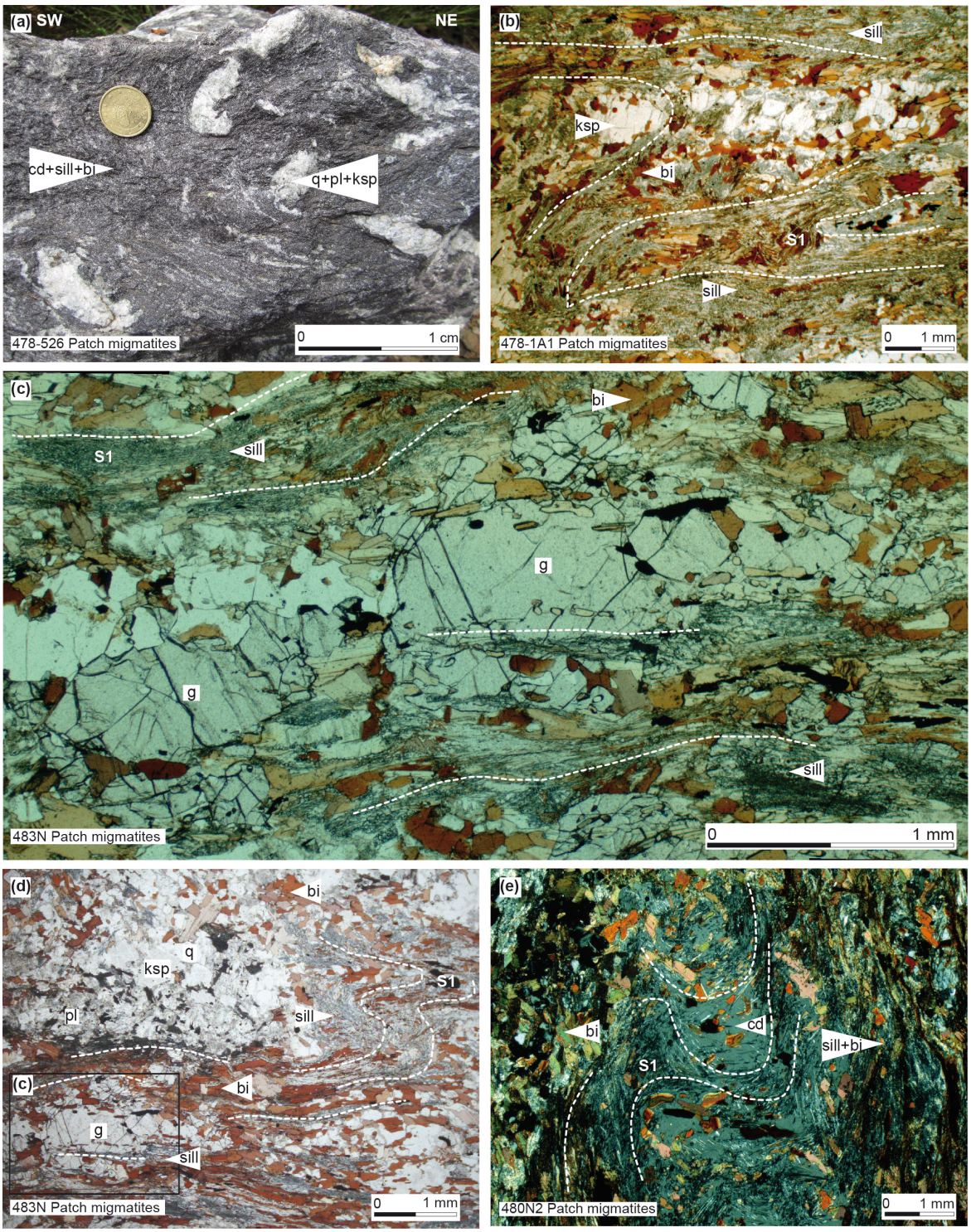



**Figure 4.4.** Macro- to microstructural relationships in patch migmatites from the Intermediate series affected by the Ceret gabbro-diorite contact aureole: (a) coarse-grained lenses of leucosome embedded by sillimanite and biotite-rich paleosome; (b) biotite and sillimanite parallel to S1 foliation folded by the D2 event and patches of K-feldspar-rich leucosome parallel to axial plane of F2 fold; (c) detail of the garnet rim from picture d including sillimanite and biotite parallel to S1 foliation; (d) biotite, sillimanite and garnet parallel to S1 foliation folded by the D2 event; and (e) cordierite poikiloblats including folded S1 foliation and S2 oriented biotite.

- ***Stromatic migmatites***

The stromatites are formed by well-foliated fine-grained melanosomes with a granolepidoblastic texture alternating with coarse-grained leucosomes with granular texture (Fig. 4.5a). Leucosomes and melanosomes are distributed parallel to S2 foliation (Fig. 4.8b).

The leucosomes are constituted by quartz, coarse-grained biotite and plagioclase with an allotriomorphic to subidiomorphic granular texture. Garnet occurs as porphyroblasts (up to 5 mm) in the boundary of leucosome-melanosome or in the leucosome (Fig. 4.5b & c). They are corroded and partially replaced by biotite and plagioclase. The melanosomes are formed by abundant biotite oriented parallel to S2 foliation or crystallizing as unoriented plates mimicking S2 and cordierite poikiloblasts. Cordierite mostly enclose biotite and spinel and no S2 pressure shadows develop around it (Fig. 4.5d). Therefore, it is interpreted as growing late- to post-D2 event. Accessory minerals are ilmenite, pyrite, apatite, zircon, monazite, and locally, green spinel included in cordierite (Fig. 4.5e).

- ***Schollen migmatites***

The schollen migmatites are constituted by fragments of fine-grained paleosomes embedded in coarse-grained leucosomes (Fig. 4.6a & b). The paleosomes are formed by alternating xenoblastic quartz and plagioclase layers with fibrolite-biotite-rich layers with granolepidoblastic microstructures (Fig. 4.6c). The leucosomes are composed of quartz, coarse-grained biotite, feldspars, garnet porphyroblasts and prismatic sillimanite, with a granoblastic to granular texture. Plagioclase is microperthitic and locally forms idiomorphic to subidiomorphic porphyroblasts (up to 2 mm). K-feldspar is very scarce. Cordierite occurs as poikiloblasts in paleosomes and leucosomes. Accessory minerals are ilmenite, pyrite, apatite, zircon, monazite, and green or brown spinel and corundum included in cordierite or prismatic sillimanite, and corundum also included in sillimanite.

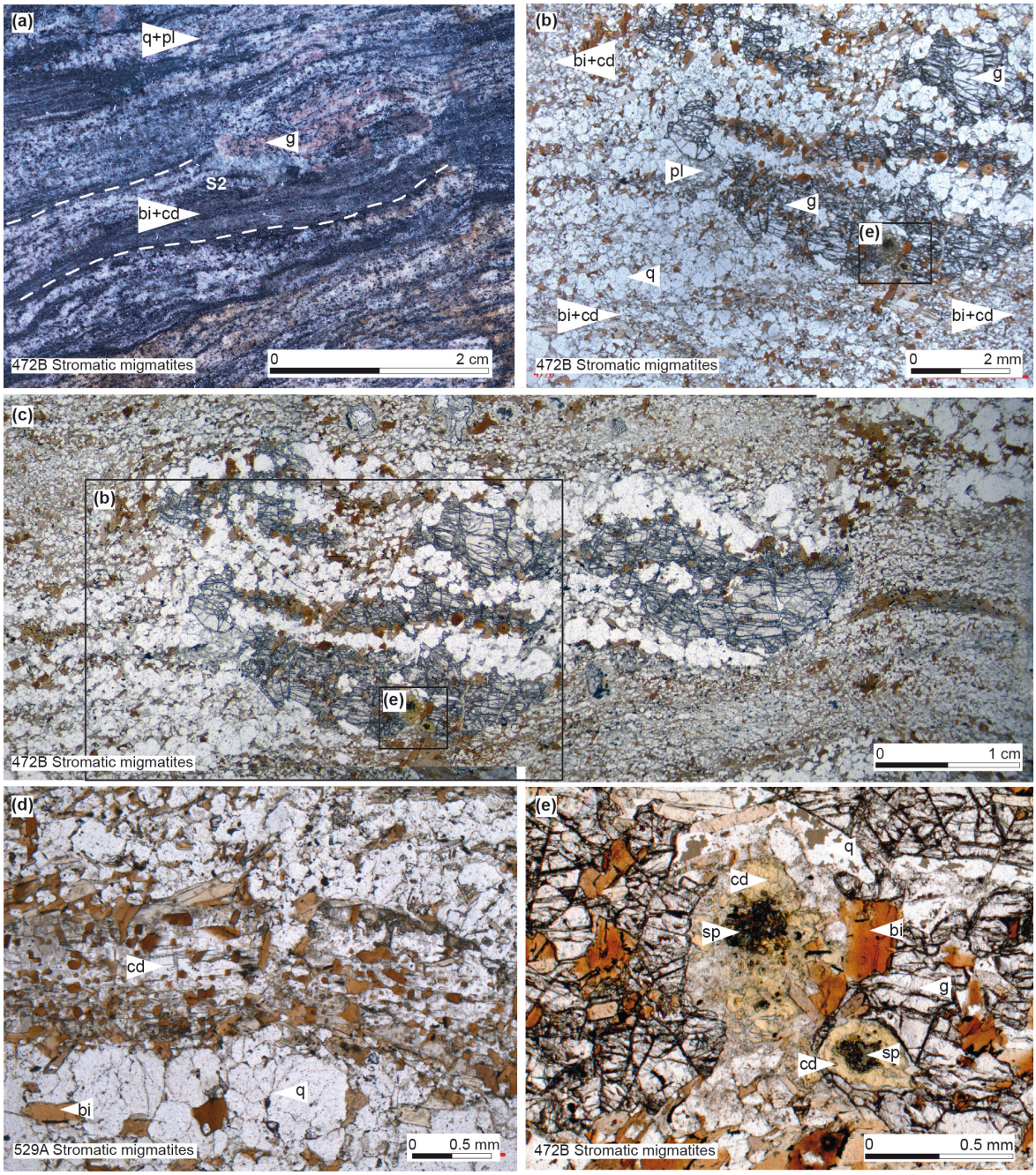



**Figure 4.5.** Macro- to microstructural relationships in stromatic migmatites from the Intermediate series affected by the Ceret gabbro-diorite contact aureole: (a) alternating fine-grained melanosome layers with coarse-grained leucosomes parallel to S2 foliation; (b) garnet porphyroblasts in the boundary of leucosome and melanosome; (c) layer of Leucosome (quartz+plagioclase+garnet) hosted by a sillimanite-poor and cordierite-rich melanosome; (d) cordierite poikiloblasts mostly enclose biotite; and (e) detail of spinel included by cordierite from picture c.

The S1 foliation is preserved in low-strain domains within the S2 fabric and is defined by alternating quartz–plagioclase-rich and biotite–fibrolite-rich layers (Fig. 4.6b & c). In places where the S2 foliation almost completely transposes the previous fabrics, it is also defined by quartz, plagioclase-rich leucosomes with local K-feldspar oriented parallel to the axial planes of F2 folds. Locally, S1 is an axial plane foliation of a former one defined by fibrolitic sillimanite, which has been interpreted as mimicking S0 (Fig. 4.6d). Bulky prismatic sillimanite (about 10 mm long) parallel to S2 fabric or radiating clusters present either in the paleosome or in the leucosome. Locally, it contains inclusion trails of ilmenite and biotite parallel to the S1 fabric. Some crystals have S2 pressure shadows, but some do not have them thus indicating that they grew syn- to late-D2 deformation (Fig. 4.6e). Garnet porphyroblasts (up to 5.5 mm) are surrounded by pressure shadows aligned parallel to the S2 indicating that the D2 deformation developed after its growth. They are surrounded by cordierite poikiloblasts (up to 3–6 mm); therefore it is interpreted as late- to post-D2 event (Fig. 4.6f & 4.8c).

- ***Residuum melanosomes***

The residuum melanosomes constitute massive rocks with no foliation visible at outcrop scale (Fig. 4.7a). They are formed by garnet porphyroblasts (up to 8 mm) embedded in a cordierite-rich matrix (Fig. 4.7b). Garnet is xenoblastic and it presents embayments. Cordierite is idiomorphic and shows cyclic twinning (Fig. 4.7c). A relic foliation is slightly shown by inclusions of biotite and opaque ore included in the cordierite or in the matrix in between cordierite (Fig. 4.8d). Sillimanite and K-feldspar are absent, although sillimanite inclusions in garnet are found in some samples. Plagioclase locally forms idiomorphic to xenomorphic porphyroblasts (up to 2 mm) and crystallizes around garnet together with biotite plates (Fig. 4.7d). Quartz is scarce (around 2% modal) and crystallizes in interstices between cordierite (Fig. 4.7e). Accessory minerals are ilmenite, pyrite, rutile, tourmaline and brown spinel, the latter included in cordierite (Fig. 4.7f).

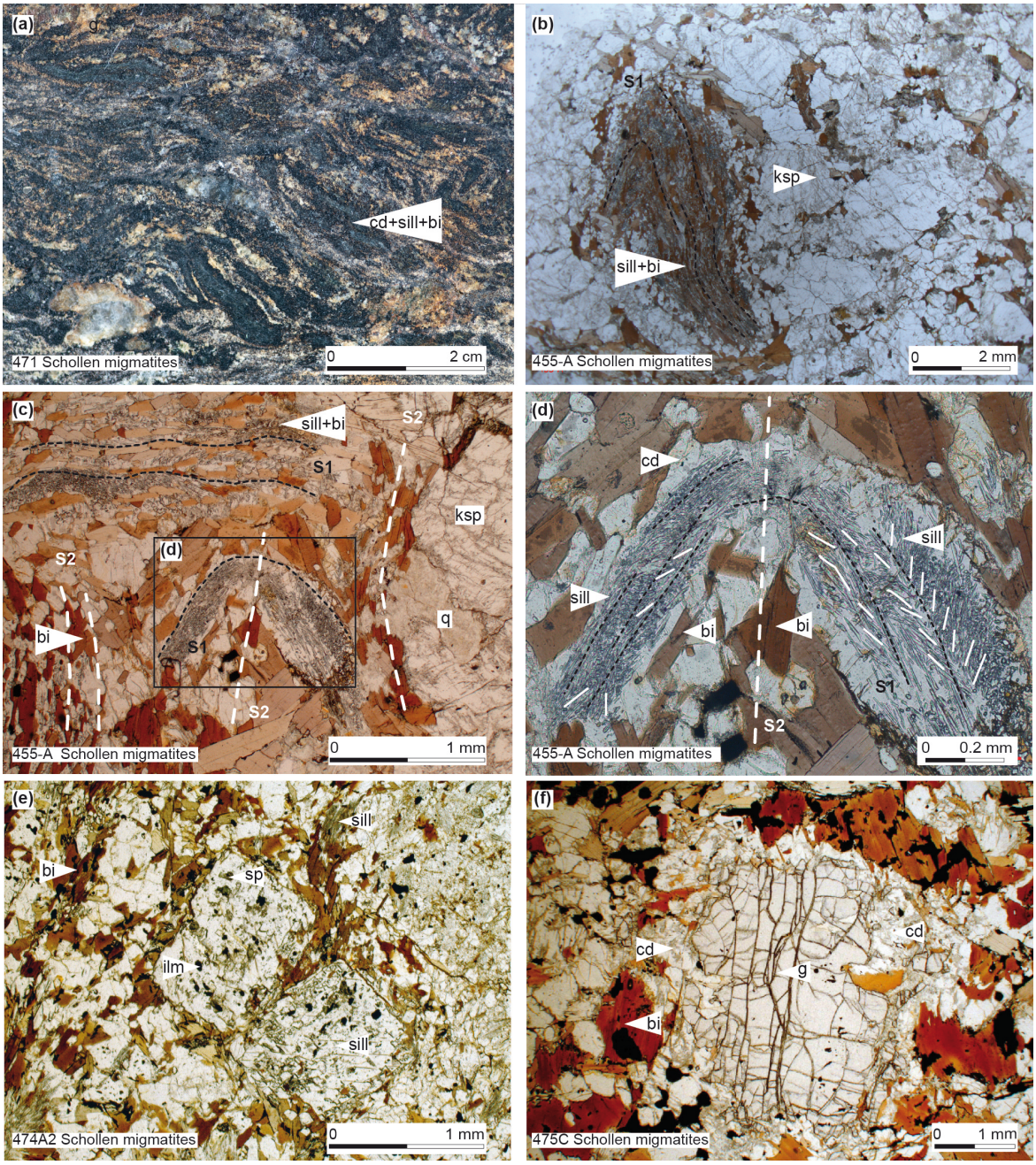



**Figure 4.6.** Macro- to microstructural relationships in schollen migmatites from the Intermediate series affected by the Ceret gabbro-diorite contact aureole: (a, b) biotite and sillimanite-rich paleosome embedded in a coarser-grained leucosome; (c) S1 foliation defined by sillimanite and biotite-rich paleosome is folded by the D2 event; (d) detail of the F2 fold: the limb are defined by S1 which is an axial plane foliation of a former one mimicking S0 and by fibrolitic sillimanite; (e) prismatic sillimanite in the leucosome with inclusions trails of biotite, ilmenite and locally, green spinel parallel to S1 fabric; and (f) cordierite corona around a garnet porphyroblast in the leucosome.

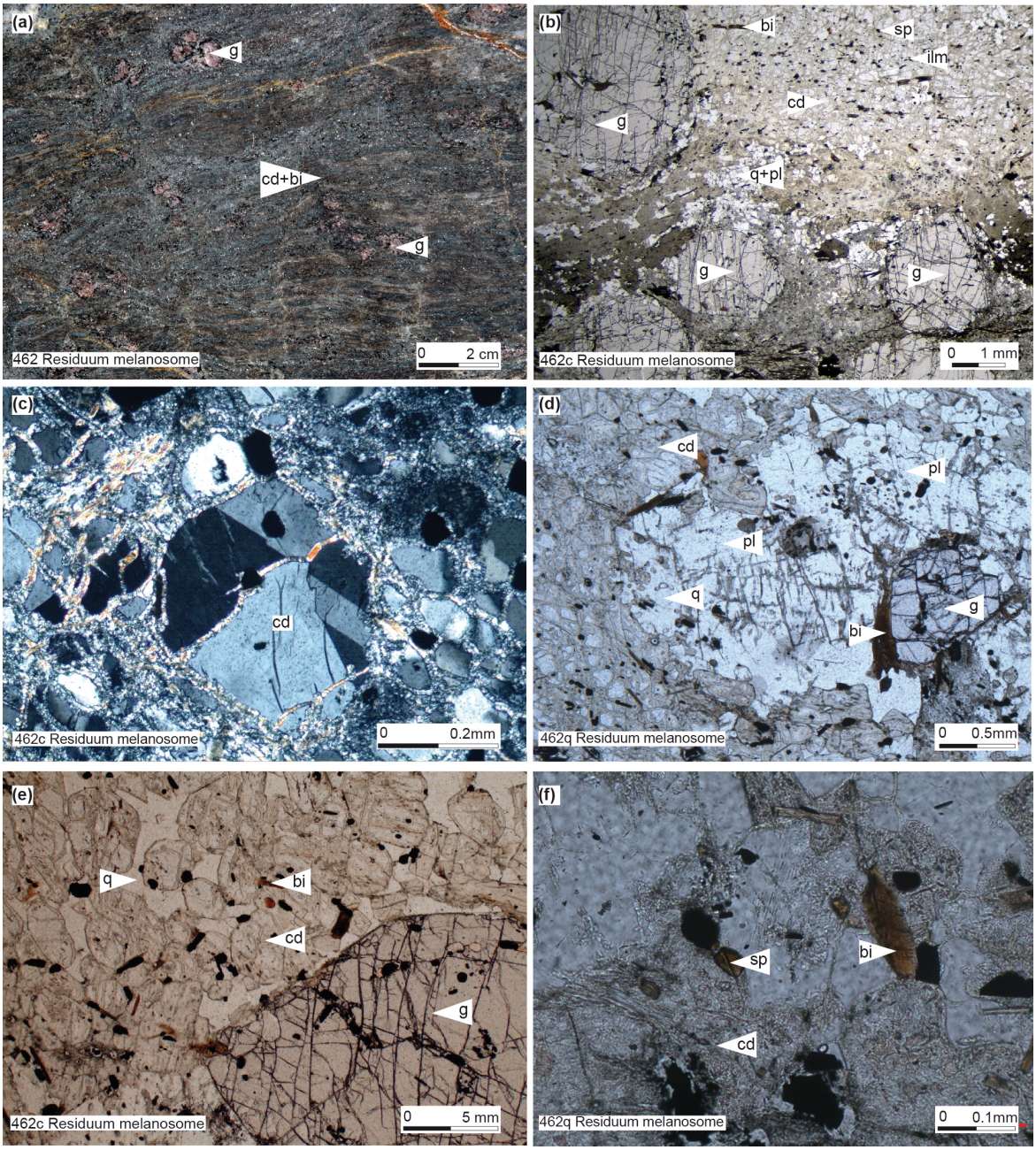



**Figure 4.7.** Macro- to microstructural relationships in residuum melanosomes from the Intermediate series affected by the Ceret gabbro-diorite contact aureole: (a) Massive residuum melanosome with granoblastic texture; (b) garnet porphyroblasts, biotite, ilmenite and brown spinel embedded in a cordierite-rich matrix; (c) idiomorphic cordierite with cyclic twinning; (d) idiomorphic to xenomorphic plagioclases together with biotite plates around garnet; (e) interstitial quartz between cordierite; and (f) brown spinel included in cordierite.

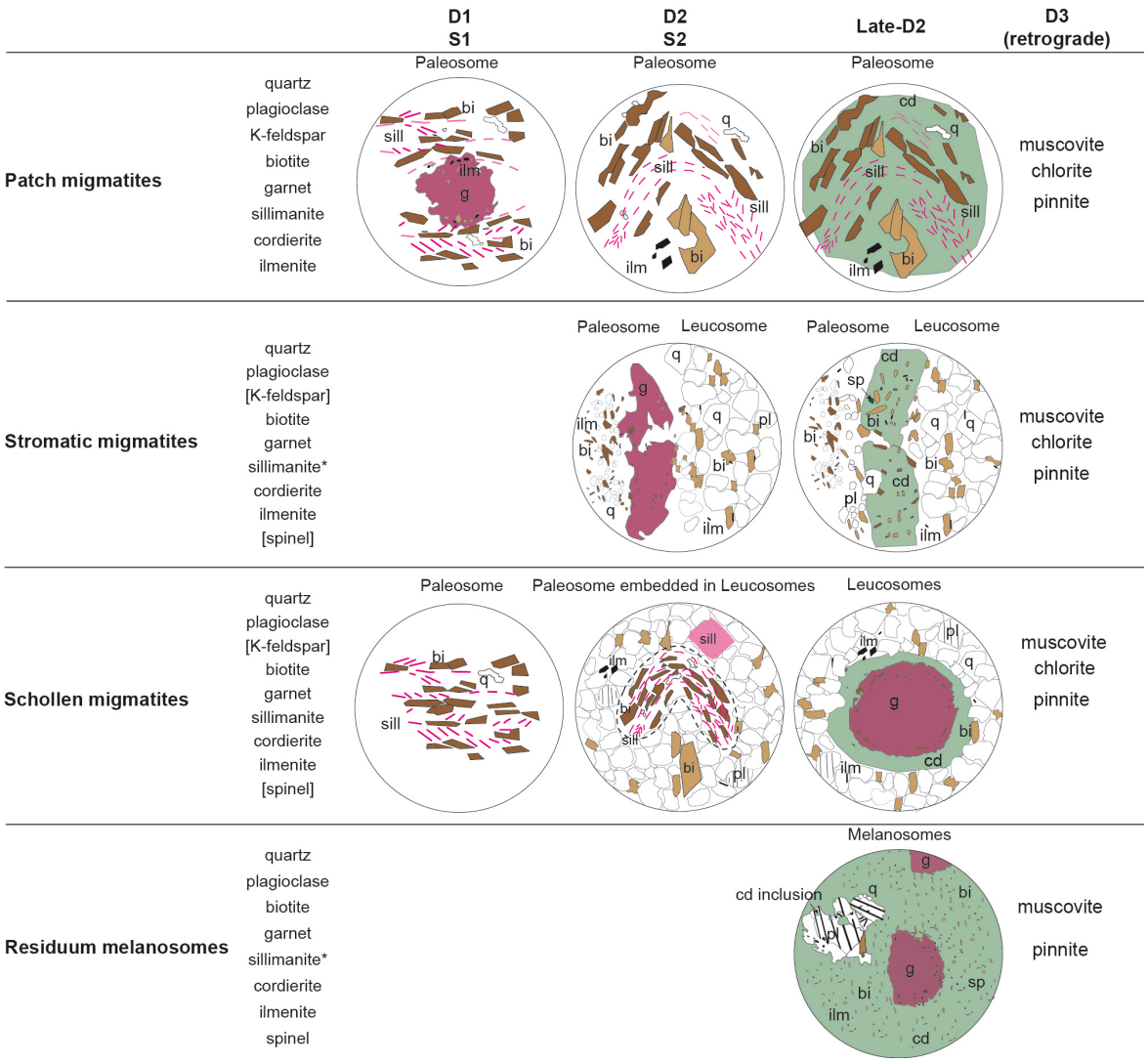



**Figure 4.8.** Sketch of the deformation events registered in the different types of migmatites from contact metamorphism around the Ceret gabbro-diorite.

In summary, crystallization-deformation relationships of different types of migmatites affected by the Ceret gabbro-diorite contact aureole suggest that the S1 and the early S2 fabrics developed within the stability field of biotite–sillimanite–garnet–quartz–plagioclase–K-feldspar, and that cordierite crystallized after the D2 deformation event (Fig. 4.3c). The mineral inclusions located only in garnet rims indicate that the rims grew during the D1 deformation event, but the cores could have been already formed during the earlier history of the rock.

On the other hand, the granular texture of leucosomes, the rational faces of plagioclase and the mineral phase distribution provide evidence of the former presence of melt at the grain scale (Ashworth & McLellan, 1985) in the stromatites

and schollen migmatites. The fact that cordierite and garnet have survived without significant retrogression indicates that they probably represent peritectic minerals preserved from the migmatitic rocks before melt loss (Powell & Downes, 1990; Brown, 2002; White & Powell, 2002).

### 4.2.4. The Lower series

The major rock types in the Lower series are fold-structured migmatites characterized by a tightly folded lithological banding with coarse-grained leucosomes alternating with fine-grained paleosomes (Fig. 4.9a & b). The main mineral assemblage is biotite, quartz and plagioclase, commonly with small garnet and, in places, with minor cordierite. K-feldspar and sillimanite are absent. Accessory minerals are ilmenite, magnetite, zircon, monazite, apatite and, locally, tourmaline. Retrograde chlorite, epidote and sericite are related to the D3 deformation zones.

The S1 foliation is defined by biotite-rich paleosome layers alternating with quartz-plagioclase-rich leucosome (Fig. 4.9b). Small rare garnet (up to 0.28 mm) is commonly included in plagioclase that occurs within the paleosome, thus indicating that it is not in equilibrium with the matrix minerals (Fig. 4.9c). The S1 foliation is tightly folded by the F2 folds and locally, it can be almost completely transposed by leucosomes parallel to the S2 foliation (see Fig. 3.2e). The presence of leucosome in the S1 and S2 fabrics indicates that both foliations developed at the presence of melt. Scarce cordierite forms poikiloblasts enclosing biotite with not pressure shadows around it (Fig. 4.9d); therefore, it is interpreted as crystallizing after the D2 event.

### 4.2.5. Late-Variscan igneous rocks

Sant Llorenç–La Jonquera igneous body is a composite batholith formed by tonalite, granodiorite, various types of granite and leucogranite. Tonalite is holocrystalline, granular and heterometric (Figs. 4.10a & b). Major minerals are quartz, plagioclase, biotite and hornblende, with minor amounts of K-feldspar. Plagioclase forms idiomorphic phenocrysts and displays oscillatory zoning as well as Carlsbad and polysynthetic twinning. Biotite and hornblende are subhedral and show a strong pleochroism from brown to reddish brown and green to light brown, respectively. Biotite crystals contain a large number of inclusions of zircon and apatite. Opaque ore and allanite are also present.

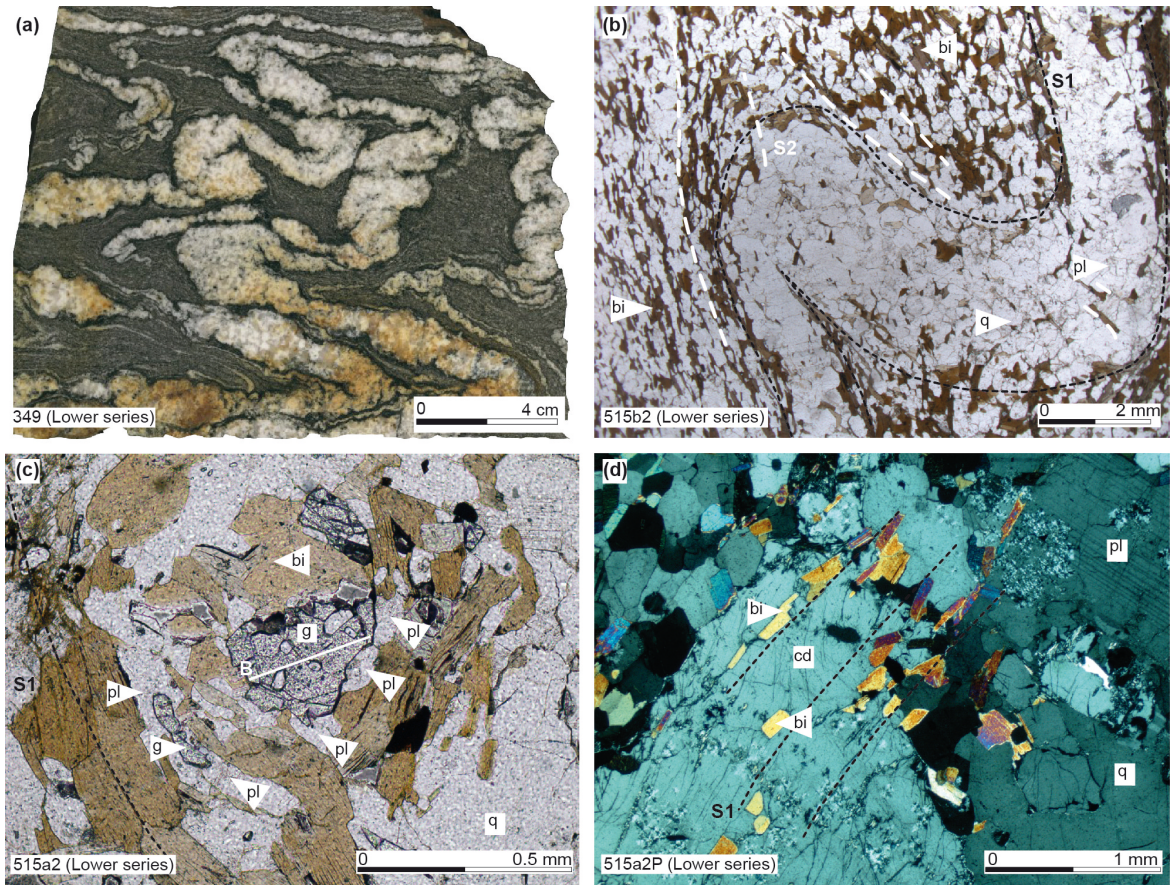



**Figure 4.9.** Macro- to microstructural relationships in migmatitic rocks from the Lower series: (a) tightly folded lithological banding and leucosome parallel to S1 foliation; (b) detail of the S1 folds with biotite crystallizing parallel to the axial plane of F2 folds in the paleosomes and quartz-feldspar bands in the leucosome; (c) corroded isolated garnet in contact with plagioclases and biotite; and (d) poikiloblastic cordierite including S1 oriented biotite.

The gabbro from the Ceret stock is heterometric and medium- to coarse-grained (Fig. 4.10c & d). It has a granular to ophitic texture and is composed of clinopyroxene, amphibole, plagioclase and biotite. Quartz is scarce and has an interstitial texture. Zircon, apatite and opaque ore are accessory minerals. Plagioclase is idiomorphic with Carlsbad and polysynthetic twinning and it is partially enclosed in clinopyroxene, amphibole or anhedral biotite. Altered olivine is locally included in clinopyroxene. Amphibole and biotite occasionally display a coronitic texture around clinopyroxene. Secondary minerals are iddingsite, white mica and uralite.

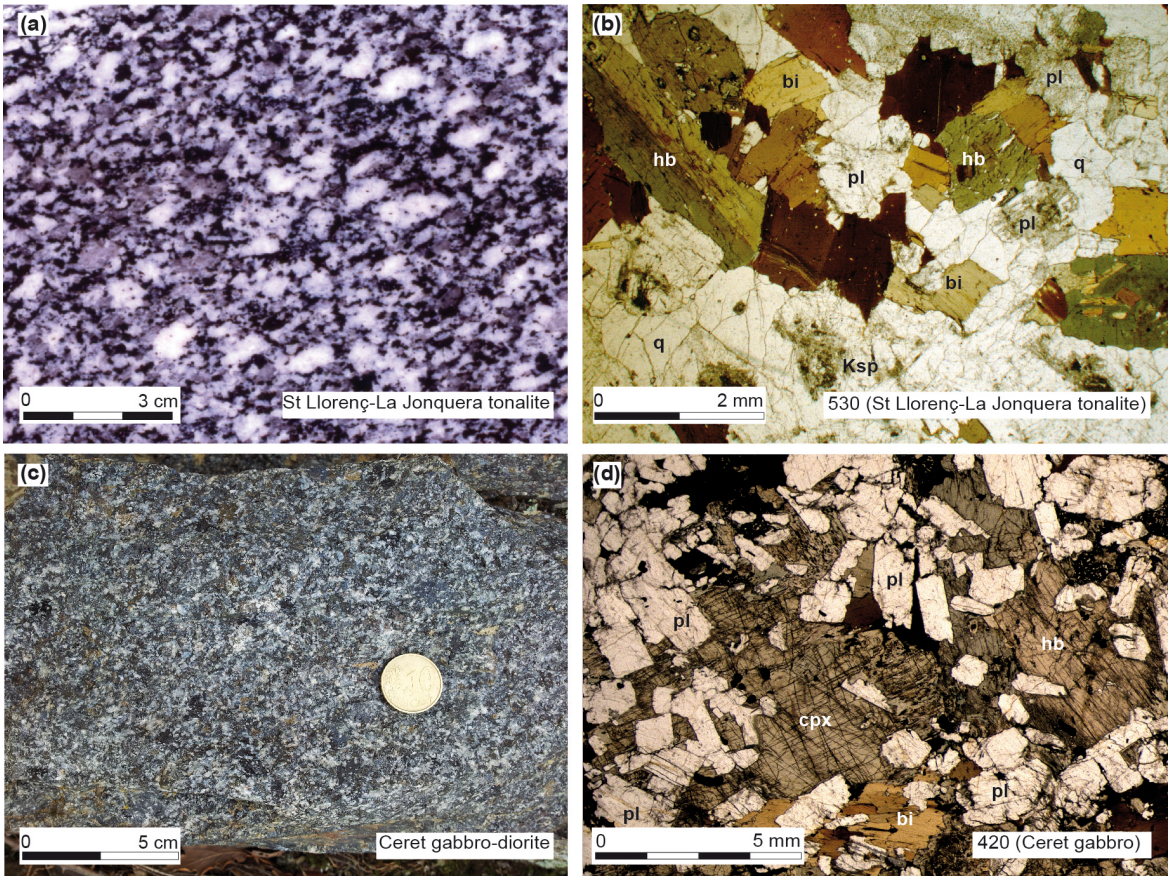



**Figure 4.10.** Meso- and microscopic photographs of Variscan igneous rocks: (a) Sant Llorenç–La Jonquera tonalite whit magmatic foliation defined by idiomorphic plagioclase and mafic minerals (biotite and hornblende) and oriented NE–SW in the photograph; (b) biotite and hornblende crystallizing in clusters in the tonalite; (c) plagioclase-rich gabbro from the Ceret stock (same outcrop as sample 420) whit slightly bigger black crystals of clinopyroxene; and (d) Clinopyroxene is almost completely surrounded by hornblende and biotite. Pyroxene includes idiomorphic plagioclase forming an ophitic texture.

## 4.3. Mineral chemistry

The composition of the most significative metamorphic minerals of metapelites from representative samples of the Upper, Intermediate and Lower series has been analyzed and compared (Tables 4.1–4.3). Special emphasis has been taken on the mineral phases of the migmatites formed next to the gabbro-diorite contact aureole. Thus, biotite, muscovite and cordierite from an andalusite–sillimanite micaschist and a sillimanite schist have been analyzed together with biotite, cordierite and garnet of

four characteristic migmatitc rocks from the inner aureole and xenoliths of the Ceret gabbro-diorite. Moreover, a fold-structured migmatite from the Lower series has been also analyzed (see Figure 4.1 for location of samples).

In all samples, single biotite grains and cordierite poikiloblasts are homogeneous and show no zoning. In the migmatites, garnets do not exhibit compositional zoning in their cores, though the rims display systematic changes that involve an increase in almandine, spessartine and $X_{Fe}$, and a decrease in pyrope and grossular. The mineral chemistry of the analyzed samples is firstly described together with the main textural characteristics of the sample and at the end of this section all samples are compared (Fig. 4.13 & 4.14).

### 4.3.1. The Upper series

**Sample 187** is representative of the andalusite–sillimanite micaschists. It has a well-preserved S1 foliation defined by alternating layers of biotite, muscovite and sillimanite with plagioclase and quartz-rich layers. Biotite has $X_{Fe}$ between 0.55 and 0.60 and Ti in the range of 0.10–0.20 p.f.u. Muscovite $X_{Fe}$ ranges between 0.47 and 0.52 and Si is around 3.05–3.09 p.f.u. Cordierite poikiloblasts have an $X_{Fe}$ = 0.41–0.43 and include the former mineral assemblage. They are roughly parallel to the external S1 fabric, and no S1 pressure shadows are developed around them.

### 4.3.2. The Intermediate series not affected by Ceret gabbro-diorite contact aureole.

**Sample 4.12b** is a sillimanite schist with cordierite and minor K-feldspar, with folded S0 layers transposed by the S1 foliation. The S1 is defined by alternating biotite, muscovite and sillimanite-rich layers with plagioclase and quartz-rich layers. Biotite has $X_{Fe}$ between 0.52 and 0.63 and Ti ranges from 0.06 to 0.19 p.f.u. Muscovite has $X_{Fe}$ = 0.45–0.59 and Si = 3.00–3.09 p.f.u. Plagioclase is albitic to oligoclasic (an = 0.08–0.27, ab =0.92–0.72, or = 0.00–0.02), and K-feldspar has up to 36% of albite (an = 0.00–0.01, ab = 0.36–0.20, or = 0.64–0.80). Cordierite poikiloblasts yield $X_{Fe}$ = 0.39–0.47 and have similar blastesis–deformation relations to those of the Upper series.

**Table 4.1.** Representative mineral analyses of an andalusite–sillimanite micaschist from the Upper series (sample 187) and of a sillimanite schist from the Intermediate series (sample 4.12b).

| | Upper series | | | Intermediate series not affected by the Ceret contact aureole | | | | |
|---|---|---|---|---|---|---|---|---|
| Mineral | bi | mu | cd | bi | mu | cd | | pl |
| Analysis | 187-3-23-bi | 187-3-34-ms | 187-3-31-cd | 4.12_bi21 | 4.12_mu41 | 4.12_cd96 | | 4.12-pl1 |
| Spot | #15 | #20 | #19 | #22 | #42 | #102 | | #61 |
| (wt%) | | | | | | | | |
| $SiO_2$ | 35.9 | 45.56 | 47.95 | 34.30 | 45.61 | 47.26 | | 61.20 |
| $TiO_2$ | 2.84 | 0.62 | 0.05 | 2.63 | 0.47 | 0.00 | | 0.01 |
| $Al_2O_3$ | 19.84 | 35.96 | 32.99 | 19.15 | 36.34 | 32.09 | | 24.39 |
| FeO | 19.7 | 1.13 | 9.58 | 21.65 | 0.97 | 8.60 | | 0.00 |
| MnO | 0.11 | 0.02 | 0.26 | 0.22 | 0.05 | 0.73 | | 0.00 |
| MgO | 8.29 | 0.58 | 7.49 | 7.72 | 0.56 | 6.54 | | 0.00 |
| CaO | 0.03 | 0.00 | 0.02 | 0.00 | 0.00 | 0.01 | | 5.53 |
| $Na_2O$ | 0.16 | 0.63 | 0.25 | 0.21 | 0.72 | 0.97 | | 8.69 |
| $K_2O$ | 8.22 | 10.08 | 0.02 | 9.48 | 10.42 | 0.02 | | 0.28 |
| Total | 95.09 | 94.58 | 98.61 | 95.36 | 95.14 | 96.22 | | 100.10 |
| Oxygen | 11 | 11 | 18 | 11 | 11 | 18 | | 8 |
| Si | 2.84 | 3.06 | 4.94 | 2.71 | 3.04 | 4.97 | | 2.71 |
| Ti | 0.17 | 0.03 | 0.00 | 0.16 | 0.02 | 0.00 | | 0.00 |
| Al | 1.85 | 2.84 | 4.01 | 1.78 | 2.85 | 3.98 | | 1.27 |
| $Fe^{3+}$ | 0.00 | 0.00 | 0.16 | 0.00 | 0.01 | 0.28 | | 0.00 |
| $Fe^{2+}$ | 1.30 | 0.06 | 0.66 | 1.43 | 0.05 | 0.48 | | 0.00 |
| Mn | 0.01 | 0.00 | 0.02 | 0.01 | 0.00 | 0.07 | | 0.00 |
| Mg | 0.98 | 0.06 | 1.15 | 0.91 | 0.06 | 1.03 | | 0.00 |
| Ca | 0.00 | 0.00 | 0.00 | 0.00 | 0.00 | 0.00 | | 0.26 |
| Na | 0.02 | 0.08 | 0.05 | 0.03 | 0.09 | 0.20 | | 0.74 |
| K | 0.83 | 0.86 | 0.00 | 0.96 | 0.88 | 0.00 | | 0.02 |
| cations | 8.00 | 7.00 | 11.00 | 8.00 | 7.00 | 11.00 | | 5.00 |
| $X_{Fe}$ ($Fe^{2+}$) | 0.57 | 0.52 | 0.37 | 0.56 | 0.45 | 0.32 | an | 0.26 |
| $X_{Fe}$ (Fetot) | 0.57 | 0.52 | 0.42 | 0.56 | 0.49 | 0.42 | ab | 0.73 |
| | | | | | | | or | 0.02 |

### 4.3.3. The Intermediate series affected by Ceret gabbro-diorite contact aureole.

**Sample 526** is a patch migmatite formed by cordierite-rich and fibrolite-poor paleosomes. It consists of biotite, fibrolite, garnet, cordierite, plagioclase, K-feldspar and quartz. Ilmenite is the main accessory mineral. Biotite, fibrolite and ilmenite are locally included in garnet rims oriented parallel to the S1 foliation. Biotite from the paleosome and included in garnet have similar compositions ($X_{Fe}$ = 0.53–0.65 and Ti = 0.13–0.30 p.f.u.). Garnet has a fairly constant distribution of elements in its core showing an increase in almandine and $X_{Fe}$, and a decrease in pyrope towards the outermost rims ($alm_{0.76\rightarrow0.84}$; $grs_{0.04}$; $prp_{0.15\rightarrow0.08}$; $sps_{0.025\rightarrow0.04}$; $X_{Fe}$ = 0.87→0.82→0.91; Fig. 4.11a). Cordierite poikiloblasts have an $X_{Fe}$ = 0.38–0.48. They enclose biotite and ilmenite with inclusion trails parallel to the external S1 and S2 fabric, and no S2

pressure shadows are developed around them.

**Sample 529** corresponds to a stromatic migmatite formed by cordierite and biotite-rich melanosomes alternating with coarse-grained leucosomes rich in plagioclase and quartz (Fig. 4.5a-c). Melanosomes exhibit a strong S2 fabric. Biotite has $X_{Fe}$ = 0.43–0.47 and Ti =0.12–0.21 p.f.u. Garnets abound in the leucosome and in the melanosome. They have a fairly constant distribution of elements in their cores and, towards the outermost rims, they have a slight increase in almandine, spessartine and $X_{Fe}$, and a decrease in pyrope ($alm_{0.65\rightarrow0.75}$; $grs_{0.03}$; $prp_{0.27\rightarrow0.14}$; $sps_{0.04\rightarrow0.07}$; $X_{Fe}$ = 0.71→0.84; Fig. 4.11b). Cordierite poikiloblasts have $X_{Fe}$ = 0.29–0.32. They include biotite and spinel and no S2 pressure shadows are developed around them.

**Sample 459** is a characteristic schollen migmatite and is formed by biotite, fibrolite and ilmenite oriented parallel to the S1 in the paleosome. S2 fabric is defined by plagioclase–quartz-rich leucosomes with prismatic sillimanite, garnet, cordierite minor K-feldspar. Biotite has $X_{Fe}$ = 0.50–0.59 and Ti =0.10–0.26 p.f.u. Garnet (up to 5.5 mm) has a fairly constant distribution of elements in its core with a slight increase of pyrope and a decrease of almandine and $X_{Fe}$ towards the rim and, at the outermost rims a slight increase in almandine, spessartine and $X_{Fe}$, and a decrease in grossular and pyrope ($alm_{0.81\rightarrow0.78\rightarrow0.80}$; $grs_{0.06\rightarrow0.04}$; $prp_{0.08\rightarrow0.12\rightarrow0.10}$; $sps_{0.03\rightarrow0.08}$; $X_{Fe}$ = 0.90→0.87→0.89; Fig. 4.11c). Cordierite poikiloblasts have $X_{Fe}$ values between 0.35–0.42. They present inclusion trails of all the minerals of the assemblage parallel to the external S1 and S2 fabrics, and no S2 pressure shadows are developed around them.

**Sample 462** is a typical residuum melanosome sample. It is formed by garnet porphyroblasts, biotite, ilmenite and brown spinel embedded in a cordierite-rich matrix (Fig. 4.7b). S2 foliation is faintly defined by biotite, ilmenite and brown spinel. Biotite from the matrix has $X_{Fe}$ = 0.42–0.55 and Ti =0.05–0.28 p.f.u. Garnet has a fairly constant distribution of elements in its core with a slight increase of pyrope and a decrease of almandine and $X_{Fe}$ towards the rim and a slight increase in almandine, spessartine and $X_{Fe}$, and a decrease pyrope at the outermost rim ($alm_{0.73\rightarrow0.68\rightarrow0.80}$; $grs_{0.03}$; $prp_{0.23\rightarrow0.26\rightarrow0.12}$; $sps_{0.025\rightarrow0.015\rightarrow0.032}$; $X_{Fe}$ = 0.77→0.72→0.87; Fig. 4.11d).

**Table 4.2.** Representative mineral analyses of the different types of migmatites from the Intermediate series affected by the Ceret contact aureole

| | Patch migmatite | | | | Stromatitic migmatite | | | | Schollen migmatite | | | | Residuum melanosome | | | |
|---|---|---|---|---|---|---|---|---|---|---|---|---|---|---|---|---|
| Sample | 526 | | | | 529 | | | | 459 | | | | 462 | | | |
| Mineral | g-core | g-rim | bi | cd | g-core | g-rim | bi | cd | g-core | g-rim | bi | cd | g-core | g-rim | bi | cd |
| Analysis | 526N-2l A_10 | 526N-2l A_40 | 526L2-9-bt | 526L2-7-cd | 529B_g2 lA_1 | 529B_g2 A_26 | 529a-1-51 bi | 529a-1-71 cd | 459h-A2_18 | 459h- A2_34 | 459L-78 | 459L-24 | 462q perfil A_23 | 462q-A_2 | 573 | 575 |
| Spot | #300 | #330 | #99 | #97 | #175 | #200 | #26 | #32 | #206 | #222 | | | #391 | #370 | | |
| (wt%) | | | | | | | | | | | | | | | | |
| $SiO_2$ | 37.23 | 36.68 | 35.03 | 48.89 | 38.13 | 38.45 | 35.93 | 48.62 | 36.56 | 37.43 | 35.38 | 48.74 | 37.64 | 37.97 | 35.39 | 48.70 |
| $TiO_2$ | 0.01 | 0.02 | 4.36 | 0.00 | 0.02 | 0.05 | 3.26 | 0.00 | 0.09 | 0.08 | 2.58 | 0.00 | 0.06 | 0.07 | 3.02 | 0.00 |
| $Al_2O_3$ | 21.07 | 20.95 | 17.90 | 31.94 | 21.51 | 21.75 | 17.67 | 32.97 | 20.85 | 21.54 | 20.36 | 33.10 | 21.40 | 21.77 | 20.46 | 33.51 |
| FeO | 35.20 | 37.49 | 21.43 | 8.98 | 34.30 | 30.51 | 17.69 | 7.11 | 36.37 | 35.71 | 18.90 | 8.85 | 33.11 | 32.73 | 16.57 | 8.26 |
| MnO | 1.70 | 1.66 | 0.08 | 0.07 | 3.14 | 1.87 | 0.07 | 0.28 | 2.43 | 1.60 | 0.10 | 0.32 | 1.00 | 0.60 | 0.00 | 0.00 |
| MgO | 3.78 | 2.30 | 8.11 | 8.17 | 3.54 | 6.77 | 11.34 | 9.14 | 1.17 | 3.32 | 8.98 | 7.85 | 5.72 | 6.56 | 10.50 | 8.76 |
| CaO | 1.48 | 1.50 | 0.01 | 0.00 | 1.26 | 1.32 | 0.00 | 0.03 | 2.43 | 1.99 | 0.00 | 0.02 | 1.07 | 1.17 | 0.00 | 0.00 |
| $Na_2O$ | 0.00 | 0.00 | 0.13 | 0.23 | 0.00 | 0.00 | 0.29 | 0.24 | 0.00 | 0.00 | 0.34 | 0.34 | 0.00 | 0.00 | 0.29 | 0.19 |
| $K_2O$ | 0.00 | 0.00 | 9.71 | 0.00 | 0.00 | 0.00 | 9.00 | 0.00 | 0.00 | 0.00 | 9.53 | 0.00 | 0.00 | 0.00 | 7.87 | 0.00 |
| Total | 100.47 | 100.60 | 96.76 | 98.28 | 101.90 | 100.72 | 95.25 | 98.39 | 99.90 | 101.67 | 96.17 | 99.20 | 100.00 | 100.87 | 94.10 | 99.41 |
| Oxygen | 12 | 12 | 11 | 18 | 12 | 12 | 11 | 18 | 12 | 12 | 11 | 18 | 12 | 12 | 11 | 18 |
| Si | 2.97 | 2.96 | 2.74 | 5.04 | 3.01 | 2.99 | 2.79 | 4.96 | 2.98 | 2.96 | 2.74 | 4.97 | 2.98 | 2.96 | 2.77 | 4.94 |
| Ti | 0.00 | 0.00 | 0.26 | 0.00 | 0.00 | 0.00 | 0.19 | 0.00 | 0.01 | 0.00 | 0.15 | 0.00 | 0.00 | 0.00 | 0.18 | 0.00 |
| Al | 1.98 | 1.99 | 1.65 | 3.88 | 2.00 | 2.00 | 1.62 | 3.97 | 2.01 | 2.01 | 1.86 | 3.98 | 2.00 | 2.00 | 1.89 | 4.00 |
| $Fe^{3+}$ | 0.07 | 0.09 | 0.00 | 0.09 | 0.00 | 0.01 | 0.00 | 0.16 | 0.02 | 0.06 | 0.00 | 0.14 | 0.04 | 0.07 | 0.00 | 0.16 |
| $Fe^{2+}$ | 2.28 | 2.44 | 1.40 | 0.69 | 2.26 | 1.98 | 1.15 | 0.45 | 2.47 | 2.30 | 1.22 | 0.62 | 2.15 | 2.06 | 1.08 | 0.54 |
| Mn | 0.11 | 0.11 | 0.01 | 0.01 | 0.21 | 0.12 | 0.00 | 0.02 | 0.17 | 0.11 | 0.01 | 0.03 | 0.07 | 0.04 | 0.00 | 0.00 |
| Mg | 0.45 | 0.28 | 0.95 | 1.25 | 0.42 | 0.79 | 1.31 | 1.39 | 0.14 | 0.39 | 1.03 | 1.19 | 0.67 | 0.76 | 1.23 | 1.32 |
| Ca | 0.13 | 0.13 | 0.00 | 0.00 | 0.11 | 0.11 | 0.00 | 0.00 | 0.21 | 0.17 | 0.00 | 0.00 | 0.09 | 0.10 | 0.00 | 0.00 |
| Na | 0.00 | 0.00 | 0.02 | 0.05 | 0.00 | 0.00 | 0.04 | 0.05 | 0.00 | 0.00 | 0.05 | 0.07 | 0.00 | 0.00 | 0.04 | 0.04 |
| K | 0.00 | 0.00 | 0.97 | 0.00 | 0.00 | 0.00 | 0.89 | 0.00 | 0.00 | 0.00 | 0.94 | 0.00 | 0.00 | 0.00 | 0.79 | 0.00 |
| cations | 8.00 | 8.00 | 8.00 | 11.00 | 8.00 | 8.00 | 8.00 | 11.00 | 8.00 | 8.00 | 8.00 | 11.00 | 8.00 | 7.99 | 7.97 | 11.00 |
| $X_{Fe}$ ($Fe^{2+}$) | 0.84 | 0.90 | 0.60 | 0.35 | 0.84 | 0.72 | 0.47 | 0.24 | 0.95 | 0.85 | 0.54 | 0.34 | 0.76 | 0.73 | 0.47 | 0.29 |
| $X_{Fe}$ (Fetot) | 0.84 | 0.90 | 0.60 | 0.38 | 0.84 | 0.72 | 0.47 | 0.30 | 0.95 | 0.86 | 0.54 | 0.39 | 0.76 | 0.74 | 0.47 | 0.35 |
| alm | 0.77 | 0.83 | | | 0.76 | 0.66 | | | 0.83 | 0.78 | | | 0.72 | 0.70 | | |
| prp | 0.15 | 0.09 | | | 0.14 | 0.26 | | | 0.05 | 0.13 | | | 0.22 | 0.25 | | |
| grs | 0.04 | 0.04 | | | 0.04 | 0.04 | | | 0.07 | 0.06 | | | 0.03 | 0.03 | | |
| sps | 0.04 | 0.04 | | | 0.07 | 0.04 | | | 0.06 | 0.04 | | | 0.02 | 0.01 | | |

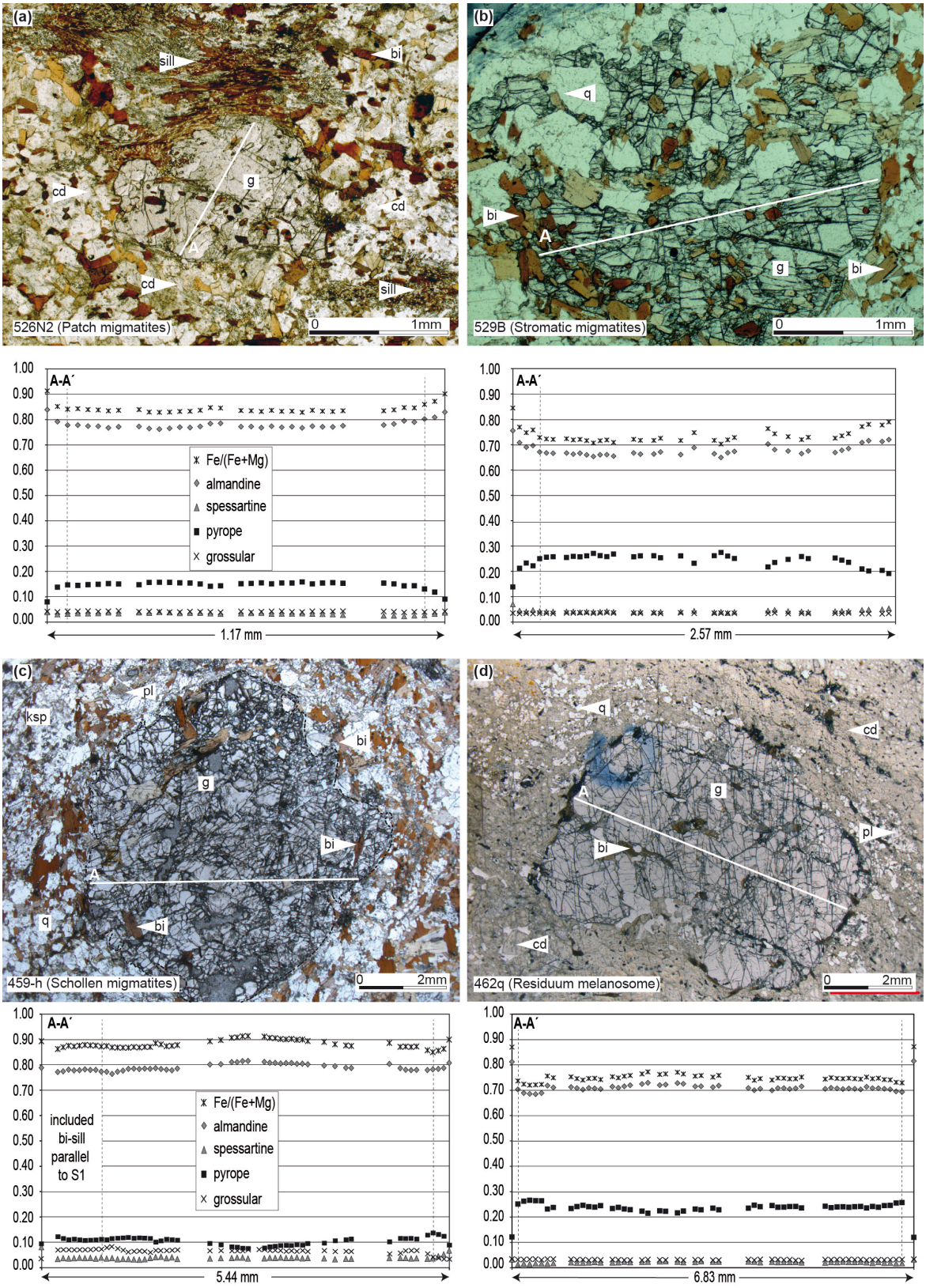



**Figure 4.11.** Chemical zoning profile exhibited by garnet for the different types of migmatites from the Intermediate series affected by the Ceret gabbro-diorite contact aureole. See text for details.

Cordierite poikiloblasts present fairly constant $X_{Fe}$ values ($X_{Fe}$= 0.33–0.35).

### 4.3.4. The Lower series.

**Sample 515** is a biotite–cordierite paragneiss with a S1 foliation folded by F2 folds (Fig. 4.9b). Garnet forms small crystals (from 50 μm to 0.28 mm), commonly included in plagioclase (Fig. 4.9c). Analyzed garnets are unzoned except for a minor increase in spessartine and $X_{Fe}$, and a decrease in pyrope at the outermost rim ($alm_{0.68–0.69}$; $grs_{0.03}$; $prp_{0.13\rightarrow0.09}$; $sps_{0.15\rightarrow0.19}$; $X_{Fe}$ = 0.84→0.88; Fig. 4.12). $X_{Fe}$ of biotite ranges between 0.48 and 0.52 and Ti = 0.10–0.18 p.f.u. Plagioclase is oligoclase (an = 0.21–0.29; ab = 0.70–0.75; or = 0.00–0.07). Cordierite has an $X_{Fe}$ = 0.33–0.35 and have inclusion trails parallel to the S1 foliation (Fig. 4.9d).

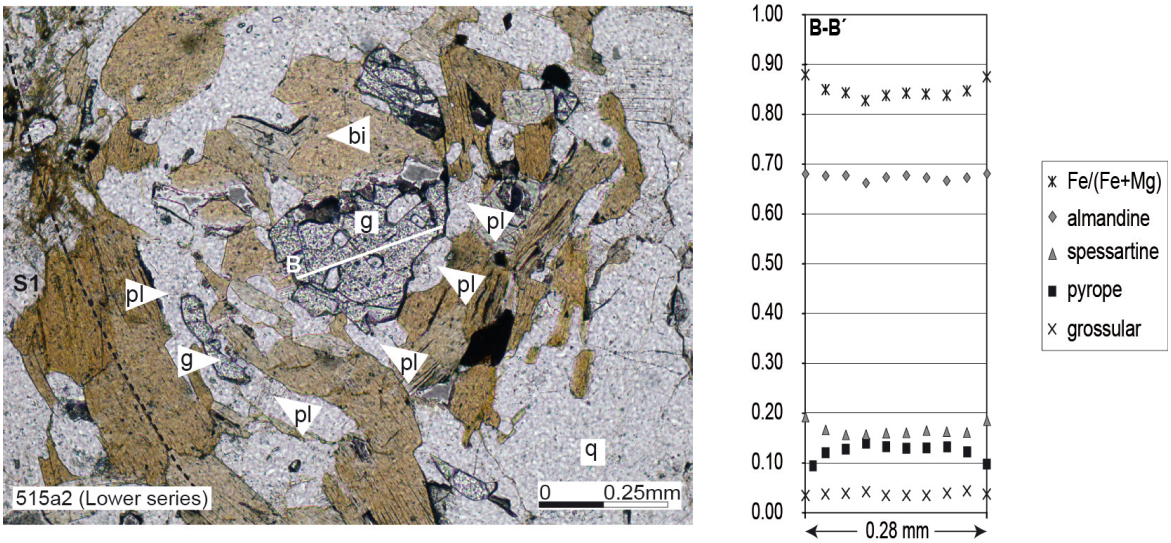



**Figure 4.12.** Chemical zoning profile exhibited by garnet for fold-structured migmatites from the Lower series (sample 515). See text for details.

The $X_{Fe}$ of biotite can be compared with that of cordierite for all the samples from the different crustal levels (Fig. 4.13). In general, biotite shows a wider compositional range than cordierite. All together the samples display a positive correlation: the Upper and Intermediate series schists not affected by Ceret contact aureole present high $X_{Fe}$ values of biotite ($X_{Fe}$=0.48 and 0.63) and cordierite ($X_{Fe}$=0.41 to 0.47). For the migmatites, the highest values correspond to patch migmatites and partly overlap with the values of non-migmatitic rocks that can be considered as the protoliths of the migmatites. The lowest $X_{Fe}$ values of biotite and cordierite (0.42 to 0.65 and 0.29

**Table 4.3.** Representative mineral analyses of a fold-structured migmatite from the Lower series (sample 515).

| Sample | 515a2 | | | | | |
|---|---|---|---|---|---|---|
| Mineral | g-core | g-rim | bi | cd | | pl |
| Analysis | 3gB_3 | 3gB_1 | bi2 | cd14 | | pl18 |
| Spot | #305 | #303 | #2 | #27 | | #112 |
| (wt%) | | | | | | |
| $SiO_2$ | 37.25 | 37.07 | 35.79 | 48.14 | | 60.42 |
| $TiO_2$ | 0.03 | 0.00 | 1.82 | 0.02 | | 0.01 |
| $Al_2O_3$ | 20.90 | 20.51 | 19.11 | 32.88 | | 24.71 |
| FeO | 30.85 | 30.33 | 17.99 | 7.92 | | 0.21 |
| MnO | 6.90 | 8.40 | 0.19 | 0.55 | | 0.00 |
| MgO | 3.19 | 2.34 | 11.01 | 8.29 | | 0.00 |
| CaO | 1.30 | 1.17 | 0.01 | 0.03 | | 6.04 |
| $Na_2O$ | 0.00 | 0.00 | 0.26 | 0.26 | | 8.47 |
| $K_2O$ | 0.00 | 0.00 | 9.05 | 0.00 | | 0.06 |
| Total | 100.42 | 99.82 | 95.23 | 98.09 | | 99.92 |
| | | | | | | |
| Oxygen | 12 | 12 | 11 | 18 | | 8 |
| Si | 2.99 | 3.01 | 2.77 | 4.95 | | 2.68 |
| Ti | 0.00 | 0.00 | 0.11 | 0.00 | | 0.00 |
| Al | 1.98 | 1.96 | 1.74 | 3.99 | | 1.29 |
| $Fe^{3+}$ | 0.04 | 0.01 | 0.00 | 0.15 | | 0.01 |
| $Fe^{2+}$ | 2.03 | 2.05 | 1.16 | 0.53 | | 0.00 |
| Mn | 0.47 | 0.58 | 0.01 | 0.05 | | 0.00 |
| Mg | 0.38 | 0.28 | 1.27 | 1.27 | | 0.00 |
| Ca | 0.11 | 0.10 | 0.00 | 0.00 | | 0.29 |
| Na | 0.00 | 0.00 | 0.04 | 0.05 | | 0.73 |
| K | 0.00 | 0.00 | 0.89 | 0.00 | | 0.00 |
| cations | 8.00 | 8.00 | 7.99 | 11.00 | | 5.00 |
| | | | | | | |
| $X_{Fe}$ ($Fe^{2+}$) | 0.84 | 0.88 | 0.48 | 0.29 | an | 0.28 |
| $X_{Fe}$ (Fetot) | 0.84 | 0.88 | 0.48 | 0.35 | ab | 0.71 |
| alm | 0.68 | 0.68 | | | or | 0.00 |
| prp | 0.13 | 0.09 | | | | |
| grs | 0.04 | 0.03 | | | | |
| sps | 0.15 | 0.19 | | | | |

to 0.48 respectively) correspond to stromatites and residuum melanosomes from the Ceret contact aureole and to fold-structured migmatites from the Lower series ($X_{\mathrm{Fe}}$ for biotite from 0.45 to 0.52 and cordierite between 0.28 and 0.35). Summarizing, the similar composition of non-migmatitic rocks and patch and schollen migmatites can be interpreted as a lack of strong differentiation between these two types of migmatites. Contrastingly, the composition of stromatitic migmatites, residuum melanosomes and fold-structured migmatites suggests that they can be linked to both different protolith composition or to a differentiation related to partial melting processes.

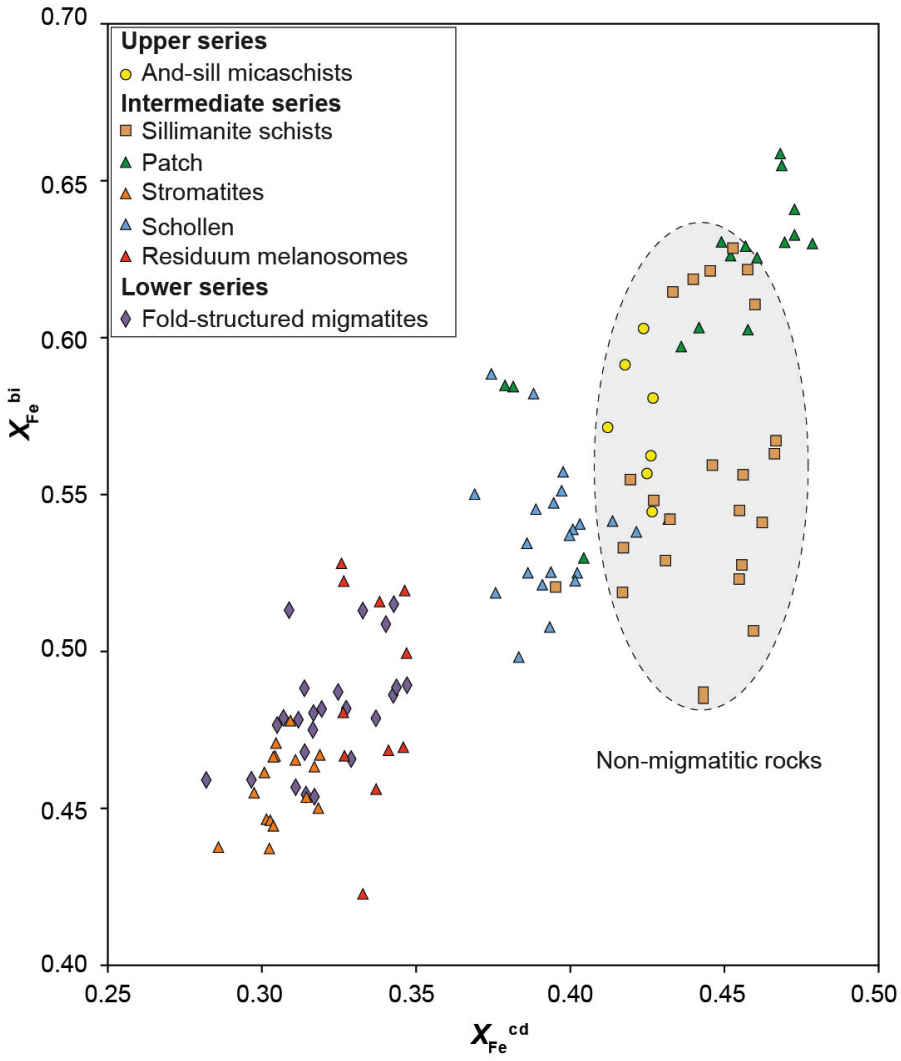



**Figure 4.13.** Biotite-cordierite $X_{Fe}$ composition relationships for the metapelites and migmatites from the different crustal levels of the Roc de Frausa Massif.

Comparing the composition of coexisting of garnet, biotite and cordierite of the Intermediate series migmatites a progressive enrichment in MgO can be observed from patch migmatites to schollen and residuum melanosomes (Fig. 4.14). Stromatic migmatites show the highest MgO values. $Al_2O_3$ content of biotite also tends to increase, though this tendency is not shared by stromatic migmatites. This enrichment in MgO is coherent with the change in whole-rock composition of the samples, also plotted in the $Al_2O_3$–FeO–MgO compositional diagram. The systematic change in composition must be related to an increase in metamorphic grade or to a melt-loss process.

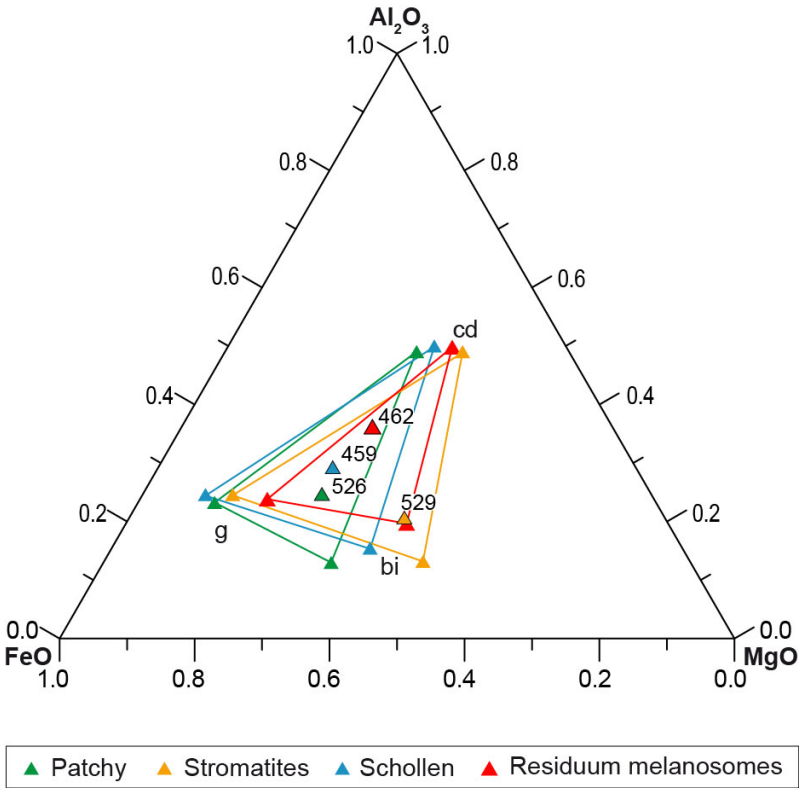



**Figure 4.14.** $Al_2O_3$–FeO–MgO compositional diagram for the different types of migmatites from the Intermediate series affected by the Ceret contact aureole. Mineral compositions (mol.%) and whole-rock analyses (mol.%) plot at progressively lower $X_{Fe}$ values for the different types.

## 4.4. Whole-rock composition

Mineral assemblages and structural types of migmatites can be related to different whole-rock compositions. The studied migmatites are peraluminic rocks with a high $CaO/Na_2O$ ratio and a variable content of $SiO_2$ and of most of the major element oxides (Table 4.4). Patch, stromatic and schollen migmatites contain from 54–64 mol.% $SiO_2$, though schollen migmatites are less rich in silica. Non-migmatitic pelites from the same area, which composition is expected to be similar to that of the protoliths of the migmatites, yield values from 56–64 mol.% $SiO_2$. This compositional field overlaps that of migmatitic samples thus suggesting variable composition of the protoliths. Silica content decreases in residuum rocks down to 40 mol.% $SiO_2$. Figure 4.15 shows the variability of the oxides of the main major elements with respect to $SiO_2$ content. With respect to non-migmatitic rocks, migmatites have more variable

contents of the rest of major elements analyzed. In general, $Al_2O_3$, FeOt, MgO and $TiO_2$ content increases with decreasing $SiO_2$ content. The rest of major elements do not show clear tendencies (Fig. 4.15).

Relations between these elements can be better visualized in triangular diagrams (Fig. 4.16). In the two most significant triangles ($SiO_2$–$Al_2O_3$–(FeO+MgO+$TiO_2$) and $SiO_2$–$Al_2O_3$–($K_2O$+$Na_2O$)), the compositions of the different types of migmatites show a linear decrease in the A/AFM and KN ratios accompanying the depletion of $SiO_2$. Vectors of mineral compositions drawn from an approximate protolith composition (black circle) separate different fields: melt-depleted rocks lie in the field limited by cordierite, garnet and plagioclase vectors, whereas melt-rich rocks lie along the quartz vector. This enrichment in the chemical composition towards the cordierite and garnet compositions in the $SiO_2$–$Al_2O_3$–(FeO+MgO+$TiO_2$) triangle coincides with the enrichment of the rocks in these minerals in residuum melanosomes. In the $SiO_2$–$Al_2O_3$–(FeO+MgO+$TiO_2$) triangle, melanosome rocks also show a variable composition of plagioclase. Melanosomes present lower CaO values than the rest of the migmatites and the estimated protolith composition. This can be interpreted as a enrichment of the melt in Ca as melt production increases (Johnson *et al.,* 2008).

The progressive shift of rock compositions from patch migmatites to residuum melanosomes towards Al, Mg and Fe rich rocks is comparable with the progressive change in mineral composition of the four types of migmatites (Fig. 4.14). This fact could be explained by originally different protoliths. Nevertheless, non-migmatitic rocks present similar composition to patch, stromatic and part of the schollen migmatites; therefore, the migmatites are considered to have originally the same protolith (Figs. 4.15 & 4.16). Assuming that the rocks started with the same composition, these relations indicate that patch, stromatites and part of the schollen could be generated *in situ* with no major change in composition. On the contrary, the melanosomes represent an end-product; in consequence, an open system and melt loss can be inferred for them (Sawyer *et al*., 1999). On the other hand, the linear relations between all the migmatites suggest an open system and the same extraction mechanism for all major elements (Riesco *et al*., 2004).

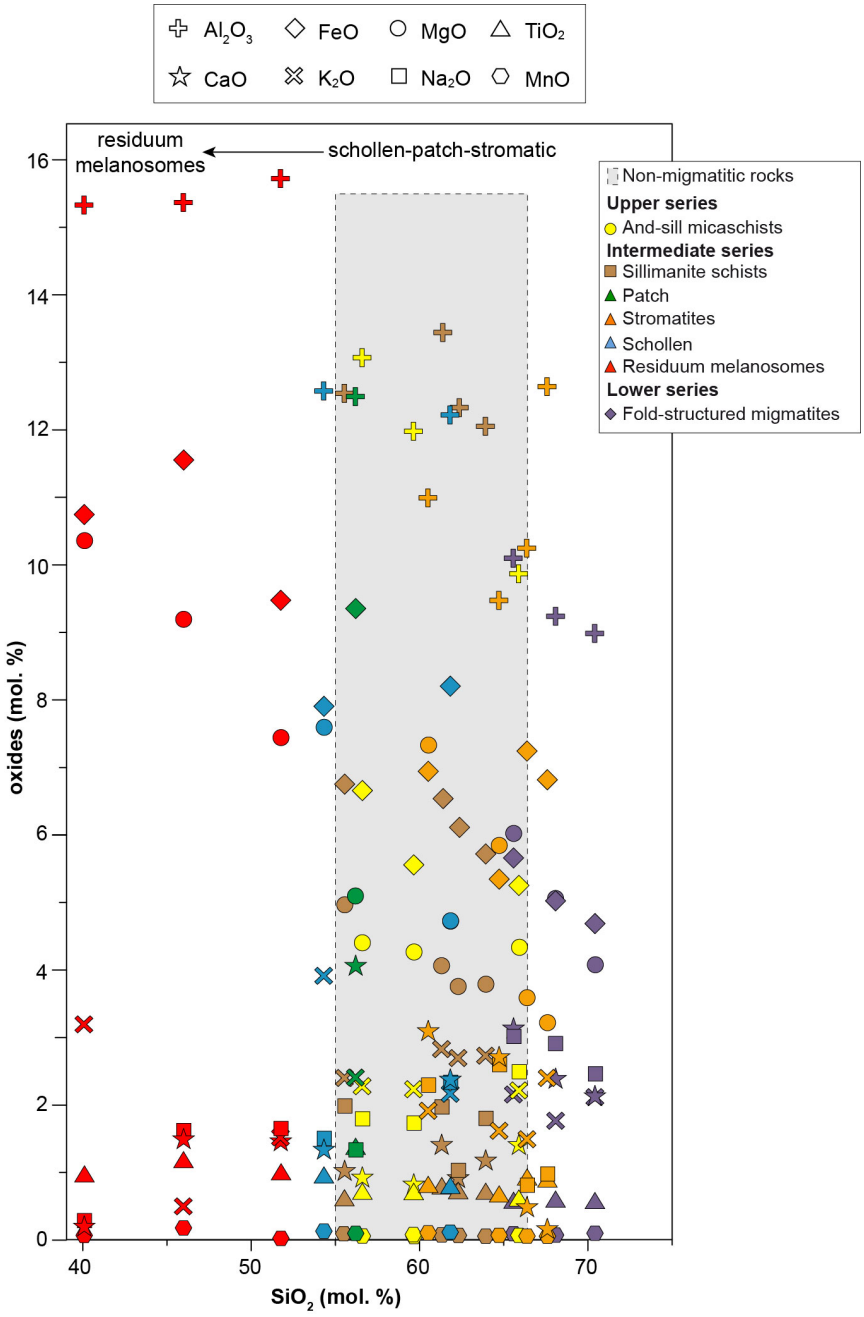



**Figure 4.15.** Harker diagram showing the correlation between $SiO_2$ and other major elements (in mol.% adjusted to 100%) for the metasedimentary rocks and migmatites from the different crustal levels of the Roc de Frausa Massif. See text for explanation.

**Table 4.4.** Representative X-Ray fluorescence (XRF) whole rock analyses of metapelites and migmatites from the different crustal levels of the Roc de Frausa Massif.

| Structural level | Intermediate series affected by the Ceret gabbro-diorite contact aureole | | | | | | | | | |
|---|---|---|---|---|---|---|---|---|---|---|
| Types of migmatites | patchy | stromatites | | | | schollen | | residuum melanosomes | | |
| Sample | 526 | 416 | 460 | 472 | 529 | 459 | 471 | 453 | 461 | 462 |
| (wt.%) | | | | | | | | | | |
| $SiO_2$ | 52.40 | 61.55 | 63.71 | 61.15 | 57.60 | 56.77 | 50.17 | 47.51 | 39.99 | 43.93 |
| $TiO_2$ | 1.71 | 1.09 | 1.18 | 0.85 | 1.04 | 0.98 | 1.18 | 1.23 | 1.29 | 1.50 |
| $Al_2O_3$ | 19.76 | 19.53 | 16.69 | 15.19 | 17.75 | 19.04 | 19.71 | 24.48 | 25.94 | 24.90 |
| $Fe_2O_3$ | 11.59 | 8.25 | 9.24 | 6.71 | 8.78 | 10.01 | 9.70 | 11.56 | 14.24 | 14.66 |
| MnO | 0.11 | 0.06 | 0.05 | 0.08 | 0.12 | 0.13 | 0.15 | 0.10 | 0.08 | 0.20 |
| MgO | 3.19 | 1.97 | 2.31 | 3.71 | 4.68 | 2.91 | 4.71 | 4.58 | 6.93 | 5.89 |
| CaO | 3.53 | 0.14 | 0.43 | 2.39 | 2.75 | 2.03 | 1.15 | 1.25 | 0.18 | 1.33 |
| $Na_2O$ | 1.29 | 0.92 | 0.81 | 2.54 | 2.26 | 2.22 | 1.44 | 1.57 | 0.30 | 1.60 |
| $K_2O$ | 3.52 | 3.43 | 2.25 | 2.40 | 2.86 | 3.12 | 5.66 | 2.19 | 4.99 | 0.75 |
| $P_2O_5$ | 0.25 | 0.06 | 0.07 | 0.24 | 0.22 | 0.11 | 0.42 | 0.10 | 0.02 | 0.04 |
| L.O.I | 2.08 | 1.42 | 2.51 | 1.93 | 1.68 | 1.42 | 2.64 | 2.70 | 5.60 | 3.69 |
| Total | 99.41 | 98.40 | 99.23 | 97.16 | 99.71 | 98.72 | 96.91 | 97.24 | 99.55 | 98.49 |
| A/CNK | 1.60 | 3.57 | 3.67 | 1.37 | 1.51 | 1.78 | 1.86 | 3.39 | 4.17 | 4.25 |
| $K_2O/Na_2O$ | 1.80 | 2.45 | 1.83 | 0.62 | 0.83 | 0.93 | 2.60 | 0.92 | 11.13 | 0.31 |
| $CaO/Na_2O$ | 3.04 | 0.16 | 0.59 | 1.04 | 1.35 | 1.01 | 0.89 | 0.88 | 0.68 | 0.92 |
| $Al_2O_3/TiO_2$ | 9.05 | 14.10 | 11.05 | 13.99 | 13.43 | 15.26 | 13.14 | 15.65 | 15.75 | 12.98 |
| $FeOt^a+MgO+TiO_2$ | 15.83 | 10.93 | 11.76 | 11.87 | 15.09 | 13.73 | 16.46 | 17.92 | 22.07 | 21.93 |

| Structural levels | Upper series | | | Intermediate series not affected by the Ceret contact aureole | | | | Lower Series | | |
|---|---|---|---|---|---|---|---|---|---|---|
| Sample | 187 | 237 | 525 | 338 | 4.12 | 523 | 528 | 349 | 515 | 524 |
| (wt.%) | | | | | | | | | | |
| $SiO_2$ | 55.58 | 63.88 | 58.90 | 61.00 | 57.52 | 54.89 | 59.90 | 67.21 | 64.32 | 61.74 |
| $TiO_2$ | 0.94 | 0.80 | 0.82 | 0.91 | 1.00 | 0.82 | 0.93 | 0.74 | 0.77 | 0.73 |
| $Al_2O_3$ | 21.77 | 16.23 | 20.07 | 19.51 | 21.40 | 21.02 | 20.12 | 14.55 | 14.83 | 16.13 |
| $Fe_2O_3$ | 8.69 | 6.77 | 7.29 | 7.25 | 8.15 | 8.87 | 7.81 | 5.95 | 6.32 | 7.08 |
| MnO | 0.07 | 0.08 | 0.06 | 0.07 | 0.09 | 0.11 | 0.08 | 0.09 | 0.09 | 0.11 |
| MgO | 2.90 | 2.82 | 2.74 | 2.43 | 2.56 | 3.29 | 2.42 | 2.62 | 3.21 | 3.81 |
| CaO | 0.85 | 1.27 | 0.76 | 1.05 | 1.23 | 0.94 | 0.82 | 1.90 | 2.12 | 2.75 |
| $Na_2O$ | 1.82 | 2.50 | 1.77 | 1.78 | 1.91 | 2.03 | 1.03 | 2.43 | 2.84 | 2.93 |
| $K_2O$ | 3.51 | 3.37 | 3.46 | 4.08 | 4.16 | 3.72 | 4.06 | 3.17 | 2.62 | 3.18 |
| $P_2O_5$ | 0.13 | 0.21 | 0.14 | 0.13 | 0.14 | 0.18 | 0.16 | 0.18 | 0.24 | 0.20 |
| L.O.I | 3.95 | 2.25 | 3.89 | 2.28 | 2.11 | 4.14 | 2.88 | 1.25 | 1.34 | 1.00 |
| Total | 100.18 | 100.16 | 99.87 | 100.46 | 100.24 | 99.98 | 100.19 | 100.06 | 98.68 | 99.65 |
| A/CNK | 2.62 | 1.61 | 2.50 | 2.11 | 2.17 | 2.32 | 2.66 | 1.34 | 1.30 | 1.22 |
| $K_2O/Na_2O$ | 1.27 | 0.89 | 1.29 | 1.51 | 1.43 | 1.21 | 2.61 | 0.86 | 0.61 | 0.71 |
| $CaO/Na_2O$ | 0.51 | 0.56 | 0.47 | 0.65 | 0.71 | 0.51 | 0.88 | 0.86 | 0.83 | 1.04 |
| $Al_2O_3/TiO_2$ | 18.24 | 15.99 | 19.28 | 16.79 | 16.84 | 20.20 | 16.94 | 15.51 | 15.18 | 17.31 |
| $FeOt^a+MgO+TiO_2$ | 11.78 | 10.21 | 10.32 | 10.23 | 11.40 | 12.34 | 10.59 | 9.35 | 10.70 | 12.27 |

[a] Total iron as FeO

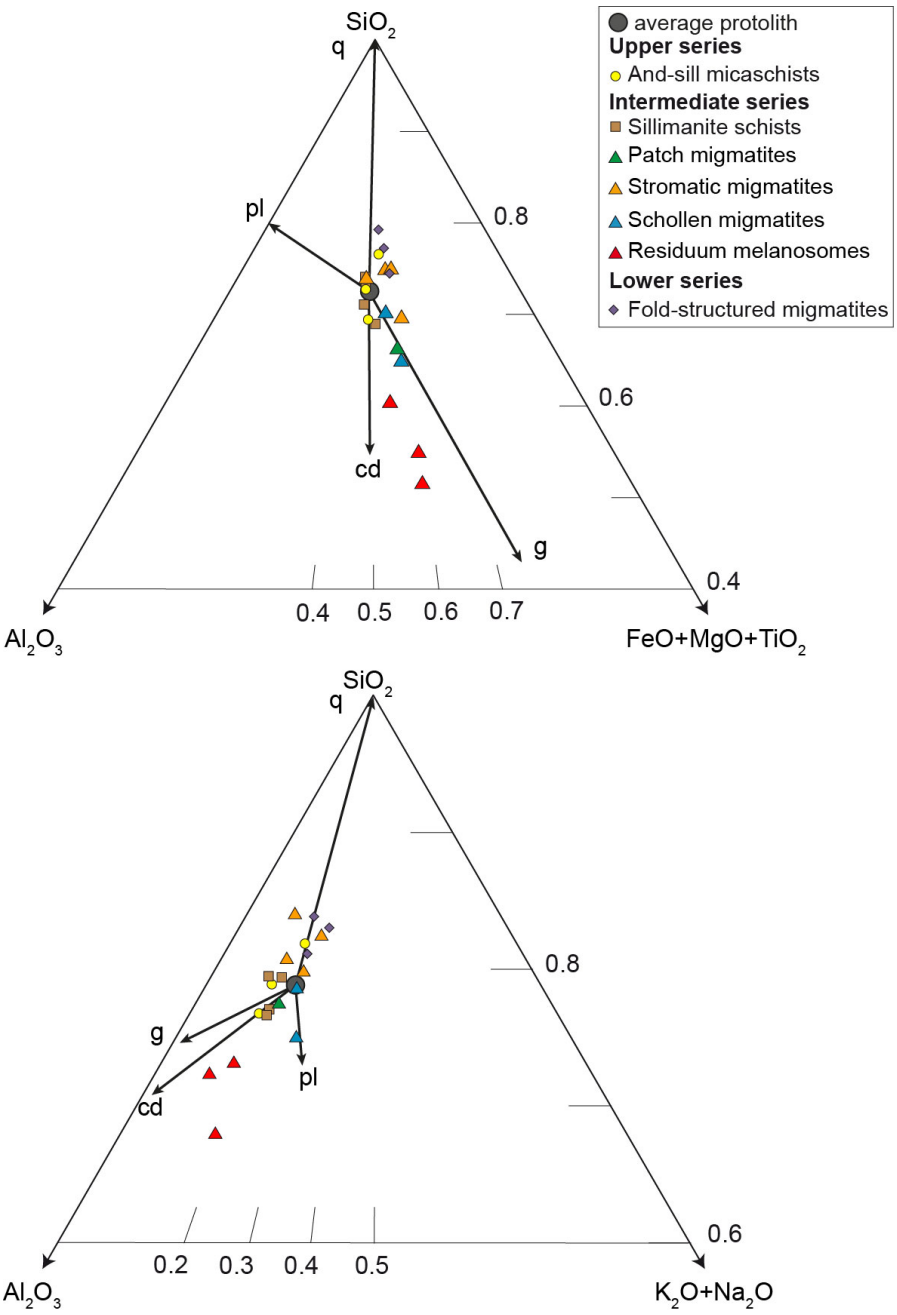



**Figure 4.16.** $SiO_2$–$Al_2O_3$–FeO+MgO+TiO2 and $SiO_2$–$Al_2O_3$–$K_2O$+$Na_2O$ ternary plots for the metasedimentary rocks and migmatites from the different crustal levels of the Roc de Frausa Massif. Mineral vectors correspond to the mean composition of the analyzed garnet, cordierite and plagioclase. See text for details.

# CHAPTER 5

## MINERAL EQUILIBRIA MODELING

With the help of a detailed microstructural study combined with thermodynamic modeling of phase equilibria, we can constrain the *P*–*T*–*d* evolution of the studied rocks and discuss the models that can account for it.

### 5.1. Calculation methods

The pseudosections were calculated using THERMOCALC 3.35 (Powell *et al.,* 1998; update 2010) and the DATASET 5.5 (Holland & Powell, 1998; November 2003 upgrade) in the system $MnO$-$Na_2O$-$CaO$-$K_2O$-$FeO$-$MgO$-$Al_2O_3$-$SiO_2$-$H_2O$-$TiO_2$-$O_2$ (MnNCKFMASHTO). The $MnO$, $TiO_2$ and $O_2$ were added in the system as the Mn incorporation in garnet is major especially at low-pressure metamorphic grades and Ti and $Fe^{3+}$ influence considerably the stability of biotite and ilmenite. A consequence of garnet being the only Mn-bearing mineral is that it is stable in the whole range of modeled *P*–*T* conditions, but this is likely to be realistic in the range of *P*–*T* conditions of interest. The activity-composition models (*a*-*x*) are from the THERMOCALC file (compiled 08/01/08), where the Mn-bearing cordierite (cd) and staurolite (st) models are combination of Mahar *et al*. (1997) and Holland & Powell (1998) and the Mn-bearing garnet (g), biotite (bi), ilmenite (ilm) and hematite (hem) models are after White *et al*. (2005). Muscovite (mu) is after Coggon & Holland (2002), silicate melt (liq) after White *et al*. (2007), feldspars (pl, ksp) from Holland & Powell (2003) and orthopyroxene (opx) and magnetite (mt) from White *et al*. (2002).

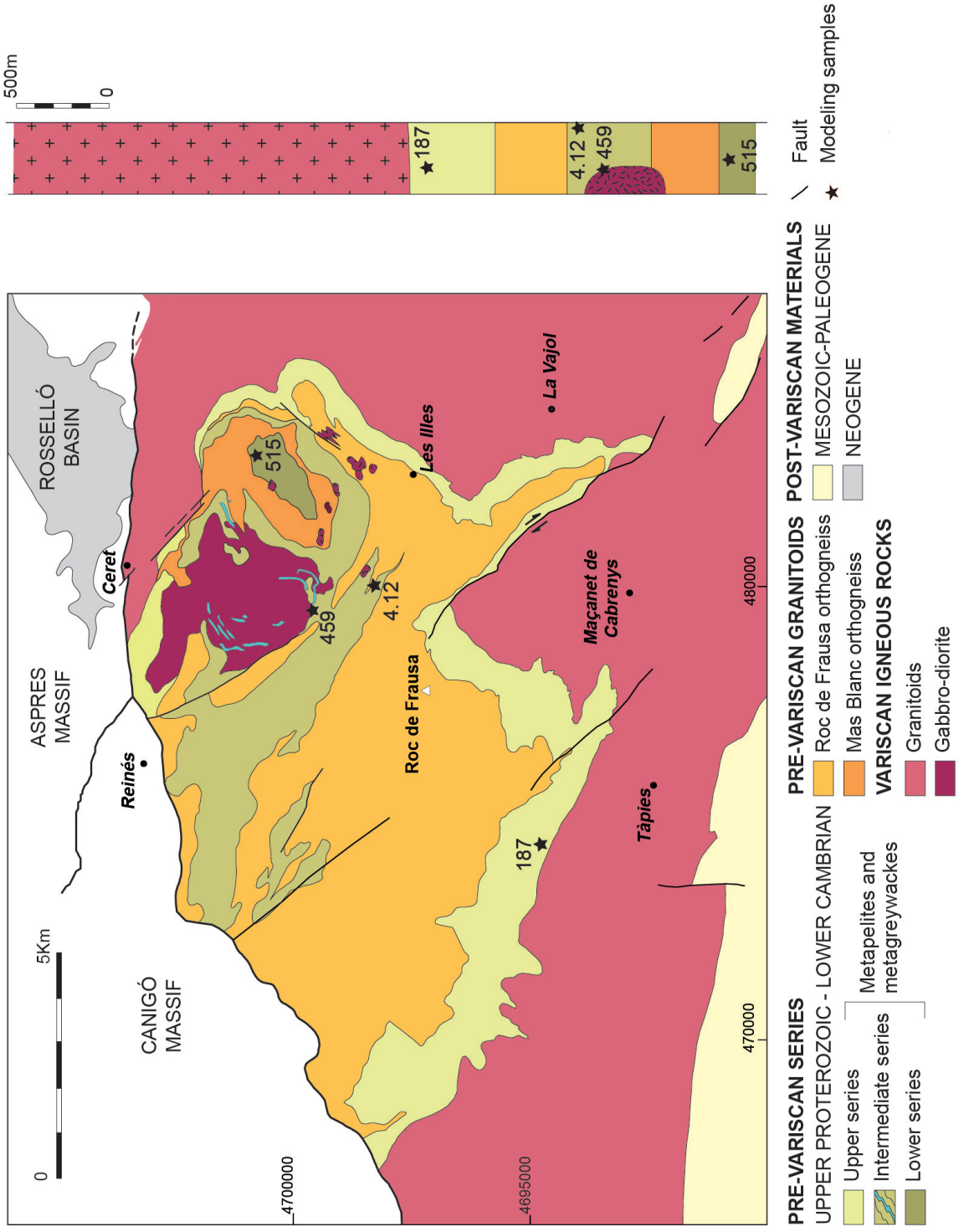
In the calculations, quartz, plagioclase and ilmenite are set in excess. For the micaschists from the Upper and Intermediate series not affected by the thermal aureole of the Ceret gabbro-diorite, $H_2O$ is also set in excess. For the migmatites from the Intermediate series around the Ceret gabbro-diorite contact aureole and from the

Lower series, the amount of $H_2O$ in the whole-rock composition was deduced from *P*–*M*($H_2O$) pseudosections (see an example in Chapter 6), in such a way that the amount of water chosen could explain the preserved mineral assemblages and chemistry of the minerals (for an approach see White & Powell, 2002). The amount of $Fe_2O_3$ for the calculations was set according to the presence or absence of magnetite in the observed assemblages. Furthermore, *P*–*T* pseudosections can be contoured for the composition and relative molar abundance of the participating minerals in each assemblage field, providing additional constraints on *P*–*T* variations during metamorphism. Thus, mineral composition and molar proportion isopleths (abbreviations listed in Analytical procedures) are plotted for the phases of interest. The isopleth notation used is: $x_{Fe}$ (mu, bi, cd) = Fe / (Fe + Mg), $x_{alm}$ = Fe / (Ca + Fe + Mg + Mn), $x_{grs}$ = Ca / (Ca + Fe + Mg + Mn), $x_{sps}$ = Mn / (Ca + Fe + Mg + Mn). They are calculated for individual rock samples.

## 5.2. Assessing *P*–*T* conditions in the MnNCKFMASHTO system

Based on contrasting mineralogy and textural relationships that indicate different sequences of crystallization, three representative samples of the three different levels and one sample of the migmatites around the Ceret gabbro were selected to estimate the *P*–*T*–*d* conditions and the thermomechanical evolution of the Pyrenean Variscan crust (Fig. 5.1).

**Figure 5.1.** Geological sketch map and synthetic stratigraphic column of the Roc de Frausa Massif with the location of the four representative samples used in calculating *P*–*T* conditions. Modified from Liesa & Carreras (1989).


500m
0
187
4.12
459
515
Fault
Modeling samples
ROSSELLÓ BASIN
ASPRES MASSIF
CANIGÓ MASSIF
Ceret
Reinés
Les Illes
La Vajol
Roc de Frausa
Maçanet de Cabrenys
Tàpies
0
5Km
4700000
4695000
470000
480000
PRE-VARISCAN SERIES
UPPER PROTEROZOIC - LOWER CAMBRIAN
Upper series
Intermediate series
Metapelites and metagreywackes
Lower series
PRE-VARISCAN GRANITOIDS
Roc de Frausa orthogneiss
Mas Blanc orthogneiss
VARISCAN IGNEOUS ROCKS
Granitoids
Gabbro-diorite
POST-VARISCAN MATERIALS
MESOZOIC-PALEOGENE
NEOGENE

### 5.2.1. The Upper series: pseudosection for sample 187

The composition of sample 187 used for calculations is in wt. % $SiO_2$ = 55.58, $TiO_2$ = 0.94, $Al_2O_3$ = 21.77, $FeO_{tot}$ = 7.81, MnO = 0.07, MgO = 2.90, CaO = 0.85, $Na_2O$ = 1.82, $K_2O$ = 3.51, $P_2O_5$ = 0.13 (see Table 4.4). The major features of the pseudosection (Fig. 5.2) include the liquid-in line at 660–685 °C between 4.7 to 2 kbar, a steep muscovite-out line at 600–650 °C, cordierite stability below 3.4 kbar and K-feldspar stability heading from 600 °C and 2 kbar to 650 °C and 3.3 kbar. Either sillimanite or andalusite is stable in most of the calculated *P–T* conditions, except for the low-pressure and high-temperature part of the diagram.

Paragenetic relations in sample 187 involve andalusite porphyroblasts with inclusion trails of ilmenite parallel to the S1 fabric. However, andalusite is wrapped by the S1 foliation, defined by muscovite, biotite and sillimanite with the well-developed S1 pressure shadows (see Fig. 4.2a). Therefore, crystallization relationships among the $Al_2SiO_5$ polymorphs indicate first growth of andalusite in the S1 fabric followed by sillimanite in the S1 foliation. This is compatible with a path from the bi–and–mu field to the bi–sill–mu field (Fig. 5.2a), which involves an increase in temperature, and may be either isobaric or accompanied by an increase or a slight decrease in pressure. The minimum pressure conditions in the presence of muscovite and sillimanite are around 3.2 kbar at 620–640 °C. The presence of cordierite poikiloblasts including the previous mineral assemblage and with no pressure shadows indicates an evolution of the *P–T* path towards the cd–bi–and–mu field. In this field the calculated isopleths closely match the analyzed mineral compositions (cordierite $X_{Fe}$ = 0.41–0.44, biotite $X_{Fe}$ = 0.57–0.60, muscovite $X_{Fe}$ = 0.50–0.52; Fig. 5.2b–d). In the pseudosection, this path involves a pressure decrease from ~3.4 kbar to ~2.6 kbar and may be almost isothermal or accompanied by a decrease in temperature.

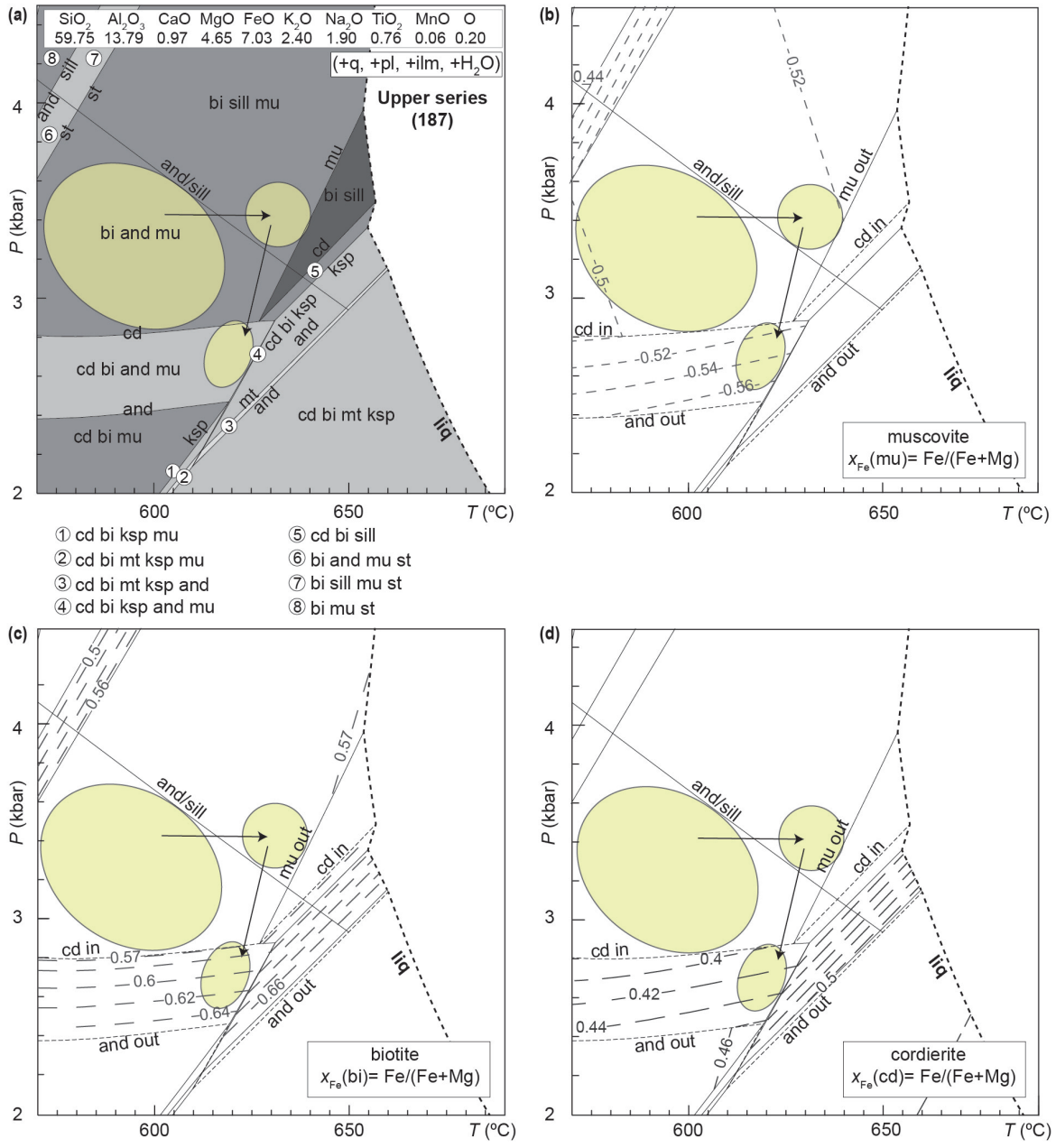



**Figure 5.2.** MnNCKFMASTHO *P*–*T* pseudosection calculated for the whole-rock composition of a representative andalusite–sillimanite micaschist from the Upper series (in moles adjusted to 100%). The *P*–*T* path is derived by comparing the modeled assemblages and isopleths with assemblages, chemistry and zoning of minerals observed in the studied sample (187). See text for details. (b–d) Enlarged and simplified parts of the pseudosection with calculated isopleths of mineral composition for the areas of interest. The solidus is underlined by a dark-dashed line.

### 5.2.2. The Intermediate series not affected by the Ceret gabbro-diorite contact aureole: pseudosection for sample 4.12b

The composition of sample 4.12b in wt. % is $SiO_2$ = 57.52, $TiO_2$ = 1.00, $Al_2O_3$ = 21.40, $FeO_{tot}$ = 7.33, MnO = 0.09, MgO = 2.56, CaO = 1.23, $Na_2O$ = 1.91, $K_2O$ = 4.16, $P_2O_5$ = 0.14 (see Table 4.4). The pseudosection (Fig. 5.3) involves the liquid-in line at 660–690 °C from 5 to 2 kbar, and steep and nearly parallel muscovite-out and K-feldspar-in lines between 600–650 °C and 2–3.7 kbar. Cordierite stabilizes below 3.4 kbar at the higher temperature part (between 630–660 °C) and ~2.8 kbar between 570–630 °C. Aluminosilicates (andalusite or sillimanite) are not stable in the low-pressure part of the diagram.

In sample 4.12b, the assemblage in the S1 foliation is underlined by muscovite, sillimanite and biotite. This mineral assemblage is compatible with the bi–sill–mu field from the pseudosection. The presence of muscovite typically ragged and replaced by fibrolitic sillimanite together with coarse-grained K-feldspar and cordierite poikiloblasts in S1 indicates that the rock could have followed a path into the cd–bi–ksp–sill field, involving decompression to ~3 kbar at a temperature of around 640–660 °C. The coexistence of muscovite and K-feldspar in the S1 fabric points to maximum *P*–*T* conditions close to the mu-out and ksp-in line. The analyzed mineral compositions (biotite $X_{Fe}$ = 0.52–0.63, muscovite $X_{Fe}$ = 0.45–0.59 and cordierite $X_{Fe}$ = 0.39–0.47) are consistent with the calculated isopleths in the cordierite stability field (Fig. 5.3c–d). The inclusions of sillimanite in muscovite laths point to retrograde muscovite growth during cooling.

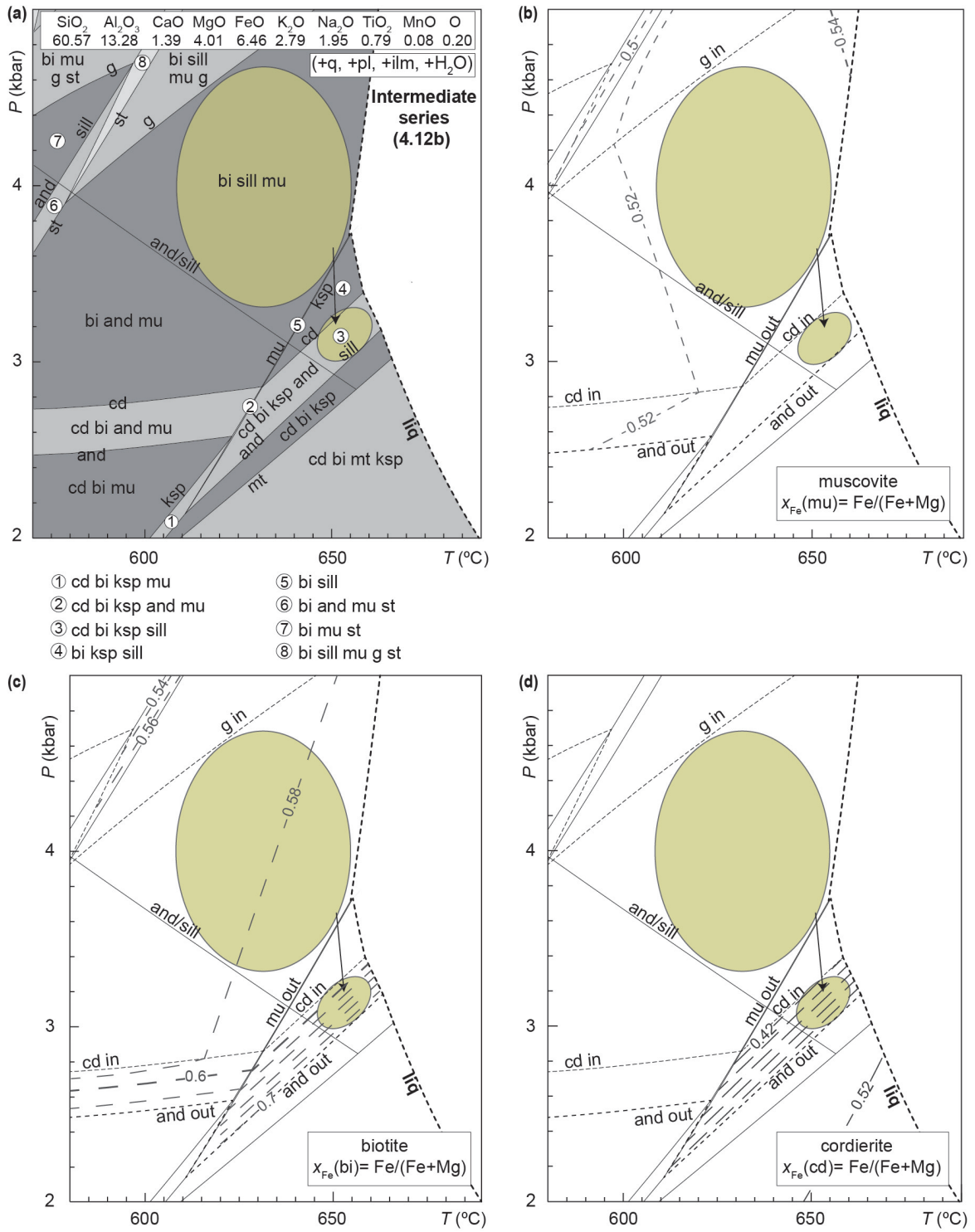



**Figure 5.3.** MnNCKFMASTHO *P–T* pseudosection calculated for the whole-rock composition of a representative sillimanite schist from the Intermediate series not affected by the Ceret gabbro-diorite contact aureole (in moles adjusted to 100%). The *P–T* path is derived by comparing the modeled assemblages and isopleths with assemblages, chemistry and zoning of minerals observed in the studied sample (4.12b). See text for details. (b–d) Enlarged and simplified parts of the pseudosection with calculated isopleths of mineral composition for the areas of interest. The solidus is underlined by a dark-dashed line.

### 5.2.3. The Intermediate series affected by the Ceret gabbro-diorite contact aureole: pseudosection for sample 459

The composition of sample 459 in wt. % is $SiO_2$ = 56.77, $TiO_2$ = 0.98, $Al_2O_3$ = 19.04, $FeO_{tot}$ = 9.00, MnO = 0.13, MgO = 2.91, CaO = 2.03, $Na_2O$ = 2.22, $K_2O$ = 3.12, $P_2O_5$ = 0.11 (see Table 4.4). $H_2O$ is set to 4.20 mol% in order to allow the stability of the observed assemblage cd–bi–g–ksp–sill at the solidus, with isopleths approximating the observed mineral compositions (for the approach see White & Powell, 2002). The major features of the pseudosection (Fig. 5.4) include a steep solidus at 665–720 °C except for a temperature jump from 695 °C to 730 °C at ~4.8 kbar when cordierite stabilizes. K-feldspar-in line has a concave-up shape from 3.6 kbar and 650 °C to 8 kbar and 720 °C and garnet stability includes almost all the investigated *P*–*T* range except for the low-pressure region between 650 °C and 710 °C. Sillimanite is stable from above 3.3 kbar and 700 °C to 7 kbar and 820 °C. Cordierite occurs below ~4–5 kbar for temperatures between 650–730 °C, and below 5–7 kbar for the high-temperature region between 730–810 °C.

Paragenetic features of sample 459 involve the S2 fabric underlined by sillimanite and biotite-rich layers alternating with K-feldspar–plagioclase–quartz-bearing layers. Rim inclusion trails in garnet formed by sillimanite, ilmenite and biotite point to crystallization of the rim in the S1 foliation. The equilibration conditions of both S1 and S2 fabric are therefore in the bi–liq–g–ksp–sill field. Oriented inclusions of biotite, sillimanite and ilmenite in garnet rims indicate garnet growth in presence of sillimanite, which may be explained in the pseudosection by increasing the molar proportion of garnet during the prograde path at the pressure climax (~7 kbar) (Fig. 5.4b). Core composition of garnet (alm = 0.78; grs = 0.06 and sps = 0.03) matches the modeled isopleths at ~7 kbar and ~730 °C whereas rim compositions (alm = 0.80; grs = 0.04 and sps = 0.08) indicate decompression (Fig. 5.4c–e). The presence of cordierite poikiloblasts including the previous mineral assemblages points to the end of the *P*–*T* path in the cd–bi–g–ksp–sill field, where the liquid-out line is reached at 4.5 kbar and 710 °C. Garnet rim (alm = 0.80; grs = 0.04 and sps = 0.08), cordierite ($X_{Fe}$ = 0.35–0.42) and biotite ($X_{Fe}$ = 0.50–0.59) compositions are consistent with the calculated isopleths in the cd–bi–g–ksp–sill field (Fig. 5.4c–g).

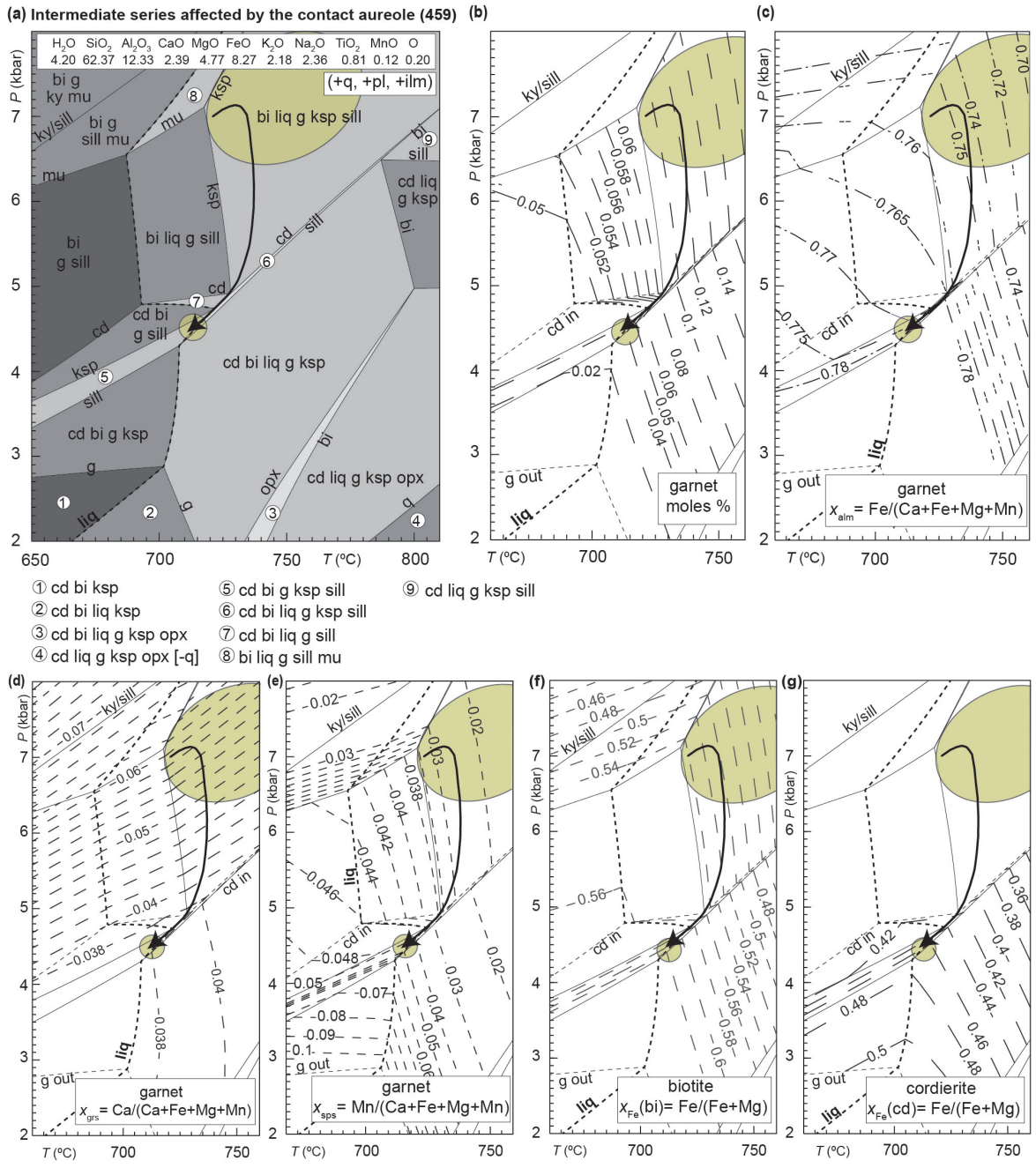



**Figure 5.4.** $H_2O$ undersaturated MnNCKFMASTHO *P–T* pseudosection calculated for the whole-rock composition from the Intermediate series affected by the Ceret gabbro-diorite contact aureole (in moles adjusted to 100%). The sample (459) corresponds to a migmatite of the inner contact aureole. The *P–T* path is derived by comparing the modeled assemblages and isopleths with assemblages, chemistry and zoning of minerals observed in the studied sample. See text for details. (b–g) Enlarged and simplified parts of the pseudosection with calculated isopleths of mineral composition and molar proportions for the areas of interest. The solidus is underlined by a dark-dashed line.

### 5.2.4. The Lower series: pseudosection for sample 515

The composition of sample 515 in wt. % is $SiO_2$ = 64.32, $TiO_2$ = 0.77, $Al_2O_3$ = 14.83, $FeO_{tot}$ = 5.68, MnO = 0.09, MgO = 3.21, CaO = 2.12, $Na_2O$ = 2.84, $K_2O$ = 2.62, $P_2O_5$ = 0.24 (see Table 4.4). $H_2O$ set to 3.80 mol% allows the stability of the observed assemblage cd–bi at the solidus (Fig. 5.5). The major features of the pseudosection include a steep solidus at 670–680 °C, sillimanite stability above 4.6–7 kbar and cordierite stability below 5.2–7 kbar. Garnet is stable in almost all the investigated *P*–*T* range except for the region below 2–5 kbar. K-feldspar is not stable in the diagram.

The major petrographic features of sample 515 involve a folded S1 foliation marked by alternating biotite-rich paleosome and quartz–plagioclase-bearing leucosome. The scarce presence of garnet always included in plagioclase, suggests that it is a relict phase, not stable with the matrix assemblage. Cordierite indicates late growth after S2 fabric. These textural features may be explained in the pseudosection by crossing the garnet-out line from the cd–bi–liq–g–mt to the cd–bi–liq–mt field as indicated by the arrow in Figure 5.5a, and suggesting decompression accompanied by decrease of temperature. Composition of garnet ($alm_{0.68–0.69}$; $grs_{0.03}$; $prp_{0.13\rightarrow0.09}$; $sps_{0.15\rightarrow0.19}$), biotite ($X_{Fe}$ = 0.48–0.52) and cordierite ($X_{Fe}$ = 0.33–0.35) are close to the calculated isopleths in this region (Fig. 5.5b–f). The *P*–*T* path cannot be traced further backwards in the absence of sillimanite or large garnet that would have preserved the earlier history, and therefore, it is suggested that the peak pressure conditions are not recorded by the sample.

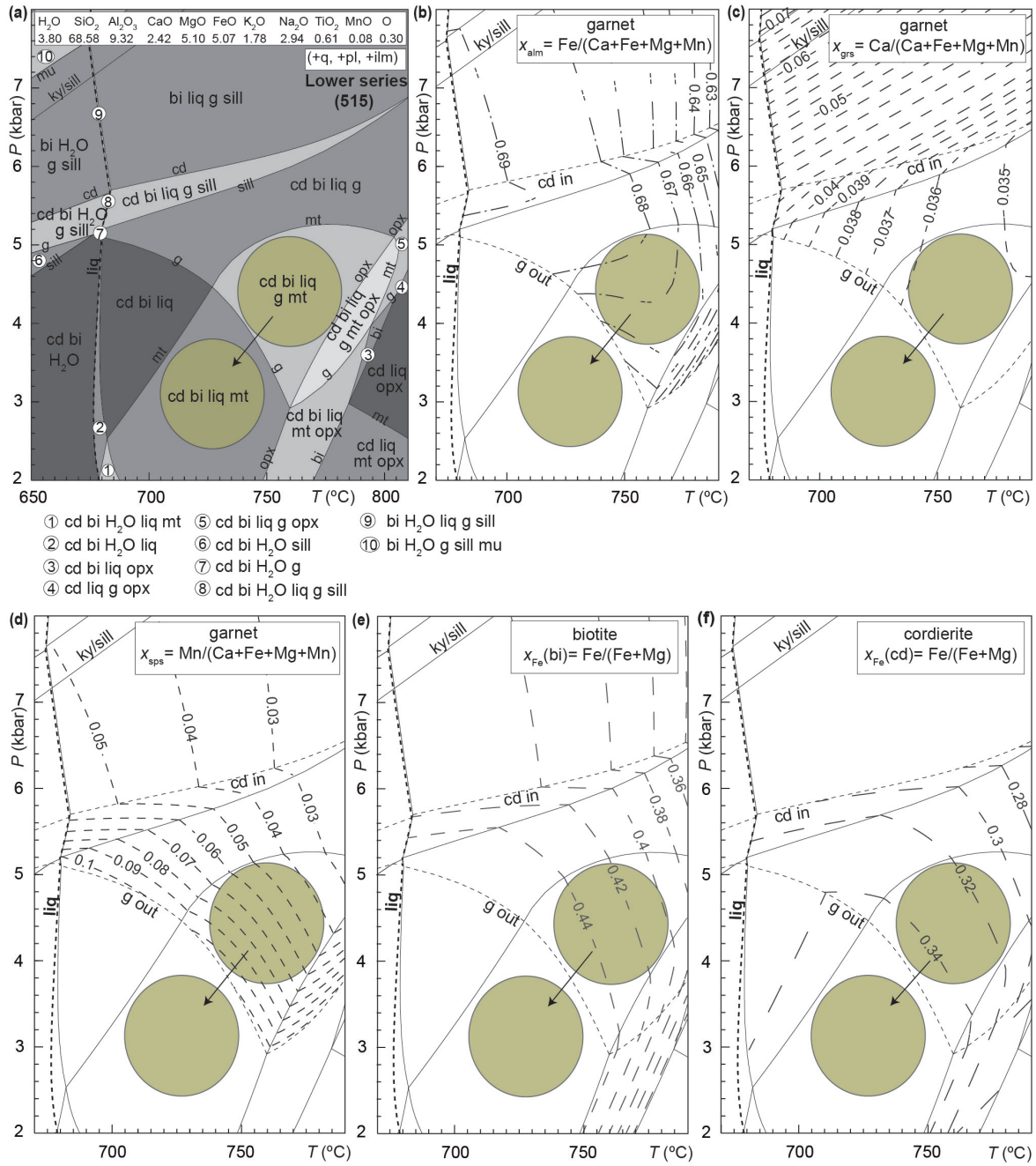



**Figure 5.5.** $H_2O$ undersaturated MnNCKFMASTHO *P*–*T* pseudosection calculated for the whole-rock composition of a fold-structured migmatite from the Lower series (in moles adjusted to 100%). The *P*–*T* path is derived by comparing the modeled assemblages and isopleths with assemblages, chemistry and zoning of minerals observed in the studied sample (515). See text for details. (b–f) Enlarged and simplified parts of the pseudosection with calculated isopleths of mineral composition for the areas of interest. The solidus is underlined by a dark-dashed line.

# CHAPTER 6

## FORWARD MODELING OF CONTACT METAMORPHIC MIGMATITES

The aim of this chapter is to explain the variety of textures, mineral associations and whole-rock compositions shown by migmatitic rocks from the Intermediate series affected by the Ceret contact aureole of the Roc de Frausa Massif (Eastern Pyrenees). Even though they are spatially close to each other, the present mineralogical, microstructural and compositional characteristics of these samples cannot be explained in simplistic terms. Thus, the correct interpretation of their evolution must take into account several aspects among which are:

(a) The *P*–*T* path followed by the different types of migmatites. It is important to know the prior, the coeval and the post-peak *P*–*T* conditions for the thermal event. In principle, the *P*–*T* path for all samples should be similar given that sampling is spatially restricted, all sample belong to the same structural level and no major tectonic discontinuities are found between them.

(b) The whole-rock composition of each migmatitic sample. It is important to estimate if the composition of the rock system remained constant during the prograde and/or retrograde stages of the metamorphic event or if it was modified. The bulk composition of the rock system can vary depending on proccesses such as fluid flow and/or melt behavior. The generated melt could be mostly stagnant, migrate out of the sample system (melt loss) or be incorporated into it from an outside source during its evolution (melt gain). If melt was lost previous to the onset of retrogression, high-temperature peak assemblages would be preserved. Conversely, if melt was available while the temperature dropped retrogression of high-temperature assemblages would take place.

In this chapter, forward modeling of phase equilibria is used to infer the *P*–*T* conditions of the last equilibration for the four migmatite types (section 6.2) and to

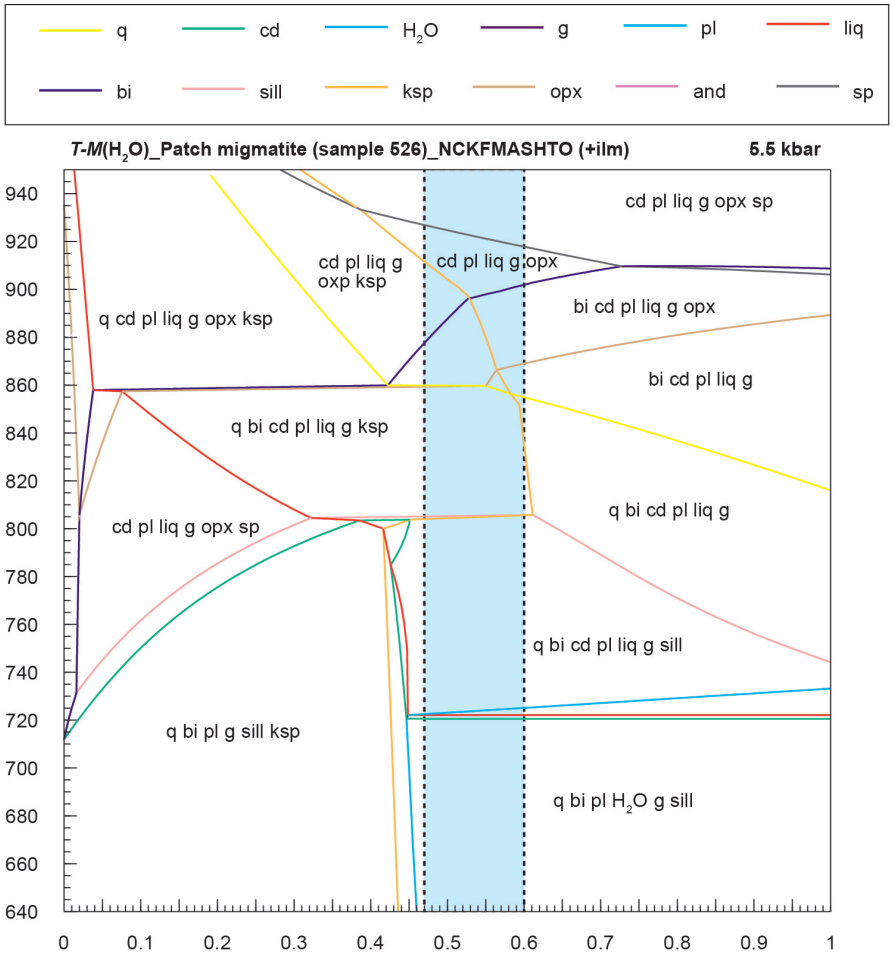
discuss possible closed- to open-system processes that may have operated in these rocks (section 6.3). Forward modeling uses *P*–*T* and *T*–*X* pseudosections to predict mineral assemblages, mineral compositions and modes for constant or variable whole-rock compositions, using internally consistent thermodynamic datasets (Powell & Holland, 2008).

## 6.1. Calculation methods

The *P*–*T* and *T*–*X* pseudosections were calculated using THERMOCALC 3.35 (Powell *et al.,* 1998; update 2010) and the 5.5 version of the thermodynamic dataset (Holland & Powell, 1998; January 2006 upgrade), for the system $Na_2O$-CaO-$K_2O$-FeO-MgO-$Al_2O_3$-$SiO_2$-$H_2O$-$TiO_2$-$O_2$ (NCKFMASHTO). The activity-composition (*a*-*x*) models are from the THERMOCALC file (compiled 28/12/07), where cordierite (cd) and staurolite (st) models are from Holland & Powell (1998) and garnet (g), biotite (bi) and silicate melt (liq) models are after White *et al*. (2007). Muscovite (mu) is after Coggon & Holland (2002), feldspars (pl, ksp) from Holland & Powell (2003), orthopyroxene (opx), spinel (sp) and magnetite (mt) from White *et al*. (2002), and Ilmenite (ilm), hematite (hem) and alternate model of magnetite (mt) for low-grade rock are after White *et al*. (2000). Rock compositions were used with the molar amounts of these oxides normalized to 100%.

In all calculations, plagioclase and ilmenite are set in excess. The amount of $H_2O$ in the whole-rock composition was deduced from *T*–*M*($H_2O$) pseudosections, adjusting the minimum amount of $H_2O$ that has to be added to the sample in order to the first fusion of the rock takes place at a minimum temperature (see Figure 6.1 as an example) and to explain the preserved mineral assemblages, mineral composition and mode variations (see White & Powell, 2002 for an example of this approach). We also checked that the water content of the pseudosection was comparable to the LOI value for the corresponding analysis. The amount of $Fe_2O_3$ for the calculations was set in a way that the modeled mineral assemblages show the presence or absence of magnetite, according to the observed assemblages. Furthermore, pseudosections were contoured for both mineral modes and mineral compositions, providing additional constraints on *P*–*T* variations during contact metamorphism. Thus, mineral

composition and molar proportion isopleths were plotted for the phases of interest. The isopleth notation used is: $x_{Fe}$ (bi, cd, g) = Fe / (Fe + Mg).




| $H_2O$ | $SiO_2$ | $Al_2O_3$ | CaO | MgO | FeO | $K_2O$ | $Na_2O$ | $TiO_2$ | O | |
|---|---|---|---|---|---|---|---|---|---|---|
| 0.00 | 60.74 | 13.50 | 4.38 | 5.51 | 10.10 | 2.60 | 1.44 | 1.49 | 0.23 | Anhydrous |
| 10.00 | 54.66 | 12.15 | 3.95 | 4.96 | 9.09 | 2.34 | 1.30 | 1.34 | 0.21 | Hydrated |

**Figure 6.1.** $T$–$M$($H_2O$) pseudosection calculated for a patch migmatite showing the minimum range of water (blue shaded area) required for minimum melting temperature. The code for the first appearance of a mineral is indicated above the diagram. The solidus is traced by a red line.

## 6.2. Closed mineral equilibria modeling in the NCKFMASHTO system

The *P*–*T* path for the four representative migmatite types (a patchy, a stromatite, a schollen migmatite and a residuum melanosome) with different mineral assemblages was estimated (see Fig. 6.2 for location of samples). We assumed that all migmatites were undergoing their first episode of fusion as deduced from the mineral assemblages and *P*–*T* conditions of the neighboring rocks not affected by the contact aureole (see Chapter 5). Thus, all metapelites would be heated from subsolidus water saturated conditions and would be dehydrated immediately after the solidus, given the known strong partitioning behavior of water into the new generated silicate melt phase. The last *P*–*T* equilibration conditions of all migmatite types must come out very similar, as the rocks samples where formed by the same set of metamorphic processes and where very near to each other during these processes. The calculation of the *P*–*T* path using a closed-system model is compulsory if we want to perform further modeling involving open-system interactions, such as melt loss or gain and/or introduction of water in the metamorphic system during the crystallization of the Ceret gabbro-diorite.

### 6.2.1. Patch migmatites: pseudosection for sample 526

Sample 526 is a representative patch migmatitic formed by cordierite-rich and fibrolite-poor paleosomes. S1 foliation is strongly folded and defined by alternating quartz–plagioclase-rich and biotite–cordierite-rich layers. The composition of sample 526 in wt. % is $SiO_2$ = 52.40, $TiO_2$ = 1.71, $Al_2O_3$ = 19.76, $FeO_{tot}$ = 10.42, MnO = 0.11, MgO = 3.19, CaO = 3.53, $Na_2O$ = 1.29, $K_2O$ = 3.52, $P_2O_5$ = 0.25 (see Table 4.4). The major features of the pseudosection (Fig. 6.3) include the steep inclined liquid-in line at 690–700 °C, garnet stability in almost all the investigated *P*–*T* range except for the low-pressure region, and K-feldspar is stable at the high-temperature and pressure regions of the pseudosection. Sillimanite is stable above 3 kbar in the low temperature region of the diagram, the sillimanite-in line up-pressure as temperature increase, so as to reach 8 kbar in the high-temperature region. Cordierite is stable in most of the diagram, below ~4.8–6 kbar for temperatures between 650–825 °C, and below 6 kbar for the high-temperature region above 825 °C.

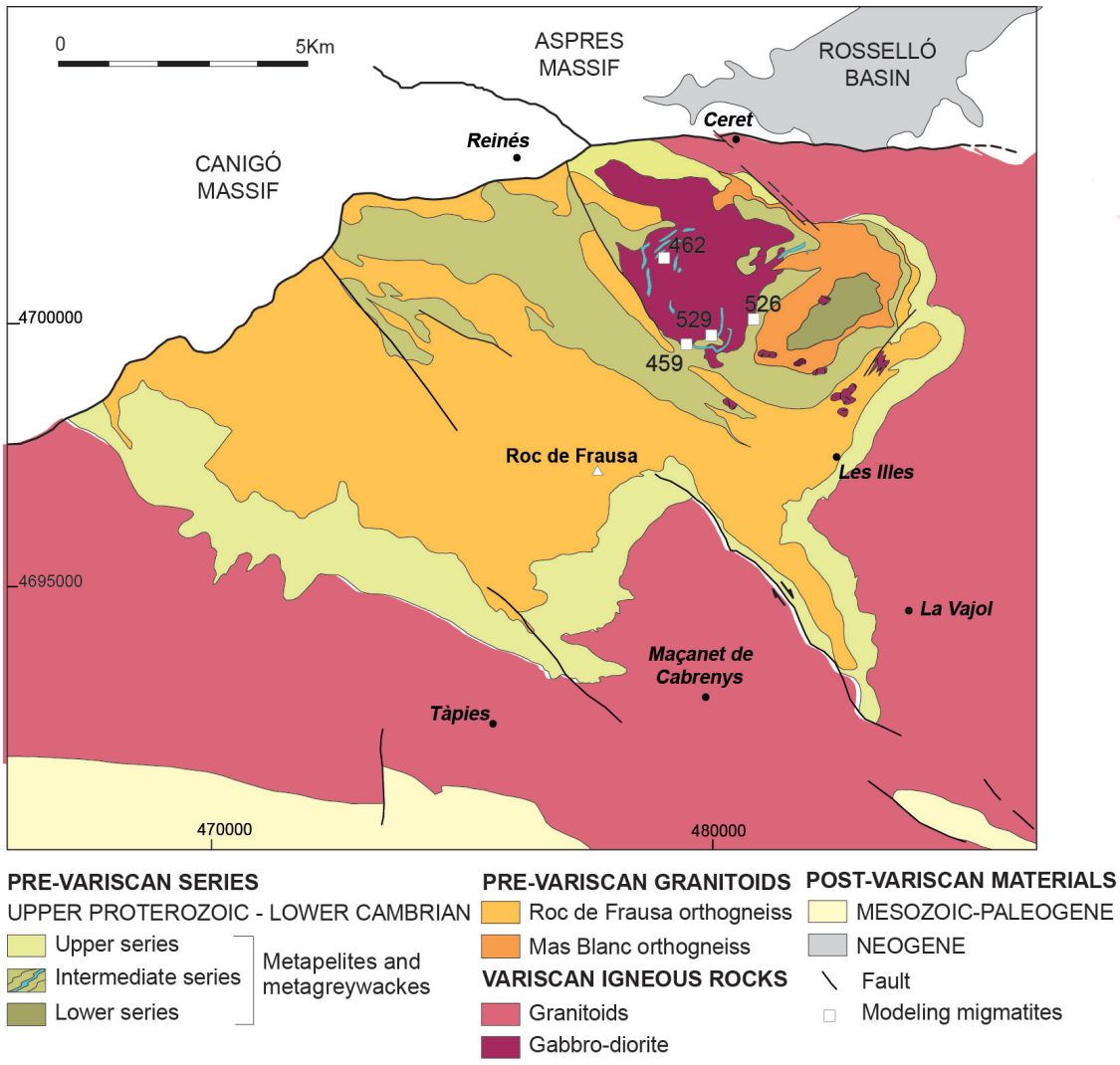



**Figure 6.2.** Geological sketch map of the Roc de Frausa Massif with the location of four characteristic migmatitic rocks used in this study. Modified from Liesa & Carreras (1989).

The crystallization sequence in sample 526 involves garnet porphyroblasts with inclusion trails of fibrolite, biotite and ilmenite parallel to S1. This fabric is folded by a subsequent D2 deformation event and included in cordierite poikiloblasts (see Fig. 4.4e) with no pressure shadows around them. Prismatic sillimanite is absent. These observations are compatible with a *P*–*T* path from the q–g–bi–sill–ksp–liq field to the q–g–bi–sill–cd–ksp–liq field (green arrow; Fig. 6.3a), involving first a pressure decrease from ~7 kbar to ~5 kbar followed by a temperature decrease from 850 °C to 720 °C. The scarceness of sillimanite in the preserved mineral association can be explained in the pseudosection by decreasing its molar proportion during decompression and cooling (Fig. 6.4). The temperature drop would retrograde the rock to the lower temperature assemblage q–g–bi–sill–cd–liq without K-feldspar. The

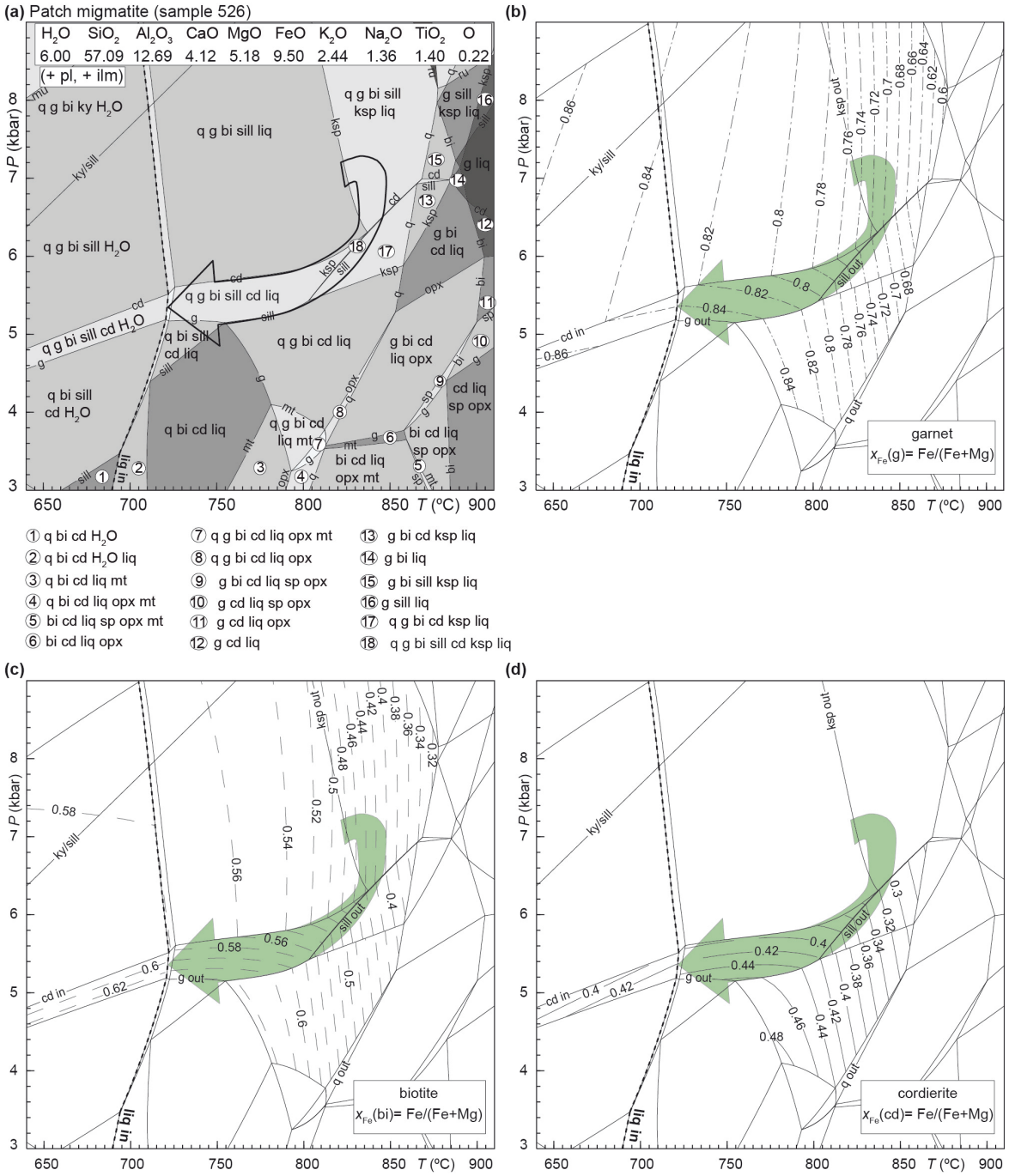



**Figure 6.3.** NCKFMASHTO *P–T* pseudosection calculated for the whole-rock composition of a patch migmatite formed at the Ceret gabbro-diorite contact aureole (in moles adjusted to 100%). The *P–T* path is derived by comparing the modeled assemblages and isopleths with the assemblages and mineral chemistry observed in the studied sample (526). See text for details. (b–d) Enlarged and simplified parts of the pseudosection with calculated isopleths of mineral composition for the areas of interest. The solidus is underlined by a dashed line.

liquid-out line would be reached at ~5 kbar and 720 °C, where the calculated isopleths closely match the mineral compositions (garnet $X_{Fe}$ (core to rim) = 0.87→ 0.82→ 0.91, biotite $X_{Fe}$ = 0.53–0.65, cordierite $X_{Fe}$ = 0.38–0.48; Fig. 6.3b–d).

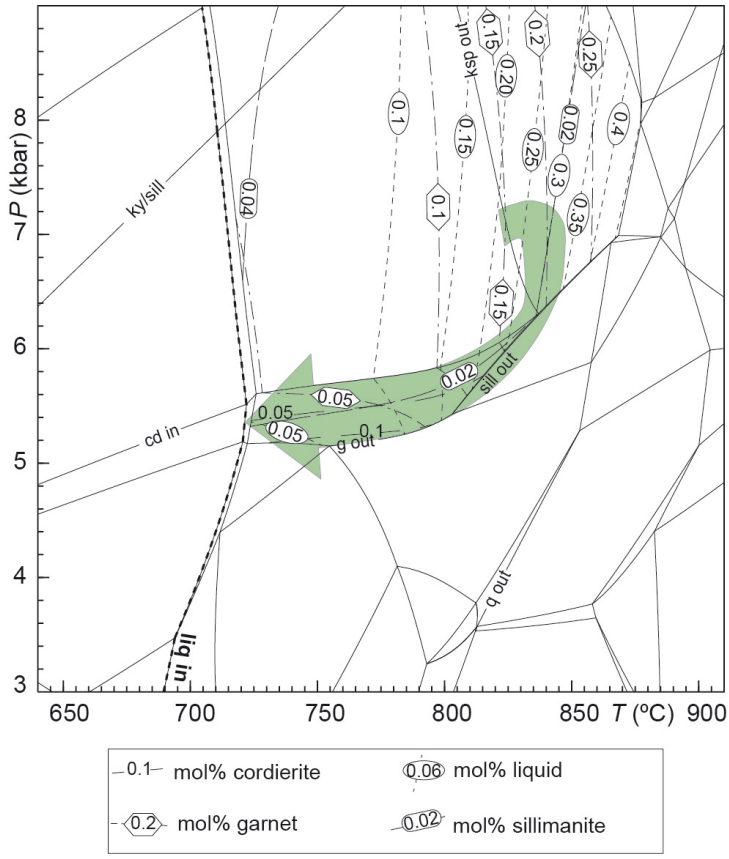



**Figure 6.4.** *P–T* pseudosection of the patch migmatite (sample 526) with calculated isopleths of the molar proportions of liquid, sillimanite, garnet and cordierite for the areas of interest. The solidus is underlined by a dashed line.

### 6.2.2. Stromatic migmatites: pseudosection for sample 529

Sample 529 is a representative stromatic migmatites formed by cordierite and biotite-rich paleosomes alternating with coarser-grained leucosomes, where folded S1 foliation is strongly transposed by S2 fabric (see Fig. 4.5). The composition of sample 529 in wt. % is $SiO_2$ = 57.60, $TiO_2$ = 1.04, $Al_2O_3$ = 17.75, $FeO_{tot}$ = 7.90, MnO = 0.12, MgO = 4.68, CaO = 2.75, $Na_2O$ = 2.26, $K_2O$ = 2.86, $P_2O_5$ = 0.22 (see Table 4.4). The major features of the pseudosection (Fig. 6.5) include a steep liquid-in line at 700–740 °C, garnet stability in almost all the investigated *P–T* range except for the low-pressure region, sillimanite stability above 6 kbar except for the high-temperature region (850–910 °C) and cordierite stable below ~6.2–7 kbar. K-feldspar is not stable

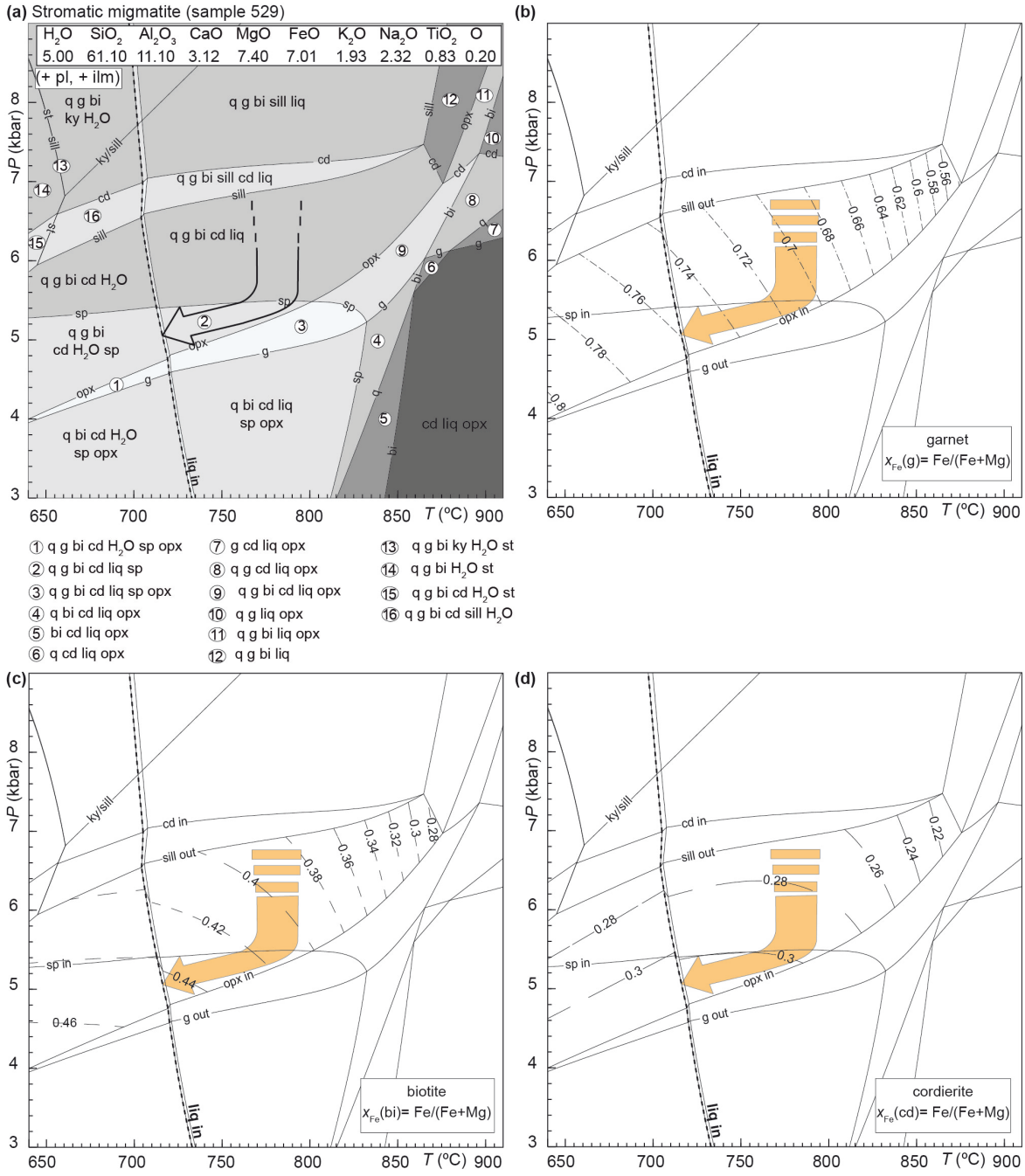



**Figure 6.5.** NCKFMASHTO *P*–*T* pseudosection calculated for the whole-rock composition of a stromatic migmatite affected by the Ceret gabbro-diorite contact aureole (in moles adjusted to 100%). The *P*–*T* path is derived by comparing the modeled assemblages and isopleths with assemblages and mineral chemistry observed in the studied sample (529). See text for details. (b–d) Enlarged and simplified parts of the pseudosection with calculated isopleths of mineral composition for the areas of interest. The solidus is underlined by a dashed line.

in any field of the diagram.

The major petrographic features of sample 529 involve the presence of cordierite poikiloblasts with no pressure shadows including biotite and green spinel. In the pseudosection, the formation of green spinel can be explained by a decrease in pressure from the q–g–bi–cd–liq field to the q–g–bi–cd–liq–sp field (orange arrow; Fig. 6.5a) and implies an increase in the mode of spinel and cordierite and a decrease in garnet content (Fig. 6.6). In the q–g–bi–cd–liq–sp field, the calculated isopleths closely match the mineral compositions of garnet ($X_{Fe}$ (core to rim) = 0.71→0.84), biotite ($X_{Fe}$ = 0.43–0.47) and cordierite ($X_{Fe}$ = 0.29–0.32; Fig. 6.5b–d). In the pseudosection, these compositions are reached close to the solidus at ~5 kbar and 720 °C. Thus, the complete path involves a pressure decrease from ~7 kbar to ~5 kbar followed by a decrease in temperature from 800 °C to 720 °C.

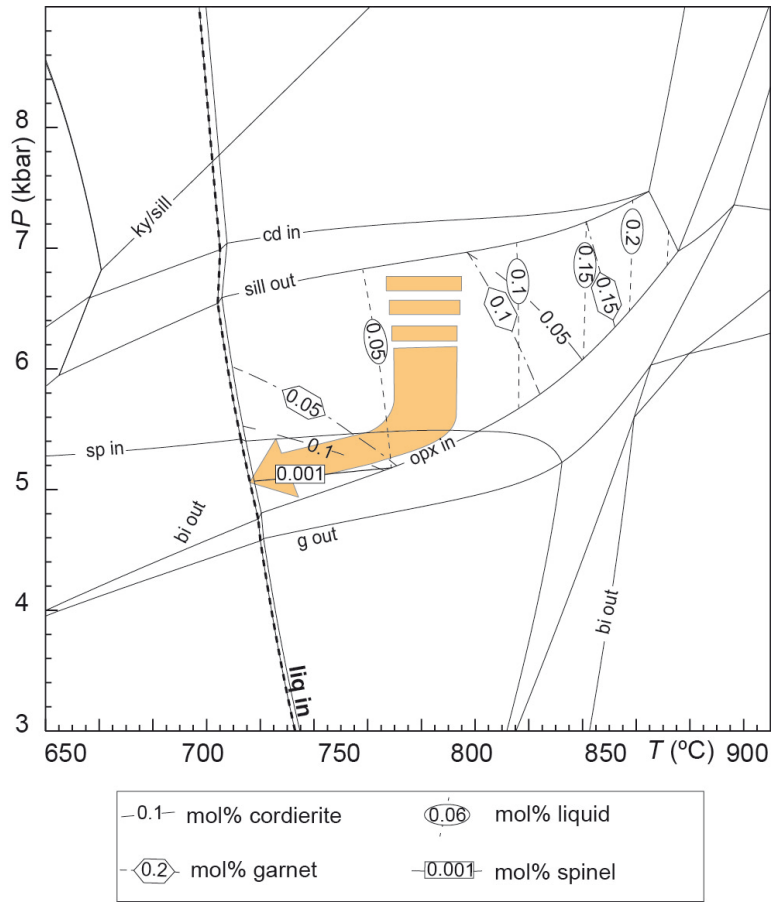



**Figure 6.6.** *P–T* pseudosection of the stromatic migmatite (sample 529) with calculated isopleths of the molar proportions of liquid, garnet, cordierite and spinel for the areas of interest. The solidus is underlined by a dashed line.

### 6.2.3. Schollen migmatites: pseudosection for sample 459

Sample 459 is a representative schollen migmatite composed of a biotite and sillimanite-rich paleosome embedded in a coarse-grained leucosome synchronous to the D2 event. The composition of sample 459 in wt. % is $SiO_2$ = 56.77, $TiO_2$ = 0.98, $Al_2O_3$ = 19.04, $FeO_{tot}$ = 9.00, MnO = 0.13, MgO = 2.91, CaO = 2.03, $Na_2O$ = 2.22, $K_2O$ = 3.12, $P_2O_5$ = 0.11 (see Table 4.4). The major features of the pseudosection (Fig. 6.7) include a steep liquid-in line at 670–690 °C, garnet stability in almost all the investigated *P*–*T* range except for the low-pressure region and K-feldspar stability heading from 3 kbar and 680 °C to 9 kbar and 800 °C. Sillimanite stability line traverses obliquely the diagram from 3 kbar–670 °C to 7 kbar–850 °C. Cordierite is stable below 5.4 kbar for temperatures below the solidus (640–680 °C), and for high-temperature region (between 680 and 910 °C), it is stable below 5.4–7 kbar.

The presence of late cordierite poikiloblasts with no pressure shadows and including the previous mineral assemblages point to a *P*–*T* path from the q–g–bi–sill–ksp–liq field to the q–g–bi–sill–cd–ksp–liq field (blue arrow; Fig. 6.7a). The presence of K-feldspar blebs within idiomorphic to subidiomorphic porphyroblasts of plaglioclase and the presence of prismatic sillimanite can be explained in the pseudosection by a decrease in temperature from the q–g–bi–sill–cd–ksp–liq field to the q–g–bi–sill–cd–liq field, where the molar proportion of sillimanite increases (Fig. 6.8) and the liquid-out line is reached at ~5 kbar and 690 °C. The composition of garnet ($X_{Fe}$ (core to rim)=0.90→0.87→0.89), biotite ($X_{Fe}$ = 0.50–0.59) and cordierite ($X_{Fe}$ = 0.35–0.42) approximately match the calculated isopleths in the q–g–bi–sill–cd–liq field (Fig. 6.7b–d). In the pseudosection, the path inferred by these microstructural relations involves a pressure decrease from ~7 kbar to ~5 kbar followed by a temperature decrease from 840 °C to 690 °C.

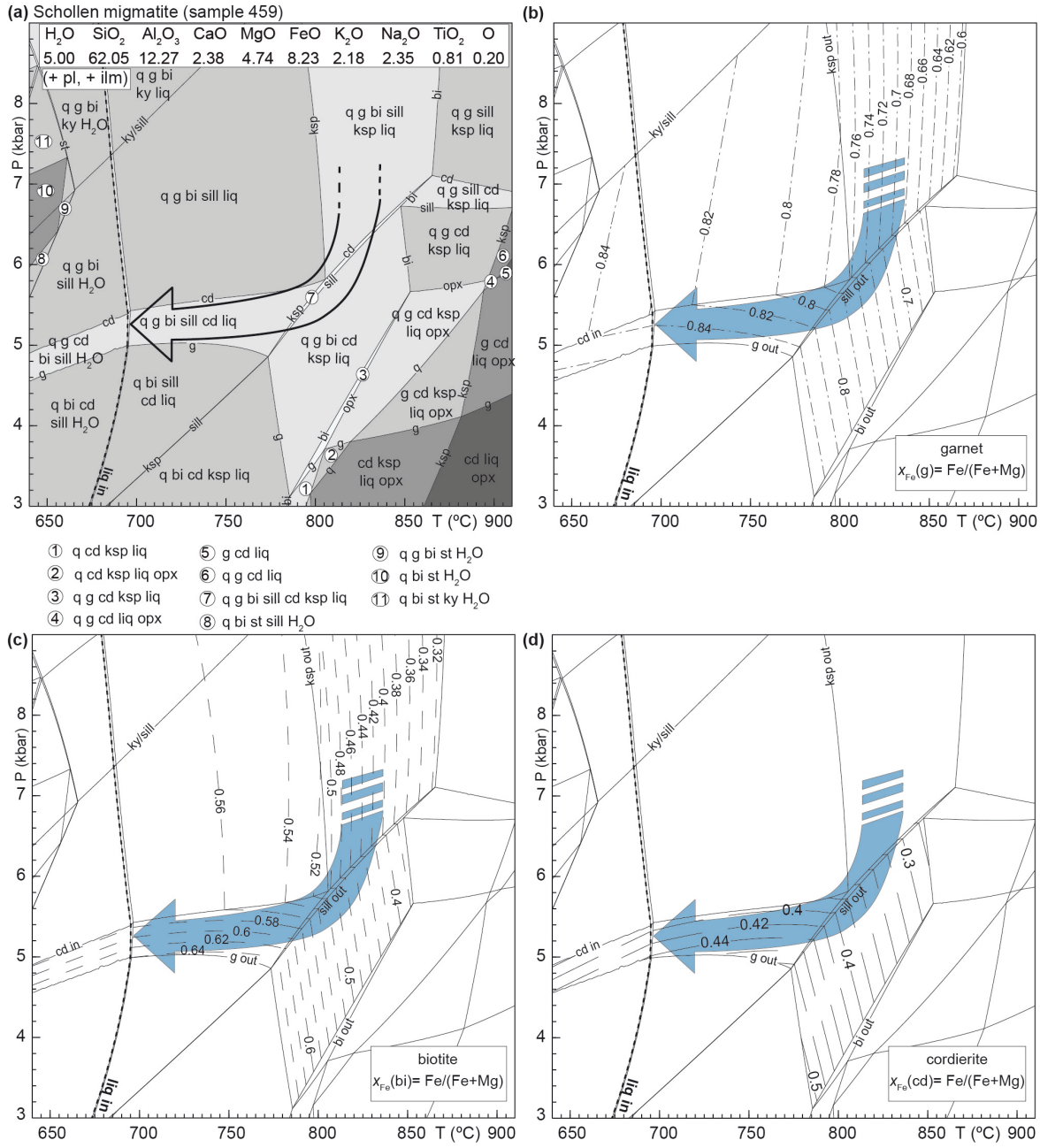



**Figure 6.7.** NCKFMASHTO *P–T* pseudosection calculated for the whole-rock compositions of a schollen migmatite affected by the Ceret gabbro-diorite contact aureole (in moles adjusted to 100%). The *P–T* path is derived by comparing the modeled assemblages and isopleths with assemblages and mineral chemistry observed in the studied sample (459). See text for details. (b–d) Enlarged and simplified parts of the pseudosection with calculated isopleths of mineral composition for the areas of interest. The solidus is underlined by a dashed line.

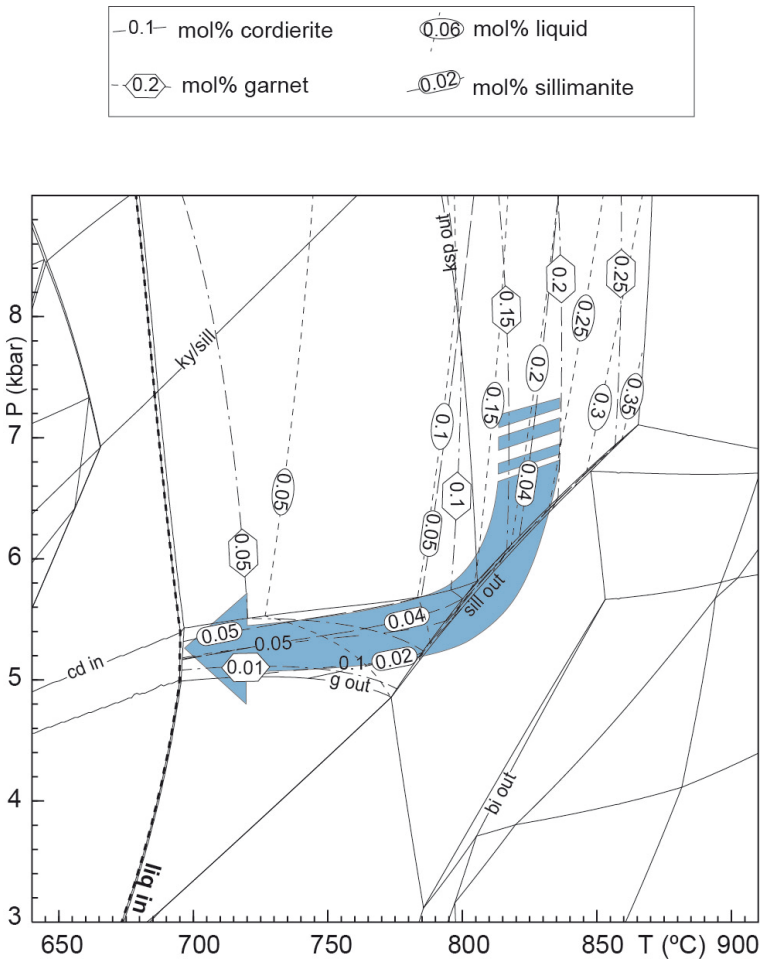



**Figure 6.8.** *P–T* pseudosection of the schollen migmatite (sample 459) with calculated isopleths of the molar proportions of liquid, sillimanite, garnet and cordierite for the areas of interest. The solidus is underlined by a dashed line.

### 6.2.4. Residuum melanosomes: pseudosection for sample 462

Sample 462 is a representative residuum melanosome formed by garnet porphyroblasts, biotite, ilmenite and brown spinel embedded in a cordierite-rich matrix (see Fig. 4.7f). The composition of sample 462 in wt. % is $SiO_2$ = 43.93, $TiO_2$ = 1.50, $Al_2O_3$ = 24.90, $FeO_{tot}$ = 13.19, MnO = 0.20, MgO = 5.89, CaO = 1.33, $Na_2O$ = 1.60, $K_2O$ = 0.75, $P_2O_5$ = 0.04 (see Table 4.4). The low $SiO_2$ content of the sample is reflected in the major features of the pseudosection (Fig. 6.9). Thus, the liquid-in line at 700–775 °C undergoes a step-like jump up pressure with decreasing temperature through the spinel and orthopyroxene breakdown lines. Garnet is stable in almost all the investigated *P–T* range except for the low-pressure region, from 3 kbar and 720 °C to 5 kbar and 910 °C. Sillimanite and cordierite stability are pressure dependent, sillimanite above ~5.6–6 kbar and cordierite below ~7.4–8 kbar. Quartz is not stable

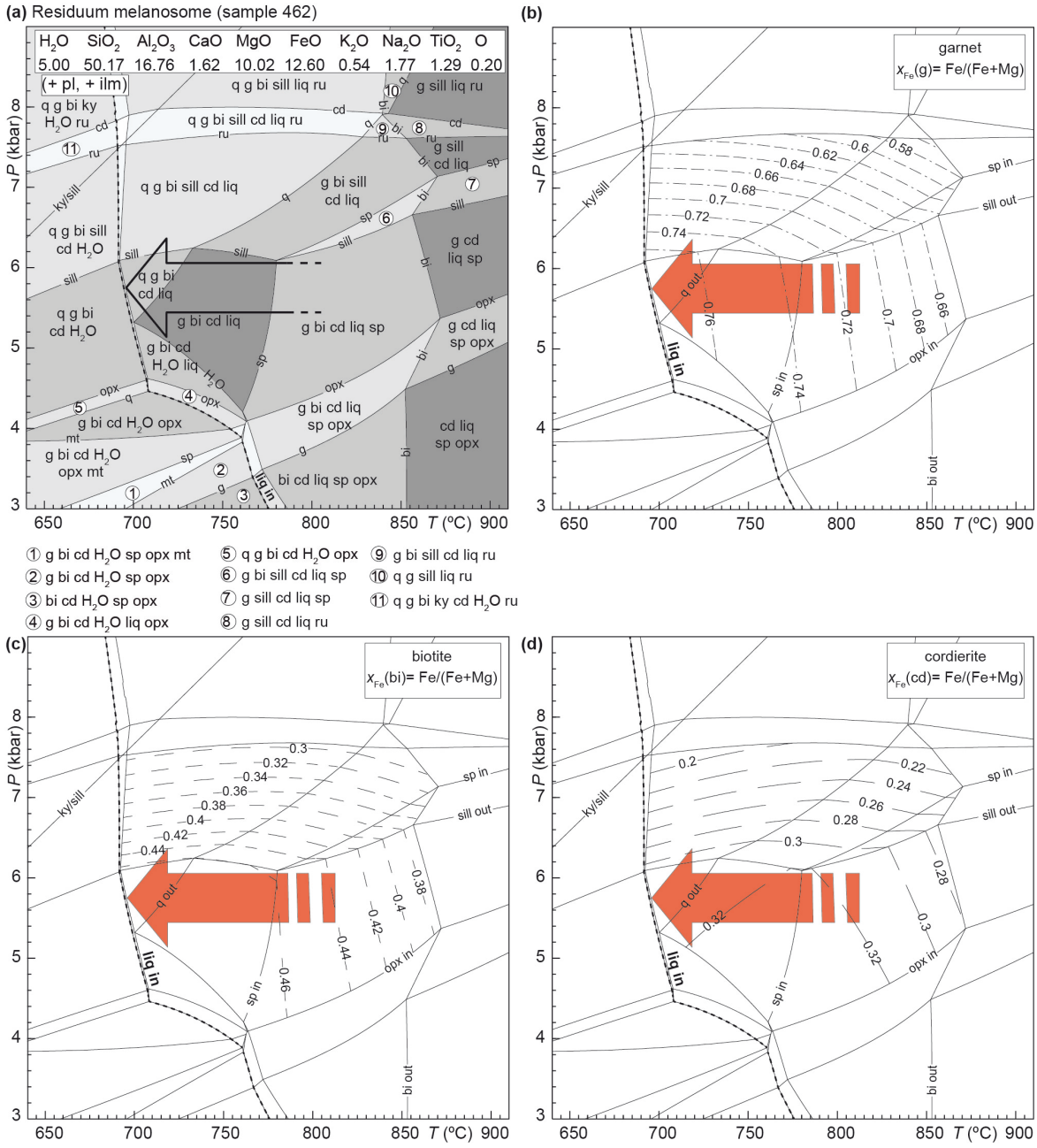



**Figure 6.9.** NCKFMASHTO *P–T* pseudosection calculated for the whole-rock compositions of a residuum melanosome located as a xenolith within the Ceret gabbro-diorite contact aureole (in moles adjusted to 100%). The *P–T* path is derived by comparing the modeled assemblages and isopleths with assemblages and mineral chemistry observed in the studied sample (462). See text for details. (b–d) Enlarged and simplified parts of the pseudosection with calculated isopleths of mineral composition for the areas of interest. The solidus is underlined by a dashed line.

in the subsolidus region of the diagram below 4.2 kbar jumping to 5.2 kbar and 705 °C to 9 kbar and 860 °C. Spinel is stable below ~3–3.8 kbar for temperatures between 660 and 760 °C, and below 4–7 kbar for the high-temperature region between 760 and 910 °C.

The presence of spinel enclosed in cordierite indicates that the rock attained the g–bi–cd–liq–sp field, where quartz would not be stable. On cooling, spinel would become unstable and a small amount of retrograde quartz would be reincorporated to the rock. In fact, the presence of thin quartz coronas around garnet and its interstitial to poikilitic habit can be explained in the pseudosection by decreasing the temperature from above 780 °C at the g–bi–cd–liq–sp field to 700 °C at the q–g–bi–cd–liq field (red arrow; Fig. 6.9a). At this temperature and around 5 kbar, the liquid-out line is reached and mineral compositions (garnet $X_{Fe}$ (core to rim) = 0.77→0.72→0.87, biotite $X_{Fe}$ = 0.42–0.55 and cordierite $X_{Fe}$ = 0.33–0.35) are close to the calculated isopleths (Fig. 6.9b-d). In the pseudosection, this path involves a temperature decrease from ~800 °C to 700 °C.

### 6.2.5. Average P–T conditions of last equilibration

The major features and topology of the pseudosections for the different types of migmatites varies in the *P–T* space depending on the whole-rock composition (Fig. 6.3 to 6.10). Globally, the position of fields and curves for patch and schollen migmatites are similar, whereas the pseudosections of the stromatite and the residuum melanosome are very different from the previous ones and between them. All pseudosections have a steep solidus that from 5 to 9 kbar takes place at a narrow range of temperature (680–710 °C). At lower pressure, the temperature range of the four solidus curves widens from 675–725 °C for the patch and schollen migmatites and from 715–775 °C for the stromatite and the residuum melanosome samples. All pseudosections also share a high-pressure stability region for sillimanite and garnet and low-pressure stability for cordierite-bearing assemblages. The width of the stability field of sillimanite, garnet and cordierite depends on the $Al_2O_3$/(MgO+FeO) ratio. Higher ratios widen down pressure the stability field of sillimanite and reduce that of cordierite and garnet, displacing down pressure the cordierite-in line and up pressure the garnet-out line. This implies wider areas with cordierite in equilibrium with garnet for residuum melanosomes, ($Al_2O_3$/(MgO+FeO)= 0.74 mol. %) and

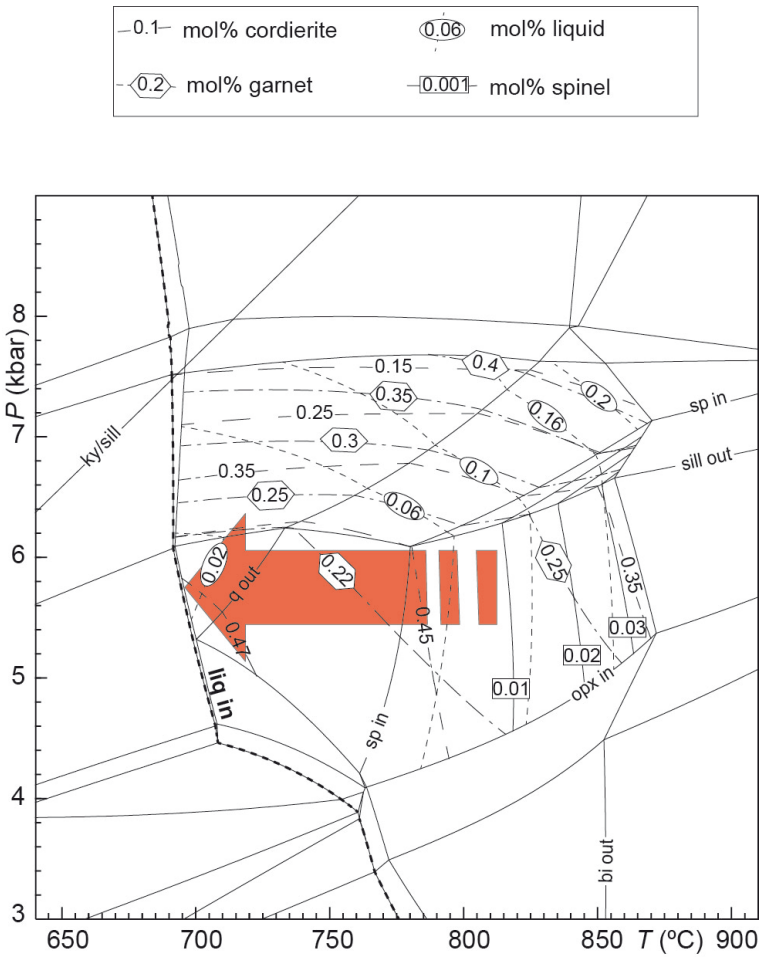



**Figure 6.10.** *P–T* pseudosection of the residuum melanosome (sample 462) with calculated isopleths of the molar proportions of liquid, garnet, cordierite and spinel for the areas of interest. The solidus is underlined by a dashed line.

progressively narrower for stromatites, patch and schollen migmatites ($Al_2O_3$/(MgO+FeO)= 0.94 mol.% for schollen). High $K_2O$ content can also be related to the stability of K-feldspar. Residuum melanosomes and stromatites have the lowest $K_2O$ values, so no K-feldspar is stable in the studied *P–T* range. Conversely, patch and schollen migmatites contain higher $K_2O$ and K-feldspar is stable in the high temperature region. In addition, spinel is only stable at low-pressure in the pseudosections corresponding to the stromatite and the residuum melanosome.

Based on pseudosection modeling, the mineral assemblage of the different migmatite types is interpreted as recording the last re-equilibration in the presence of melt that occurred along a exhumation and cooling *P–T* path. The late crystallization of cordierite in the transition from the q–g–bi–sill–ksp–liq field to the q–g–bi–sill–cd–ksp–liq field occurs on decompression at temperatures between 800–

850 °C and 780–840 °C for patch and schollen migmatites, respectively (Figs. 6.3 & 6.5). Following the crystallization sequences, consumption of K-feldspar and further crystallization of cordierite would take place during cooling until the solidus was reached at about 690–720 °C (Fig. 6.3 to 6.10). The pressure ranges, along which the cooling part of the *P*–*T* path took place, are also limited by the cordierite-out line from the high-pressure side and by the garnet-out line from the low-pressure side for the patch and the schollen migmatites, whereas for stromatite and residuum melanosome the cooling path is limited by sillimanite-in line and by the orthopyroxene-in line from the high-pressure side and from the low-pressure side, respectively.

The *P*–*T* paths of the four samples are clockwise and depict nearly isothermal decompression followed by nearly isobaric cooling to the solidus, so only the retrograde part of the path is recorded. In order to set the average pressure of the different types of migmatites on the last re-equilibration, the four paths have been superimposed in a single *P*–*T* diagram (Fig. 6.11). The average pressure obtained is approximately 5.5 kbar for all samples, which is consistent with the fact that they are located at the same crustal level and would coincide with the final emplacement of the Ceret gabbro-diorite stock. At the moment, there is not pressure constraint on the earlier stages of emplacement and crystallization of the gabbro. Nevertheless, according to the *P*–*T* condictions obtained in the migmatites, the first registered pressure is around 7 kbar. During a second stage, the already crystallized gabbro-diorite probably cooled down along the same isobaric path as the aureole samples. Cooling temperatures registered run from ~850 °C to approximately at 700 °C, corresponding to the solidus for migmatite samples.

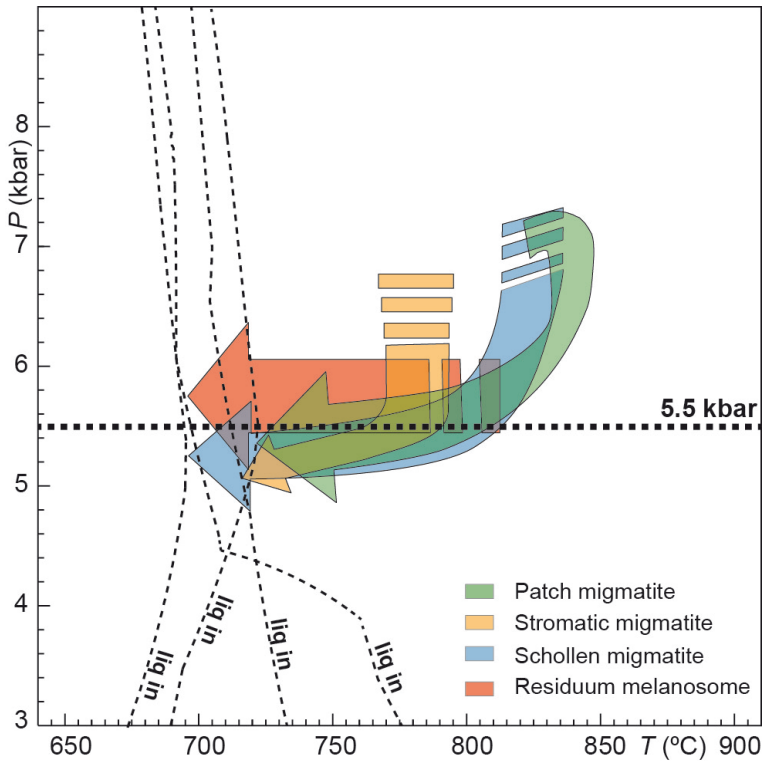



**Figure 6.11.** *P–T* diagram showing the different paths of migmatitic rocks affected by the Ceret contact aureole. The solidus for the different samples is underlined by a dashed line.

## 6.3. Modeling of open-system processes

The *P–T* paths calculated in the previous section considered a closed system for each migmatite type. Closed-system behavior is unlikely to occur during evolution of migmatitic complexes, as has been shown by several authors (e.g., Hasalová *et al*. 2008). Melt-loss processes are common at high-melt percentages, when the rock looses its coherence (rheological melt percentage – Arzi, 1978). Such system involving melt-loss have been modeled using THERMOCALC by White & Powell (2002). Open-system interactions during melt flow have also been modeled by Hasalová *et al*. (2008). Given that molar melt proportions calculated at peak metamorphic conditions for the different migmatite types in the inner Ceret contact aureole range from 6 to 30 mol.%, it is likely that open-system processes could have taken place. Another type of open-system behavior that can occur in migmatitic complexes is $H_2O$-fluxed melting. This hydrous driven melting is likely to occur in cases where magma bodies crystallize enhancing migmatization in the contact aureole.

The purpose of this section is to evaluate the ability of various closed- to open-system processes to account for the different mineral assemblages and the variations in mineral and whole-rock chemistry compositions recorded in the migmatites. Another major point is to estimate the amount of melt gained and lost during the processes and compare it with the amount of leucosome now present in the migmatites. In order to fulfil these goals we tested the influence of water in the system as incorporating a fluid phase into the metasediments would enhance melting and result in a variety of mineral assemblages on retrogression and cooling. The fluid phase could have been released from the crystallizing gabbro-diorite and could have infiltrated the metasediments. Moreover, part of the fluid fraction could also come from dehydration-melting reactions going on in locations next to the aureole, mainly involving the hydrous phases muscovite and/or biotite

Because open-system processes may have operated during contact metamorphism, the whole-rock composition of each migmatitic rock type does not likely correspond to an original protolith composition. For this reason, a model composition for a hypotethical common protolith was reconstructed using the average composition of several neighboring non-migmatitic rocks. The composition of the hypothetical protolith in wt. % is $SiO_2$ = 59.02, $TiO_2$ = 0.87, $Al_2O_3$ = 19.77, $FeO_{tot}$ = 7.00, MnO = 0.08, MgO = 2.77, CaO = 1.00, $Na_2O$ = 1.85, $K_2O$ = 3.75, $P_2O_5$ = 0.16. Consequently, forward modeling in two different scenarios was calculated for this composition in the NCKFMASTHO system (see Calculation methods section 6.1.) at an average pressure of 5.5 kbar, where the last re-equilibration of all types of migmatites took place (Fig. 6.11). The two envisaged scenarios are:

(1) One single melting event with variable fluid content (system open only to $H_2O$) (Fig. 6.12); and

(2) Multiple melt loss–rehydration events (Figs. 6.13 & 6.14).

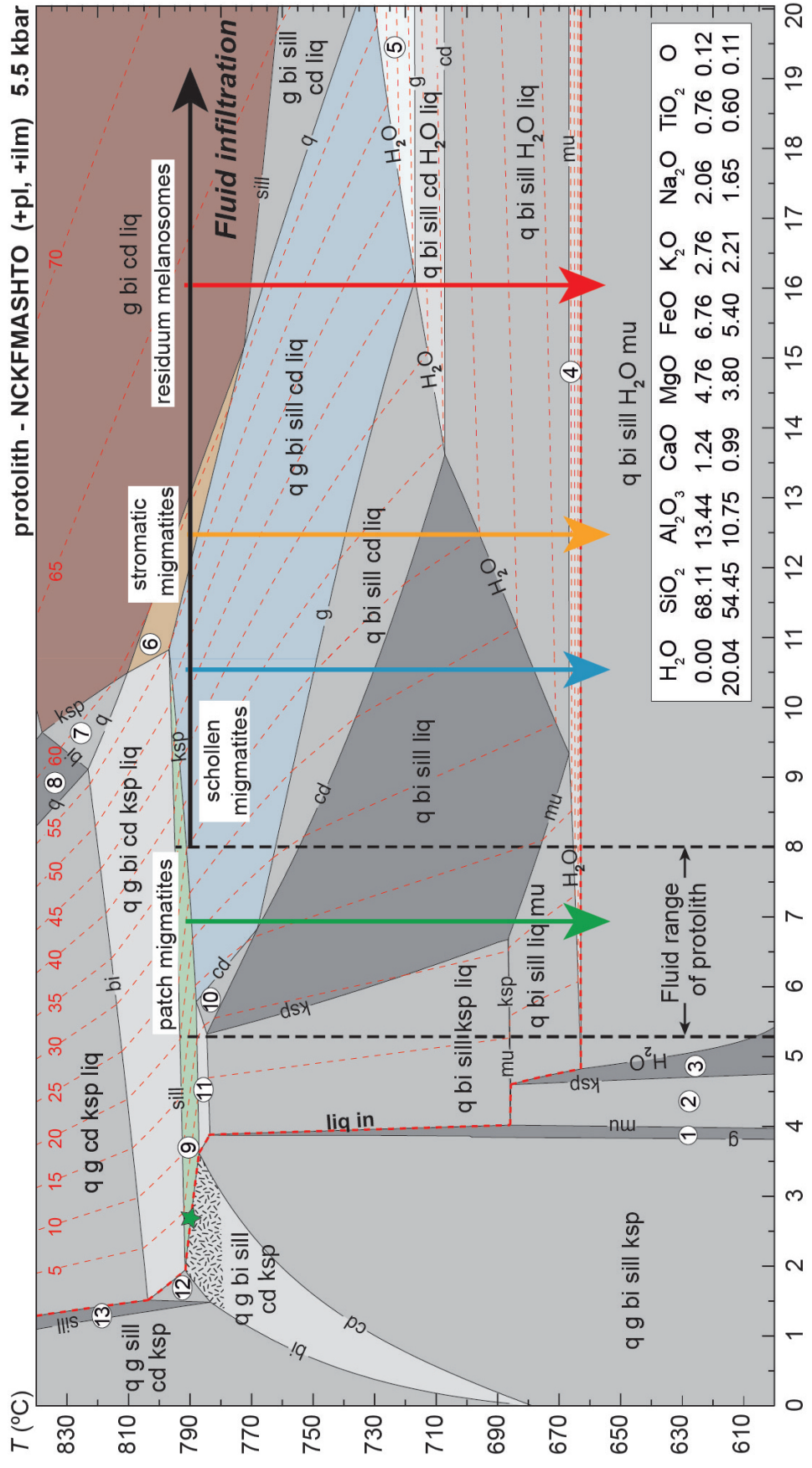
### 6.3.1. A single melting event with variable fluid content

To test whether the mineral assemblages of the different samples can be related by differing amounts of $H_2O$ (either initial of produced by fluid infiltration) of the same hypothetical protolith undergoing contact metamorphism, a $T$–$M(H_2O)$ pseudosection was constructed at a fixed average pressure of 5.5 kbar (Fig. 6.12). In this

pseudosection, the *X*-axis represents the proportion of water added to the protolith: X=0 indicates the protolith rock composition assuming 0% water content (unlikely) and X=20 represents the 20 mol.% of water added to the rock. The considered temperature range is from subsolidus (600 °C) to 840 °C. This diagram shows the effect of a single melting event for a metapelite with the protolith composition. A notable feature of this diagram is the step-like jumps down temperature with increasing water content through the biotite and muscovite breakdown melting steps. Other major features involve the mineral assemblages of the different migmatite types at high temperature along $M(H_2O)$, the stabilization of K-feldspar at low $M(H_2O)$ sector and the loss of sillimanite and quartz at high temperature and high $M(H_2O)$ region of the diagram.

For $M(H_2O)$ values less than 11 mol.% (<55 mol.% melt) and at a narrow temperature range of around 790 °C, the q–g–bi–sill–cd–ksp assemblage from patch migmatites (green field) is stable. On the high-temperature side, this mineral assemblage is limited by the sillimanite-out line and on the low-temperature side by the K-feldspar-out line. For $M(H_2O)$ values between 6–20 mol.% (15–70 mol.% melt) and at a wide temperature range (between 710–790 °C), the q–g–bi–sill–cd assemblage from schollen migmatites (blue field) is reproduced, whereas at high temperature regions (>760 °C) the assemblages from stromatic migmatites (orange field) and from residuum melanosomes (red field) are stable.

The estimated fluid content of the protolith should be from 5.35 to 8 mol.% $H_2O$. The former value represents the minimum amount of water contained in the rock required for a minimum melting temperature, whereas 8 mol.% $H_2O$ is the LOI value of the analyses for neighboring Roc de Frausa metapelites not affected by the Ceret gabbro-diorite. If fluid infiltration takes place in the system at a temperature of 790 °C (path indicated by the horizontal black arrow) and from 8 mol.% $H_2O$, the different mineral assemblages from the migmatites will be reproduced along the path. K-feldspar, sillimanite and quartz will be consumed with increasing melt proportions along pure $H_2O$-fluxed (hydrous) melting. As the system is closed for melt, it will retain all the melt formed. On cooling, the peak assemblages will be retrogressed to a muscovite-sillimanite-biotite schist in the amphibolite facies just below the solidus (*c.* 660 °C) with different proportions of $H_2O$. For residuum melanosomes (red vertical


protolith - NCKFMASHTO (+pl, +ilm) 5.5 kbar
T (°C)
M(H2O)
Fluid infiltration
residuum melanosomes
stromatic migmatites
schollen migmatites
patch migmatites
Fluid range of protolith
liq in
q g bi cd liq
q g cd ksp liq
q g bi cd ksp liq
q g bi sill cd ksp
q g bi sill cd ksp liq
q g bi sill ksp
q bi sill cd H2O liq
q bi sill cd liq
q bi sill liq
q bi sill H2O liq
q bi sill H2O mu
q g bi sill ksp liq
q bi sill ksp liq mu
q bi sill liq mu
q g bi sill cd ksp
q g bi sill cd liq
q g bi sill
cd ksp
q g sill
cd ksp
H2O 0.00 68.11 13.44 1.24 4.76 6.76 2.76 2.06 0.76 0.12
20.04 54.45 10.75 0.99 3.80 5.40 2.21 1.65 0.60 0.11
① q bi sill ksp
② q bi sill ksp mu
③ q bi sill mu
④ q bi sill H2O liq mu
⑤ q g bi sill cd H2O liq
⑥ q g bi cd liq
⑦ g bi cd ksp liq
⑧ g cd ksp liq
⑨ q g bi sill cd ksp liq
⑩ q g bi sill liq
⑪ q g bi sill ksp liq
⑫ q g bi cd ksp
⑬ q g cd ksp
20 molar % liquid

line) at high $M(H_2O)$, there will be a molar increase in quartz and sillimanite together with a decrease in garnet and cordierite. Muscovite will become stable just before the solidus is crossed at 660 °C. For stromatites (orange vertical line), the modal content of garnet and cordierite will decrease in favour of sillimanite until muscovite appears and the solidus is crossed. For schollen migmatites (blue vertical line), there will be a molar decrease in garnet and cordierite until muscovite will appear and the solidus crossed. For patch migmatites (green star) at the estimated fluid range of the protolih (relatively low $M(H_2O)$, the mineral assemblage q–g–bi–sill–cd–ksp will be retrogressed (green vertical line), decreasing K-feldspar, garnet and cordierite content until muscovite appears and the solidus is reached. Thus, in all cases the conversion of the granulite facies assemblages to upper amphibolite will occur below 710–770 °C, while the different migmatite types would still contain approximately 20–60 mol.% melt. It is obvious that retaining this amount of melt in the rock is not rheologically plausible (Arzi, 1978; Powell & Downes, 1990), especially if the process is accompanied by deformation (Brown, 1994; Sawyer *et al.,* 1999), as is the case for the Roc de Frausa Massif.

However, the only way to explain the assemblage of patch migmatites (green star) will be to assume an initial water content between 3 mol.% and 5 mol.% in the protolith. On cooling, this assemblage will be preserved, as the solidus is crossed near 790 °C. In fact, these migmatites have scarce leucosome and register the longest history of all rocks in the aureole, probably because the system run out of melt, so intense retrogression did not take place.

In conclusion, an open system mechanism involving influx of water from outside of the system cannot explain the preservation of the different types of migmatites if originated from a unique protholit. The mineral assemblages of the schollen, stromatic and residual migmatites can be reproduced by infiltrating a fluid phase at the approximately 790 °C and 5.5 kbar but they would not be preserved on cooling if

**Figure 6.12.** $T$–$M(H_2O)$ pseudosection calculated for the whole-rock composition of a hypothetical metapelitic protolith (in moles adjusted to 100%) at 5.5 kbar and contoured for the molar proportions of liquid. $M(H_2O)$ is the molar content of water in mol. %. The four-color cooling and fluid infiltration paths are discussed in the text. Black stippled field indicates partial preservation of granulite facies assemblages. The solidus is underlined by a dashed red line.

the system remains closed to melt loss. Only an initial small amount of water can explain the preservation of patch migmatites present in the massif. Therefore, we have explored if multiple partial melt loss and fluid infiltration events taking place for a unique protolith can explain all the features of the different types of the migmatites and this is discussed next.

### 6.3.2. Multiple melt loss–rehydration events

In order to preserve the observed granulite facies assemblages, a series of $T$–$X_{\text{melt loss}}$ diagrams alternating with $T$–$M(H_2O)$ diagrams were calculated for the average composition of the hypothetical protolith at a fixed average pressure of 5.5 kbar. The diagrams show five melt-loss events alternating with four fluid-infiltration events. In the fluid infiltration events, a small amount of water is incorporated in the system (~2–4.7 mol.% $H_2O$) and the melt produced (~11–22 mol.% melt) is completely extracted leaving a residual rocks (Fig. 6.13). In the $T$–$X_{\text{melt}}$ –$M(H_2O)$ diagram (Fig. 6.14), the $X$-axis corresponds alternatively to the accumulated melt proportion removed from the protolith at a constant peak temperature (790 °C) and pressure (5.5 kbar) and to the water infiltrated into the system. X=0 represents the protolith rock composition assuming no melt loss, whereas X=0.63 represents the accumulated melt lost in mol.% at the last event.

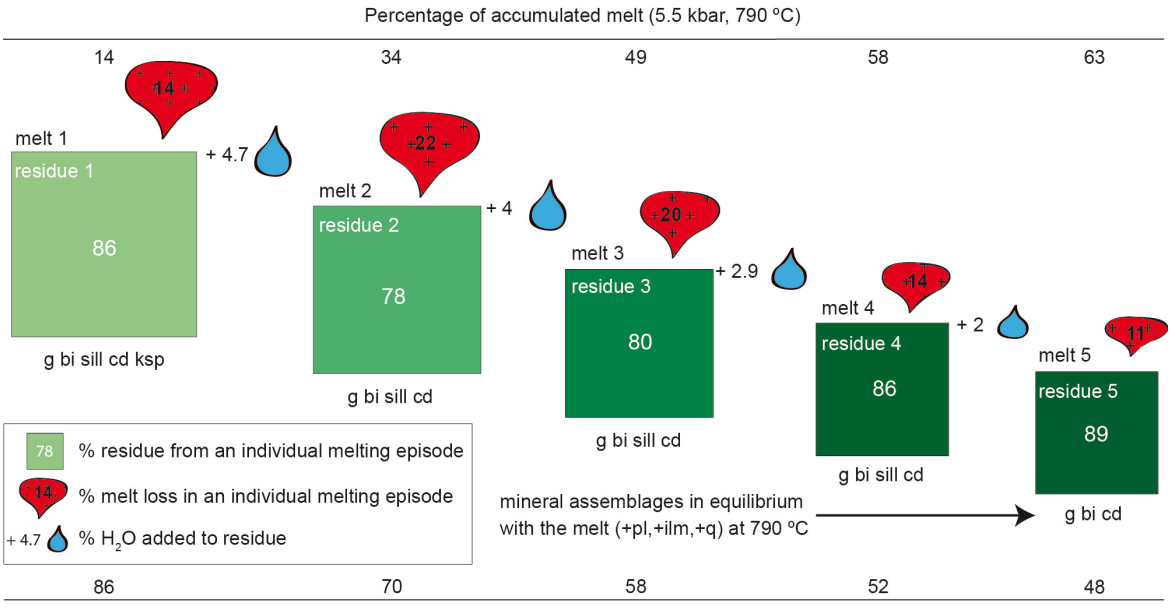
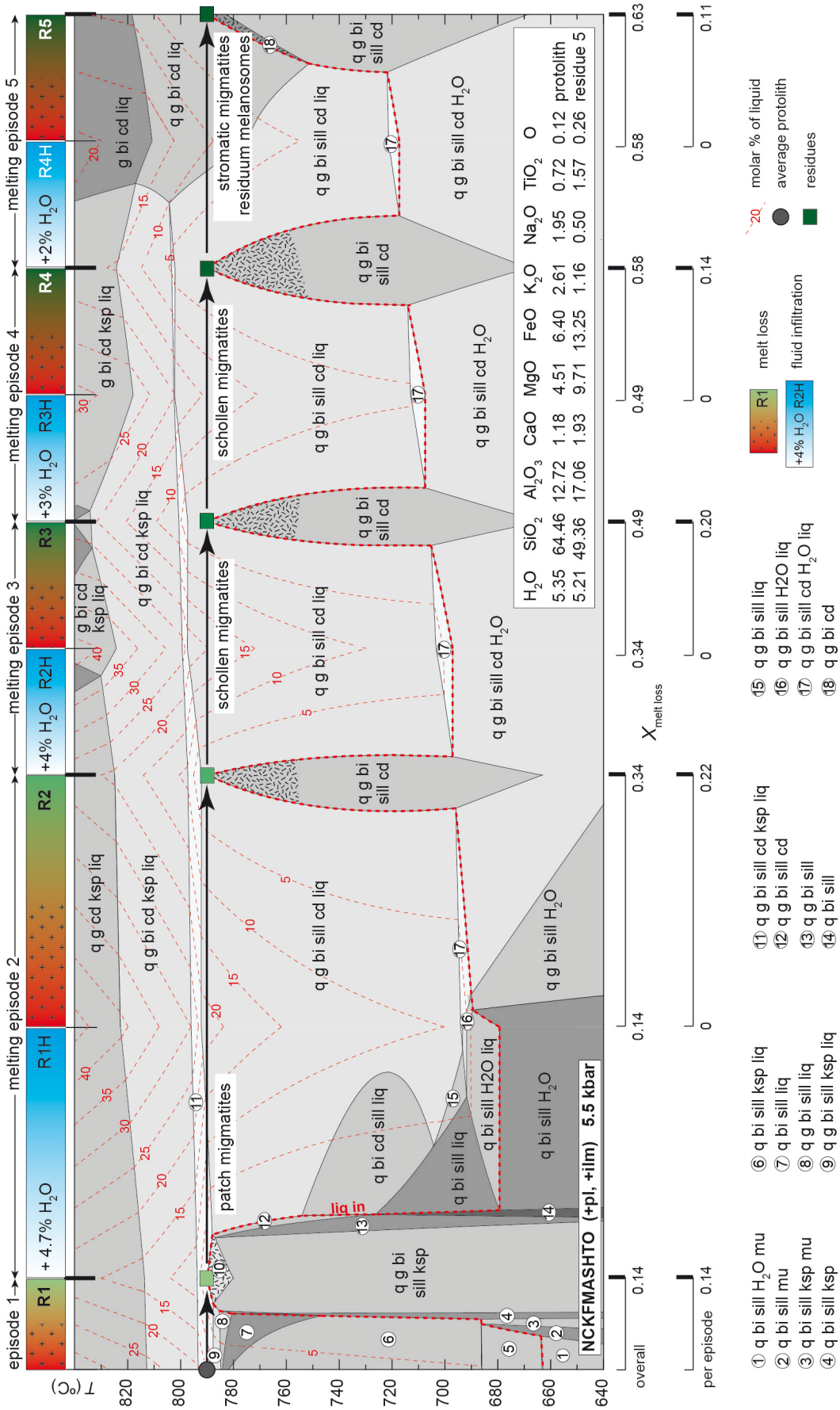



**Figure 6.13.** Sketch ilustrating the five episodes of melt loss alternating with four fluid-infiltration events at 5.5 Kbar and 790 °C.

The most remarkable feature of this diagram is the effect on the shape of the solidus of removing melt and infiltrating fluid. In every melt-loss event, the solidus draws a steep up-temperature slope, whereas in fluid-infiltration events it traces a down-temperature one. The diagram has been constructed in such a way that in the melt extracting events the system runs out of melt at 790 °C, because it has been considered that a syn-deformational environment (syn-S2) would be favourable to the extraction of the generated melt.

At a temperature of 790 °C and for a minimum amount of water (~5 mol.% $H_2O$) contained in the protolith, the rock contains 14 mol.% melt in equilibrium with the mineral assemblage of q–g–bi–sill–cd–ksp observed on patch migmatites. If the first generated melt (14 mol. %) is completely removed from the system, the rock will follow a horizontal path while decreasing the melt proportion until it reaches the solidus. It is important to consider that no new $H_2O$ is infiltrated during these melt-loss events. At this point (residue R1, green square), there will be neither melt nor free water in the system. The stable modeled assemblage (q–g–bi–sill–cd–ksp) corresponds to patch migmatites and will be preserved after cooling, similarly to the previous model with only variable $H_2O$ (compare Figs. 6.12 & 6.14-R1).

If residue (R1) is rehydrated (R1H from hydrated R1 with +4.7 mol.% $H_2O$), more melt will be generated (~22 mol. %). The resultant path will follow a horizontal line and K-feldspar will be consumed. The new assemblage (q–g–bi–sill–cd–liq) will be retrogressed on cooling to an hydrous assemblage. It will only be preserved if melt is removed until the solidus is intersected at 790 °C. At this point (residue R2), the modeled assemblage (q–g–bi–sill–cd) coincides with that of schollen migmatites and will be preserved as K-feldspar has been consumed during this path. Several fluid-infiltration events will be followed by melt-loss events. Eventually, the q–g–bi–cd assemblage from a final residue (R5) will be formed and preserved in the solidus at 790 °C. This assemblage is equivalent with that of stromatites and residuum melanosomes. The accumulated melt proportion extracted from the rock system after the $5^{th}$ melting episode is around 63 mol.% (Fig. 6.13). In contrast, the residuum left after melt extraction is 48 mol.%.


episode 1
melting episode 2
melting episode 3
melting episode 4
melting episode 5
R1
+ 4.7% H2O
R1H
R2
+4% H2O
R2H
R3
+3% H2O
R3H
R4
+2% H2O
R4H
R5
T (°C)
NCKFMASHTO (+pl, +ilm) 5.5 kbar
patch migmatites
schollen migmatites
stromatic migmatites
residuum melanosomes
liq in
q g bi sill ksp
q bi cd sill liq
q bi sill liq
q bi sill H2O liq
q bi sill H2O
q g bi sill cd liq
q g bi sill cd H2O
q g bi cd ksp liq
q g cd ksp liq
g bi cd ksp liq
g bi cd liq
H2O SiO2 Al2O3 CaO MgO FeO K2O Na2O TiO2 O
5.35 64.46 12.72 1.18 4.51 6.40 2.61 1.95 0.72 0.12 protolith
5.21 49.36 17.06 1.93 9.71 13.25 1.16 0.50 1.57 0.26 residue 5
overall
per episode
Xmelt loss
melt loss
fluid infiltration
molar % of liquid
average protolith
residues
① q bi sill H2O mu
② q bi sill mu
③ q bi sill ksp mu
④ q bi sill ksp
⑤ q bi sill liq mu
⑥ q bi sill ksp liq
⑦ q bi sill liq
⑧ q g bi sill liq
⑨ q g bi sill ksp liq
⑩ q g bi sill cd ksp
⑪ q g bi sill cd ksp liq
⑫ q g bi sill cd
⑬ q g bi sill
⑭ q bi sill
⑮ q g bi sill liq
⑯ q g bi sill H2O liq
⑰ q g bi sill cd H2O liq
⑱ q g bi cd

The variation in modal amount of the different phases predicted by the model during the continuous episodes of melt extraction and hydrous melting is shown graphically in Figure 6.15. The diagram displays a distinct increase in cordierite mode and a moderate increase in garnet, and a decrease and/or consumption of K-feldspar, sillimanite, biotite, quartz and melt following the five melting episodes. This modal evolution is similar to that found in the different types of migmatites from patch migmatites, schollen and stromatite and residuum melanosomes. In conclusion, a model sequence of $H_2O$-fluxed melting alternating with melt extraction episodes results in a spectrum of peak assemblages ranging from sillimanite–K-feldspar rich domains, through cordierite–garnet rich and sillimanite-absent domains and can explain the preservation of granulitic assemblages. The proposed model implies high volumes of melt removed (around 63 mol.%) from the rock to preserve the assemblages found in the migmatites of the Roc de Frausa Massif and a reduction of the original rock to less than 50 mol.%.

***Comparison between modeled and analyzed rock compositions***

The melt loss–fluid infiltration model implies a change in the whole-rock composition of the residue. A further approach to test the model can be done comparing the whole-rock compositions obtained from modeling (Table 6.1) with the analyzed metamorphic and igneous rocks from the Roc de Frausa Massif (see Tables 4.4 & 6.2).

The compositional diagram from Figure 6.16 shows the whole-rock composition obtained from modeling for residues 1 to 5, the calculated composition of the anatectic melt at solidus at 5.5 kbar for the four migmatite types (Table 6.1), the composition of the analyzed non-migmatitic and migmatitic metapelites (see Table 4.4) and that of a series of plutonic rocks (from gabbro to leucogranite) from Sant Llorenç–La Jonquera pluton and Ceret stock (Table 6.2). In the $SiO_2$–$Al_2O_3$–($FeO$+$MgO$+$TiO_2$) and $SiO_2$–$Al_2O_3$–($K_2O$+$Na_2O$) ternary plots (Fig. 6.16), a linear

**Figure 6.14.** Calculated $T$–$X_{\text{melt loss}}$ pseudosection at 5.5 kbar showing the effect of multiple partial melt loss–fluid infiltration episodes. $X_{\text{melt loss}}$ is the proportion of melt removed from the protolith composition at 790 °C in mol. %. The five black horizontal arrows are discussed in the text. Stippled fields indicate partial preservation of granulite facies assemblages. The solidus is underlined by a dashed red line.

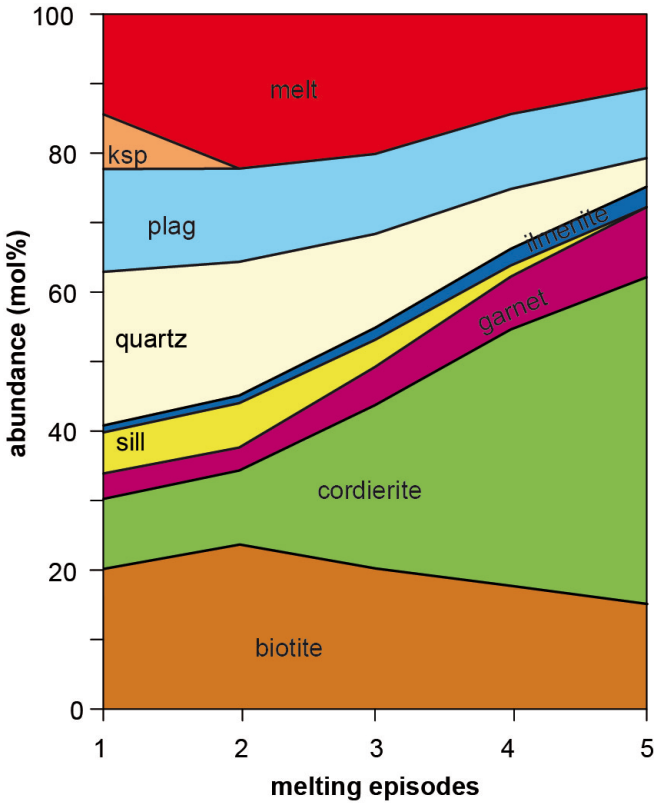



**Figure 6.15.** Diagram showing the mineral proportions for the different melting episodes calculated by THERMOCALC.

decrease in the A/AFM and K/KN ratios accompanies the depletion of $SiO_2$ (grey arrow) of all modeled and analyzed rocks. On one end lie leucogranites and modeled anatectic melts with similar compositions, whereas on the other end lie residuum melanosomes and the 5$^{th}$ modeled residue. The fact that all modeled and analyzed rocks are well aligned suggests a model of progressive melt extraction in the migmatites during contact metamorphism and reinforces the idea of open-system behavior from a common original protolith composition. The alignment also suggests the same extraction mechanism for all major elements (Riesco *et al.,* 2004).

These relations indicate that patch and schollen migmatites would not have modified their composition. On the contrary, residuum melanosomes represent an end-product, in consequence, an open system and melt loss can be inferred for them (Sawyer *et al.,* 1999; White & Powell, 2002). However, a late melt injection need to be proposed for the stromatic migmatites, as the mineral assemblages of stromatites are similar to those of residuum melanosomes, while the whole-rock composition is comparable with the compositions of the patch and schollen migmatites.

**Table 6.1.** Residue and anatectic melt bulk compositions calculated by THERMOCALC in mol.%. The residues are calculated for each melting episode and the anatectic melt compositions at the solidus for a patch migmatite (sample 526), a stromatic migmatite (sample 529), a schollen migmatite (sample 459) and a residuum melanosome (sample 462).

| | *T* (°C) | *P* (kbar) | $H_2O$ | $SiO_2$ | $Al_2O_3$ | CaO | MgO | FeO | $K_2O$ | $Na_2O$ | $TiO_2$ | O |
|---|---|---|---|---|---|---|---|---|---|---|---|---|
| residue 1 | 790 | 5.5 | 3.44 | 63.92 | 13.50 | 1.31 | 5.24 | 7.37 | 2.50 | 1.75 | 0.84 | 0.14 |
| residue 2 | 790 | 5.5 | 4.36 | 59.71 | 14.39 | 1.50 | 6.43 | 8.94 | 2.15 | 1.32 | 1.03 | 0.17 |
| residue 3 | 790 | 5.5 | 4.70 | 55.52 | 15.46 | 1.69 | 7.77 | 10.70 | 1.76 | 0.93 | 1.25 | 0.21 |
| residue 4 | 790 | 5.5 | 5.01 | 52.10 | 16.33 | 1.83 | 8.84 | 12.11 | 1.43 | 0.68 | 1.43 | 0.24 |
| residue 5 | 790 | 5.5 | 5.21 | 49.36 | 17.06 | 1.93 | 9.71 | 13.25 | 1.16 | 0.50 | 1.57 | 0.26 |
| Anatectic melt I (sample 526) | 722 | 5.5 | 30.21 | 57.65 | 6.30 | 0.27 | 0.07 | 0.26 | 1.14 | 4.11 | 0.00 | 0.00 |
| Anatectic melt II (sample 529) | 712 | 5.5 | 29.91 | 57.91 | 6.06 | 0.35 | 0.18 | 0.47 | 0.92 | 4.20 | 0.00 | 0.00 |
| Anatectic melt III (sample 459) | 694.5 | 5.5 | 28.72 | 59.36 | 6.26 | 0.55 | 0.10 | 0.35 | 1.75 | 2.90 | 0.00 | 0.00 |
| Anatectic melt IV (sample 462) | 697 | 5.5 | 30.40 | 57.37 | 6.17 | 0.24 | 0.13 | 0.35 | 0.85 | 4.50 | 0.00 | 0.00 |

**Table 6.2.** Representative whole-rock compositions of the late-Variscan igneous rocks from Sant Llorenç–La Jonquera pluton (tonalite to leucogranite) and from Ceret gabbro-diorite stock.

| Igneous rock type | gabbro | tonalites | granodiorites | monzogranite | granites | leucogranite |
|---|---|---|---|---|---|---|
| Sample | 419 | (216-217-218-220-530) | (213-214-310-365-414) | 533 | (336-3637-370-424) | 215 |
| (wt.%) | | | | | | |
| $SiO_2$ | 51.88 | 62.11 | 68.03 | 68.36 | 70.59 | 74.26 |
| $TiO_2$ | 1.16 | 0.66 | 0.42 | 0.35 | 0.35 | 0.08 |
| $Al_2O_3$ | 17.81 | 17.26 | 15.15 | 15.99 | 14.60 | 13.97 |
| $Fe_2O_3$ | 9.53 | 5.29 | 3.42 | 3.47 | 2.82 | 0.84 |
| MnO | 0.13 | 0.07 | 0.06 | 0.06 | 0.02 | 0.03 |
| MgO | 4.99 | 1.61 | 0.96 | 0.69 | 0.73 | 0.16 |
| CaO | 8.09 | 4.89 | 2.98 | 3.23 | 1.78 | 0.89 |
| $Na_2O$ | 2.58 | 3.35 | 3.40 | 3.24 | 3.20 | 3.59 |
| $K_2O$ | 1.64 | 3.08 | 3.84 | 3.60 | 4.44 | 4.89 |
| $P_2O_5$ | 1.08 | 0.92 | 0.95 | 1.02 | 0.78 | 0.90 |
| L.O.I | 0.23 | 0.18 | 0.12 | 0.11 | 0.27 | 0.27 |
| Total | 99.12 | 99.42 | 99.32 | 100.10 | 99.55 | 99.88 |
| A/CNK | 0.86 | 0.97 | 1.00 | 1.06 | 1.10 | 1.09 |
| $K_2O/Na_2O$ | 0.42 | 0.61 | 0.74 | 0.73 | 0.91 | 0.90 |
| $CaO/Na_2O$ | 3.47 | 1.61 | 0.97 | 1.10 | 0.62 | 0.27 |
| $Al_2O_3/TiO_2$ | 12.03 | 20.55 | 28.39 | 35.77 | 32.90 | 136.78 |
| $FeOt^a+MgO+TiO_2$ | 16.49 | 7.40 | 4.61 | 4.15 | 3.71 | 0.99 |

[a] Total iron as FeO

The alignment of the different types of granitoids from Sant Llorenç–La Jonquera pluton with the composition of the migmatites suggests that the melt formed during the migmatization process could have been incorporated into the granitoids thus contaminating them. In this scheme, leucosomes would have contributed to the formation of leucogranites. According to Vilà *et al.* (2005), the calc-alkaline granitoids were produced by fractional crystallization of a granodioritic magma generated by partial melting of metatonalites at granulite facies conditions in the lower crust and the leucogranites would correspond to the most evolved liquids. These authors also suggest heterogeneous mantle sources for hydrous mafic magmas. Nevertheless, further work has to be done to verify the link between migmatization and the formation of plutonic bodies in the area.

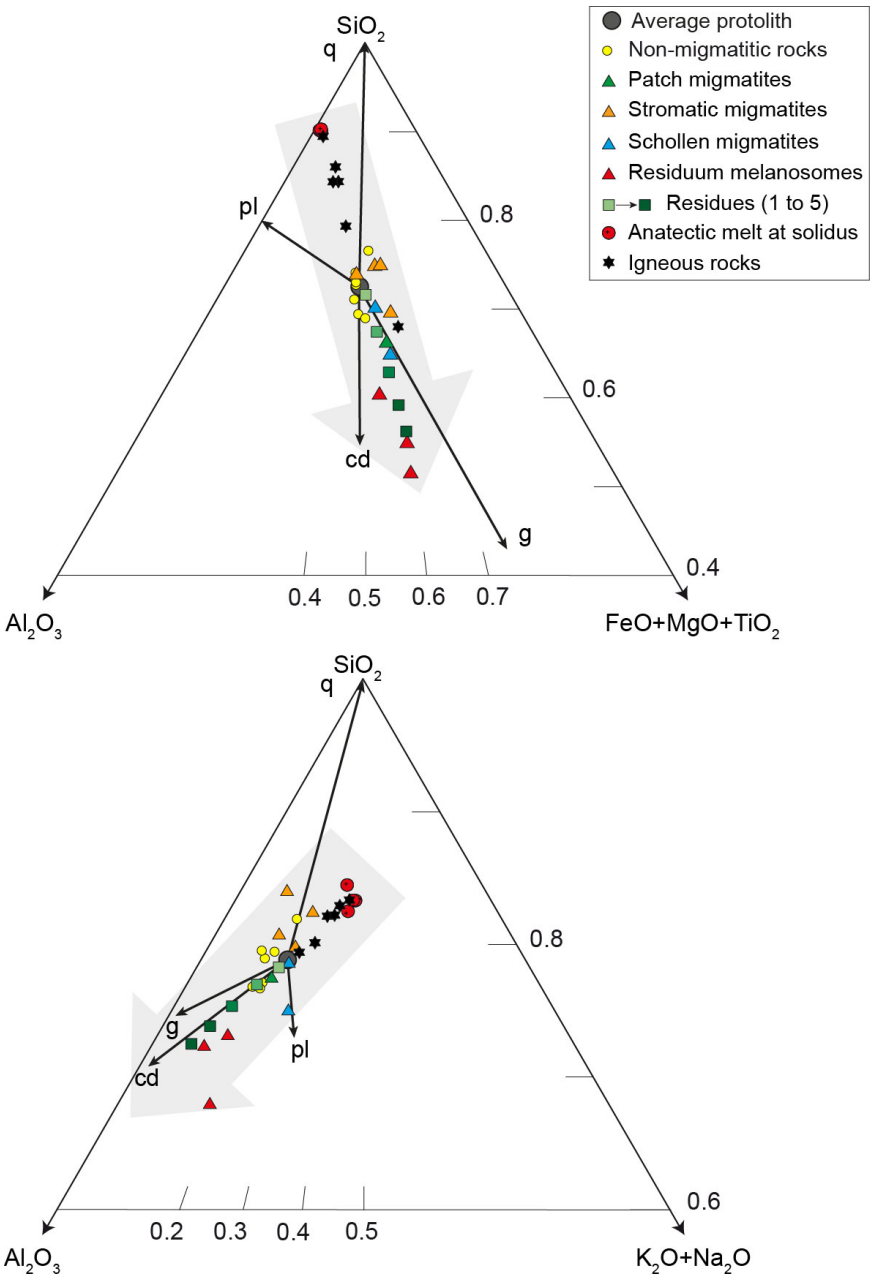



**Figure 6.16.** $SiO_2$–$Al_2O_3$–($FeO+MgO+TiO_2$) and $SiO_2$–$Al_2O_3$–($K_2O+Na_2O$) ternary plots representing the composition of the hypotethical protolith, the different types of migmatites, the representative igneous rocks and the compositions calculated by THERMOCALC for residues 1–5 and for the anatectic melt at the solidus. See text and Table 6.1 for further information.

# CHAPTER 7

## ZIRCON U–Pb GEOCHRONOLOGY

The most popular accessory mineral geochronometer for dating metamorphism in amphibolite- and higher-grade pelitic rocks is arguable the monazite (e.g., Cocherie *et al*., 2005; Faure *et al*., 2010), which is fairly common in aluminous metamorphic rock types (Overstreet, 1967). It has high concentrations of U and Th (up to 1 and 10 wt. %, respectively; Spear & Pyle, 2002), typically low initial common Pb (<1 ppm; Parrish, 1990), and strong resistance to radiogenic Pb loss via diffusion (Parrish, 1990; Smith & Giletti, 1997; Harrison *et al*., 2002; Cherniak *et al.,* 2004). A main approach consists in separating monazite grains from the heavy-mineral fraction and subsequently mounted in resin, then ground and polished to obtain cross section of the grains. However, the separation process in the selected migmatite samples was unproductive. For this reason, we opted for using zircon, not only in the migmatites but also in two Late-Variscan plutonic rocks emplaced in different crustal levels using sensitive high-resolution ion microprobe-reverse geometry (SHRIMP-RG).

Zircon U–Pb geochronology is a widely used tool to determine the ages of intermediate and felsic magmatic rocks as zircon easily grows during the early crystallization of the magma (e.g., Hoskin & Schaltegger, 2003). However, under granulite facies conditions, the occurrence of zircon depends on the availability of zirconium in the system (e.g., Fraser *et al*., 1997). Furthermore, the difficulty of zircon to dissolve and the high closure temperature of the U–Pb isotopic system allow the preservation of inherited ages in xenocrystic domains in igneous and metamorphic rocks. Since single zircon grains usually display a multistage evolution, it is not easy to date high-temperature metamorphic processes (Kempe *et al.,* 2000; Corfu *et al.,* 2003; Castiñeiras *et al.,* 2008b). Consequently, the chronological data of the thermal processes are combined with trace element chemistry on zircon and textures revealed by cathodoluminescence in order to clarify the interpretation of the ages.

## 7.1. Methodology

### 7.1.1. Sample preparation

Mineral separation was performed at the Universitat de Barcelona and the Universidad Complutense (Madrid) following standard techniques. The samples were crushed using a jaw crusher and sieved to get the <0.1 mm fraction. The zircons were separated by first concentrating the heavy minerals with a Wilfley table. This was followed by magnetic separation with a Frantz isodynamic separator and by density separation with methylene iodide. Between 40 and 60 zircon grains per sample were handpicked under a binocular microscope at the Stanford-US Geological Survey Microanalysis Center (SUMAC). They were chosen in accordance with size, length-to-breadth ratio, roundness, color, and other salient morphological features to exclude detrital or inherited grains. The preferred zircons were then mounted separately on glass slides with a double-sided adhesive in 1x6 mm parallel rows together with some chips of zircon standard R33 (Black *et al*., 2004). After being set in epoxy resin, the mounts were polished down to expose their central portions by using 1500 grit wet sandpaper and polished with 6 μm and 1 μm diamond abrasive on a lap wheel. Internal structure, inclusions, fractures and physical defects were identified by transmitted and reflected light under a petrographic microscope, and by cathodoluminescence under a JEOL JSM 5600 electron microscope housed at SUMAC. The mounted grains were washed with 1 N HCl and distilled water, dried in a vacuum oven, and coated with Au. Mounts sat in a loading chamber at high pressure ($10^{-7}$ Torr) for several hours before being moved into the source chamber for zircon dating.

### 7.1.2. Analytical Methods

U–Th–Pb isotopic and elemental analyses of zircon were performed on the Bay SHRIMP-RG operated by the SUMAC facility during three analytical sessions in October 2010.

Secondary ions were generated from the target spot with an $O^{2-}$ primary ion beam varying from 4 to 6 nA. The primary ion beam produced a spot with a diameter of ~25 μm and a depth of 1–2 μm for an analysis time of 15 min. The analyzed areas were selected after studying images of the grains obtained by cathodoluminescence and by transmitted light microphotography. Data for each spot were collected utilizing five-

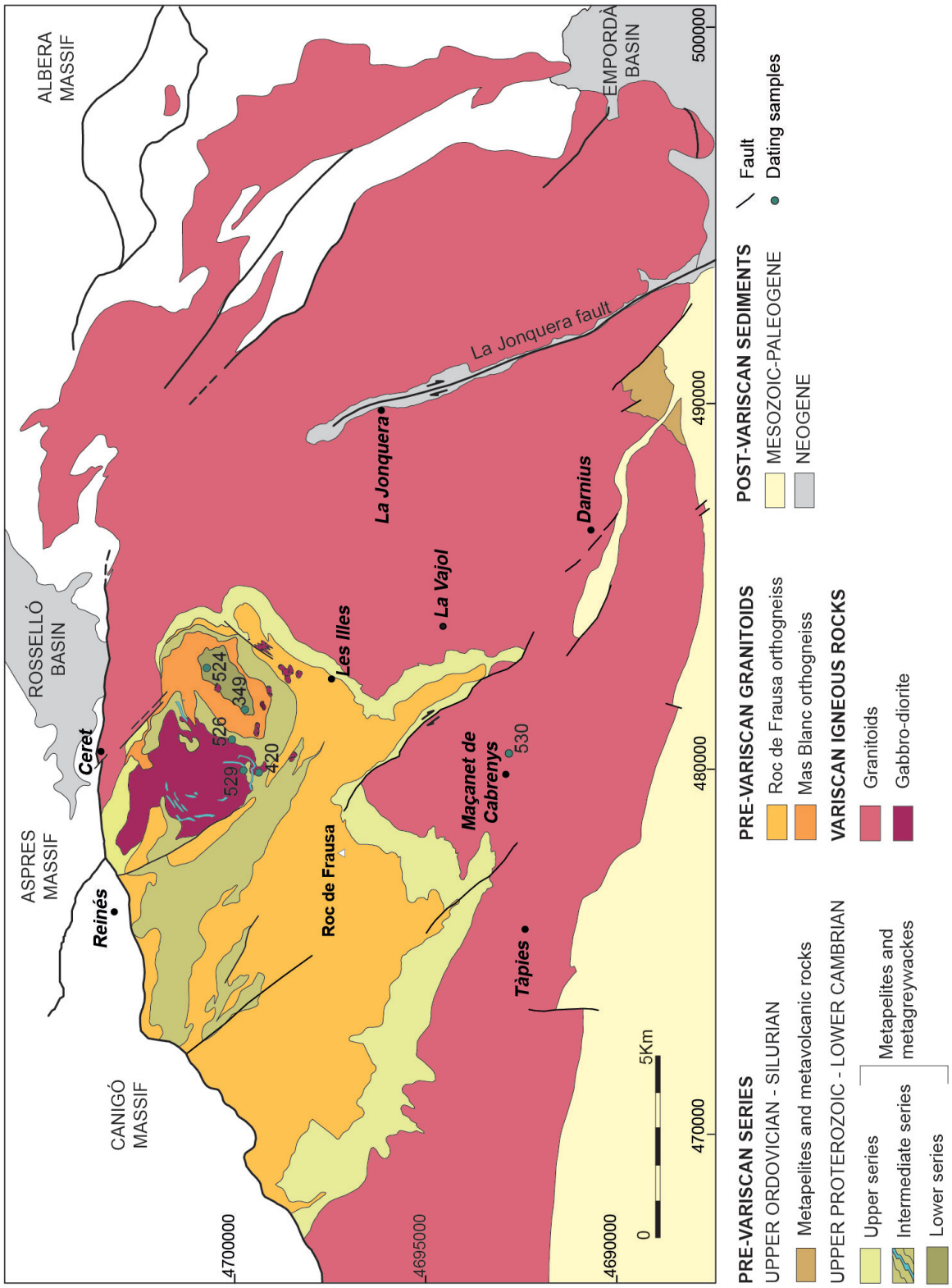
cycle runs through the mass stations. Counting time for $^{206}Pb$ was increased according to the Paleozoic age of the samples to improve counting statistics and precision of the $^{206}Pb/^{238}U$ age. The isotopic compositions were calibrated against R33 ($^{206}Pb^*/^{238}U$ = 0.06716, equivalent to an age of 419 Ma, Black *et al.,* 2004), which was analyzed every fourth analysis. Calibration errors for $^{206}Pb/^{238}U$ ratios of R33 for the different analytical sessions were 0.37%, 1.48% and 0.43% (2σ). The calculated external errors were incorporated when data from all sessions and mounts were compiled together.

La to Yb, Y and Hf were measured concurrently with the U–Th–Pb analyses as additional masses on each pass through the mass range. The concentrations of U, Th, Hf and rare earth elements (REE) were calibrated using an in-house zircon standard (MAD) and are reproducible at 2–4% (1σ), except for La (15%) because of the typically low concentration of La (see Barth & Wooden, 2010). Praseodymium was calculated from neighboring elements because CeH cannot be resolved from the praseodymium peak. CeH contributes significantly to the counts at $^{141}Pr$ because of its relatively high concentration and the low amount of praseodymium.

The analytical procedure for zircon dating is detailed by Williams (1997). Data reduction was carried out using Squid software (Ludwig, 2002), which follows the methods described by Williams (1997), and Ireland & Williams (2003). An in-house Excel spreadsheet and Isoplot 3.41 software (Ludwig, 2003) were used to create the graphs. All the ages are based on $^{206}Pb/^{238}U$ ratios corrected from common Pb using the $^{207}Pb$ method. The Pb composition used for initial Pb corrections ($^{204}Pb/^{206}Pb$ = 0.0554, $^{207}Pb/^{206}Pb$ = 0.864 and $^{208}Pb/^{206}Pb$ = 2.097) was estimated from Stacey & Kramers (1975).

## 7.2. Zircon description

To determine the chronological relations between the regional migmatization event, the magmatism and the migmatization around gabbro-diorite Ceret stock (Fig. 7.1), we selected: (1) two migmatites from the Lower series, (2) two late-Variscan igneous rocks, and (3) two migmatites from the Intermediate series affected by the Ceret gabbro-diorite contact aureole.


ALBERA MASSIF
ROSSELLÓ BASIN
EMPORDÀ BASIN
ASPRES MASSIF
CANIGÓ MASSIF
Ceret
Reinés
Roc de Frausa
Les Illes
La Jonquera
La Vajol
Darnius
Maçanet de Cabrenys
Tàpies
La Jonquera fault
524
349
526
529
420
530
500000
490000
480000
470000
4700000
4695000
4690000
0
5Km
PRE-VARISCAN SERIES
UPPER ORDOVICIAN - SILURIAN
Metapelites and metavolcanic rocks
UPPER PROTEROZOIC - LOWER CAMBRIAN
Upper series
Intermediate series
Lower series
Metapelites and metagreywackes
PRE-VARISCAN GRANITOIDS
Roc de Frausa orthogneiss
Mas Blanc orthogneiss
VARISCAN IGNEOUS ROCKS
Granitoids
Gabbro-diorite
POST-VARISCAN SEDIMENTS
MESOZOIC-PALEOGENE
NEOGENE
Fault
Dating samples

### 7.2.1. Migmatites from the Lower series

Zircons obtained from the lowermost migmatites (samples 349 and 524) are small and scarce. In fact, less than a hundred grains were extracted from ~12 kg of each sample. Zircon grains can be colorless or colored in different brownish and purple tones and are practically free of visible inclusions. Given their morphology, two groups of zircon grains can be distinguished: (1) Sub-rounded stubby grains with pitted and dull surfaces that are interpreted as detrital zircon; and (2) idiomorphic grains with highly variable habits and secondary and shiny faces that are interpreted as metamorphic zircon. Cathodoluminescence images of the latter reveal a varied population of cores with scarce irregular dark rims (Fig. 7.2). The cores have an assortment of textures, including oscillatory, sector and soccer-ball zoning, and contrasting luminescence responses, from low to high. These characteristics suggest that the cores represent former detrital grains, magmatic in origin, which are overgrown during metamorphism.

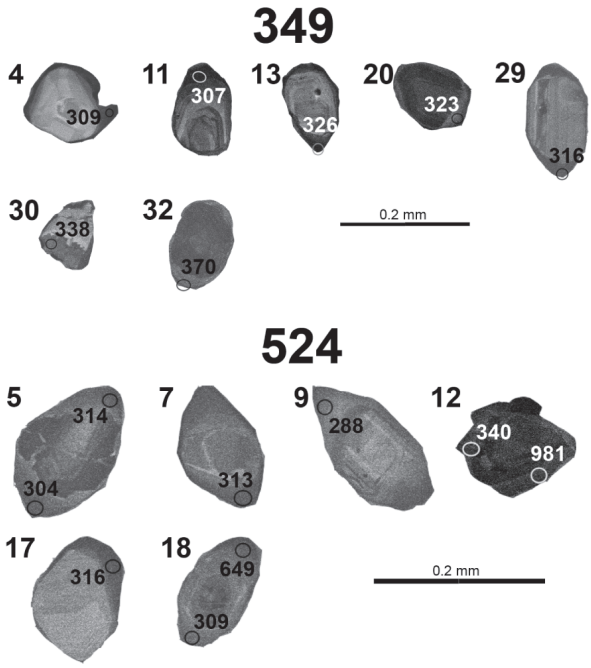



**Figure 7.2.** Cathodoluminescence images of the analyzed zircon rims from migmatites of the Lower series (samples 349 and 524) with the location of the SHRIMP spots.

**Figure 7.1.** Geological sketch map of the Roc de Frausa Massif and Sant Llorenç–La Jonquera plutonic complex with the location of representative samples used in this study. Modified from Liesa (1994).

### 7.2.2. Sant Llorenç–La Jonquera tonalite and Ceret stock gabbro

Zircon crystals from the tonalite of the Sant Llorenç–La Jonquera batholith (sample 530) are colorless, pale yellow or light purple and contain few visible inclusions. They form short prisms with differently shaped pyramid terminations and length-to-breadth ratios between 1:2 and 1:4. Under cathodoluminescence, zircons display broad moderately luminescent oscillatory zones typical of magmatic environments, and in a few grains less luminescent homogeneous cores can also be discerned (Fig. 7.3).

Zircons from the Ceret stock gabbro (sample 420) are moderately elongated prisms with rounded terminations, variable aspect ratios (1:1 to 1:3) and abundant inclusions. They are generally broken. Cathodoluminescence images reveal definite core-rim structures that can be observed even under the transmitted light microscope. The cores exhibit a non-luminescent weakly oscillatory and sector zoning surrounded by variably thick rims (~25 μm thick) that are highly luminescent and display a subtle broad oscillatory zoning (Fig. 7.3).

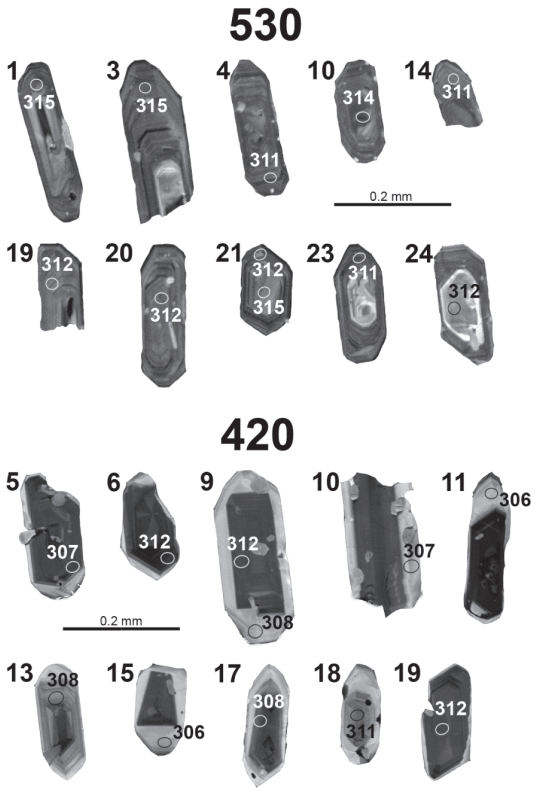



**Figure 7.3.** Cathodoluminescence images of the analyzed zircons from a Sant Llorenç–La Jonquera tonalite (sample 530) and a Ceret stock gabbro (sample 420) with the location of the SHRIMP spots.

### 7.2.3. Migmatites from the Intermediate series affected by the Ceret gabbro-diorite contact aureole

Only one of the migmatites from the Ceret stock contact aureole produced a zircon yield (sample 529), whereas sample 526 was devoid of this mineral. As in the lowermost migmatites, zircon grains are variably colored and display two distinct morphologies: one corresponding to detrital zircon and the other to metamorphic zircon.

## 7.3. Zircon U–Pb dating

Analytical results for zircon U–Pb dating are presented in tables 7.1, 7.2 and 7.3, and plotted in figures 7.4 and 7.5. The uncertainties for the data are given at the 1σ level in the tables and the error ellipses and crosses are represented at the 2σ level. Depending on the amount of data, the mean square weighted deviation (MSWD) has to be lower than a theoretical value to confirm the statistical validity of the calculated age (Wendt & Carl, 1991). Ages younger than 1,000 Ma are reported using the 207-corrected $^{206}Pb/^{238}U$ ratio, whereas older ages are reported using the 204-corrected $^{207}Pb/^{206}Pb$ ratio.

### 7.3.1. Migmatites from the Lower series

In sample 349, thirty-seven analyses were performed on thirty-six zircon grains (Table 7.1). Areas with clear magmatic textures were avoided, as they could represent inherited zones, so all the analyses were focused on rims or areas with homogeneous zoning that were presumably metamorphic. However, only seven analyses yielded ages younger than 400 Ma, whereas the remaining 30 spots yielded ages between 600 and 2,740 Ma, which were interpreted as inheritance. Owing to the scatter in the young ages (Fig. 7.4a, inset), obtaining a valid age from these seven analyses is quite difficult. We can consider the two oldest analyses in this group as outliers, and calculate the weighted average with the remaining five analyses. However, the high MSWD obtained in this calculation (26) indicates that these data do not represent a consistent population. The best statistical estimate is obtained anchoring only three data to a common Pb composition of 0.857, giving a lower intercept age of 320 ± 13 Ma (Fig. 7.4a). Once again, the high MSWD value (9.9)

indicates that the considered analyses do not constitute a consistent population, so this number must be regarded only as the upper limit for the age of metamorphism.

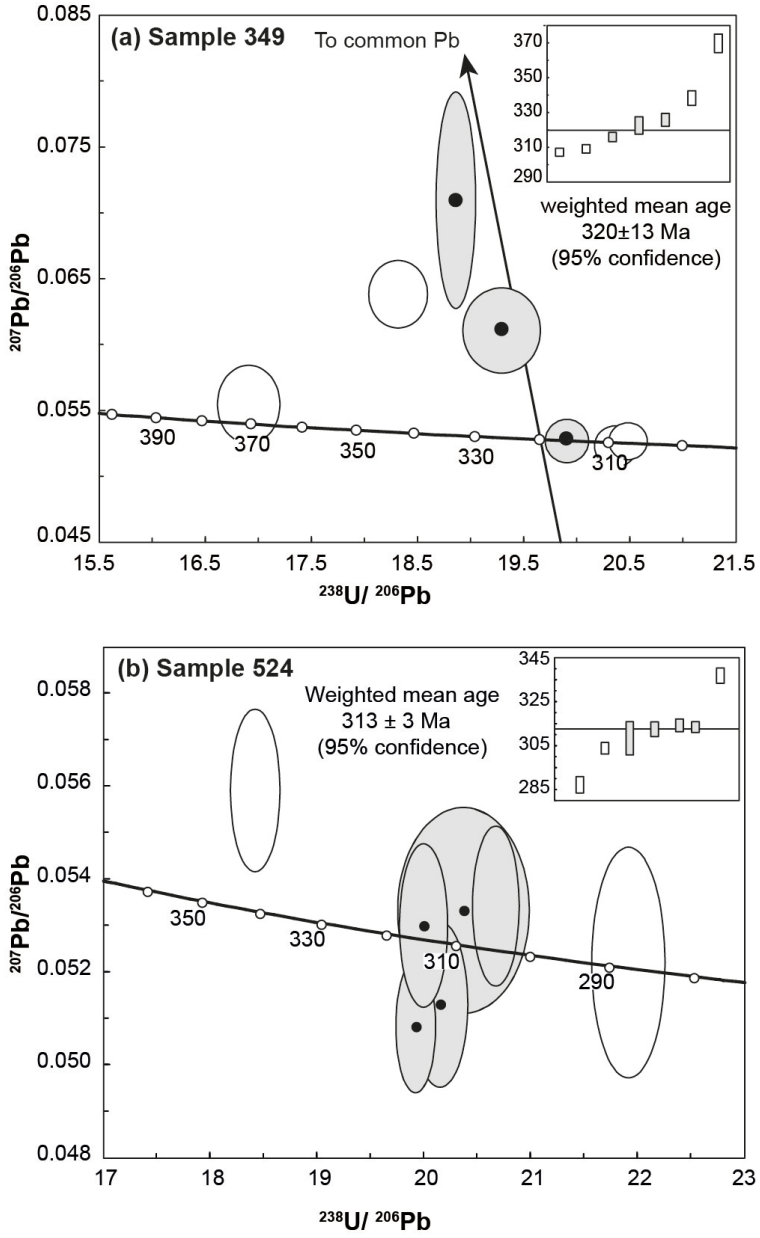



**Figure 7.4.** Tera-Wasserburg diagrams of SHRIMP U–Pb zircon ages from the fold-structured migmatites of the Lower series: (a) sample 349 and (b) sample 524. The grey solid ellipses represent the data used to obtain the weighted mean age (inset), whereas the white ellipses were discarded. Inherited ages are not shown for clarity. Error ellipses are ± 2σ.

In sample 524, twenty-two spot analyses also located at the rims were carried out on twenty zircon grains (Table 7.1). Only seven analyses yielded Variscan ages, sensu lato (i.e., lower than 340 Ma). In this case, the two extreme values can be regarded as clear outliers (Fig. 7.4b], inset), and we calculate the weighted average using the rest

of the analyses. Once more, the result produces a high MSWD (13) that can be considerably lowered if we only consider four spots to calculate the weighted mean, resulting in an age of 315 ± 4 Ma, with an acceptable MSWD value (2.0; Fig. 7.4b). The rest of the analyses yielded inherited ages between 650 and 2,660 Ma.

**Table 7.1.** U-Th-Pb SHRIMP-RG analytical data for zircons from the fold-structured migmatites of the Lower series (samples 349 and 524).

| | | | | | | | Uncorrected ratios | | $^{204}$Pb Corrected ratios | | | | |
|---|---|---|---|---|---|---|---|---|---|---|---|---|---|
| Spot Name | Description[a] | Common $^{206}$Pb (%)[b] | U (ppm) | Th (ppm) | $^{232}$Th/$^{238}$U | "Age" [d] | $^{238}$U/$^{206}$Pb [e] | $^{207}$Pb/$^{206}$Pb [e] | $^{238}$U/$^{206}$Pb*[c] [e] | $^{207}$Pb*/$^{206}$Pb*[c] [e] | $^{207}$Pb*/$^{235}$U [c] [e] | $^{206}$Pb*/$^{238}$U [c] [e] | error correlation |
| **349** | | | | | | | | | | | | | |
| 11 | r | 0.04 | 1267 | 9 | 0.01 | **307.2 ± 1.1** | 20.48 ± 0.4 | 0.0529 ± 1.1 | 20.48 ± 0.4 | 0.0526 ± 1.1 | 0.35 ± 1.2 | 0.0488 ± 0.4 | 0.3043 |
| 4 | r | -0.01 | 1234 | 5 | 0.00 | **309.2 ± 1.2** | 20.36 ± 0.4 | 0.0525 ± 1.2 | 20.37 ± 0.4 | 0.0521 ± 1.3 | 0.35 ± 1.3 | 0.0491 ± 0.4 | 0.2946 |
| 29 | r | 0.02 | 931 | 5 | 0.01 | **316.0 ± 1.3** | 19.90 ± 0.4 | 0.0529 ± 1.3 | 19.96 ± 0.4 | 0.0507 ± 1.9 | 0.35 ± 1.9 | 0.0501 ± 0.4 | 0.2197 |
| 20 | r | 1.04 | 294 | 3 | 0.01 | **322.5 ± 2.5** | 19.29 ± 0.8 | 0.0612 ± 2.1 | 19.61 ± 0.9 | 0.0480 ± 7.3 | 0.34 ± 7.4 | 0.0510 ± 0.9 | 0.1177 |
| 13 | HcPb | 2.24 | 1084 | 9 | 0.01 | **325.8 ± 1.9** | 18.86 ± 0.4 | 0.0710 ± 4.7 | 19.33 ± 0.5 | 0.0512 ± 8.3 | 0.36 ± 8.3 | 0.0517 ± 0.5 | 0.0608 |
| 30 | r | 1.33 | 389 | 47 | 0.12 | **338.2 ± 2.1** | 18.32 ± 0.6 | 0.0639 ± 1.6 | 18.70 ± 0.7 | 0.0471 ± 6.6 | 0.35 ± 6.7 | 0.0535 ± 0.7 | 0.1069 |
| 32 | r | 0.21 | 440 | 5 | 0.01 | **369.6 ± 2.6** | 16.91 ± 0.7 | 0.0556 ± 2.2 | 17.11 ± 0.8 | 0.0461 ± 6.6 | 0.37 ± 6.6 | 0.0584 ± 0.8 | 0.1187 |
| 15 | HcPb | 6.30 | 570 | 14 | 0.03 | 416.9 ± 2.3 | 14.02 ± 0.5 | 0.1061 ± 1.1 | 14.24 ± 0.6 | 0.0945 ± 2.5 | 0.92 ± 2.6 | 0.0702 ± 0.6 | 0.2290 |
| 28 | r, inher | -0.12 | 331 | 60 | 0.19 | 607.5 ± 3.6 | 10.13 ± 0.6 | 0.0591 ± 1.4 | 10.14 ± 0.6 | 0.0581 ± 1.7 | 0.79 ± 1.8 | 0.0986 ± 0.6 | 0.3362 |
| 1 | r, inher | 0.08 | 703 | 50 | 0.07 | 636.1 ± 2.5 | 9.64 ± 0.4 | 0.0615 ± 1.1 | 9.64 ± 0.4 | 0.0609 ± 1.2 | 0.87 ± 1.3 | 0.1037 ± 0.4 | 0.3194 |
| 14 | r, inher | 0.07 | 1004 | 56 | 0.06 | 654.2 ± 2.2 | 9.35 ± 0.3 | 0.0620 ± 0.8 | 9.36 ± 0.3 | 0.0614 ± 0.9 | 0.90 ± 1.0 | 0.1068 ± 0.3 | 0.3461 |
| 7 | r, inher | 0.01 | 828 | 357 | 0.45 | 787.1 ± 2.7 | 7.70 ± 0.3 | 0.0654 ± 0.7 | 7.70 ± 0.3 | 0.0652 ± 0.7 | 1.17 ± 0.8 | 0.1298 ± 0.3 | 0.4263 |
| 10 | r, inher | -0.19 | 671 | 48 | 0.07 | 819.3 ± 3.4 | 7.39 ± 0.4 | 0.0648 ± 0.9 | 7.40 ± 0.4 | 0.0644 ± 0.9 | 1.20 ± 1.0 | 0.1352 ± 0.4 | 0.4197 |
| 24 | HcPb | 2.02 | 264 | 29 | 0.11 | 834.7 ± 6.0 | 7.09 ± 0.7 | 0.0836 ± 1.2 | 7.23 ± 0.8 | 0.0671 ± 4.6 | 1.28 ± 4.6 | 0.1383 ± 0.8 | 0.1762 |
| 23 | r, inher | -0.20 | 395 | 57 | 0.15 | 897.6 ± 32 | 5.80 ± 0.6 | 0.0718 ± 1.0 | 5.82 ± 0.6 | 0.0690 ± 1.6 | 1.63 ± 1.7 | 0.1718 ± 0.6 | 0.3384 |
| 2 | r, inher | 0.13 | 234 | 77 | 0.34 | 919.9 ± 5.6 | 6.51 ± 0.6 | 0.0708 ± 1.2 | 6.51 ± 0.6 | 0.0708 ± 1.2 | 1.50 ± 1.4 | 0.1536 ± 0.6 | 0.4484 |
| 16 | r, inher | 0.03 | 166 | 51 | 0.32 | 921.3 ± 7.9 | 6.51 ± 0.9 | 0.0700 ± 1.5 | 6.51 ± 0.9 | 0.0694 ± 1.5 | 1.47 ± 1.8 | 0.1536 ± 0.9 | 0.4969 |
| 8 | r, inher | 0.15 | 803 | 26 | 0.03 | 924.8 ± 3.6 | 6.47 ± 0.4 | 0.0711 ± 0.8 | 6.47 ± 0.4 | 0.0709 ± 0.8 | 1.51 ± 0.9 | 0.1544 ± 0.4 | 0.4323 |
| 27 | r, inher | 1.98 | 926 | 78 | 0.09 | 949.5 ± 2.6 | 6.18 ± 0.3 | 0.0873 ± 0.8 | 6.18 ± 0.3 | 0.0871 ± 0.9 | 1.94 ± 0.9 | 0.1619 ± 0.3 | 0.2914 |
| 12 | r, inher | -0.11 | 934 | 72 | 0.08 | 952.2 ± 3.2 | 6.29 ± 0.3 | 0.0699 ± 0.6 | 6.29 ± 0.3 | 0.0698 ± 0.6 | 1.53 ± 0.7 | 0.1590 ± 0.3 | 0.4675 |
| 27.2 | r, inher | -0.02 | 1487 | 120 | 0.08 | 959.0 ± 2.4 | 6.24 ± 0.3 | 0.0709 ± 0.5 | 6.24 ± 0.3 | 0.0708 ± 0.5 | 1.57 ± 0.5 | 0.1604 ± 0.3 | 0.4647 |
| 22 | r, inher | -0.16 | 241 | 143 | 0.61 | 961.8 ± 5.9 | 6.22 ± 0.6 | 0.0698 ± 1.2 | 6.23 ± 0.6 | 0.0691 ± 1.3 | 1.53 ± 1.5 | 0.1605 ± 0.6 | 0.4291 |
| 26 | r, inher | -0.02 | 1250 | 23 | 0.02 | 967.5 ± 2.5 | 6.18 ± 0.3 | 0.0712 ± 0.5 | 6.18 ± 0.3 | 0.0710 ± 0.6 | 1.58 ± 0.6 | 0.1619 ± 0.3 | 0.4249 |
| 3 | r, inher | -0.06 | 462 | 207 | 0.46 | 995.1 ± 4.5 | 5.99 ± 0.5 | 0.0718 ± 0.8 | 6.00 ± 0.5 | 0.0717 ± 0.8 | 1.65 ± 1.0 | 0.1668 ± 0.5 | 0.4781 |
| 19 | r, inher | 0.09 | 581 | 28 | 0.05 | 1015 ± 20 | 5.87 ± 0.4 | 0.0737 ± 0.9 | 5.87 ± 0.4 | 0.0731 ± 1.0 | 1.71 ± 1.1 | 0.1702 ± 0.4 | 0.3586 |
| 17 | r, inher | 0.27 | 1171 | 41 | 0.04 | 1070 ± 10 | 5.87 ± 0.3 | 0.0752 ± 0.5 | 5.87 ± 0.3 | 0.0751 ± 0.5 | 1.76 ± 0.6 | 0.1704 ± 0.3 | 0.5405 |
| 18 | r, inher | 0.67 | 906 | 992 | 1.13 | 2114 ± 6 | 2.67 ± 0.3 | 0.1315 ± 0.3 | 2.67 ± 0.3 | 0.1312 ± 0.3 | 6.77 ± 0.4 | 0.3741 ± 0.3 | 0.6839 |
| 31 | HcPb | 8.17 | 328 | 135 | 0.42 | 2293 ± 16 | 4.50 ± 0.6 | 0.1489 ± 0.7 | 4.52 ± 0.6 | 0.1454 ± 0.9 | 4.43 ± 1.1 | 0.2210 ± 0.6 | 0.5792 |
| 33 | HcPb | 8.07 | 556 | 13 | 0.02 | 2296 ± 33 | 4.15 ± 0.5 | 0.1523 ± 1.5 | 4.19 ± 0.5 | 0.1456 ± 1.9 | 4.79 ± 2.0 | 0.2387 ± 0.5 | 0.2662 |
| 25 | HcPb | 7.31 | 168 | 39 | 0.24 | 2322 ± 21 | 3.93 ± 1.0 | 0.1495 ± 1.1 | 3.94 ± 1.0 | 0.1480 ± 1.2 | 5.18 ± 1.6 | 0.2540 ± 1.0 | 0.6253 |
| 21 | HcPb | 4.67 | 245 | 86 | 0.36 | 2412 ± 14 | 2.76 ± 0.5 | 0.1578 ± 0.8 | 2.77 ± 0.5 | 0.1559 ± 0.8 | 7.76 ± 1.0 | 0.3611 ± 0.5 | 0.5001 |
| 5 | HcPb | 3.26 | 581 | 261 | 0.47 | 2429 ± 6 | 2.53 ± 0.4 | 0.1578 ± 0.4 | 2.53 ± 0.4 | 0.1575 ± 0.4 | 8.57 ± 0.5 | 0.3947 ± 0.4 | 0.7278 |
| 35 | r, inher | 0.71 | 247 | 133 | 0.56 | 2466 ± 8 | 2.20 ± 0.6 | 0.1612 ± 0.5 | 2.20 ± 0.6 | 0.1610 ± 0.5 | 10.08 ± 0.8 | 0.4543 ± 0.6 | 0.7455 |
| 6 | HcPb | 2.15 | 1252 | 379 | 0.31 | 2469 ± 4 | 2.34 ± 0.3 | 0.1614 ± 0.2 | 2.34 ± 0.3 | 0.1613 ± 0.2 | 9.52 ± 0.4 | 0.4281 ± 0.3 | 0.7903 |
| 36 | HcPb | 5.77 | 621 | 59 | 0.10 | 2476 ± 6 | 2.86 ± 0.3 | 0.1625 ± 0.3 | 2.86 ± 0.3 | 0.1620 ± 0.3 | 7.80 ± 0.4 | 0.3493 ± 0.3 | 0.6675 |
| 9 | r, inher | 0.19 | 330 | 181 | 0.57 | 2491 ± 7 | 2.13 ± 0.5 | 0.1634 ± 0.4 | 2.13 ± 0.5 | 0.1633 ± 0.4 | 10.55 ± 0.6 | 0.4686 ± 0.5 | 0.7649 |
| 34 | r, inher | -0.19 | 1144 | 340 | 0.31 | 2737 ± 5 | 1.88 ± 0.3 | 0.1895 ± 0.3 | 1.88 ± 0.3 | 0.1894 ± 0.3 | 13.88 ± 0.4 | 0.5315 ± 0.3 | 0.6594 |
| **524** | | | | | | | | | | | | | |
| 9.2 | r | 0.02 | 341 | 8 | 0.03 | **287.5 ± 1.8** | 21.92 ± 0.6 | 0.0522 ± 1.9 | 21.95 ± 0.6 | 0.0509 ± 2.4 | 0.32 ± 2.5 | 0.0455 ± 0.6 | 0.2613 |
| 5 | r | 0.12 | 799 | 7 | 0.01 | **304.1 ± 1.3** | 20.68 ± 0.4 | 0.0534 ± 1.3 | 20.70 ± 0.4 | 0.0525 ± 1.5 | 0.35 ± 1.6 | 0.0483 ± 0.4 | 0.2746 |
| 18.1 | r | 0.10 | 484 | 7 | 0.02 | **308.6 ± 3.8** | 20.37 ± 1.2 | 0.0533 ± 1.7 | 20.41 ± 1.2 | 0.0518 ± 2.3 | 0.35 ± 2.6 | 0.0490 ± 1.2 | 0.4778 |
| 7 | r | -0.16 | 811 | 12 | 0.02 | **312.7 ± 1.7** | 20.15 ± 0.5 | 0.0513 ± 1.4 | 20.15 ± 0.5 | 0.0514 ± 1.4 | 0.35 ± 1.5 | 0.0496 ± 0.5 | 0.3564 |
| 5.2 | r | 0.04 | 851 | 9 | 0.01 | **314.4 ± 1.5** | 20.00 ± 0.5 | 0.0530 ± 1.4 | 20.00 ± 0.5 | 0.0530 ± 1.4 | 0.37 ± 1.4 | 0.0500 ± 0.5 | 0.3215 |
| 17 | r | -0.24 | 1199 | 8 | 0.01 | **316.4 ± 1.2** | 19.93 ± 0.4 | 0.0508 ± 1.1 | 19.91 ± 0.4 | 0.0516 ± 1.3 | 0.36 ± 1.4 | 0.0502 ± 0.4 | 0.2754 |
| 12 | r | 0.33 | 769 | 12 | 0.02 | **339.6 ± 1.7** | 18.43 ± 0.5 | 0.0559 ± 1.3 | 18.45 ± 0.5 | 0.0548 ± 1.6 | 0.41 ± 1.7 | 0.0542 ± 0.5 | 0.3063 |
| 18.2 | HcPb | 7.74 | 700 | 10 | 0.01 | 649.2 ± 3.9 | 8.71 ± 0.5 | 0.1247 ± 2.4 | 8.71 ± 0.5 | 0.1244 ± 2.4 | 1.97 ± 2.5 | 0.1148 ± 0.5 | 0.1860 |
| 20 | r, inher | 0.08 | 2125 | 414 | 0.20 | 718.1 ± 1.5 | 8.48 ± 0.2 | 0.0639 ± 0.4 | 8.48 ± 0.2 | 0.0638 ± 0.4 | 1.04 ± 0.5 | 0.1179 ± 0.2 | 0.4556 |
| 16 | r, inher | 1.01 | 483 | 68 | 0.15 | 813.7 ± 4.3 | 7.36 ± 0.5 | 0.0746 ± 1.5 | 7.42 ± 0.5 | 0.0680 ± 2.2 | 1.26 ± 2.3 | 0.1348 ± 0.5 | 0.2394 |
| 11 | r, inher | 0.06 | 118 | 52 | 0.46 | 882.1 ± 8.1 | 6.81 ± 0.9 | 0.0690 ± 1.8 | 6.82 ± 0.9 | 0.0683 ± 1.9 | 1.38 ± 2.1 | 0.1466 ± 0.9 | 0.4351 |
| 10 | r, inher | 0.12 | 1348 | 97 | 0.07 | 910.3 ± 2.7 | 6.59 ± 0.3 | 0.0704 ± 0.8 | 6.59 ± 0.3 | 0.0703 ± 0.8 | 1.47 ± 0.9 | 0.1518 ± 0.3 | 0.3440 |
| 4 | r, inher | -0.20 | 2100 | 28 | 0.01 | 970.8 ± 2.2 | 6.17 ± 0.2 | 0.0698 ± 0.9 | 6.17 ± 0.2 | 0.0697 ± 0.9 | 1.56 ± 0.9 | 0.1622 ± 0.2 | 0.2553 |
| 12.2 | r, inher | -0.26 | 954 | 91 | 0.10 | 980.7 ± 3.3 | 6.10 ± 0.3 | 0.0696 ± 1.2 | 6.10 ± 0.3 | 0.0694 ± 1.2 | 1.57 ± 1.3 | 0.1638 ± 0.3 | 0.2687 |
| 3 | r, inher | -0.09 | 752 | 34 | 0.05 | 987.3 ± 3.4 | 6.05 ± 0.3 | 0.0713 ± 0.6 | 6.05 ± 0.3 | 0.0712 ± 0.6 | 1.62 ± 0.7 | 0.1653 ± 0.3 | 0.4726 |
| 1 | r, inher | 1.03 | 436 | 100 | 0.24 | 1722 ± 15 | 3.62 ± 0.5 | 0.1055 ± 0.8 | 3.62 ± 0.5 | 0.1054 ± 0.8 | 4.02 ± 1.0 | 0.2765 ± 0.5 | 0.4984 |
| 6 | r, inher | 0.05 | 360 | 55 | 0.16 | 1883 ± 10 | 2.95 ± 0.5 | 0.1154 ± 0.5 | 2.95 ± 0.5 | 0.1152 ± 0.6 | 5.38 ± 0.7 | 0.3384 ± 0.5 | 0.6611 |
| 14 | HcPb | 7.73 | 414 | 70 | 0.17 | 2363 ± 9 | 3.96 ± 0.9 | 0.1523 ± 0.5 | 3.97 ± 0.9 | 0.1515 ± 0.5 | 5.27 ± 1.0 | 0.2521 ± 0.9 | 0.8603 |
| 13 | HcPb | 10.06 | 63 | 27 | 0.44 | 2375 ± 52 | 3.09 ± 1.2 | 0.1881 ± 1.1 | 3.23 ± 1.3 | 0.1526 ± 3.0 | 6.51 ± 3.3 | 0.3094 ± 1.3 | 0.3983 |
| 2 | r, inher | 0.98 | 204 | 213 | 1.08 | 2461 ± 9 | 2.23 ± 0.6 | 0.1607 ± 0.5 | 2.23 ± 0.6 | 0.1605 ± 0.5 | 9.92 ± 0.8 | 0.4482 ± 0.6 | 0.7547 |
| 19 | HcPb | 2.04 | 555 | 27 | 0.05 | 2466 ± 9 | 2.33 ± 0.4 | 0.1610 ± 0.5 | 2.33 ± 0.4 | 0.1610 ± 0.5 | 9.53 ± 0.7 | 0.4293 ± 0.4 | 0.5829 |
| 15 | r, inher | -0.58 | 166 | 54 | 0.34 | 2660 ± 19 | 1.93 ± 0.8 | 0.1810 ± 1.1 | 1.93 ± 0.8 | 0.1807 ± 1.1 | 12.93 ± 1.4 | 0.5190 ± 0.8 | 0.5803 |

[a] Zircon characterization: r=rim; inher= inheritance; HcPb= high common Pb.
[b] Negative values denote reversely discordant analyses.
[c] Pb* denotes radiogenic lead
[d] Errors are 1$\sigma$ (absolute values).
[e] Errors are expressed in percentage (%)
"Age <1000 Ma are based on 207Pb corrected $^{206}$Pb/$^{238}$U ratios. whereas ages >1000 Ma are calcuted from 204Pb corrected $^{206}$Pb/$^{207}$Pb ratios".

### 7.3.2. Sant Llorenç–La Jonquera tonalite and Ceret stock gabbro

In sample 530 (a tonalite from the Sant Llorenç–La Jonquera batholith), thirty-one spot analyses were performed on thirty zircon grains (Table 7.2). Individual results range between 315 and 293 Ma. Taking into account the cathodoluminescence texture of the zircon grains, most of the cores yielded the oldest ages, whereas data from the rims were usually younger. The best estimate for the age of the cores was obtained from five analyses (Fig. 7.5a) yielding a mean age of 314.2 ± 1.5 Ma, with an MSWD of 0.11. Two of these analyses had moderate common Pb contents and were connected with the concordant analyses by means of a line anchored to a common Pb composition of 0.857. As regards the rims, a reliable estimation for their age was obtained from 13 analyses, yielding a mean age of 311.0 ± 0.9 Ma with an MSWD of 0.38. The remaining thirteen analyses represented ages younger than 308 Ma and were probably attributed to variable radiogenic Pb loss since they were obtained from both cores and rims. The difference in age between cores and rims suggests that the former might represent antecrysts (Charlier *et al.,* 2005), i.e., crystals formed slightly earlier on the crystallization path.

In sample 420 (a gabbro from the Ceret stock), twenty-four spots were analyzed on nineteen zircons with clear core-rim structures. The data were evenly distributed between 315 and 294 Ma (Table 7.2, Fig. 7.5b), with the cores usually older than the rims. The weighted mean obtained from the twelve core analyses (~309 Ma) had a high MSWD, suggesting that the data contained more than one age population. In a further appraisal, we used the Sambridge & Compston (1994) approach to extract these age populations, considering the core analyses that were unaffected by Pb loss. By doing so, two age groups were established, namely an older one of 312.0 ± 1.6 Ma (MSWD= 0.15 for four analyses) and a younger one of 307.6 ± 1.5 Ma (MSWD= 0.24 for five analyses). As regards the rim analyses, the six younger values were clearly affected by Pb loss (Fig. 7.5b). However, the best estimate for their ages was obtained from four other analyses, yielding a mean age of 307.0 ± 3.5 Ma with an MSWD of 0.10.

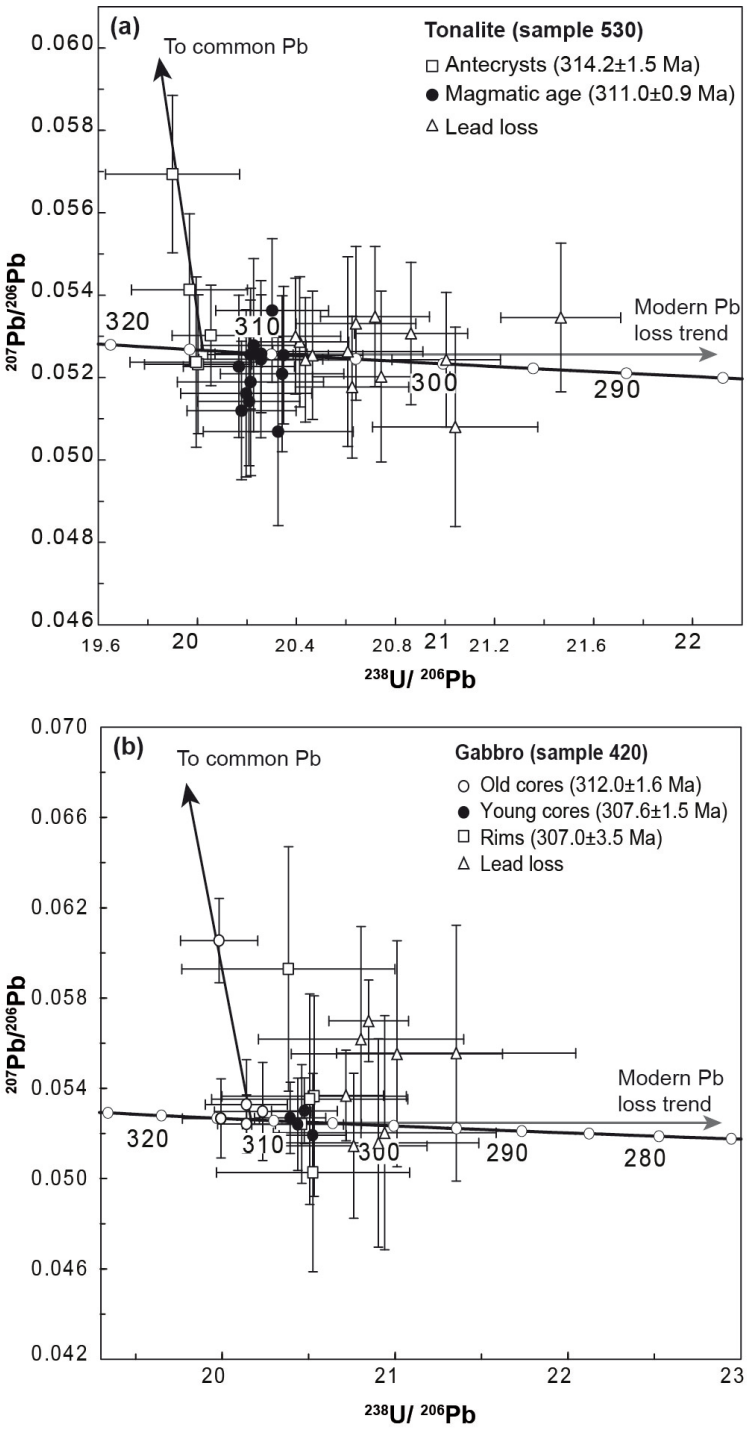



**Figure 7.5.** Tera-Wasserburg diagrams of zircon U–Pb ages from Variscan igneous rocks: (a) Sant Llorenç–La Jonquera tonalite (sample 530) and (b) Ceret stock gabbro (sample 420). Error crosses are ± 2σ.

**Table 7.2.** U-Th-Pb SHRIMP-RG analytical data for zircons from the Sant Llorenç–La Jonquera tonalite (samples 530) and the Ceret stock gabbro (sample 420).

| Spot Name | Description[a] | Common $^{206}Pb$ (%)[b] | U (ppm) | Th (ppm) | $^{232}Th/^{238}U$ | $^{207}Pb$ Corrected $^{206}Pb/^{238}U$ Age[d] | Uncorrected ratios $^{238}U/^{206}Pb$[e] | Uncorrected ratios $^{207}Pb/^{206}Pb$[e] | $^{204}Pb$ Corrected ratios $^{238}U/^{206}Pb^{*}$[c][e] | $^{204}Pb$ Corrected ratios $^{207}Pb^{*}/^{206}Pb^{*}$[c][e] |
|---|---|---|---|---|---|---|---|---|---|---|
| **530** | | | | | | | | | | |
| 1 | r,o | 0.18 | 501 | 135 | 0.28 | 314.5 ± 1.8 | 19.97 ± 0.6 | 0.0541 ± 1.7 | 20.00 ± 0.6 | 0.0527 ± 2.1 |
| 2 | r,o | 0.04 | 698 | 242 | 0.36 | 308.2 ± 1.5 | 20.41 ± 0.5 | 0.0529 ± 1.5 | 20.45 ± 0.5 | 0.0515 ± 1.9 |
| 3 | r,o | -0.04 | 594 | 169 | 0.29 | 314.6 ± 1.7 | 20.00 ± 0.5 | 0.0523 ± 1.6 | 20.01 ± 0.5 | 0.0520 ± 1.7 |
| 4 | r,o | 0.02 | 663 | 258 | 0.40 | 311.0 ± 1.7 | 20.23 ± 0.5 | 0.0528 ± 2.0 | 20.26 ± 0.5 | 0.0516 ± 2.3 |
| 5 | r,o | 0.01 | 639 | 191 | 0.31 | 299.8 ± 1.6 | 21.00 ± 0.5 | 0.0524 ± 1.6 | 21.01 ± 0.5 | 0.0521 ± 1.6 |
| 6 | c,s | 0.13 | 607 | 236 | 0.40 | 303.5 ± 1.6 | 20.72 ± 0.5 | 0.0535 ± 1.6 | 20.74 ± 0.5 | 0.0527 ± 2.0 |
| 7 | r,o | 0.13 | 570 | 149 | 0.27 | 309.6 ± 1.7 | 20.30 ± 0.6 | 0.0536 ± 1.6 | 20.33 ± 0.6 | 0.0525 ± 2.0 |
| 8 | r,o | 0.00 | 879 | 313 | 0.37 | 309.3 ± 1.4 | 20.35 ± 0.4 | 0.0525 ± 1.6 | 20.37 ± 0.4 | 0.0517 ± 1.8 |
| 9 | r,o | 0.11 | 496 | 156 | 0.33 | 304.7 ± 1.8 | 20.64 ± 0.6 | 0.0533 ± 1.7 | 20.65 ± 0.6 | 0.0529 ± 1.8 |
| 10 | c,s | 0.05 | 1131 | 1058 | 0.97 | 313.5 ± 1.2 | 20.05 ± 0.4 | 0.0530 ± 1.2 | 20.06 ± 0.4 | 0.0527 ± 1.3 |
| 11 | c,s | 0.53 | 478 | 353 | 0.76 | 314.4 ± 2.1 | 19.90 ± 0.7 | 0.0569 ± 1.7 | 20.00 ± 0.7 | 0.0527 ± 3.4 |
| 12 | r,o | -0.01 | 707 | 254 | 0.37 | 308.0 ± 1.5 | 20.44 ± 0.5 | 0.0524 ± 1.4 | 20.44 ± 0.5 | 0.0524 ± 1.4 |
| 13 | c,s | -0.19 | 274 | 73 | 0.27 | 299.9 ± 2.4 | 21.04 ± 0.8 | 0.0508 ± 2.4 | 21.06 ± 0.8 | 0.0500 ± 2.6 |
| 14 | r,o | -0.02 | 462 | 128 | 0.29 | 310.7 ± 1.9 | 20.26 ± 0.6 | 0.0524 ± 1.8 | 20.28 ± 0.6 | 0.0517 ± 2.2 |
| 15 | r,o | 0.16 | 587 | 183 | 0.32 | 293.0 ± 1.7 | 21.47 ± 0.6 | 0.0535 ± 1.7 | 21.48 ± 0.6 | 0.0530 ± 1.8 |
| 16 | r,o | -0.15 | 660 | 195 | 0.30 | 311.8 ± 1.6 | 20.21 ± 0.5 | 0.0514 ± 1.5 | 20.23 ± 0.5 | 0.0506 ± 1.7 |
| 17 | c,s | -0.05 | 353 | 93 | 0.27 | 303.7 ± 2.0 | 20.74 ± 0.7 | 0.0520 ± 2.0 | 20.78 ± 0.7 | 0.0507 ± 2.4 |
| 18 | r,o | 0.06 | 846 | 282 | 0.34 | 308.4 ± 1.4 | 20.40 ± 0.4 | 0.0530 ± 1.3 | 20.42 ± 0.5 | 0.0522 ± 1.6 |
| 19 | r,o | -0.18 | 565 | 172 | 0.31 | 312.3 ± 1.7 | 20.18 ± 0.5 | 0.0512 ± 1.6 | 20.19 ± 0.5 | 0.0506 ± 1.8 |
| 20 | c,h | -0.04 | 538 | 203 | 0.39 | 312.1 ± 1.7 | 20.17 ± 0.6 | 0.0523 ± 1.7 | 20.18 ± 0.6 | 0.0516 ± 1.8 |
| 21 | c,s | -0.04 | 370 | 76 | 0.21 | 314.7 ± 2.1 | 20.00 ± 0.7 | 0.0524 ± 2.0 | 20.00 ± 0.7 | 0.0524 ± 2.0 |
| 21.2 | r,o | -0.12 | 442 | 120 | 0.28 | 311.9 ± 2.1 | 20.20 ± 0.7 | 0.0516 ± 2.0 | 20.15 ± 0.7 | 0.0533 ± 2.6 |
| 22 | r,o | -0.09 | 520 | 138 | 0.27 | 305.5 ± 1.7 | 20.62 ± 0.6 | 0.0518 ± 1.7 | 20.63 ± 0.6 | 0.0514 ± 1.7 |
| 23 | r,o | 0.00 | 778 | 320 | 0.43 | 310.6 ± 1.4 | 20.26 ± 0.5 | 0.0526 ± 1.4 | 20.29 ± 0.5 | 0.0512 ± 1.9 |
| 24 | c,h | -0.09 | 313 | 204 | 0.67 | 311.5 ± 2.3 | 20.21 ± 0.7 | 0.0519 ± 2.2 | 20.25 ± 0.7 | 0.0504 ± 2.7 |
| 25 | c,s | -0.23 | 294 | 68 | 0.24 | 310.3 ± 2.3 | 20.33 ± 0.7 | 0.0507 ± 2.3 | 20.33 ± 0.7 | 0.0507 ± 2.3 |
| 26 | r,o | 0.00 | 645 | 246 | 0.39 | 307.5 ± 1.5 | 20.46 ± 0.5 | 0.0525 ± 1.5 | 20.46 ± 0.5 | 0.0525 ± 1.5 |
| 27 | c,h | 0.02 | 302 | 215 | 0.73 | 305.4 ± 2.3 | 20.61 ± 0.7 | 0.0526 ± 2.2 | 20.61 ± 0.7 | 0.0526 ± 2.2 |
| 28 | c,h | -0.06 | 421 | 144 | 0.35 | 309.5 ± 1.9 | 20.34 ± 0.6 | 0.0521 ± 1.8 | 20.38 ± 0.6 | 0.0507 ± 2.2 |
| 29 | r,o-s | 0.00 | 879 | 320 | 0.38 | 311.3 ± 1.3 | 20.21 ± 0.4 | 0.0526 ± 1.3 | 20.23 ± 0.4 | 0.0520 ± 1.4 |
| 30 | r,o-s | 0.09 | 542 | 134 | 0.26 | 301.6 ± 1.7 | 20.86 ± 0.5 | 0.0531 ± 1.6 | 20.90 ± 0.6 | 0.0517 ± 2.0 |
| **420** | | | | | | | | | | |
| 1 | o | 0.16 | 568 | 233 | 0.42 | 303.4 ± 1.6 | 20.72 ± 0.5 | 0.0537 ± 1.9 | 20.73 ± 0.5 | 0.0530 ± 2.0 |
| 2 | o-s | 0.06 | 731 | 344 | 0.49 | 307.2 ± 1.4 | 20.48 ± 0.5 | 0.0530 ± 1.4 | 20.50 ± 0.5 | 0.0520 ± 1.6 |
| 2.2 | r | 0.42 | 50 | 18 | 0.37 | 293.8 ± 4.8 | 21.35 ± 1.6 | 0.0556 ± 5.1 | 21.35 ± 1.6 | 0.0556 ± 5.1 |
| 3 | r | -0.10 | 68 | 23 | 0.35 | 301.5 ± 4.2 | 20.90 ± 1.4 | 0.0516 ± 4.5 | 20.98 ± 1.4 | 0.0488 ± 6.0 |
| 4 | o | 0.15 | 583 | 190 | 0.34 | 307.7 ± 1.6 | 20.43 ± 0.5 | 0.0537 ± 1.5 | 20.40 ± 0.5 | 0.0548 ± 1.9 |
| 4.2 | r | 0.75 | 48 | 14 | 0.30 | 309.6 ± 5.6 | 20.17 ± 1.8 | 0.0586 ± 5.0 | 20.82 ± 2.2 | 0.0332 ± 33.5 |
| 5 | o | -0.07 | 673 | 286 | 0.44 | 306.9 ± 1.5 | 20.52 ± 0.5 | 0.0519 ± 1.4 | 20.53 ± 0.5 | 0.0516 ± 1.5 |
| 6 | o-s | -0.02 | 942 | 637 | 0.70 | 312.4 ± 1.3 | 20.14 ± 0.4 | 0.0524 ± 1.2 | 20.12 ± 0.4 | 0.0533 ± 1.4 |
| 7 | o | 0.02 | 612 | 257 | 0.43 | 308.5 ± 1.6 | 20.39 ± 0.5 | 0.0527 ± 1.5 | 20.41 ± 0.5 | 0.0520 ± 1.6 |
| 7.2 | r | 0.40 | 63 | 21 | 0.35 | 298.6 ± 4.4 | 21.01 ± 1.5 | 0.0555 ± 4.5 | 21.01 ± 1.5 | 0.0555 ± 4.5 |
| 8 | r | 0.48 | 62 | 23 | 0.39 | 301.3 ± 4.3 | 20.80 ± 1.4 | 0.0562 ± 4.4 | 21.07 ± 1.5 | 0.0459 ± 11.6 |
| 9 | r | -0.28 | 67 | 22 | 0.34 | 307.5 ± 4.2 | 20.53 ± 1.4 | 0.0503 ± 4.4 | 20.53 ± 1.4 | 0.0503 ± 4.4 |
| 9.2 | c,o | 0.08 | 376 | 91 | 0.25 | 312.1 ± 1.9 | 20.14 ± 0.6 | 0.0533 ± 1.9 | 20.15 ± 0.6 | 0.0528 ± 2.0 |
| 10 | r | 0.13 | 70 | 26 | 0.39 | 306.6 ± 4.3 | 20.51 ± 1.4 | 0.0535 ± 4.4 | 20.51 ± 1.4 | 0.0535 ± 4.4 |
| 11 | r | 0.85 | 56 | 20 | 0.37 | 306.2 ± 4.7 | 20.38 ± 1.5 | 0.0593 ± 4.6 | 20.38 ± 1.5 | 0.0593 ± 4.6 |
| 12 | o | 0.58 | 513 | 153 | 0.31 | 300.3 ± 1.7 | 20.85 ± 0.6 | 0.0570 ± 1.6 | 20.97 ± 0.6 | 0.0524 ± 3.0 |
| 13 | o-s | -0.01 | 216 | 152 | 0.73 | 307.6 ± 2.6 | 20.46 ± 0.8 | 0.0524 ± 2.5 | 20.48 ± 0.8 | 0.0515 ± 2.8 |
| 14 | o-s,c | -0.12 | 143 | 85 | 0.62 | 303.6 ± 3.1 | 20.76 ± 1.0 | 0.0515 ± 3.1 | 20.80 ± 1.0 | 0.0501 ± 3.7 |
| 14.2 | r | -0.04 | 54 | 20 | 0.38 | 300.8 ± 4.7 | 20.94 ± 1.5 | 0.0520 ± 5.0 | 21.10 ± 1.6 | 0.0461 ± 8.6 |
| 15 | r | 0.15 | 79 | 26 | 0.34 | 306.1 ± 4.0 | 20.53 ± 1.3 | 0.0537 ± 4.1 | 20.62 ± 1.3 | 0.0503 ± 6.5 |
| 16 | r | 0.00 | 526 | 360 | 0.71 | 314.6 ± 1.8 | 19.99 ± 0.6 | 0.0527 ± 1.7 | 20.04 ± 0.6 | 0.0509 ± 2.3 |
| 17 | c,o-s | -0.01 | 377 | 119 | 0.33 | 308.0 ± 2.0 | 20.44 ± 0.7 | 0.0524 ± 2.0 | 20.47 ± 0.7 | 0.0510 ± 2.5 |
| 18 | c,s | 0.05 | 335 | 188 | 0.58 | 310.8 ± 2.2 | 20.23 ± 0.7 | 0.0530 ± 2.0 | 20.25 ± 0.7 | 0.0524 ± 2.2 |
| 19 | c,s | 0.99 | 493 | 143 | 0.30 | 311.8 ± 1.8 | 19.98 ± 0.6 | 0.0605 ± 1.5 | 20.16 ± 0.6 | 0.0536 ± 4.3 |

[a] Zircon characterization: o=oscillatory zoning; c=core; r=rim; h=homogeneous; s=sector zoning.

[b] Negative values denote reversely discordant analyses.

[c] Pb* denotes radiogenic lead

[d] Errors are 1σ (absolute values).

[e] Errors are expressed in percentage (%)

### 7.3.3. Migmatites from the Intermediate series affected by the Ceret gabbro-diorite contact aureole

In sample 529, seventeen spot analyses were carried out in the same number of zircon grains (Table 7.3), focusing on the rims or areas with zoning that could be attributed to metamorphic zircon. The ages vary between 570 and 2,700 Ma and were interpreted as inheritance.

## 7.4. Zircon U, Th, Hf and REE composition

Zircon contains significant amounts of elements such as Hf, Y and rare earth elements (REE), that are present in trace quantities in rocks but can be used as geochemical tracers (e.g., Hoskin & Schaltegger, 2003). For example, in metamorphic zircon, there is a connection between heavy REE and the presence of garnet, whereas the appearance of plagioclase can be evaluated by the Eu anomaly (Rubatto, 2002). In magmatic zircon, trace elements furnish details on magmatic processes (Gagnevin *et al.,* 2010), the characteristics of the source regions (Belousova *et al.,* 1998) and the age interpretation (Castiñeiras *et al.,* 2010). Some elemental concentrations and ratios, such as Hf, Th/U and Yb/Gd, vary systematically with temperature in zircon, and can be used as indices of fraction or melt evolution (Claiborne *et al.,* 2006; Barth & Wooden, 2010).

U, Th, Hf and trace element composition of zircon was used for the migmatitic and magmatic samples studied to gain insight into their petrogenesis. Analytical results of the composition of zircon are presented in tables 7.4 and 7.5, and plotted in figures 7.6 to 7.9.

### 7.4.1. Migmatites from the Lower series

Uranium concentrations in both migmatites (samples 349 and 524) are similar and range from 250 to 1,100 ppm (Table 7.4; Fig. 7.6). Thorium contents range between 2.5 and 8 ppm in sample 349, whereas sample 524 has slightly higher values, between 6.5 and 11 ppm. In the U versus Th graph (Fig. 7.6a), both samples define a compact cluster around the 0.01 Th/U ratio. In the Eu/Eu* versus Hf diagram (Fig. 7.6b), the concentrations of hafnium in both migmatites are comparable, ranging

**Table 7.3.** U-Th-Pb SHRIMP-RG analytical data for zircons from the migmatites from the Ceret stock contact aureole (sample 529).

| Spot Name | Description[a] | Common $^{206}Pb$ (%)[b] | U (ppm) | Th (ppm) | $^{232}Th/^{238}U$ | "Ages" [d] | Uncorrected ratios | | $^{204}Pb$ Corrected ratios | | | | |
|---|---|---|---|---|---|---|---|---|---|---|---|---|---|
| | | | | | | | $^{238}U/^{206}Pb$ [e] | $^{207}Pb/^{206}Pb$ [e] | $^{238}U/^{206}Pb^{*}$ [c] [e] | $^{207}Pb^{*}/^{206}Pb^{*}$ [c] [e] | $^{207}Pb^{*}/^{235}U$ [c] [e] | $^{206}Pb^{*}/238U$ [c] [e] | error correlation |
| **529** | | | | | | | | | | | | | |
| 11 | r. inher | -0.20 | 331 | 35 | 0.11 | 567.3 ± 8.8 | 10.89 ± 1.6 | 0.0574 ± 2.1 | 10.90 ± 1.6 | 0.0569 ± 2.2 | 0.72 ± 2.7 | 0.0918 ± 1.6 | 0.5907 |
| 1 | r. inher | 0.08 | 152 | 63 | 0.43 | 579.4 ± 9.6 | 10.62 ± 1.7 | 0.0600 ± 2.2 | 10.62 ± 1.7 | 0.0600 ± 2.2 | 0.78 ± 2.7 | 0.0941 ± 1.7 | 0.6193 |
| 16 | r. inher | 0.31 | 124 | 35 | 0.29 | 786.0 ± 13.4 | 7.69 ± 1.8 | 0.0680 ± 2.1 | 7.69 ± 1.8 | 0.0680 ± 2.1 | 1.22 ± 2.7 | 0.1301 ± 1.8 | 0.6496 |
| 6 | r. inher | -0.04 | 186 | 88 | 0.49 | 915.1 ± 15.3 | 6.56 ± 1.7 | 0.0692 ± 1.6 | 6.56 ± 1.7 | 0.0687 ± 1.7 | 1.44 ± 2.4 | 0.1524 ± 1.7 | 0.7118 |
| 12 | r. inher | 0.03 | 189 | 155 | 0.85 | 1311 ± 23 | 4.39 ± 1.6 | 0.0855 ± 1.1 | 4.40 ± 1.6 | 0.0848 ± 1.2 | 2.66 ± 2.0 | 0.2275 ± 1.6 | 0.8114 |
| 4 | r. inher | 0.66 | 318 | 298 | 0.97 | 1769 ± 13 | 3.35 ± 1.5 | 0.1085 ± 0.7 | 3.35 ± 1.5 | 0.1082 ± 0.7 | 4.45 ± 1.7 | 0.2986 ± 1.5 | 0.9104 |
| 15 | r. inher | 0.20 | 156 | 111 | 0.74 | 1868 ± 83 | 3.00 ± 1.7 | 0.1149 ± 4.5 | 3.00 ± 1.7 | 0.1142 ± 4.6 | 5.24 ± 4.9 | 0.3330 ± 1.7 | 0.3531 |
| 3 | r. inher | 0.17 | 72 | 64 | 0.91 | 1873 ± 54 | 3.02 ± 2.0 | 0.1140 ± 3.0 | 3.02 ± 2.0 | 0.1146 ± 3.0 | 5.23 ± 3.6 | 0.3313 ± 2.0 | 0.5436 |
| 9 | r. inher | 0.51 | 36 | 33 | 0.94 | 2057 ± 78 | 2.71 ± 2.2 | 0.1286 ± 4.3 | 2.71 ± 2.2 | 0.1270 ± 4.4 | 6.46 ± 4.9 | 0.3686 ± 2.2 | 0.4380 |
| 17 | HcPb | 2.61 | 334 | 68 | 0.21 | 2120 ± 10 | 3.06 ± 1.5 | 0.1317 ± 0.6 | 3.06 ± 1.5 | 0.1317 ± 0.6 | 5.94 ± 1.6 | 0.3269 ± 1.5 | 0.9344 |
| 18 | r. inher | 0.05 | 428 | 121 | 0.29 | 2158 ± 13 | 2.52 ± 1.5 | 0.1346 ± 0.7 | 2.52 ± 1.5 | 0.1345 ± 0.7 | 7.36 ± 1.7 | 0.3968 ± 1.5 | 0.8993 |
| 10 | r. inher | 1.43 | 143 | 219 | 1.57 | 2171 ± 37 | 2.71 ± 1.7 | 0.1357 ± 2.1 | 2.71 ± 1.7 | 0.1355 ± 2.1 | 6.90 ± 2.7 | 0.3694 ± 1.7 | 0.6263 |
| 14 | r. inher | 0.03 | 69 | 66 | 0.99 | 2272 ± 31 | 2.36 ± 2.0 | 0.1440 ± 1.8 | 2.37 ± 2.0 | 0.1437 ± 1.8 | 8.37 ± 2.7 | 0.4227 ± 2.0 | 0.7416 |
| 2 | HcPb | 2.05 | 153 | 96 | 0.64 | 2382 ± 83 | 2.45 ± 1.7 | 0.1535 ± 4.9 | 2.45 ± 1.7 | 0.1532 ± 4.9 | 8.62 ± 5.2 | 0.4083 ± 1.7 | 0.3245 |
| 8 | r. inher | 1.34 | 37 | 18 | 0.52 | 2553 ± 22 | 2.15 ± 2.3 | 0.1703 ± 1.3 | 2.15 ± 2.3 | 0.1695 ± 1.3 | 10.88 ± 2.6 | 0.4656 ± 2.3 | 0.8715 |
| 13 | r. inher | 0.92 | 115 | 94 | 0.85 | 2572 ± 44 | 2.10 ± 1.7 | 0.1717 ± 2.6 | 2.10 ± 1.7 | 0.1715 ± 2.6 | 11.26 ± 3.1 | 0.4762 ± 1.7 | 0.5442 |
| 5 | HcPb | 2.41 | 493 | 191 | 0.40 | 2616 ± 12 | 2.16 ± 1.5 | 0.1762 ± 0.7 | 2.16 ± 1.5 | 0.1761 ± 0.7 | 11.22 ± 1.7 | 0.4621 ± 1.5 | 0.9031 |
| 7 | r. inher | 1.37 | 189 | 338 | 1.85 | 2702 ± 9 | 1.99 ± 1.7 | 0.1856 ± 0.6 | 1.99 ± 1.7 | 0.1854 ± 0.6 | 12.82 ± 1.7 | 0.5014 ± 1.7 | 0.9467 |

[a] Zircon characterization: r=rim; inher= inheritance; HcPb= high common Pb.

[b] Negative values denote reversely discordant analyses.

[c] Pb* denotes radiogenic lead

[d] Errors are 1σ (absolute values).

[e] Errors are expressed in percentage (%)

"Age <1000 Ma are based on 207Pb corrected $^{206}Pb/^{238}U$ ratios. whereas ages >1000 Ma are calcuted from 204Pb corrected $^{206}Pb/^{207}Pb$ ratios".

from 10,400 to 14,100 ppm. By contrast, the Eu/Eu* anomaly is deeper in sample 524 than in sample 349. In the Yb/Gd versus Ce/Sm graph (Fig. 7.6c), Yb/Gd values range between 35 and 120, with the lowest values corresponding to sample 524. The difference in the Ce/Sm ratio in both samples is small, with sample 349 having slightly higher values.

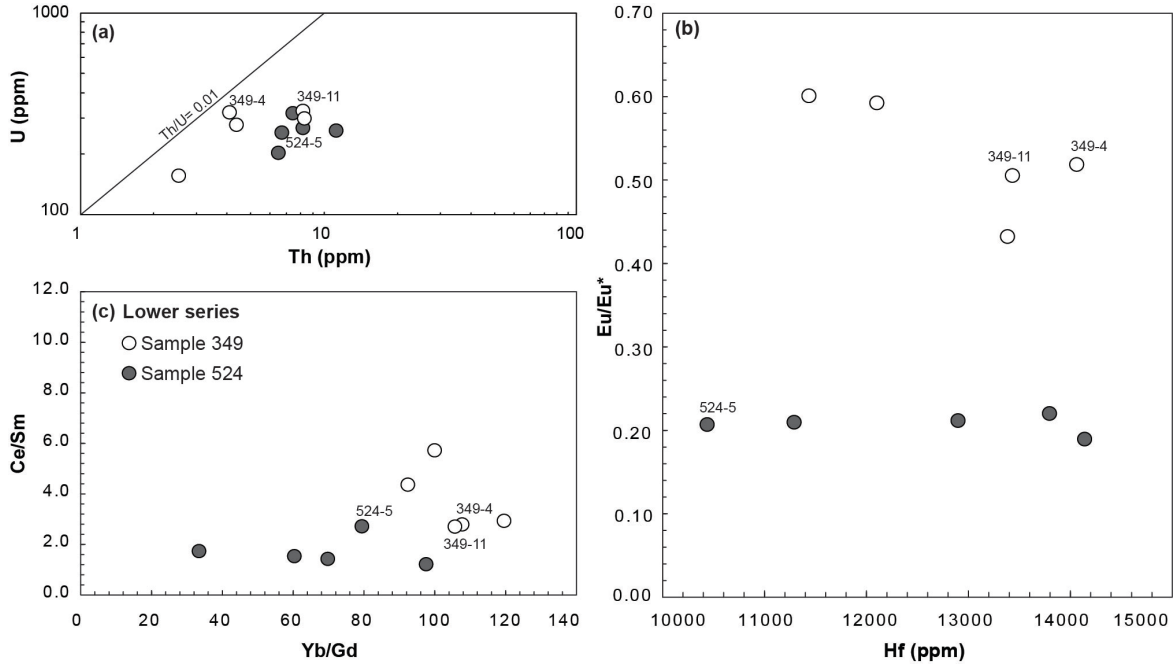



**Figure 7.6.** Compositional diagrams for zircon from the fold-structured migmatites of the Lower series (samples 349 and 524): (a) U versus Th, (b) Hf versus Eu/Eu* and (**c**) Yb/Gd versus Ce/Sm. The marked analyses are those not used to get the mean age.

In the REE chondrite-normalized diagram (Figs. 7.7a & b), the patterns defined by the migmatite samples are typical of high-grade and magmatic zircon, with a progressive fractionation from the heavy to the light REE and two prominent anomalies in cerium (positive) and europium (negative).

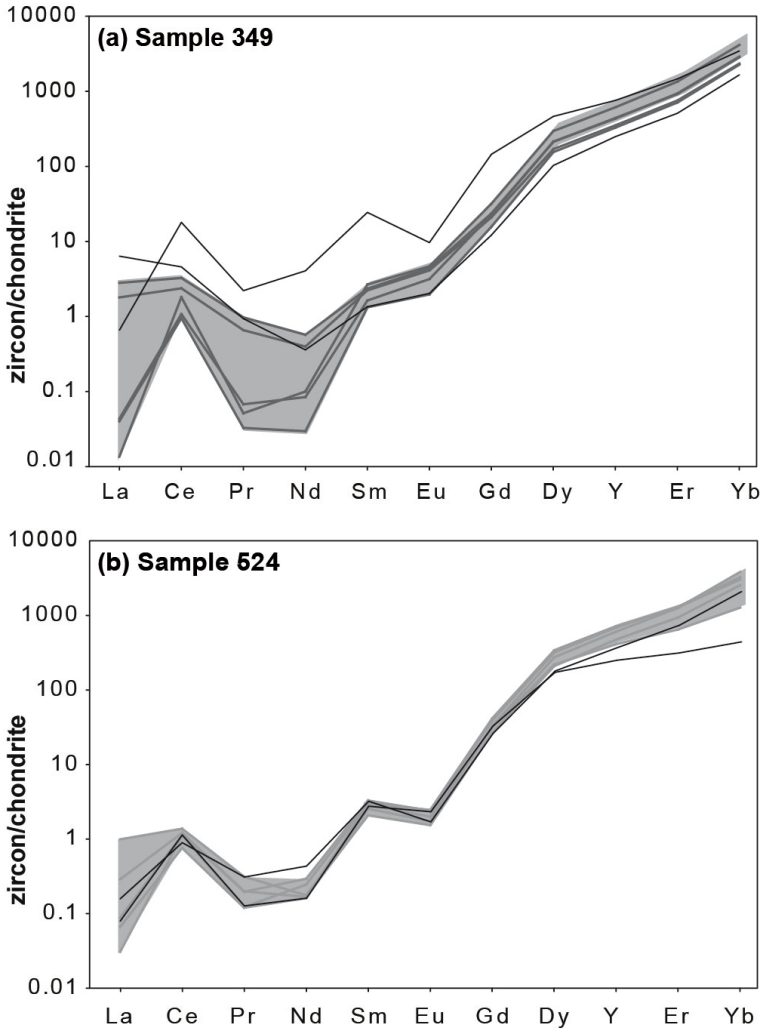



**Figure 7.7.** Chondrite-normalized rare earth (REE) patterns for the fold-structured migmatites from the Lower series: (a) sample 349 and (b) sample 524. Chondrite normalization according to Anders & Grevesse (1989), modified by Korotev (1996).

**Table 7.4.** U, Th, Hf and trace element (REE) composition of zircon for the fold-structured migmatites from the Lower series (samples 349 and 524). Concentrations are given ppm.

| Samples | 524 | | | | | 349 | | | | |
|---|---|---|---|---|---|---|---|---|---|---|
| Spot number | 5 | 5.2 | 7 | 17 | 18.1 | 4 | 11 | 13 | 20 | 29 |
| U | 659 | 730 | 689 | 1022 | 414 | 1041 | 1080 | 907 | 247 | 786 |
| Th | 6.67 | 8.14 | 11.14 | 7.40 | 6.45 | 4.07 | 8.15 | 8.26 | 2.52 | 4.35 |
| Hf | 10437 | 13796 | 12898 | 14140 | 11291 | 14062 | 13433 | 12102 | 13383 | 11435 |
| La | 0.317 | 0.010 | 0.028 | 0.021 | 0.092 | 0.014 | 0.004 | 0.907 | 0.013 | 0.582 |
| Ce | 1.13 | 0.92 | 0.94 | 0.62 | 0.99 | 0.90 | 1.51 | 2.72 | 0.79 | 1.98 |
| Nd | 0.11 | 0.15 | 0.18 | 0.10 | 0.10 | 0.05 | 0.06 | 0.36 | 0.02 | 0.25 |
| Sm | 0.42 | 0.60 | 0.66 | 0.51 | 0.57 | 0.33 | 0.54 | 0.48 | 0.27 | 0.45 |
| Eu | 0.12 | 0.19 | 0.18 | 0.13 | 0.15 | 0.24 | 0.36 | 0.34 | 0.15 | 0.32 |
| Gd | 7.11 | 11.14 | 10.38 | 8.75 | 8.45 | 6.16 | 8.62 | 6.39 | 4.24 | 5.69 |
| Dy | 69 | 112 | 105 | 91 | 72 | 71 | 99 | 71 | 52 | 57 |
| Er | 203 | 280 | 286 | 274 | 140 | 206 | 295 | 202 | 155 | 165 |
| Yb | 565 | 672 | 724 | 853 | 283 | 651 | 929 | 638 | 507 | 526 |
| Y | 1011 | 1526 | 1466 | 1292 | 877 | 934 | 1320 | 947 | 704 | 756 |
| Th/U | 0.010 | 0.011 | 0.016 | 0.007 | 0.016 | 0.004 | 0.008 | 0.009 | 0.010 | 0.006 |
| Yb/Gd | 79.4 | 60.3 | 69.8 | 97.5 | 33.4 | 105.7 | 107.7 | 99.9 | 119.6 | 92.4 |
| Eu/Eu* | 0.21 | 0.22 | 0.21 | 0.19 | 0.21 | 0.52 | 0.51 | 0.59 | 0.43 | 0.60 |
| Ce/Sm | 2.72 | 1.54 | 1.42 | 1.22 | 1.73 | 2.70 | 2.79 | 5.72 | 2.93 | 4.36 |
| U/Ce | 583 | 791 | 735 | 1642 | 417 | 1161 | 714 | 334 | 313 | 397 |

Eu/Eu* is normalized to chondrite values

### 7.4.2. Sant Llorenç–La Jonquera tonalite and Ceret stock gabbro

In sample 530, the compositional difference between antecryst analyses and rim analyses, including those affected by Pb-loss is only discernible in some elements and elemental ratios (Table 7.5). In the Th/U versus Yb/Gd graph (Fig. 7.8a), analyses define two distinct trends. Three out of five antecryst analyses and two rim analyses have a gentle negative slope, whereas the rest of the analyses define a steeper negative slope. In the Yb/Gd versus Ce/Sm graph (Fig. 7.8b), there is a positive correlation between both ratios. The analyses cluster in two groups: one of the groups with three antecryst and two rim analyses at the low Yb/Gd–Ce/Sm end; and the another group with the remaining analyses at the high Yb/Gd–Ce/Sm end. In a chondrite-normalized plot (Fig. 7.8c), the rims (grey lines) show relatively homogeneous patterns, whereas core analyses (dark lines) have heterogeneous patterns with variable sizes of Eu and Ce anomalies.

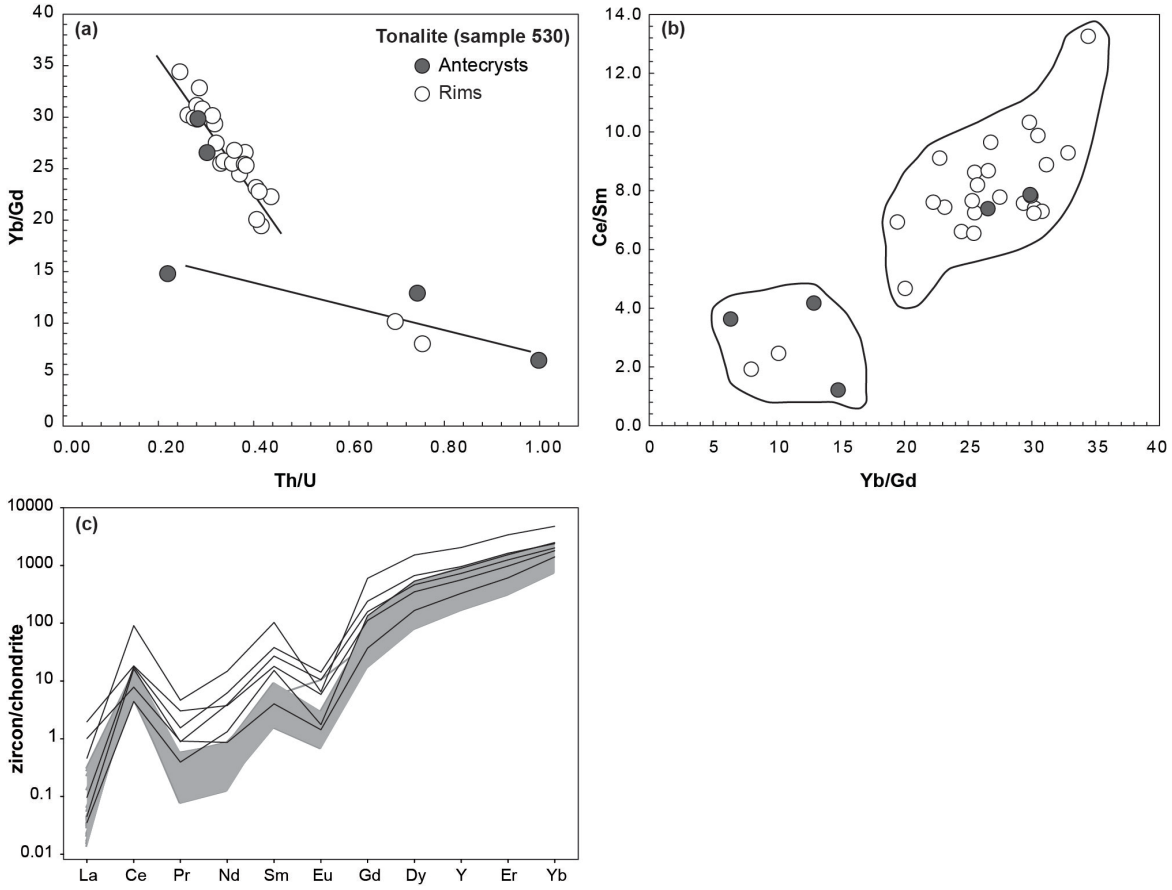



**Figure 7.8.** Compositional diagrams for zircon from the Sant Llorenç–La Jonquera tonalite (sample 530): (a) Th/U versus Yb/Gd plot, (b) Yb/Gd versus Ce/Sm plot and (c) chondrite normalized REE patterns. Chondrite normalization as in Figure 7.7.

In sample 420, the compositional differences between the cores and the rims are more pronounced (Table 7.5). In the Eu/Eu* versus Hf graph (Fig 7.9a), the data define a negative correlation, with cores having a higher Hf content and a deeper Eu anomaly than rims. In the ∑REE versus Hf graph (Fig. 7.9b), the correlation of the data is positive, with the rims depleted in REE and Hf with respect to the cores. Furthermore, there is also a slight difference between the old and the young cores. By contrast, other compositional ratios such as the Ce/Sm and Yb/Gd ratios do not show marked variations. This is evident in Figure 7.9c, where the core and rim patterns are identical and the only difference is the lower content in REE of the rims with respect to the cores.

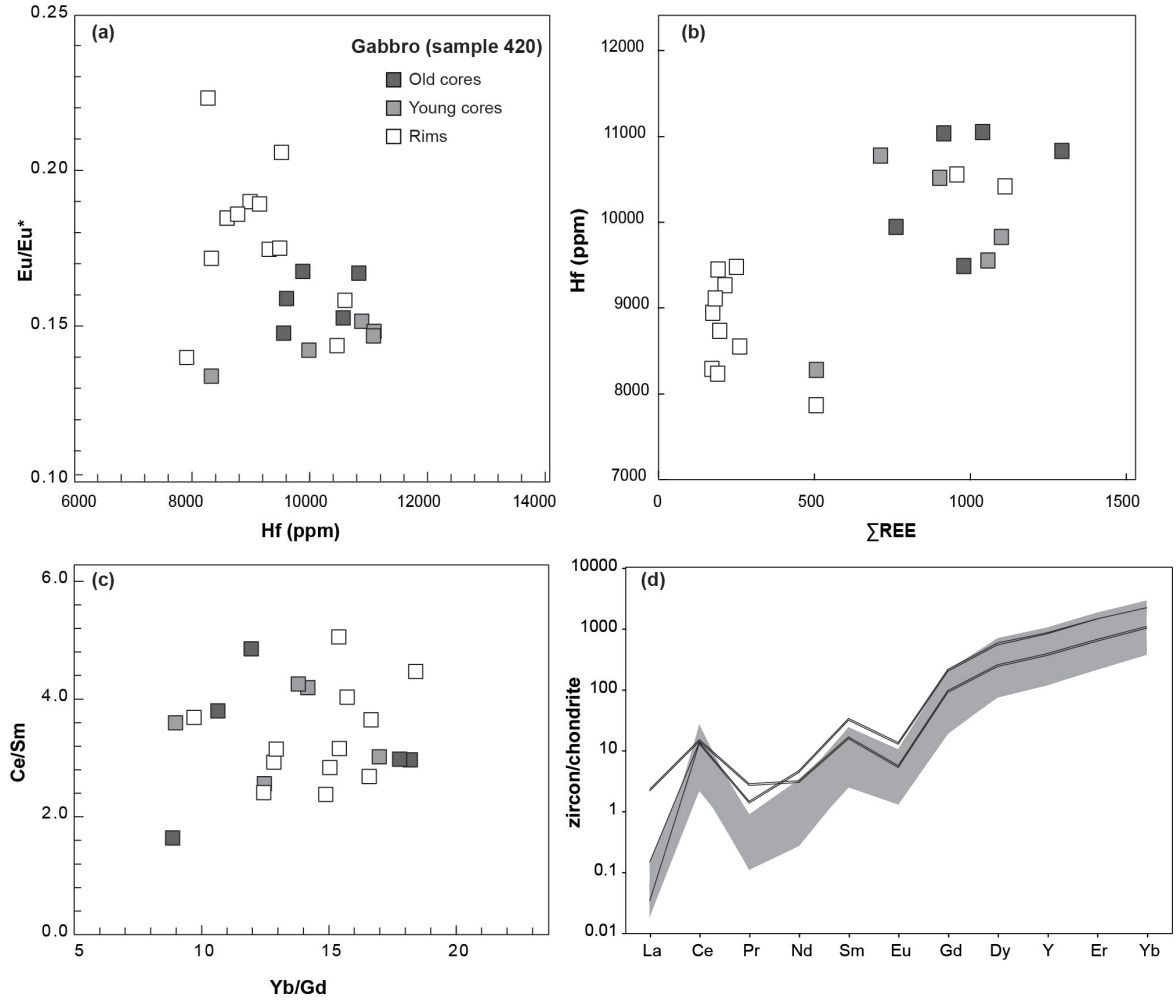



**Figure 7.9.** Compositional diagrams for zircon from the Ceret stock gabbro (sample 420): (a) Hf versus Eu/Eu* plot, (b) ∑REE versus Hf plot and (c) Yb/Gd versus Ce/Sm plot.

**Table 7.5.** U, Th, Hf and trace element (REE) composition of zircon for the Sant Llorenç–La Jonquera tonalite (samples 530) and the Ceret stock gabbro (sample 420). Concentrations are given ppm.

| Spot number | U | Th | Hf | La | Ce | Nd | Sm | Eu | Gd | Dy | Er | Yb | Y | Th/U | Yb/Gd | Ce/Sm | Eu/Eu* | U/Ce |
|---|---|---|---|---|---|---|---|---|---|---|---|---|---|---|---|---|---|---|
| **530** | | | | | | | | | | | | | | | | | | |
| 1 | 518 | 147 | 11838 | 0.368 | 7.10 | 0.61 | 0.90 | 0.12 | 10.7 | 57.9 | 137 | 320 | 730 | 0.28 | 29.9 | 7.87 | 0.12 | 73 |
| 2 | 712 | 264 | 11348 | 0.012 | 8.17 | 0.37 | 1.24 | 0.13 | 13.3 | 70.7 | 154 | 325 | 855 | 0.37 | 24.5 | 6.61 | 0.10 | 87 |
| 3 | 610 | 184 | 12001 | 0.013 | 7.64 | 0.27 | 1.03 | 0.13 | 11.5 | 61.4 | 140 | 307 | 764 | 0.30 | 26.6 | 7.39 | 0.12 | 80 |
| 4 | 687 | 283 | 12784 | 0.006 | 12.50 | 0.42 | 1.37 | 0.15 | 15.3 | 78.6 | 171 | 347 | 931 | 0.41 | 22.8 | 9.11 | 0.10 | 55 |
| 5 | 658 | 209 | 11531 | 0.084 | 9.31 | 0.61 | 1.23 | 0.87 | 12.4 | 69.3 | 162 | 363 | 864 | 0.32 | 29.3 | 7.57 | 0.68 | 71 |
| 6 | 618 | 257 | 13019 | 0.113 | 12.65 | 0.56 | 1.83 | 0.11 | 19.5 | 96.6 | 201 | 380 | 1145 | 0.42 | 19.5 | 6.93 | 0.05 | 49 |
| 7 | 600 | 165 | 14020 | 0.017 | 6.48 | 0.27 | 0.83 | 0.09 | 9.2 | 49.4 | 118 | 275 | 620 | 0.28 | 29.9 | 7.82 | 0.10 | 93 |
| 8 | 899 | 342 | 11468 | 0.017 | 8.71 | 0.36 | 1.33 | 0.16 | 15.0 | 78.1 | 178 | 381 | 964 | 0.38 | 25.4 | 6.55 | 0.11 | 103 |
| 9 | 505 | 170 | 10993 | 0.013 | 9.42 | 0.35 | 1.15 | 0.15 | 13.5 | 73.5 | 163 | 347 | 887 | 0.34 | 25.7 | 8.20 | 0.12 | 54 |
| 10 | 1176 | 1174 | 10992 | 0.169 | 79.61 | 9.95 | 21.94 | 0.55 | 166.7 | 512.7 | 740 | 1065 | 4451 | 1.00 | 6.4 | 3.63 | 0.03 | 15 |
| 11 | 511 | 380 | 12150 | 0.709 | 16.41 | 2.59 | 3.93 | 0.50 | 31.6 | 120.7 | 217 | 408 | 1245 | 0.74 | 12.9 | 4.17 | 0.14 | 31 |
| 12 | 726 | 278 | 11857 | 0.015 | 8.89 | 0.39 | 1.02 | 0.12 | 11.4 | 62.9 | 139 | 303 | 756 | 0.38 | 26.6 | 8.68 | 0.11 | 82 |
| 13 | 285 | 80 | 12637 | 0.011 | 5.46 | 0.09 | 0.55 | 0.06 | 6.3 | 37.9 | 86 | 193 | 450 | 0.28 | 30.5 | 9.88 | 0.10 | 52 |
| 14 | 481 | 140 | 12110 | 0.009 | 6.62 | 0.26 | 0.91 | 0.11 | 10.8 | 60.3 | 142 | 333 | 763 | 0.29 | 30.8 | 7.30 | 0.11 | 73 |
| 15 | 603 | 200 | 12098 | 0.006 | 7.85 | 0.30 | 0.91 | 0.11 | 11.0 | 55.2 | 128 | 282 | 688 | 0.33 | 25.5 | 8.63 | 0.11 | 77 |
| 16 | 689 | 216 | 12199 | 0.015 | 7.85 | 0.29 | 1.09 | 0.15 | 12.4 | 68.9 | 164 | 373 | 878 | 0.31 | 30.2 | 7.23 | 0.13 | 88 |
| 17 | 361 | 101 | 12089 | 0.024 | 5.29 | 0.21 | 0.60 | 0.10 | 8.1 | 47.5 | 114 | 252 | 605 | 0.28 | 31.1 | 8.88 | 0.14 | 68 |
| 18 | 868 | 308 | 12414 | 0.102 | 9.67 | 0.41 | 1.33 | 0.20 | 15.2 | 80.0 | 181 | 387 | 985 | 0.36 | 25.5 | 7.25 | 0.13 | 90 |
| 19 | 585 | 188 | 12164 | 0.012 | 9.05 | 0.33 | 1.16 | 0.14 | 15.0 | 81.3 | 190 | 412 | 1021 | 0.32 | 27.5 | 7.78 | 0.10 | 65 |
| 20 | 553 | 225 | 12231 | 0.008 | 9.61 | 0.55 | 2.06 | 0.25 | 22.3 | 107.4 | 222 | 448 | 1267 | 0.41 | 20.1 | 4.67 | 0.11 | 57 |
| 21 | 386 | 85 | 14200 | 0.013 | 4.06 | 0.92 | 3.34 | 0.15 | 38.0 | 183.7 | 340 | 562 | 1958 | 0.22 | 14.8 | 1.21 | 0.04 | 95 |
| 21.2 | 458 | 131 | 12363 | 0.008 | 5.81 | 0.16 | 0.63 | 0.08 | 7.4 | 42.5 | 105 | 241 | 554 | 0.29 | 32.8 | 9.29 | 0.11 | 79 |
| 22 | 538 | 152 | 12525 | 0.006 | 7.22 | 0.19 | 0.70 | 0.10 | 8.3 | 45.9 | 109 | 247 | 581 | 0.28 | 29.8 | 10.33 | 0.13 | 75 |
| 23 | 803 | 350 | 12224 | 0.011 | 10.26 | 0.39 | 1.35 | 0.16 | 15.3 | 77.1 | 165 | 341 | 907 | 0.44 | 22.3 | 7.60 | 0.10 | 78 |
| 24 | 323 | 225 | 9869 | 0.017 | 14.48 | 2.70 | 5.89 | 0.88 | 44.7 | 159.6 | 278 | 453 | 1601 | 0.70 | 10.1 | 2.46 | 0.16 | 22 |
| 25 | 302 | 74 | 12664 | 0.012 | 4.68 | 0.12 | 0.35 | 0.06 | 5.0 | 28.0 | 71 | 172 | 376 | 0.25 | 34.4 | 13.26 | 0.14 | 65 |
| 26 | 665 | 269 | 11537 | 0.021 | 12.51 | 0.49 | 1.68 | 0.19 | 19.8 | 105.2 | 228 | 458 | 1207 | 0.40 | 23.2 | 7.43 | 0.10 | 53 |
| 27 | 308 | 232 | 9301 | 0.036 | 15.76 | 4.23 | 8.20 | 1.19 | 67.4 | 229.8 | 361 | 539 | 2095 | 0.75 | 8.0 | 1.92 | 0.15 | 20 |
| 28 | 441 | 159 | 12581 | 0.048 | 10.15 | 0.31 | 1.05 | 0.10 | 11.2 | 63.6 | 140 | 300 | 766 | 0.36 | 26.8 | 9.65 | 0.09 | 43 |
| 29 | 914 | 351 | 12415 | 0.005 | 9.73 | 0.35 | 1.27 | 0.16 | 14.2 | 75.2 | 168 | 360 | 917 | 0.38 | 25.3 | 7.65 | 0.12 | 94 |
| 30 | 560 | 147 | 12231 | 0.008 | 5.87 | 0.20 | 0.79 | 0.12 | 9.3 | 54.1 | 125 | 281 | 668 | 0.26 | 30.2 | 7.40 | 0.13 | 95 |
| **420** | | | | | | | | | | | | | | | | | | |
| 1 | 587 | 256 | 10397 | 0.016 | 11.81 | 1.25 | 3.99 | 0.62 | 43.0 | 185.2 | 328 | 536 | 1814 | 0.44 | 12.5 | 2.96 | 0.14 | 50 |
| 2 | 761 | 380 | 11019 | 0.011 | 11.38 | 0.87 | 2.70 | 0.45 | 32.0 | 152.1 | 276 | 441 | 1530 | 0.50 | 13.8 | 4.22 | 0.15 | 67 |
| 2.2 | 52 | 20 | 8273 | 0.023 | 1.90 | 0.24 | 0.66 | 0.11 | 6.0 | 26.7 | 49 | 88 | 271 | 0.38 | 14.6 | 2.86 | 0.17 | 27 |
| 3 | 71 | 25 | 9093 | 0.015 | 2.37 | 0.21 | 0.53 | 0.10 | 5.3 | 26.7 | 52 | 95 | 278 | 0.36 | 17.9 | 4.50 | 0.19 | 30 |
| 5 | 695 | 314 | 10815 | 0.018 | 12.17 | 1.51 | 4.69 | 0.77 | 50.7 | 224.5 | 386 | 614 | 2157 | 0.45 | 12.1 | 2.59 | 0.15 | 57 |
| 6 | 982 | 702 | 9820 | 0.009 | 20.81 | 1.43 | 4.27 | 0.76 | 43.6 | 195.3 | 329 | 506 | 1853 | 0.71 | 11.6 | 4.87 | 0.17 | 47 |
| 7 | 634 | 282 | 11032 | 0.013 | 13.94 | 0.91 | 3.25 | 0.54 | 37.3 | 176.5 | 308 | 500 | 1716 | 0.45 | 13.4 | 4.28 | 0.15 | 45 |
| 7.2 | 65 | 23 | 8927 | 0.007 | 2.34 | 0.19 | 0.58 | 0.12 | 5.9 | 25.9 | 49 | 90 | 266 | 0.36 | 15.3 | 4.06 | 0.19 | 28 |
| 8 | 64 | 26 | 8534 | 0.008 | 2.37 | 0.30 | 0.99 | 0.18 | 9.2 | 39.5 | 74 | 133 | 396 | 0.40 | 14.5 | 2.41 | 0.19 | 27 |
| 9 | 69 | 24 | 9246 | 0.012 | 2.53 | 0.21 | 0.69 | 0.13 | 6.9 | 30.9 | 60 | 112 | 321 | 0.34 | 16.2 | 3.67 | 0.18 | 27 |
| 9.2 | 387 | 99 | 10770 | 0.010 | 4.75 | 0.34 | 1.59 | 0.32 | 20.9 | 105.7 | 211 | 370 | 1130 | 0.26 | 17.7 | 2.99 | 0.17 | 82 |
| 10 | 73 | 29 | 9460 | 0.013 | 2.72 | 0.34 | 1.11 | 0.23 | 10.3 | 39.9 | 71 | 124 | 372 | 0.40 | 12.1 | 2.44 | 0.21 | 27 |
| 11 | 58 | 22 | 8717 | 0.013 | 2.27 | 0.25 | 0.71 | 0.13 | 6.7 | 30.4 | 55 | 101 | 300 | 0.38 | 15.0 | 3.19 | 0.19 | 26 |
| 12 | 534 | 168 | 10533 | 0.019 | 6.96 | 0.69 | 2.57 | 0.46 | 29.9 | 150.6 | 281 | 483 | 1499 | 0.32 | 16.1 | 2.71 | 0.16 | 77 |
| 13 | 224 | 166 | 8272 | 0.020 | 13.51 | 1.99 | 3.72 | 0.44 | 26.7 | 86.8 | 143 | 232 | 805 | 0.74 | 8.7 | 3.63 | 0.13 | 17 |
| 14 | 146 | 93 | 7851 | 0.727 | 12.16 | 1.92 | 3.27 | 0.42 | 25.2 | 82.9 | 142 | 237 | 814 | 0.64 | 9.4 | 3.71 | 0.14 | 12 |
| 14.2 | 56 | 22 | 8215 | 0.012 | 2.14 | 0.28 | 0.67 | 0.17 | 7.5 | 29.6 | 55 | 94 | 294 | 0.40 | 12.6 | 3.18 | 0.22 | 26 |
| 15 | 81 | 28 | 9427 | 0.006 | 2.95 | 0.18 | 0.58 | 0.11 | 6.6 | 28.1 | 54 | 99 | 297 | 0.35 | 15.0 | 5.08 | 0.18 | 27 |
| 16 | 537 | 394 | 9496 | 0.019 | 17.60 | 1.67 | 4.60 | 0.69 | 43.8 | 171.7 | 290 | 451 | 1657 | 0.73 | 10.3 | 3.83 | 0.15 | 31 |
| 17 | 386 | 131 | 9928 | 0.039 | 6.29 | 0.54 | 2.07 | 0.33 | 23.6 | 117.8 | 223 | 391 | 1223 | 0.34 | 16.6 | 3.05 | 0.14 | 61 |
| 18 | 351 | 209 | 9546 | 0.046 | 11.02 | 2.81 | 6.61 | 1.01 | 56.2 | 190.5 | 308 | 482 | 1801 | 0.60 | 8.6 | 1.67 | 0.16 | 32 |
| 19 | 508 | 156 | 10507 | 0.010 | 6.36 | 0.51 | 2.12 | 0.38 | 26.8 | 136.9 | 266 | 464 | 1456 | 0.31 | 17.3 | 3.01 | 0.15 | 80 |

Eu/Eu* is normalized to chondrite values

# CHAPTER 8

## DISCUSSION

### 8.1. Metamorphism-deformation-magmatism relationships

The Roc de Frausa Massif presents a crustal section deformed and metamorphosed during the Variscan orogeny and intruded by Variscan igneous rocks. Variscan deformation can be ascribed to two phases D1 and D2. The D1 is marked by tight to isoclinal small-scale synschistose folds and the most prominent D1 structure is a sub-horizontal foliation (S1). The most conspicuous D2 structures are tight upright folds facing to the NW with steep NE–SW axial planes. The D2 heterogeneously overprints the D1, thus in high-grade metamorphic domains it develops a penetrative axial plane foliation (S2) whereas in low-grade metamorphic domains the S2 foliation is not formed. The D3 is characterized by NW–SE folds compatible with steep dextral shear zones. It affects the pre-Variscan rocks and Variscan intrusives and retrogrades where it is associated with greenschist facies retrogression. N and S of the studied area the F3 folds involve Mesozoic rocks, and therefore the D3 event can be attributed to the Alpine orogeny.

Regional metamorphic zonation marked by metamorphic grade increasing with depth is broadly parallel to lithostratigraphy and to the S1 foliation. Three metamorphic zones can be observed: an andalusite zone for the upper crustal levels (the Upper series), a sillimanite zone for the intermediate levels (the Intermediate series) and a migmatite zone for the deepest crustal levels (the Lower series), which crop out in the core of the massif. At all levels, index minerals of the different metamorphic zones define the S1 and/or the S2 foliation and cordierite is always the last mineral to crystallize. In the Upper series, inclusion trails in andalusite porphyroblasts and in the Intermediate series, sillimanite and micas parallel to the S1 foliation document crystal growth during the development of the S1 foliation. In both Upper and Intermediate series, cordierite postdates the D1 event. These observations

indicate that D1 episode was broadly coeval with the peak of regional metamorphism. In the Lower series, paleosome–leucosome banding of the fold-structured migmatites parallel to the S1 indicate that anatexis took place during the D1 event and prevailed during the D2 event as indicated by the F2 folds and axial planar leucosomes. In this level, cordierite grows late- to post-D2.

Variscan igneous rocks are pre- to syn-kinematic with the D2 deformation event as shown by the preferred orientation of the magmatic fabric. A calc-alkaline composite granitoid intruded at the top of the Upper series, approximately parallel to the S1 and a narrow contact aureole (cd–bi) was formed around it. A gabbro-dioritic stock intruded at the Intermediate series synchronously to the D2 event, cutting across the lithologies parallel to the pervasive S1 foliation. A high-temperature contact aureole with widespread migmatization was developed around it. In these migmatites from the Intermediate series, garnet rims with included biotite and sillimanite oriented parallel to the limb of the F2 folds provide the earlier history registered in the massif and suggest growth of garnet during the S1 foliation. Contact metamorphic microstructures with the S2 foliation in gabbros and diorites and with leucosomes parallel to the axial plane of F2 folds partially erase the D1 record. As at fold-structured migmatites from the Lower series, cordierite crystallized late- to post-D2 event.

According to the relationships between metamorphism, deformation and magmatism, the main S1 foliation is preserved in the entire massif and is coeval with the peak of regional metamorphism. Calc-alkaline igneous rocks of Sant Llorenç-La Jonquera intruded post-D1 and pre-D2. The S2 foliation is developed in the higher-grade metamorphic rocks and is coeval with the emplacement of the hornblende gabbros and diorites of the mafic complexes at deeper levels.

## 8.2. Interpretations of the different types of migmatites affected by the Ceret gabbro-diorite contact aureole

Different types of granulite facies migmatites were formed in the inner aureole and xenoliths of the Ceret gabbro-dioritic stock at the last stages of the Variscan orogeny. The type of migmatite depends on the interplay of several variables among which are: the microstructures preserved, the proportions of paleosome, leucosome and melanosome, the mineral assemblages and the whole-rock and mineral compositions.

The migmatites range from patch to stromatic and schollen types in the inner contact aureole, whereas schollen to residuum melanosomes are found as xenoliths inside the gabbro-diorite. The meso- to microscopic structural features preserved in each migmatite type reflect different histories. In patch and schollen migmatites, paleosomes-mesosomes record two high-temperature deformation events (D1 and D2); contrastingly, leucosomes register a shorter deformation history synchronous to the D2 event. In patch migmatite domains the amount of leucosome is limited, in contrast increasing volumes are present in schollen. Stromatic migmatites are leucosome-rich and preserve a well-formed S2 foliation defined by leucosome–melanosome layers transposing the S1 foliation. Residuum melanosomes present scarce leucosome and only register a weak S2 foliation due to the absence of leucosome and the preserved mineral assemblage.

Three mineral assemblages characterize the different types of migmatites. Patch and schollen migmatites present the assemblage biotite–sillimanite–cordierite–garnet–plagioclase–quartz±K-feldspar, whereas stromatites and residuum melanosomes contain no K-feldspar and sillimanite. Biotite and fibrolitic sillimanite generate garnet and melt from dehydration-melting during the prograde history (D1). K-feldspar would also be formed by this reaction and consumed later in the history of the rock. Radiating clusters of coarse prismatic sillimanite can be produced by a retrograde reaction with melt coeval with the D2 event. Cordierite and intergrowths of cordierite with spinel are formed as a back reaction with melt or as a retrograde reaction.

The whole-rock composition is highly variable. $SiO_2$ content varies from 40–64 wt.%. A decreasing $SiO_2$ content is proportional to an enrichment in $Al_2O_3$, MgO and FeO and a depletion in alkalis (Figs. 4.15 & 4.16). Patch, stromatites and schollen migmatites show the highest amount of $SiO_2$, whereas residuum melanosomes contain the lowest values. Non-migmatitic rocks outside the contact aureole within the Roc de Frausa Massif that are interpreted as a possible protolith composition present a mean $SiO_2$ content of around 55 to 64 wt.%.

Regarding the mineral composition of migmatites, $X_{Fe}$ values of garnet, biotite and cordierite are highly variable (Fig. 4.14). Patch and schollen migmatites show the highest values of $X_{Fe}$ (garnet, $X_{Fe}$ = 0.82–0.91; biotite, $X_{Fe}$ = 0.50–0.65; cordierite, $X_{Fe}$ = 0.35–0.48), whereas stromatites and residuum melanosomes present the lowest ones (garnet, $X_{Fe}$ = 0.71–0.87; biotite, $X_{Fe}$ = 0.42–0.55; cordierite, $X_{Fe}$ = 0.29–0.35). Biotite and cordierite of the non-migmatitic rocks yield $X_{Fe}$ values around 0.50 to 0.63 and around 0.40 to 0.50 respectively (Fig. 4.13).

Taking into account all the mentioned characteristics and comparing the studied migmatites with the composition of the hypothetical protolith, we can conclude that the different types of migmatites could have evolved from a common protolith. Patch and schollen migmatites are rocks that have not modified their mineral and whole-rock composition and presumably the melt formed would be *in situ*. This fact is reinforced by the presence of paleosome with biotite and sillimanite (fibrolite) following S1 foliation. The preservation of mineral assemblages with abundant biotite coexisting with sillimanite and minor or no K-feldspar and subordinate cordierite and garnet can be interpreted as a partial retrograde reaction, because of a limited amount of water flux in the system. Conversely, residuum melanosomes are restitic rocks strongly modified with respect to the protolith. They represent an end-product where the melt had been extracted, in consequence, an open system can be inferred for them (Sawyer *et al*., 1999; White & Powell, 2002). Melt loss would be coherent with the low $X_{Fe}$ ratios of biotite and cordierite and with the low $SiO_2$ and alkalis content. The abundance of cordierite and spinel coexisting with garnet can be explained by a retrograde reaction that consumed completely sillimanite and quartz. This reaction can be formed with abundant water flux in the system. Stromatitic migmatites are rocks that have modified the $X_{Fe}$ ratios of coexisting biotite and

cordierite but not the whole-rock composition with respect to the protolith. As in residuum melanosomes, stromatites would have totally consumed sillimanite and K-feldspar to form abundant cordierite and spinel coexisting with garnet.

In conclusion, these tendencies reflect that the migmatites are attributed to an increasing volume of melt from patch migmatites to residuum melanosomes that infiltrated through and expelled. Although, stromatites migmatites present a different behavior since they are the richest in silica, but their mineral composition is impoverished in $X_{Fe}$.

## 8.3. *P–T–d* evolution

The petrological study and pseudosection modeling have shown that the rocks from different crustal levels (the Upper, Intermediate and Lower series) record different *P–T* histories and peak metamorphic conditions. The evidences for the *P–T* paths and their relation to the fabric development of the different rock types is now summarized and discussed.

### 8.3.1. Prograde paths, peak conditions and early retrogression

In the micaschists of the Upper series, the well-developed S1 pressure shadows of sillimanite around andalusite porphyroblasts indicate isobaric heating at around 3 kbar from 580 °C to 640 °C in the shallow-dipping D1 fabric, where peak conditions are determined from muscovite–biotite isopleths. Late cordierite overgrowing the S1 fabric indicates the end of the decompression path into the cordierite stability field (Fig. 8.1). The peak conditions are in agreement with thermobarometric calculations of Liesa & Carreras (1989) who obtained 650 °C and 3–3.5 kbar.

In the Intermediate series not affected by the Ceret contact aureole, the assemblage defining the S1 foliation contains the index minerals biotite–muscovite–sillimanite, indicating equilibration between 3.5 and 4.5 kbar at 600–660 °C. Later coarse-grained K-feldspar and cordierite poikiloblats overgrow the S1 fabric and point to decompression into 3–3.5 kbar at 640–660 °C (Fig. 8.1).

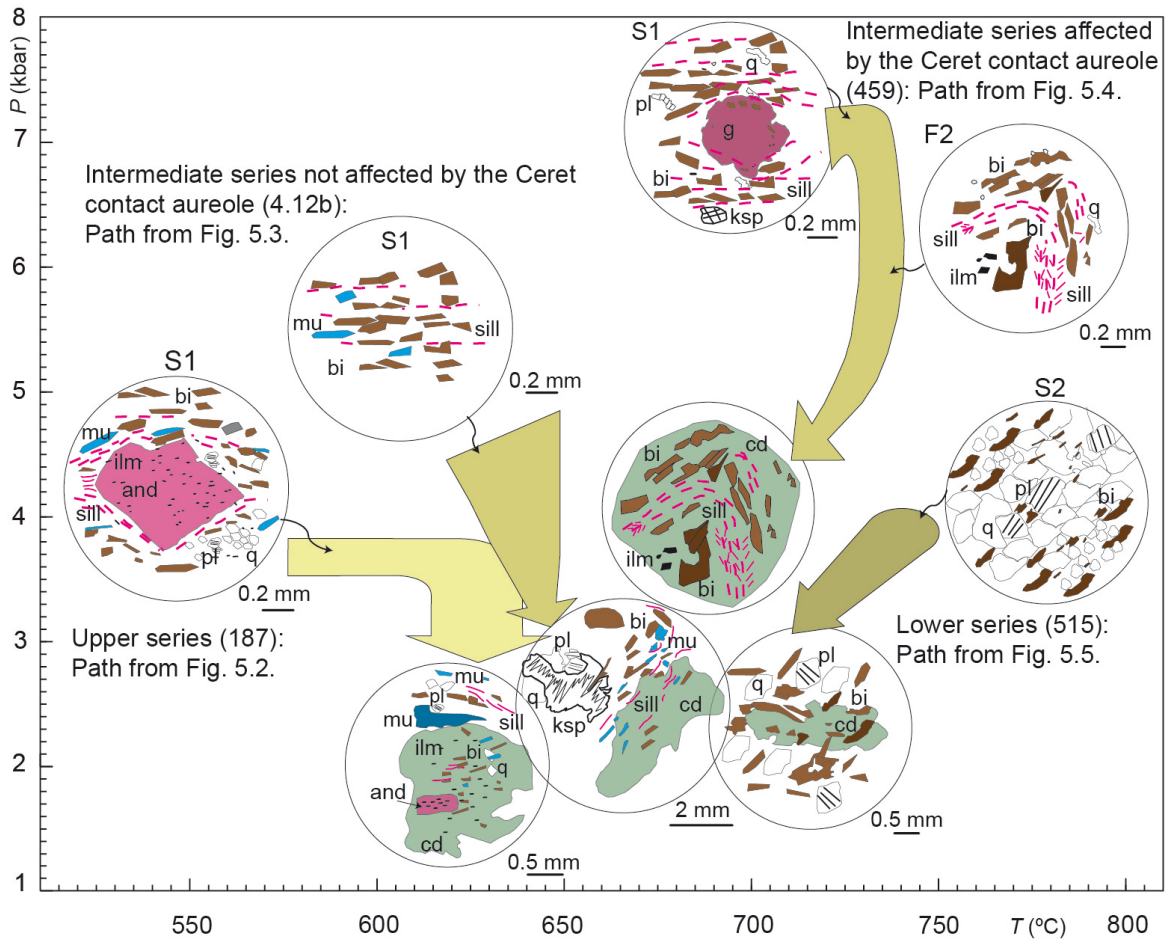



**Fig. 8.1.** *P–T* paths and sketches of the petrological successions for representative samples from the different levels of the Roc de Frausa Massif. See text for discussion.

In the Intermediate series affected by the contact aureole of Ceret gabbro-diorite, the assemblage within the S1 fabric is biotite–sillimanite–garnet–plagioclase–quartz–K-feldspar. Garnet cores are interpreted as diffusionally equilibrated at "peak" *P–T* conditions, where the rock spent long time enough to flatten its compositional profile (Fig. 4.11). Thus the peak is constrained by the assemblage and garnet core compositional isopleth to around ~730 °C and ~7 kbar. Microstructure of garnet at the rim is characterized by oriented inclusions of biotite and sillimanite, which indicate growth of garnet over the S1 fabric. This is consistent with crossing the garnet molar isopleths with increasing temperature in the pseudosection and is interpreted as heating at 7 kbar within the S1 fabric to temperature peak. Cordierite coronas formed around garnet and texturally related to the S2 fabric suggest decompression to biotite–sillimanite–garnet–cordierite–plagioclase–quartz–K-feldspar. Garnet rim composition and this assemblage indicate conditions of 710 °C

and 4.5 kbar. This late metamorphic reequilibration is attributed to the thermal effect of the Ceret gabbro-diorite intrusion during isothermal decompression. The temperature estimated using pseudosection modeling is slightly higher compared to those obtained by thermometry for the composition of coexisting garnet and retrograde biotite (about 650–700 °C; Liesa & Carreras, 1989).

The migmatites from the Lower series contain the assemblage with index minerals garnet–biotite–cordierite. Small garnet grains are included in plagioclase, suggesting that they are a relic phase, not stable with the matrix assemblage. In the pseudosection, such a microstructure is explained by decompression associated with cooling from 3.5–5 kbar at $T$ >750 °C to about 700 °C at around 3 kbar. These $P$–$T$ conditions are also supported by the composition of biotite and cordierite. The rocks may have been originally in deeper crustal levels, but strong equilibration in the cordierite stability field obliterated the early $P$–$T$ evolution.

### 8.3.2. Implications of the P–T–d paths

$P$–$T$–$d$ paths imply that the crystalline rocks underwent a clockwise orogenic evolution marked by heating followed by isothermal decompression. The heating is recorded within the S1 fabric in the Upper series and in the Intermediate series affected by the Ceret gabbro-diorite contact aureole. This event is probably associated with a moderate crustal thickening of exceptionally hot crust. The crystallization of cordierite poikiloblasts points to a subsequent isothermal decompression around ~3 kbar (Fig. 8.1). From this depth, the complete crustal section would share the exhumation history. The migmatites from the Intermediate series affected by Ceret contact aureole froze at 4.5 kbar, therefore they did not register the last decompression and cooling history. In high-grade metamorphic rocks, the decompression is connected with the steep S2 fabric, whereas in the intermediate-grade rocks, the late cordierite statically overgrows the S1 foliation and therefore cannot be directly correlated with the D2 event. Almost constant temperature maintained by lower crustal rocks during exhumation to middle crustal levels (~3 kbar of vertical displacement) can be explained by several factors. The most important is the relative rapidity of the decompression, as well as the syntectonic intrusion of the Ceret gabbro-diorite. The intrusion can transfer heat

laterally (~100 °C with respect to the rocks away from the contact aureole) and it can thermally affect exhumed medium-grade rocks of the Intermediate series.

In summary, correlation of *P*–*T* paths with mineral chemistry and crystallization-deformation relations of rocks formed at different crustal levels allows tracing the history of the Variscan orogeny in Pyrenees. We can infer that rocks with different *P*–*T* histories and from different crustal levels are characterized by broadly isothermal decompression and that the intrusion of hot igneous bodies constituted a way to transfer heat from the core of the orogen laterally and vertically at the late stages of the orogeny.

In addition, the *P*–*T*–*d* evolution obtained in the Roc de Frausa Massif agree with *P*–*T* estimates obtained by thermometry for the composition of coexisting phases in different massifs of Pyrenees. Many of them have followed *P*–*T* paths that involved decompression under prograde or retrograde conditions. Their *P*–*T* paths are clockwise, see the Bossòst (Pouget, 1991; Mezger *et al*., 2004) and the Lys-Caillaouas (Kriegsman *et al*., 1989) massifs of the Central Pyrenees; the Canigó (Gibson, 1991), the Cap de Creus (Druguet, 2001) and the Albera (Vilà *et al.,* 2007) massifs in the Eastern Pyrenees; and the Trois Seigneurs (Kriegsman, 1989) and the Saint Bathélémy (de Saint Blanquat *et al*., 1990) and the Agly (Guitard *et al*., 1995) massifs of the North Pyrenean zone. The metamorphic gradient inferred from the last equilibration *P*–*T* conditions is around 67–71 °C/km for the Roc de Frausa Massif. This gradient is similar to those calculated in other Pyrenean massifs: Hospitalet (67 °C/km; van den Eeckhout, 1986), Cap de Creus (80 °C/km; Druguet, 2001), Trois-Seigneurs (100 °C/km; Wickham and Oxburgh, 1986) and to the general gradient given for the entire Variscan Pyrenees (70 °C/km; Zwart, 1968 and 65 °C/km; Guitard *et al.*, 1995). Therefore, the continuous prograde zonation and the thermal gradient displayed in the Roc de Frausa Massif provide a representative example of the metamorphic conditions and the average thermal gradient attained in the Pyrenean segment at the end of the Variscan orogeny.

## 8.4. High-temperature metamorphic processes in the migmatites

In spite of the mentioned differences in structures, mineral assemblages and composition (see section 8.2), the paths followed by the four types of migmatites are similar. None of them records a prograde path. The oldest registered history corresponds to a decompression path from 7–5 kbar followed by isobaric cooling from 850 °C to approximately 700 °C. The mineral assemblages preserved are those of the solidus as the retrograde history is water undersaturated. The migmatites will not register a late subsolidus history apart of limited retrogression of the mineral assemblages because reaction rates will be slow and the solidus assemblage will metastably persist. Thus, the shared *P*–*T* path justifies a common process for producing the different types of migmatites where the preserved mineral assemblages represent final products. Introducing water into the system can be seen as reasonable as it dissolves into the melt and modifies its composition (Holland & Powell, 2001).

Pseudosection modeling reveals that water incorporated into the melting system controls the structures of the migmatites, the mineral assemblages and the amount of melt produced in the rocks (e.g., Collins *et al.*, 1989; White *et al*., 2005; Hasalová *et al*., 2008). The crystallizing gabbro-diorite intruded at mid-crustal levels of the Roc de Frausa Massif could release fluid that would be infiltrated into the melt. We must take into account that the magma forming the gabbro-diorite is a hydrous magma and that the gabbro contains hornblende and biotite. The models were done at 5.5 kbar according to the pseudosections for the four migmatitic types (Fig. 6.11). The diagrams show that the four rocks share this part of the path, thus using this pressure increases the chances of reliability of the model. With respect to temperature, diagrams from figures 6.12 and 6.14 show that the temperature chosen for modeling must be around 790 °C as the mineral assemblages of the four types of migmatites can be reproduced. The stability field of patch migmatites constrains a narrow temperature range (790 ± 2 °C). The *T*–*M*($H_2O$) diagram (Fig. 6.12) indicates that the assemblage for the patch migmatites can only be reproduced at very low water content (3 mol.% $H_2O$). The mineral assemblages of schollen, stromatites and residuum melanosomes are also reproduced in equilibrium with melt proportions

between 45–65 mol.% melt; however, as the system is closed for the melt the assemblages would not be preserved when cooling.

A model of multiple melt loss–fluid infiltration events (Fig. 6.14) can explain the preservation of the four different types of granulite facies migmatites. Concerning the amount of water infiltrated in every event, we introduced it in small batches from 5–2 mol.% thus considering that the gabbro-diorite would gradually expel it on crystallizing. The proposed model provides a mechanism with open-system behavior, producing a big amount of melt (up to 60 mol.%) along the high-*T* history of the rock, most of which would be expelled. Melt extraction would be enhanced by the D2 deformation event taking place concomitantly to the intrusion. The melt production is maximum on the second melting episode and smaller in subsequent episodes and the solidus takes place progressively at higher temperature. The rock volume will be reduced down to 48 mol.% and the characteristic mineral assemblages will be preserved. Consequently, the mineral proportions of the preserved minerals will vary considerably through the process, as they predict a distinct increase in the content of cordierite and secondly garnet and a decrease in K-felsdpar, sillimanite, quartz and melt (Fig. 6.15). As suggested by White & Powell (2002), phase diagram modeling of the effect of melt loss shows that the amount of melt that has to be removed from a rock to preserve a granulite facies assemblages varies markedly with rock composition and the number of partial melt loss events

Fluid infiltration-melt depletion processes in an open-system are demonstrated by the comparison between the composition of the anatectic melt and residues obtained by modeling with the whole-rock composition of migmatites and the composition of plutonic rocks from the same area (Fig. 6.16). At a greater scale this process could be responsible for the differentiation of the crust and the migration of magmas to the upper crust. However, this possibility remains to be proved until geochemical evidence for the association between both magmatic and migmatitic rock types are established.

## 8.5. Timing of the Variscan thermal evolution in the Eastern Pyrenees

Summarizing the results obtained by U–Pb zircon dating, a thermal evolution is registered through the late stages of the Variscan orogeny in the Eastern Pyrenees. This evolution is the result of an early migmatization followed by the intrusion of two igneous bodies.

The earliest migmatization was coeval with the main deformation (D1). It is recorded in the deepest levels of the Upper Proterozoic to Lower Cambrian series of the Roc de Frausa Massif. The Variscan partial melting history of the migmatites is poorly constrained by zircon geochronology since zircon recrystallization is generally limited to thin discontinuous rims. Nevertheless, an approximate estimate for the onset of crustal melting can be between 320 ± 13 Ma and 315 ± 4 Ma (Serpukhovian–Bashkirian). Furthermore, REE contents and various elemental ratios of these rims show a relatively homogeneous composition, which suggests that the process of zircon crystallization was by dissolution-precipitation. The compositional difference between the two analyzed samples (349 and 524) observed in Eu/Eu* and Ce/Sm suggests that zircon rims from sample 349 precipitated from less evolved melts than those of sample 524, which precipitated from possibly less oxidized melts that had undergone substantial feldspar crystallization.

The intrusion of the composite Sant Llorenç–La Jonquera plutonic complex (314–311 Ma) and the Ceret stock (312–307 Ma) was pre- to syn-kinematic with the D2 deformation event, respectively. The Sant Llorenç–La Jonquera plutonic sheet was emplaced in between the medium-grade Upper Proterozoic–Lower Cambrian series and the low-grade Upper Ordovician–Silurian metasediments. At the base of the La Jonquera sheet, tonalite magmas intruded between 314.2 ± 1.5 (core ages) and 311.0 ± 0.9 Ma (rim ages). The ages are significantly older than the previously estimated (282 ± 5 Ma on Rb–Sr whole-rock (Cocherie, 1984) and 295 ± 7 Ma on U–Pb zircon (Maurel, 2003)). The variable REE contents of zircons (Fig. 7.8), the heterogeneous patterns of the core analyses and the relatively homogeneous patterns of the rims together with the variable size of the Eu and Ce anomalies support the interpretation

of zircon cores as antecrysts. The gabbro–diorite Ceret stock was emplaced in deeper layers of the Upper Proterozoic–Lower Cambrian series. Two magmatic pulses are revealed by cathodoluminescence (Fig. 7.3) and transmitted light microscopy, and are also demonstrated by the trace element compositional differences between non-luminescent cores and luminescent rims of zircons (Fig. 7.9). The non-luminescent cores correspond to an early magmatic pulse that occurred at 312 ± 1.6 Ma. They grew from a more evolved magma where most of the plagioclase had already crystallized, in accordance with the deeper Eu anomalies. The young ages obtained from the cores (307.6 ± 1.5 Ma) probably represent lead loss. The luminescent rims correspond to a second pulse that took place at 307.0 ± 3.5 Ma. They originated from a second and less evolved magma where plagioclase had not completely crystallized, as suggested by the lower Hf content and the shallower Eu anomaly (Fig. 7.9a). The absence of meso- and microscopic evidence of physical mixing (mingling) suggests that the mixture was complete; therefore, the existence of these two magmatic pulses is only recorded in zircon. In summary, zircon geochemistry suggests a complex magmatic history for the Sant Llorenç–La Jonquera suite and the gabbro-diorite Ceret stock. This history includes long-lived magmatic chambers fed by several pulses of magma and mixing of magmas with different geochemical characteristics. Moreover, the trace element geochemistry of zircons for these rocks supports the proposal of Vilà *et al.* (2005) that these two igneous bodies are geochemically diverse and belong to genetically distinct igneous suites produced in different levels of the lithosphere.

In the migmatites from the Ceret gabbro contact aureole, Variscan rims around inherited zircon are absent. This suggests that zirconium was retained in the pre-existing zircon grains and was barely dissolved during the migmatization event with the result that isotopic re-equilibration was incomplete.

## 8.6. Comparison of thermal events with neighboring areas of the Variscan belt

### 8.6.1. Thermal events in the Pyrenean segment of the Variscan belt

The crustal heating recorded in the Eastern Pyrenees during the late stages of the Variscan orogeny has also been observed in the entire Pyrenees (Fig. 8.2). The available geochronological data indicate that an early thermal episode occurred over a time span of *c.* 7 m.y. coeval with the main deformation event. This early episode is registered in deep-seated intrusives as the Ax granite in the Aston Massif (Central Pyrenees), a deformed deep-seated granite and a charnockite in the Agly Massif (North-Pyrenean massifs). They yield ages between 321–314 Ma (Table 8.1) similar to those obtained for the early partial melting episode recorded in the deepest migmatites of the Roc de Frausa Massif (320–315 Ma). However, younger U–Pb ages (310 ± 25 Ma and 295 ± 5 Ma) have been obtained for the deepest granulitic paragneisses of the Saint Barthelemy Massif (Delaperrière *et al*., 1994).

This episode was followed by the emplacement of mafic rocks in the middle crust and subordinate to large calc-alkaline plutons in the upper crust. Few geochronological data are available for the former. In the Agly Massif, the Tournefort diorite yields a U–Pb age of 308.3 ± 1.2 Ma (Olivier *et al.,* 2008). This age is younger than that of the first magmatic pulse of the Ceret gabbro–diorite (312 ± 1.6 Ma, recorded in the antecrystic cores) but comparable to the second one, dated at 307.0 ± 3.5 Ma (recorded in the rims). The emplacement of the large upper crustal calc-alkaline plutons of the Pyrenees could have lasted for about 15 m.y. This episode could have been diachronic (314–301 Ma) along the Pyrenees. The ages obtained in this work for the Sant Llorenç–La Jonquera plutonic complex are in the older range if we consider those yielded by recent studies on other calc-alkaline intrusive bodies of the Pyrenees (between 312 to 301 Ma, see Fig. 8.2 and Table 8.1). Moreover, the ages obtained in this work record a multiple intrusion history that has not been reported to date.

### 8.6.2. Thermal events in the Variscan segments of the Montagne Noire (SE France) and the Catalan Costal Ranges (NE Iberia)

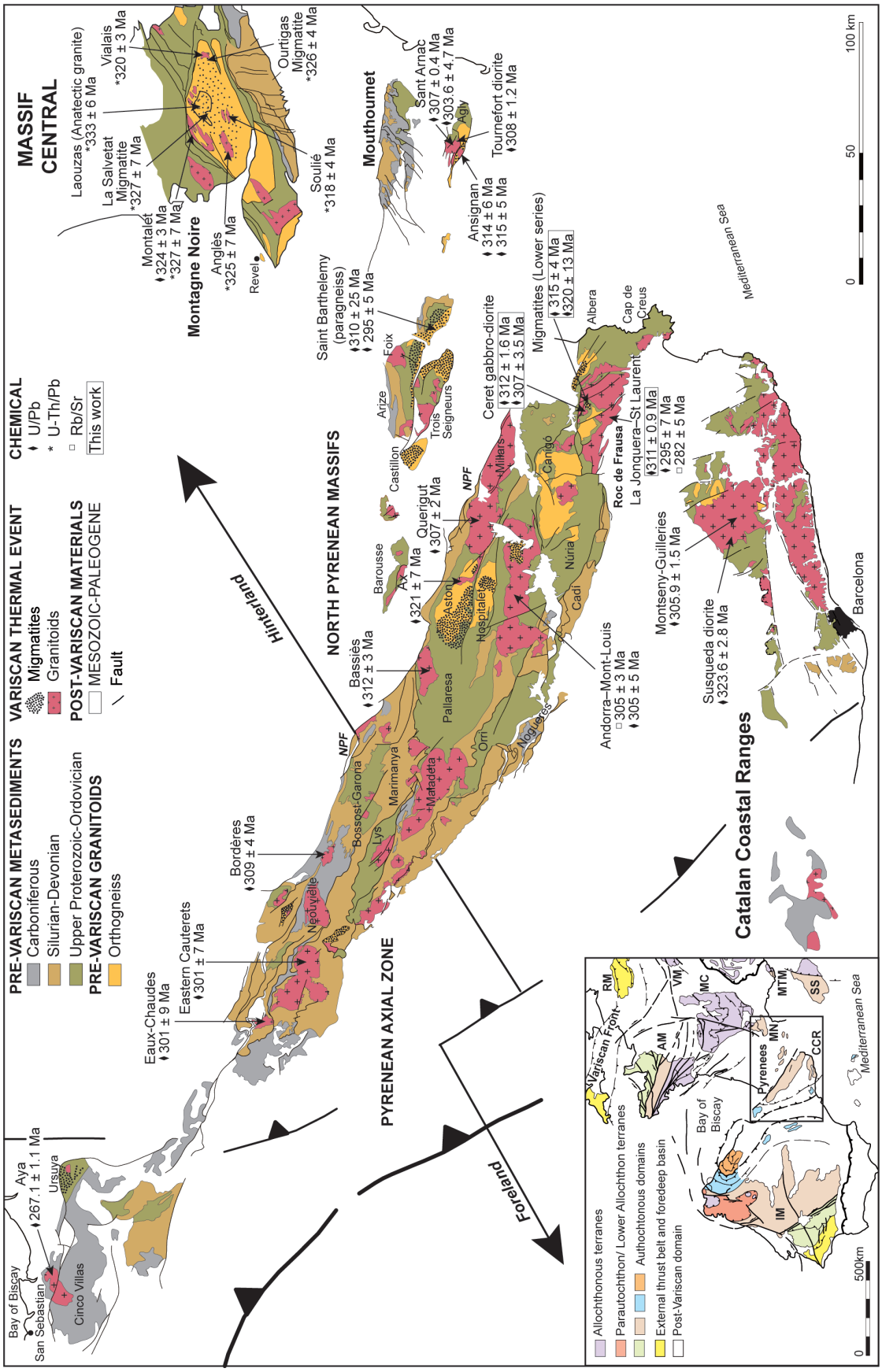
The timing of the thermal evolution of the Pyrenean Variscides can be correlated with the ages obtained for the closest neighboring areas (Montagne Noire and the Catalan Coastal Ranges) that form part of the Northern Gondwana margin and the northern branch of the Ibero-Armorican arc (Julivert *et al.,* 1972; Martínez Catalán, 1990; Barnolas & Chiron, 1996).

Despite the lack of continuity of Variscan outcrops between these three localities, the available data for migmatites and intrusive rocks (Table 8.1) point to older ages and longer thermal histories to the northeast (Fig. 8.2). Thus, in Montagne Noire, three main episodes of crustal melting are recognized by Faure *et al.* (2010). According to these authors, the first dated episode corresponds to the emplacement of an anatectic granite (333 ± 6 Ma). The second episode is recorded in the migmatites at the core of the dome at 327–326 Ma coeval with the emplacement of the Montalet pluton. The last episode corresponds to the intrusion of late- to post-migmatitic plutons ranging from 325 to 318 Ma. For the Northern Catalan Coastal Ranges (Guilleries Massif), mid crustal intrusives concomitant with the main foliation provide ages around 324 Ma, whereas an upper crustal granite yield zircon ages of 306 Ma and leucogranite veins give ages between 305–299 Ma (Martínez *et al.,* 2008).

### 8.6.3. Time-space configuration of the Variscan belt in NE Iberia (Pyrenees–Catalan Coastal Ranges) and SE France (Montagne Noire)

The chronological relationships between the migmatitic and magmatic episodes in the Pyrenees, the Catalan Coastal Ranges and Montagne Noire can also be integrated into the stratigraphy, the structural evolution and the metamorphic record. This will allow to constrain the progression of events during the Variscan orogeny and to establish a zonation of this segment of the belt.

**Fig. 8.2.** Sketch of the Variscan zonation in NE Iberia and S France, modified from Druguet (2001), with the available ages of the migmatites and intrusive rocks. NPF: North-Pyrenean Fault.


MASSIF CENTRAL
Montagne Noire
Mouthoumet
NORTH PYRENEAN MASSIFS
PYRENEAN AXIAL ZONE
Catalan Coastal Ranges
Hinterland
Foreland
NPF
Bay of Biscay
San Sebastian
Cinco Villas
Aya
267.1 ± 1.1 Ma
Ursuya
Eaux-Chaudes
301 ± 9 Ma
Eastern Cauterets
301 ± 7 Ma
Bordères
309 ± 4 Ma
Neouvielle
Bossost-Garona
Lys
Marimanya
Maladeta
Pallaresa
Orri
Nogueres
Bassiès
312 ± 3 Ma
Barousse
Ax
321 ± 7 Ma
Querigut
307 ± 2 Ma
Aston
Hospitalet
Arize
Foix
Castillon
Trois Seigneurs
Saint Barthelemy (paragneiss)
310 ± 25 Ma
295 ± 5 Ma
Ceret gabbro-diorite
312 ± 1.6 Ma
307 ± 3.5 Ma
Millars
Canigó
Núria
Cadi
Migmatites (Lower series)
315 ± 4 Ma
320 ± 13 Ma
Albera
Cap de Creus
Roc de Frausa
La Jonquera–St Laurent
311 ± 0.9 Ma
295 ± 7 Ma
282 ± 5 Ma
Andorra–Mont-Louis
305 ± 3 Ma
305 ± 5 Ma
Montseny-Guilleries
305.9 ± 1.5 Ma
Susqueda diorite
323.6 ± 2.8 Ma
Barcelona
Mediterranean Sea
Laouzas (Anatectic granite)
333 ± 6 Ma
La Salvetat Migmatite
327 ± 7 Ma
Montalet
324 ± 3 Ma
327 ± 7 Ma
Anglès
325 ± 7 Ma
Revel
Soulié
318 ± 4 Ma
Ourtigas Migmatite
326 ± 4 Ma
Vialais
320 ± 3 Ma
Agly
Sant Arnac
307 ± 0.4 Ma
303.6 ± 4.7 Ma
Ansignan
314 ± 6 Ma
315 ± 5 Ma
Tournefort diorite
308 ± 1.2 Ma
PRE-VARISCAN METASEDIMENTS
Carboniferous
Silurian-Devonian
Upper Proterozoic-Ordovician
PRE-VARISCAN GRANITOIDS
Orthogneiss
VARISCAN THERMAL EVENT
Migmatites
Granitoids
POST-VARISCAN MATERIALS
MESOZOIC-PALEOGENE
Fault
CHEMICAL
U/Pb
U-Th/Pb
Rb/Sr
This work
0
50
100 km
Allochthonous terranes
Parautochthon/ Lower Allochthon terranes
Authochtonous domains
External thrust belt and foredeep basin
Post-Variscan domain
Variscan Front
RM
VM
MC
MTM
SS
AM
MN
CCR
Pyrenees
IM
Bay of Biscay
Mediterranean Sea
0
500km

The earlier thermal episode generating migmatites in the oldest pre-Variscan stratigraphic series of the Central–Eastern Pyrenees and Montagne Noire (Fig. 8.2) was coeval with the main deformation event. This event is characterized by south-verging folds in deep levels and south-directed thrusts in the upper crust. As for the Pyrenean chain as a whole, the metamorphic isograds are discordant to the stratigraphic succession. Towards the W–SW, the metamorphic zonation reaches higher levels of the series (Zwart, 1986), thus indicating that the preserved metamorphic zonation is subsequent to the main deformation event.

Calc-alkaline intrusions are approximately emplaced at the same structural-metamorphic levels throughout the Pyrenees, the Catalan Coastal Ranges and Montagne Noire and probably in the ductile-to-brittle transition zone. However, towards the W–SW they progressively intruded into younger levels of the series: from Upper Proterozoic–Lower Paleozoic to the NE to Devonian–Carboniferous series to the SW (Fig. 8.2). Since plutons were contemporaneous with or subsequent to a late deformation event (e.g., Autran *et al.,* 1970; Zwart, 1979; Bouchez & Gleizes, 1995), this correlation suggests that the series were deformed before or at the same time as plutons were emplaced and that (2) the metamorphic zonation predates or is synchronous to the late thermal episode giving rise to magmatism.

These relationships are consistent with the foreland propagation of the orogen from NE to SW. Similarly, the time-space distribution of migmatites and plutons along the Pyrenees, the Catalan Coastal Ranges and Montagne Noire is in line with the relative position of the hinterland and foreland of the southern branch of the Variscan belt. Thus, the polarity of Variscan structures in the three areas indicates that the foreland propagating orogeny advanced southwestwards across the area (Martínez Catalán, 1990; Carreras & Debat, 1996; Matte, 2001). In high structural levels, the syn-orogenic deposits are younger towards the W–SW (Delvolvé, 1996). As for the sedimentology of the Devonian, the shallowest facies are located in the southwestern part of the Pyrenees (García-Sansegundo *et al.,* 2011).

A number of zonation models have been developed for the Pyrenees. In line with the present-day distribution, Carreras & Debat (1996) and Druguet (2001) proposed a NW–SE trending zonation model for the three areas, from external shallow-seated zones in the W–SW (Western and Central Pyrenees and the Southwestern Catalan

**Table 8.1.** Available ages for migmatites and intrusive rocks of the Variscan Belt at the Pyrenees, the Catalan Coastal Ranges and Montagne Noire.

| Locality | Ages (Ma) | Authors | Methods | Techniques |
|---|---|---|---|---|
| ***PYRENEES*** | | | | |
| ***Migmatites*** | | | | |
| **Roc de Frausa Massif** | | | | |
| Migmatites (Lower Series) | 320 ± 13 | **This work** | U-Pb Zircon | SHRIMP-RG |
| | 315 ± 4 | **This work** | U-Pb Zircon | SHRIMP-RG |
| **Saint Barthelemy** | | | | |
| paragneiss | 310 ± 25 | Delaperrière *et al*., 1994 | U-Pb Zircon/monazite | |
| | 295 ± 5 | Delaperrière *et al*., 1994 | U-Pb Zircon/monazite | |
| ***Deep crustal intrusives*** | | | | |
| **Aston Massif** | | | | |
| Ax granite | 321 ± 7 | Denèle *et al.,* 2007 | U-Pb Zircon | |
| **Agly Massif** | | | | |
| deformed deep-seated granite | 317 ± 3 | Olivier *et a*l., 2004 | U-Pb Zircon | ID-TIMS |
| Ansignan charnockite | 314 ± 6 | Respaut & Lancelot, 1983 | U-Pb Zircon | |
| | 315 ± 5 | Postaire, 1984 | U-Pb Zircon | |
| ***Mid crustal intrusives*** | | | | |
| **Agly Massif** | | | | |
| Tournefort diorite | 308.3 ± 1.2 | Olivier *et al.,* 2008 | U-Pb Zircon | ID-TIMS |
| **Roc de Frausa Massif** | | | | |
| Ceret gabbro | 312 ± 1.6 | **This work** | U-Pb Zircon | SHRIMP-RG |
| | 307.6 ± 1.5 | **This work** | U-Pb Zircon | SHRIMP-RG |
| | 307 ± 3.5 | **This work** | U-Pb Zircon | SHRIMP-RG |
| ***Calc-alkaline upper intrusives*** | | | | |
| La Jonquera –Sant Llorenç | 282 ± 5 | Cocherie, 1984 | whole-rock Rb/Sr | |
| | 295 ± 7 | Maurel, 2003 | U-Pb Zircon | SIMS |
| | 314.2 ± 1.5 | **This work** | U-Pb Zircon | SHRIMP-RG |
| | 311.0 ± 0.9 | **This work** | U-Pb Zircon | SHRIMP-RG |
| Saint Arnac | 303.6 ± 4.7 | Olivier *et al.,* 2008 | U-Pb Zircon | ID-TIMS |
| Querigut | 307 ± 2 | Roberts *et al.,* 2000 | U-Pb Zircon | |
| Andorra - Mont-Louis | 305 ± 3 | Romer & Soler, 1995 | U-Pb titanite | |
| | 305 ± 5 | Maurel *et al.,* 2004 | U-Pb Zircon | SIMS |
| Bassiès | 312 ± 3 | Paquette *et al.,* 1997 | U-Pb Zircon | |
| Eastern Cauterets | 301 ± 7 | Ternet *et al.,* 2004 | U-Pb Zircon | |
| Eaux-Chaudes | 301 ± 9 | Ternet *et al.,* 2004 | U-Pb Zircon | |
| Bordères | 309 ± 4 | Gleizes *et al.,* 2006 | U-Pb Zircon | SIMS |
| Aya (alkaline) | 267.1 ± 1.1 | Denèle *et al.,* 2011 | U-Pb Zircon | LA-ICPMS |
| ***MONTAGNE NOIRE*** | | | | |
| ***Migmatites*** | | | | |
| La Salvetat | 327 ± 7 | Faure *et al.,* 2010 | U-Th-Pb monazite | EPMA |
| Ourtigas | 326 ± 4 | Faure *et al.,* 2010 | U-Th-Pb monazite | EPMA |
| ***Anatectic granite*** | | | | |
| Laouzas | 333 ± 6 | Faure *et al.,* 2010 | U-Th-Pb monazite | EPMA |
| Montalet granite | 324 ± 3 | Faure *et al.* 2010 | U-Pb Zircon | SIMS |
| | 327 ± 7 | Faure *et al.* 2010 | U-Th-Pb monazite | EPMA |
| ***Late- to Post-Migmatitic granite*** | | | | |
| Anglès | 325 ± 7 | Faure *et al.,* 2010 | U-Th-Pb monazite | EPMA |
| Vialais | 320 ± 3 | Faure *et al.,* 2010 | U-Th-Pb monazite | EPMA |
| Soulié | 318 ± 4 | Faure *et al.,* 2010 | U-Th-Pb monazite | EPMA |
| ***CATALAN COASTAL RANGES*** | | | | |
| **Montseny-Guilleries Massif** | | | | |
| Susqueda diorite | 323.6 ± 2.8 | Martínez *et al.,* 2008 | U-Pb Zircon | SHRIMP-RG |
| granite | 305.9 ± 1.5 | Martínez *et al.,* 2008 | U-Pb Zircon | SHRIMP-RG |
| leucogranite | 305.3 ± 1.9 | Martínez *et al.,* 2008 | U-Pb Zircon | SHRIMP-RG |
| | 301.5 ± 1.7 | Martínez *et al.,* 2008 | U-Pb Zircon | SHRIMP-RG |
| | 299.0 ± 2.3 | Martínez *et al.,* 2008 | U-Pb Zircon | SHRIMP-RG |

Coastal Ranges) to internal and deep-seated rocks northeastwards (Fig. 8.2). By contrast, García-Sansegundo *et al.* (2011) devised a structural zonation for the Pyrenees, where the boundary between the hinterland and the foreland would correspond to E–W Variscan thrusts or Alpine reactivated Variscan thrusts. In this regard, most of the Central and Eastern Pyrenees would have hinterland affinity and would be located to the north of the foreland areas. In accordance with the presence of an anatectic zone and the timing of intrusion of granitoids, we distinguish a Northeastern zone and a Southwestern zone. The Northeastern zone is constituted by the Central–Eastern Pyrenees, the Northern part of the Catalan Coastal Ranges and Montagne Noire. This zone is characterized by the presence of migmatites and plutons emplaced in deep levels of the crust, with U–Pb zircon ages between 333–300 Ma. The Southwestern zone is formed by the Western Pyrenees and the Southern part of the Catalan Coastal Ranges. In this area, plutonic rocks are emplaced in high levels of the Variscan crust (Devonian–Carboniferous). The only U–Pb zircon dating available corresponds to the Aya pluton. This pluton is transitional between calc-alkaline and alkaline and indicates that some granitoids are younger than 300 Ma (Table 8.1).

### 8.6.4. Correlation with the autochthonous and allochthonous domains of Central and Southeastern Variscan segments of Europe

The Variscan Pyrenees represent an autochthonous domain of the southern branch of Northern Gondwana (e.g., Martínez Catalán, 1990) and can therefore be correlated with the equivalent domains that crop out in the Central and Northern parts of the Iberian Massif, the Western–Central part of the Maures Massif and South Sardinia (Fig. 8.3).

In the Central and Northern parts of the Iberian Massif, the Ibero-Armorican arc is constituted by several zones such as: the Cantabrian Zone, the Western Astur-Leonese Zone and the Central Iberian Zone. The Cantabrian Zone and the Western Astur-Leonese Zone are located in the centre of the arc and consist of the fold and thrust belt. The Central Iberian Zone occupies the external part of the arc and forms the hinterland (Fig. 8.3). Granitoids crop out in the three zones but migmatites are only found in the Central Iberian Zone. In this Zone, several anatectic episodes occurred between 352–297 Ma (Montero *et al.,* 2004; Bea *et al*., 2006; Castiñeiras *et*

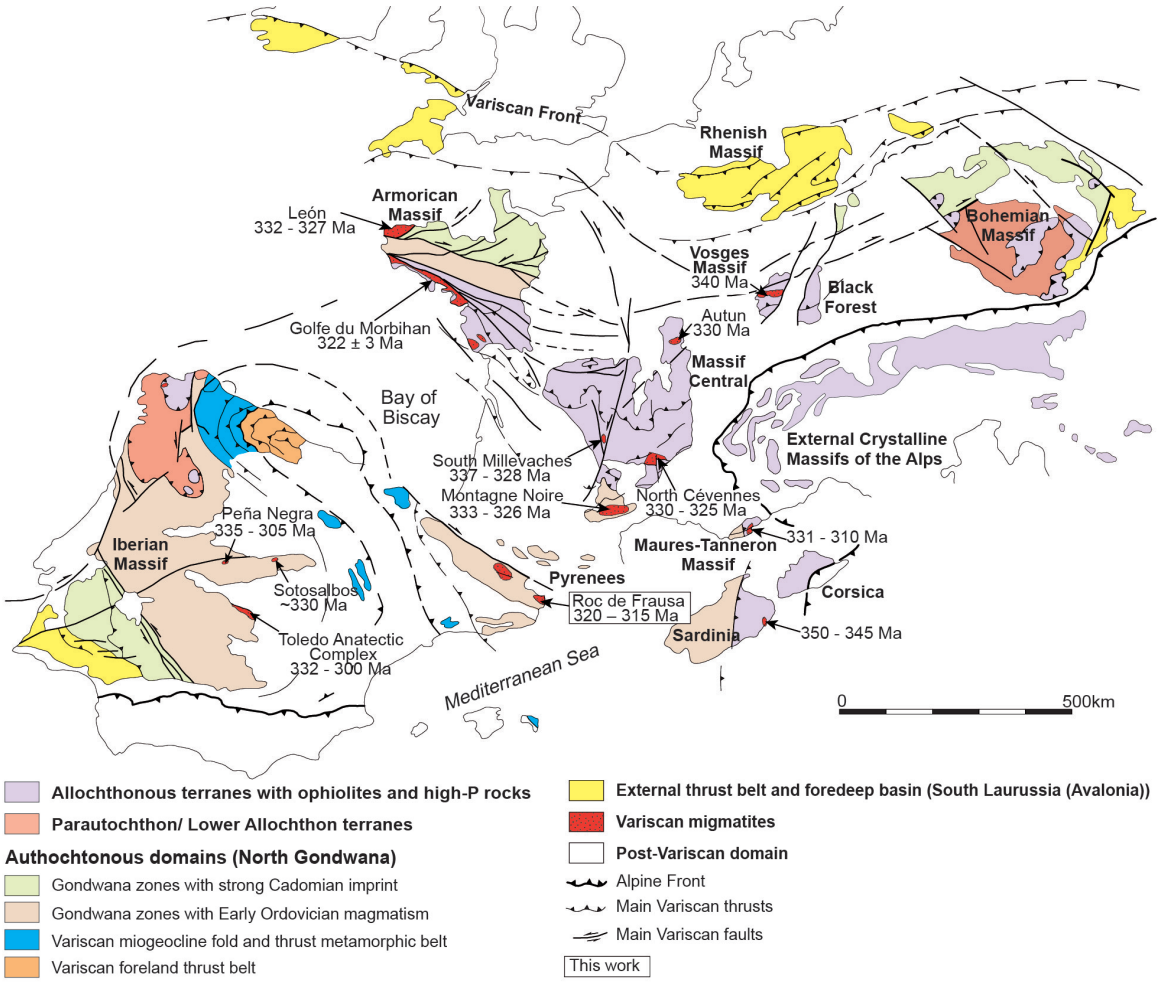



**Fig. 8.3.** Sketch of the Variscan belt, modified from Martínez Catalán (2011), showing the widespread location of the Middle Carboniferous partial melting event.

*al*., 2008b) with a maximum between 335–305 Ma. Syn-orogenic magmatism began at *c.* 350–340 Ma (Pérez-Estaún & Bea, 2004) and ended at *c.* 320–315 Ma (e.g., Fernández-Suárez *et al*., 2000). Post-orogenic magmatism took place between 310–295 Ma (Lago *et al*., 2004; Bea *et al.,* 2006; Orejana *et al.,* 2009). Post-orogenic magmatism is younger in the external zones (Cantabrian and Western Astur-Leonese) than in the Central Iberian Zone (<297 Ma, Gutiérrez-Alonso *et al*., 2011). Based on the structural evolution and the presence or absence of metamorphism, García-Sansegundo *et al*. (2011) correlated the Central–Eastern Pyrenees with the Western Astur-Leonese Zone and the Western Pyrenees with the Cantabrian Zone.

Taking into account the occurrence and ages of the migmatites, the Central Iberian Zone can be better correlated with the hinterland domains of the Central–Eastern Pyrenees and Montagne Noire. Furthermore, the time span and abundance of

granitoids in these two areas and in the Northern Catalan Coastal Ranges are comparable to those of the Central Iberian Zone. These features, together with other similarities in the stratigraphy and the structural style, point to a close relationship between the two hinterland areas, as suggested by Martínez Catalán *et al*. (2007) and Gutiérrez-Alonso *et al*. (2011). However, it is not possible to establish accurately the limit of the hinterland-foreland in the Pyrenees.

In the Southeastern Variscan belt of Europe, the autochthonous domain of the Central–Western part of the Maures Massif preserves a prograde Barrovian sequence with scattered signs of partial melting and absence of granitoids. Central–South Sardinia constitutes a non-metamorphic fold-and-thrust belt. However, the Eastern part of the Maures–Tanneron Massif and the Northern part of Sardinia have mainly migmatitic high-grade metamorphic rocks intruded by Carboniferous granitoids in the deeper crustal levels. According to some authors (Martínez Catalán, 1990; Matte, 1991, Martínez Catalán *et al.,* 2007), these domains may be regarded as more internal parts of the Variscan orogen, where the allochtonous or parautochtonous domains crop out and continue towards the west of Europe (Vosges, Black Forest, French Massif Central, Southern domain of the Armorican Massif and Galicia–Trás-os-Montes Zone). Geochronological data on these domains (Fig. 8.3) suggest that partial melting began at around 350 Ma, with a maximum between 330–320 Ma (e.g., Innocent *et al.,* 2003; Turrillot *et al.,* 2009; Faure *et al.,* 2010). Subsequently, syn- to late-kinematic granites were emplaced around 330–320 Ma (e.g., Cocherie *et al*., 2005; Bé Mézème *et al.,* 2006). Finally, post-orogenic magmatism occurred between 310–295 Ma (e.g., Demoux *et al*., 2008; Corsini & Rolland, 2009; Rolland *et al*., 2009).

To sum up, the ages discussed above indicate that the Variscan thermal event lasted longer towards the more internal zones of the orogen since it initiated c. 30 m.y. earlier than in the Eastern Pyrenees and ended around 300 Ma in both areas. Towards the foreland of the Variscan orogen, magmatic activity was younger than in the more internal zones as indicated by Johnston & Gutiérrez-Alonso (2010).

## 8.7. Geodynamic interpretation of the *P–T–t–d* evolution of the Eastern Pyrenees

The geodynamic interpretation of the Variscan basement in the Pyrenees is still controversial, as a number of models have been explained to clarify the geodynamic scenario of the last thermal episode occurred during 320–300 Ma. For this thermal episode, a model of lithosphere scale extension associated with elevated heat flux (Wickham & Oxburgh, 1986; Wickham, 1987; van den Eeckhout & Zwart, 1988; Vissers, 1992) or a late Carboniferous transpressional event (e.g., Carreras & Capellà, 1994; Gleizes *et al.,* 1998; Druguet, 2001; Román-Berdiel *et al.,* 2004) have been considered.

Extensional tectonic setting appears to be a viable mechanism to generate anomalous high geothermal gradient and high temperature metamorphism and crustal melting at different crustal levels. However, this model is not consistent with the geological features of the Variscan Pyrenees due to the prevalence of upright, isoclinal tight folds with an associated axial plane foliation developed during the D2 event (e.g., Matte & Mattauer, 1987). According to above cited authors, the two major deformation events recognized in the Variscan Pyrenees reflect a broad transpressional regime starting with a horizontal shortening phase characterized by south-verging folding and thrusting, followed by a wrench-dominated dextral transpressional phase. Notwithstanding the evidence, this model can be discarded as the late deformation event (D3) and shear zones can be attributed to Alpine orogeny as indicated zircon dating in the shear zones yielding ages from 100 Ma to 40 Ma (Maurel, 2003).

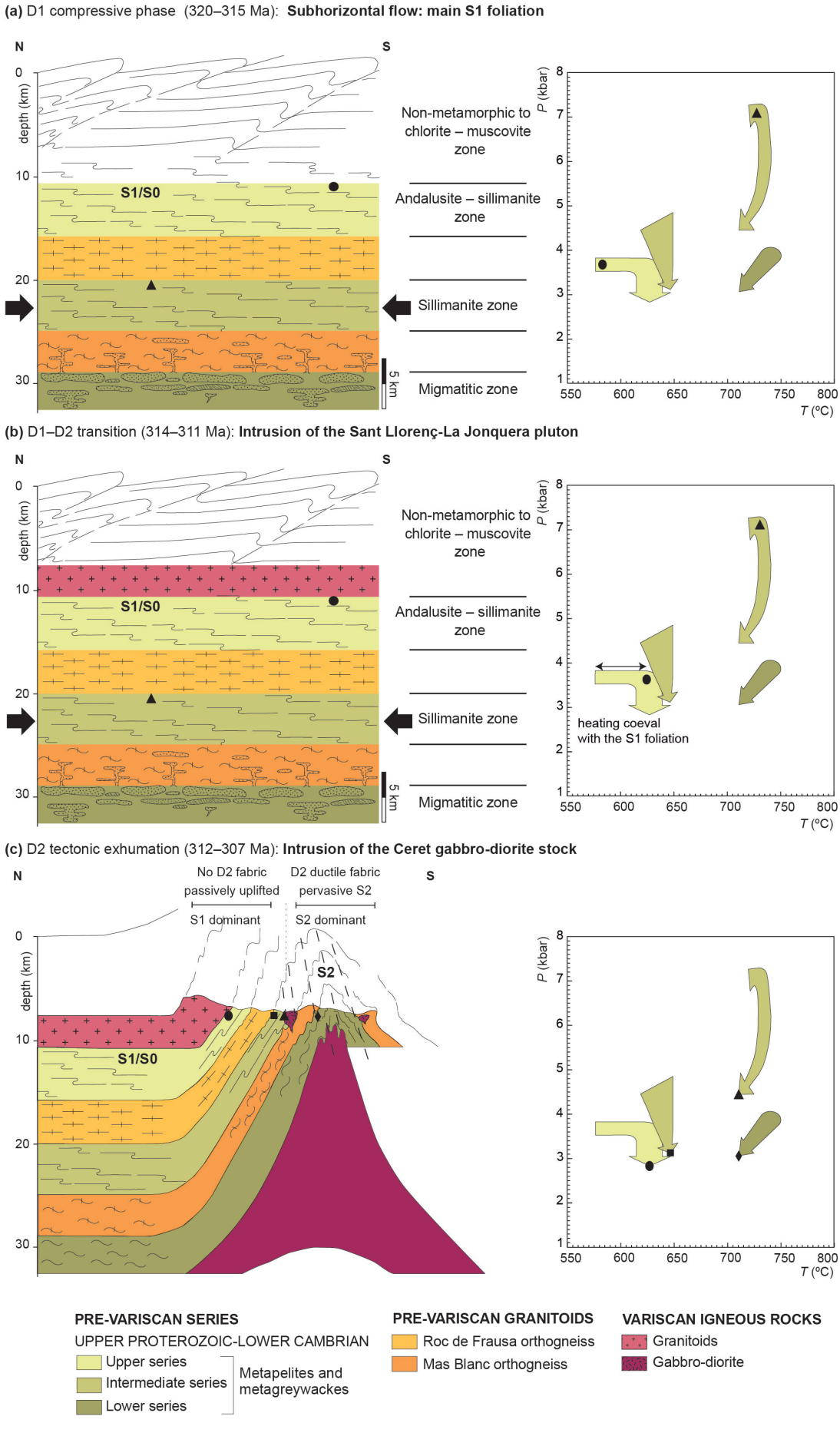
The integrated study of textures and deformation-crystallization relations combined with phase diagram modeling and geochronology allow to unravel the *P–T–t–d* evolution of a crustal section in the Eastern Pyrenees during the waning stages of the Variscan orogeny. The global sequence of events has been constructed from the record of metamorphic rocks of different crustal levels (the Upper, Intermediate and Lower series) affected by regional or contact metamorphism and from geochronological data from migmatites and igneous rocks of the Roc de Frausa

Massif. Combining these data a three-stage evolutionary model can be established for the Variscan segment of the Eastern Pyrenees (Fig. 8.4).

(1) The first stage is characterized by a collisional event associated with crustal thickening during the Serpukhovian–Bashkirian (320–315 Ma; Aguilar *et al*., in review), which results in a clockwise *P*–*T* path (Fig. 8.4a). This event is recorded by the development of the main subhorizontal S1 foliation indicating important lower crustal flow during SW directed thrusting in the upper crustal levels of the orogen (e.g., Vilà *et al.,* 2007). Maximum depth registered in the upper crustal Lower Paleozoic sequences is ~10 km thickness (e.g., Liesa 1994; Vilà *et al*., 2007) during this period (Fig. 8.4a). In contrast, the pressure increase in deeper crustal levels attained ~20 km thickness, as shown by isobaric heating or moderate pressure increase in the Upper and the Intermediate series to ~3.4 kbar and ~7 kbar, respectively. The migmatites of the Lower series were formed exclusively in the deepest crustal levels, being consistent with previous studies from Ayora *et al.* (1993) and Guitard *et al*. (1995). The petrological studies carried out by Azambre & Guitard (2001) also emphasize that the crust was only moderately thickened. High-*T* and relatively Low-*P* metamorphism related to crustal thickening may be generated only when the heat is advected within the crust (Sandiford & Powell, 1991). These authors showed that an increase of heat flow at Moho depth and consequent melting of the lower crust can happen during simultaneous removal of the mantle lithosphere during crustal thickening.

(2) The second stage is associated with the intrusion of Sant Llorenç–La Jonquera granitoids during the Bashkirian (314–311 Ma; Aguilar *et al*., in review). Melting took place deep in the continental crust (>25 km according to Sawyer *et al.,* 2011). Nevertheless, the granitoid was intruded at upper crustal levels where the transition from ductile to brittle rheology or other factors occurred and the ascent was arrested

**Fig. 8.4.** Geodynamic model for the tectonic evolution of the last stages of Variscan orogeny in the Roc de Frausa Massif and summary of *P*–*T* paths (Fig. 8.1). Idealized position of the studied samples is indicated by circles. (a) The D1 deformation event took place during the compressive phase at 320–315 Ma. (b) The Sant Llorenç–La Jonquera pluton intruded post-D1 and pre-D2 during 314–311 Ma at the upper crustal level. (c) The emplacement of Ceret gabbro-diorite stock and the D2 deformation event occur during the tectonic exhumation at 312–307 Ma.


(a) D1 compressive phase (320–315 Ma): Subhorizontal flow: main S1 foliation
N
S
depth (km)
S1/S0
Non-metamorphic to chlorite – muscovite zone
Andalusite – sillimanite zone
Sillimanite zone
Migmatitic zone
5 km
P (kbar)
T (°C)
(b) D1–D2 transition (314–311 Ma): Intrusion of the Sant Llorenç-La Jonquera pluton
heating coeval with the S1 foliation
(c) D2 tectonic exhumation (312–307 Ma): Intrusion of the Ceret gabbro-diorite stock
No D2 fabric passively uplifted
D2 ductile fabric pervasive S2
S1 dominant
S2 dominant
S2
PRE-VARISCAN SERIES
UPPER PROTEROZOIC-LOWER CAMBRIAN
Upper series
Intermediate series
Lower series
Metapelites and metagreywackes
PRE-VARISCAN GRANITOIDS
Roc de Frausa orthogneiss
Mas Blanc orthogneiss
VARISCAN IGNEOUS ROCKS
Granitoids
Gabbro-diorite

(Brown & Solar, 1999; Brown, 2007; Sawyer *et al.,* 2011). The intrusion took place after D1 or early during D2 as the granitoid sheet is preferentially emplaced approximately parallel to the main S1 foliation and is folded by the subsequent deformation event (D2), recording syntectonic pervasive melt flow through the deforming crust. The isobaric heating *P*–*T* path registered by the Upper series can be related to the intrusion and the peak conditions for these rocks were reached during the transition from D1 to D2 (Fig. 8.4b). Therefore, the abundance of broadly coeval granitoids suggests that the ascent of copious volumes of crustal-derived magmas to shallow crustal levels played a major role transferring heat (De Yoreo *et al*., 1991).

(3) The third stage is associated with isothermal decompression as indicated by the *P*–*T* path and by the intrusion of mantle derived mafic rocks during the Late Bashkirian–Moscovian (312–307 Ma; Aguilar *et al*., in review). Our interpretation is based on: (a) the clear *P* decrease shown by the *P*–*T*–*t*–*d* evolutions recorded by different rocks coupled with the intrusion of subordinate mafic rocks at mid-crustal levels and, (b) the upright folding associated with subvertical (S2) foliation in high-grade metamorphic domains. Consequently, the late HT–LP overprint is a combination of rapid decompression associated with massive and syntectonic input of mafic hot magma. Such a model, based on the tectonic exhumation of the hot lower and middle crust, can essentially be achieved by buoyancy-driven ascent in a diapiric structure (Soula *et al.,* 1986b) or by crustal-scale folding. Both mechanisms can account for a symmetrical architecture and for vertical material transfer. Thus, the obtained data are consistent with syn-convergent doming, rapid elevation of deep crustal units and their juxtaposition to shallow crustal levels. The verticalization of originally horizontal S1 fabric, its entire transposition to S2 in the core of F2 antiform and syntectonic intrusion of gabbroic magma are characteristic features of the core. The geometry of structurally higher series is consistent with passive growth of crustal dome marked by, thinning of crustal layers, decreasing amount of exhumation laterally and lateral transfer of heat from the core of dome such as was comprehensively presented by Druguet (2001) for a nearby Cap de Creus example. The degree to which the system is driven by gravity as suggested e.g., by Soula *et al*. (1986b) and Pouget (1991) and/or by lateral shortening advocated by Druguet (2001) needs to be quantified.

The general picture arisen in the Eastern Pyrenees suggests that the *P–T–t–d* evolutions is characterized by a pressure decrease of at least of 3 kbar for the deep-crustal levels, equivalent to about 11 km of exhumation during the D2 deformation event. The exhumation of migmatitic rocks was related to the ascent of large volumes of asthenospheric material, with a gradually distributed thermal metamorphic overprint with thermal peak conditions at ~730 °C. It is inferred that the emplacement of mafic intrusions at mid-crustal level was the major cause of the HT metamorphism and crustal anatexis. The occurrence of scattered mafic intrusions of limited size suggests that the thermal anomaly originated in the upper mantle and migrated towards shallower levels. In addition, strong exhumation and cooling of the high-grade rocks associated to the subvertical overprinting of the thermal structure were probably produced during the domal uplift of the previously buried and heated mountain roots.

In summary, the different crustal levels are mechanically coupled during this event and the thermal evolution of exhumed rocks is shared (Fig. 8.4). This new model of thermomechanical evolution of the Pyrenean Variscan crust suggests intimate relationships between the flux of orogenic lower crust, growth of crustal dome and associated magma flushing from the base of the crust to mid-crustal levels.

# CHAPTER 9

## CONCLUSIONS

An integrated structural, petrological and geochronological study combined with mineral equilibria modeling has been carried out in medium- to high-grade metamorphic rocks and in associated igneous rocks of the Variscan segment of the Eastern Pyrenees (Roc de Frausa Massif). From these data we can conclude that:

**(a)** Structural analysis across the entire Roc de Frausa Massif reveals two main Variscan deformation events (D1 and D2). D1 is marked by tight to isoclinal small-scale folds and the most prominent D1 structure is a sub-horizontal foliation (S1). The most conspicuous D2 structures are tight upright folds facing to the NW with steep NE–SW axial planes. The major fabric in all units is the S1 metamorphic foliation, heterogeneously reworked by a sub-vertical F2 folding. In the high-grade metamorphic rocks it constitutes an almost complete transposition of S1 foliation by a sub-vertical S2 foliation. At upper crustal levels, calc-alkaline granitoids of Sant Llorenç–La Jonquera intruded interkinematically between D1 and D2 events, whereas at deeper levels, hornblende gabbros and diorites of the mafic complexes are emplaced synchronously to the D2 event.

**(b)** Petrographic and microstructural study show that index minerals of the three metamorphic zones (andalusite zone, sillimanite and migmatite zone) define the S1 and/or the S2 foliation and that cordierite is always the last mineral to crystallize.

**(c)** The *P*–*T*–*d* paths deciphered for a set of individual samples from different crustal levels of the Roc de Frausa Massif record a clockwise orogenic evolution marked by heating followed by broadly isothermal decompression of at least ~3 kbar for the deep-crustal levels, equivalent to about 11 km of exhumation during the D2 deformation event. The decompression is reflected by the crystallization of cordierite overgrowing the steep S2 fabric in high-grade metamorphic rocks and the S1 foliation in the intermediate-grade metamorphic rocks. The exhumation of hot mid- to deep-

crustal levels was related to the ascent of large volumes of asthenospheric material, with a gradually distributed thermal metamorphic overprint with thermal peak conditions at ~730 °C. This fact suggests that the intrusion of hot igneous bodies constituted a way to transfer heat laterally from the core of the orogen at the late stages of the orogeny.

**(d)** Four types of migmatites have been recognized around the Ceret gabbro-diorite contact aureole. They can be characterized by a variety of textures, mineral associations and whole-rock compositions. They range from patch to schollen types in the inner aureole and from schollen migmatites to residuum melanosomes inside the gabbro-dioritic body as xenoliths. The meso- to microscopic structural features preserved in each migmatite type preserve different histories. Patch and schollen migmatites record a long high-temperature deformation history (D1 and D2), whereas stromatic migmatites and residuum melanosome register a shorter deformation history synchronous to the D2 event.

Three high-grade mineral assemblages characterize the different types of migmatites. Patch and schollen migmatites present biotite–sillimanite–cordierite–garnet–plagioclase–quartz±K-feldspar and stromatic migmatites and residuum melanosomes lack K-feldspar and sillimanite. The preservation of these mineral assemblages is consistent with open-system behavior for several episodes of fluid infiltration and variable proportions of melt loss. Melt loss would have occurred during the retrograde melting history concomitant with the D2 deformation event. The proposed model here provides a mechanism for producing a big amount of melt (up to 60 mol. %) along the high-*T* history of the rock, most of which would be expelled, and a reduction of the rock residuum up to 50 mol.% by infiltrating water from the crystallizing gabbro-diorite. This would be responsible for the change of composition of the migmatites to ultramafic residua. Conversely, an injection of melt is proposed to explain stromatic migmatites, as they have a whole-rock composition similar to both patch and schollen migmatites but present a restitic mineral assemblage comparable to that of residuum melanosome alternating with leucosome veins. The fluids infiltrated into the melt can be released by crystallizing gabbro-diorite intruded at mid-crustal levels and by dehydration-melting of nearby metapelites. At a greater scale this process could be responsible for the

differentiation of the crust and the migration of magmas to the upper crust. However, geochemical evidence is needed to confirm this hypothesis.

**(e)** U–Pb SHRIMP geochronological study on zircon from Variscan migmatites and Late-Variscan igneous rocks allow to clarify the thermal evolution of the area, which is recorded in three episodes:

(1) An early migmatization registered in the deepest crustal levels of the massif during the Serpukhovian–Bashkirian (320–315 Ma), and coeval with the main deformation event (D1). This thermal episode is also responsible for the intrusion of deep-seated granitoids in other Pyrenean massifs (Agly and Aston).

(2) Emplacement of the calc-alkaline Sant Llorenç–La Jonquera plutonic complex at upper crustal levels during the Late Bashkirian (314–311 Ma), interkinematic between D1 and D2 deformation events.

(3) Intrusion of the Ceret gabbro–diorite stock at middle crustal levels during the Late Bashkirian–Moscovian (312–307 Ma) synchronous with the D2 deformation event. Cathodoluminescence, transmitted light microscope and trace element chemistry of zircon show two magmatic pulses separated by a time span of *c.* 5 m.y. Migmatites were formed in the Ceret gabbro contact aureole but the absence of Variscan rims around inherited zircon prevented us from independently date the episodes.

**(f)** Space-time correlation of the Variscan segment of the Pyrenees with neighboring areas (the Catalan Coastal Ranges and Montagne Noire) of the authoctonous domains of the Northern Gondwana margin allow us to draw a NW–SE trending zonation model. Internal and deep-seated zones located towards the north-northeast would have a longer thermal history (330–300 Ma). External shallow-seated zones located towards the west–southwest would have a shorter thermal history (310–300 Ma).

Comparison of this zonation with that of Western Iberia suggests that the Central–Eastern Pyrenees, the Northern Catalan Coastal Ranges and the Montagne Noire can be correlated with the Central Iberian Zone, whereas the western–southwestern areas of the Pyrenees and the Catalan Coastal Ranges correspond to the Western Astur-Leonese Zone.

**(e)** Combining the data from the record of metamorphic rocks of different crustal levels affected by regional or contact metamorphism and from geochronological data for migmatites and igneous rocks of the Roc de Frausa Massif, a three-stage evolutionary model can be established for the Variscan segment of the Eastern Pyrenees:

(1) A moderate crustal thickening of exceptionally hot crust is probably related to an early migmatization of the deepest crustal levels during the main deformation D1 event on the Serpukhovian–Bashkirian (320–315 Ma).

(2) The interkinematic emplacement of calc-alkaline granitoids at upper crustal levels took place during the Late Bashkirian (314–311 Ma); and

(3) The tectonic exhumation of the hot lower and middle crust was coeval with the intrusion of mafic rocks at middle crustal levels and with the second deformation event (D2) that occurred during the Late Bashkirian–Moscovian (312–307 Ma).

# REFERENCES


Aguilar, C., Liesa, M., Castiñeiras, P. & Navidad, M. in review. Late-Variscan metamorphic and magmatic evolution in the eastern Pyrenees revealed by U–Pb age zircon dating. *Journal of the Geological Society, London.*

Anders, E. & Grevesse, N. 1989. Abundances of the elements: meteoritic and solar. *Geochimica et Cosmochimica Acta,* **53**, 197–204.

Arzi, A. A. 1978. Critical phenomena in the rheology of partially melted rocks. *Tectonophysics*, **44**, 173–184.

Ashworth, J. R. & McLellan, E. L. 1985. *Textures*. In: Ashworth, J. R. (ed.) *Migmatites*, Blackie, Glasgow, 180–204 pp.

Autran, A. & Guitard, G. 1969. Mise en évidence de nappes hercyniennes de style penninique dans la série métamorphique du massif du Roc de France (Pyrénées orientales): Liaison avec la nappe du Canigou. *Comptes Rendus de l'Académie des Sciences*, Paris, **269**, 2479–2499.

Autran, A., Fonteilles, M. & Guitard, G. 1970. Relations entre les intrusions de granitoïdes, l'anatexie et le metamorphisme regional considérés principalement du point de veu du rôle de l'eau: cas de la chaîne hercynienne des Pyrénées orientales. *Bulletin Societe Geologique de France,* **12**, 673–731.

Ayora, C., Liesa, M. & Delgado, J. 1993. Low-thermal-gradient Hercynian metamorphism in the eastern Pyrenees. *Journal Metamorphic Geology*, **11**, 49–58.

Azambre, B. & Guitard, G. 2001. Disthène et staurotide reliques dans les métapelites du Canigou (Pyrénées orientales). Relations avec les épisodes hercyniens de basse et moyenne pressions. *Comptes Rendus Académie des Sciences,* Paris, **333**, 601–609.

Barnolas, A. & Chiron, J. C. 1996. Synthèse gèologique et géophysique des Pyrénées. Vol. 1: Introduction. Géophysique. Cycle Hercynien. Bulletin de la Société Géologique de France and Instituto Geológico y Minero de España, Orléans and Madrid, 729 pp.

Barth, A. P. & Wooden, J. L. 2010. Coupled elemental and isotopic analyses of polygenetic zircons from granitic rocks by ion microprobe, with implications for

melt evolution and the sources of granitic magmas. *Chemical Geology,* **277**, 149–159.

Bé Mézème E., Cocherie, A., Faure, M., Legendre, O. & Rossi, Ph. 2006. Electron microprobe monazite geochronology of magmatic events: Examples from Variscan migmatites and granitoids, Massif Central, France. *Lithos*, **87**, 276–288.

Bea, F., Montero, P., Gonzalez-Lodeiro, F., Talavera, C., Molina, J. F., Scarrow, J., Whitehouse, M. J. & Zinger, T. 2006. Zircon thermometry and U-Pb ion-microprobe dating of the gabbros and associated migmatites of the Variscan Toledo anatectic complex, Central Iberia. *Journal of Geological Society of London,* **163**, 847–855.

Bell, T. H. & Rubenach, M. J. 1983. Sequential porphyroblast growth and crenulation cleavage development during progressive deformation. *Tectonophysics,* **92**, 171-194.

Bell, T. H. & Welch, P. W. 2002. Prolonged Acadian orogenesis: revelations from foliation intersection axis (FIA) controlled monazite dating of foliations in porphyroblasts and matrix. *American Journal of Science*, **302**, 549–581.

Belousova, E. A., Griffin, W. L. & Pearson, N. J. 1998. Trace element composition and cathodoluminescence properties of sourthern Africa Kimberlitic zircons. *Mineralogical Magazine,* **62**, 355–336.

Black, L. P., Kamo, S. L., Allen, C. M., Davis, D. W., Aleinikoff, J. N., Valley, J. W., Mundil, R. M., Campbell, I. H., Korsch, R. J., Williams, I. S. & Foudoulis, C. 2004. Improved 206Pb/238U microprobe geochronology by the monitoring of a trace-element-related matrix effect, SHRIMP, ID-TIMS, ELA-ICP-MS and oxygen isotope documentation for a series of zircon standards. *Chemical Geology*, **205,** 115–140.

Bouchez, J. L. & Gleizes, G. 1995. Two-stage deformation of the Mont Louis-Andorra granite pluton (Variscan Pyrenees) inferred from magnetic susceptibility anisotropy. *Journal of the Geological Society of London,* **152**, 669–679.

Brown, M. 1994. The generation, segregation, ascent and emplacement of granite magma: the migmatite-to-crustally-derived granite connection in thickened orogens. *Earth Science Reviews*, **36**, 83–130.

Brown, M. & Solar, G. S. 1999. The mechanism of ascent and emplacement of granite magma during transpression: a syntectonic granite paradigm. *Tectonophysics*, **312**, 1–33

Brown, M. 2002. Retrograde processes in migmatites and granulites revisited. *Journal of Metamorphic Geology,* **20**, 25–40.

Brown, M. 2007. Crustal melting and melt extraction, ascent and emplacement in orogens: Mechanisms and consequences. *Journal of the Geological Society of London*, **164**, 709–730

Carreras, J. & Capellà, I. 1994. Tectonic levels in the Paleozoic basement of the Pyrenees: a review and a new interpretation. *Journal of Structural Geology*, **16**, 1509–1524.

Carreras, J. & Debat, P. (coords.) 1996. La Tectonique Hercynienne. In: Barnolas, A. & Chiron, J. C. (eds) *Synthèse gèologique et géophysique des Pyrénées. Vol. 1: Introduction. Géophysique. Cycle Hercynien*. Bulletin de la Société Géologique de France and Instituto Tecnológico Geominero de España, Orléans and Madrid, pp. 585–677.

Casas, J. M. & Torrades, P. 2008. Structure of the Els Banys d'Arles mesozoic trough. *Geogaceta*.

Castiñeiras, P., Navidad, M., Liesa, M., Carreras, J. & Casas, J. M. 2008a. U–Pb zircon ages (SHRIMP) for Cadomian and Early Ordovician magmatism in the eastern Pyrenees: New insights into the pre-Variscan evolution of the northern Gondwana margin. *Tectonophysics,* **461**, 228–239.

Castiñeiras, P., Villaseca, C., Barbero, L. & Martín Romera, C. 2008b. SHRIMP U–Pb zircon dating of anatexis in high-grade migmatite complexes of central Spain: implications in the Hercynian evolution of central Iberia. *International Journal of Earth Sciences,* **97**, 35–50.

Castiñeiras, P., Díaz García, F. & Gómez Barreiro, J. 2010. REE-assisted U–Pb zircon age (SHRIMP) of an anatectic granodiorite: constraints on the evolution of the A Silva granodiorite, Iberian allochthonous complexes. *Lithos*, **116**, 153–166.

Charlier, B. L. A., Wilson, C. J. N., Lowenstern, J. B., Blake, S., van Calsteren, P. W. C. & Davidson, J. P. 2005. Magma generation at a large, hyperactive silicic volcano (Taupo, New Zealand) revealed by U-Th and U–Pb systematics in zircons. *Journal of Petrology*, **46**, 3–32.

Cherniak, D. J., Watson, E. B., Grove, M. & Harrison, T. M. 2004. Pb diffusion in monazite: a combined RBS/SIMS study. *Geochimica et Cosmochimica Acta*, **68**, 829–840.

Claiborne, L. L., Miller, C. F., Walker, B. A., Wooden, J. L., Mazdab, F. K. & Bea, F. 2006. Tracking magmatic processes through Zr/Hf ratios in rocks and Hf and Ti zoning in zircon: an example from the Spirit Mountain batholith, Nevada. *Mineralogical Magazine,* **70**, 517–543.

Cocherie, A. 1984. Interaction manteau-croûte: son role dans la génèse d'associations plutoniques calco-alcalines, contraintes géochimiques (élements en traces et isotopes du strontium et de l'oxygène). PhD thesis. Universitè de Rennes.

Cocherie, A., Be Mezeme, E., Legendre, O., Fanning, C. M., Faure, M. & Rossi, Ph. 2005. Electron-micropobe dating as a tool for determining the closure of Th-U-Pb systems in migmatitic monazites. *American Mineralogist*, **90**, 607–618.

Collins, W. J., Flood, R. H., Vernon, R. H. & Shaw, S. E. 1989. The Wuluma granite, Arunta Block, central Australia: an example of in situ, near-isochemical granite formation in a granulite-facies terrane. *Lithos*, **23**, 63–83.

Coggon, R. & Holland, T. J. B. 2002. Mixing properties of phengitic micas and revised garnet-phengite thermobarometers. *Journal of Metamorphic Geology*, **20**, 683–696

Corfu, F., Hanchar, J. M., Hoskin, P. W. O. & Kinny, P. 2003. Atlas of zircon textures. In: Hanchar, J. M. & Hoskin, P. W. O. (eds) *Zircon*. Reviews in Mineralogy and Geochemistry, 53. Mineralogical Society of America, Washington, pp. 468–500.

Corsini, M. & Rolland, Y. 2009. Late evolution of the southern European Variscan Belt: exhumation of the lower crust in a context of oblique convergence. *Comptes Rendus Geosciences*, **341**, 241–223.

De Yoreo, J. J., Lux, D. R. & Guidotti, C. V. 1991. Thermal modelling in low-pressure/high-temperature metamorphic belt. *Tectonophysic,* **188**, 209–238.

Debon, F., Enrique, P. & Autran, A. 1995. Magmatisme Hercynian. In: Barnolas, A. & Chiron, J. C. (eds) *Synthèse gèologique et géophysique des Pyrénées. Vol. 1: Introduction. Géophysique. Cycle Hercynien*. Bulletin de la Société Géologique de France and Instituto Geológico y Minero de España, Orléans and Madrid, pp. 303–359.

Delaperrière, E., de Saint-Blanquat, M., Brunel, M. & Lancelot, J. 1994. Géochronologie U–Pb sur zircons et monazites dans le massif du Saint Barthelemy (Pyrénées, France): discussion des ages des événements variues et pré-varisques. *Bulletin de la Société géologique de France*, **165**, 101–112.

Delvolvé, J. J. (coord.) 1996. Carbonifère à faciès Culm. In: Barnolas, A. & Chiron, J. C. (eds) *Synthèse gèologique et géophysique des Pyrénées. Vol. 1: Introduction. Géophysique. Cycle Hercynien*. Bulletin de la Société Géologique de France and Instituto Geológico y Minero de España, Orléans and Madrid, pp. 303–359.

Demoux, A., Schärer U. & Corsini, M. 2008. Variscan evolution of the Tanneron massif, SE France, examined through U-Pb monazite ages. *Journal of the Geological Society of London*, **165**, 467–478.

Denèle, Y., Olivier, P., Gleizes, G. & Barbey, P. 2007. The Hospitalet gneiss dome (Pyrénées) revisited: lateral flow during Variscan transpression in the middle crust. *Terra Nova*, **19**, 445–453.

Denèle, Y., Olivier. Ph., Gleizes, G. & Barbey, P. 2009. Decoupling between the middle and upper crust during transpression-related lateral flow: Variscan evolution of the Aston gneiss dome (Pyrenees, France). *Tectonophysics*, **477**, 244–261.

Denèle, Y., Paquette, J. L., Olivier, Ph. & Barbey, P. 2011. Permian granites in the Pyrenees: the Aya pluton (Basque Country). *Terra Nova*, **0**, 1–9.

Druguet, E. & Hutton, D. H. W. 1998. Syntectonic anatexis and magmatism in a mid-crustal transpressional shear zone: an example from the Hercynian rocks of the Eastern Pyrenees. *Journal of Structural Geology*, **20**, 905–916.

Druguet, E. 2001. Development of high thermal gradients by coeval transpression and magmatism during the Variscan orogen: insights from the Cap the Creus (eastern Pyrenees). *Tectonophysics*, **332**, 275–293.

van den Eeckhout, B. 1986. A case study of a mantled gneiss antiform, the Hospitalet Massif, Pyrenees (Andorra, France). *Geol. Ultraiectina*, **45**, 196 pp.

van den Eeckhout, B. & Zwart, H. J. 1988. Variscan crustal-scale extensional shear zone in the Pyrenees. *Geology*, **16**, 135–138.

Estévez, A. 1973. La vertiente meridional del Pirineo Catalán al N del curso medio del Río Fluviá. Tesis Doctoral Universidad de Granada. Publ. Univ. Granada. 514 pp.

Faure, M., Cocherie, A., Bé Mézème, E., Charles, N. & Rossi, P. 2010. Middle Carboniferous crustal melting in the Variscan Belt: New insights from U-Th-Pbtot. monazite and U–Pb zircon ages of the Montagne Noire Axial Zone (southern French Massif Central). *Gondwana Research,* **18**, 653–673.

Fernández-Suárez, J., Gutiérrez-Alonso, G., Jenner, G. A. & Tubrett, M. N. 2000. New ideas on the Proterozoic–Early Palaeozoic evolution of NW Iberia: insights from U–Pb detrital zircon ages. *Precambrian Res*., **102**, 185–206.

Fontboté, J. M., Muñoz, J. A. & Santanach, P. 1986. On the consistency of proposed models for the Pyrenees with the structure of the eastern parts of the belt. *Tectonophysics,* **129**, 291–301.

Fraser, G., Ellis, D. & Eggins, S. 1997. Zirconium abundance in granulite-facies minerals, with implications for zircon geochronology in high-grade rocks. *Geology*, **25**, 607–610.

Gagnevin, D., Daly, J. S. & Kronz, A. 2010. Zircon texture and chemical composition as a guide to magmatic processes and mixing in a granitic environment and coeval volcanic system. *Contributions to Mineralogy and Petrology,* **159**, 579–596.

García-Sansegundo, J., Poblet, J., Alonso J. L. & Clariana, P. 2011. Hinterland-foreland zonation of the Variscan orogen in the central Pyrenees: comparison with the northern part of the Iberian Variscan Massif. *The Geological Society of London*, Special Publications, **349**, 169–184.

Geyssant, J., Grandjacquet, C. & Guitard, G. 1978. La terminaison de la nappe de gneiss dy Canigou au nord-est du massif du Roc de France (Pyrénées orientales) et ses replisements tardifs. *Comptes Rendus Academie Sciences de Paris*, **287**, 1187–1190.

Gibson, R. L. 1991. Hercynian low-pressure–high-temperature regional metamorphism and subhorizontal foliation development in the Canigou massif, Pyrenees, France. Evidence for crustal extension. *Geology*, **19**, 380–383.

Gibson, R. L. & Bickle, M. J. 1994. Thermobarometric constraints on the conditions of metamorphism in the Canigou massif, Pyrenees: implications for Hercynian geothermal gradients. *Journal of the Geological Society of London*, **151**, 987–997.

Gleizes, G., Leblanc, G. & Bouchez, J. L. 1998. The main phase of the Variscan orogeny in the Pyrenees is a dextral transpression. In: Holdsworth, R. E., Strachan, R. A. & Dewey, J. F. (eds) *Continental Transpressional and Transtensional Tectonic*. Geological Society of London, Special Publication, **135**, pp. 267–273.

Gleizes, G., Crevon, G., Asrat, A. & Barbey, P. 2006. Structure, age and mode of emplacement of the Hercynian Bordères-Louron pluton (central Pyrenees, Frances). *International Journal of Earth Sciences*, **95**, 1039–1052.

Guitard, G. 1970. Le métamorphisme hernynien mesozonal et les gneiss oeillés du massif du Canigou (Pyrénées Orientales). PhD Thesis. Mem. B.R.G.M., **63**, 317 pp.

Guitard, G., Vielzeuf, D. & Martínez, F. 1995. Métamorphisme Hercynian. In: Barnolas, A. & Chiron, J. C. (eds) *Synthèse gèologique et géophysique des Pyrénées. Vol. 1: Introduction. Géophysique. Cycle Hercynien.* Bulletin de la Société Géologique de France and Instituto Geológico y Minero de España, Orléans and Madrid, pp. 303–359.

Gutiérrez-Alonso, G., Fernández-Suárez, J., Jeffries, T. E., Johnston, S. T., Pastor-Galán, D., Murphy, J. B., Franco, M. P. & Gonzalo, J. C. 2011. Diachronous post-orogenic magmatism within a developing orocline in Iberia, European Variscides. *Tectonophysic*, **30**, 1-17.

Harrison, T. M., Catlos, E. J. & Montel, J. M. 2002. U–Th–Pb dating of phosphate minerals. *Reviews in Mineralogy and Geochemistry*, **48**, 523–558.

Hasalová, P., Stípska, P., Powell, R., Schulmann, K., Janousek, V. & Lexa, O. 2008. Transforming mylonitic metagranite by open-system interactions during melt flow. *Journal of Metamorphic Geology*, **26**, 55–80.

Holdaway, M. J. & Lee, S. M. 1977. Fe+Mg cordierite stability in high grade pelitic rocks based on experimental, theoretical and natural observations. *Contributions to Mineralogy and Petrology*, **63**, 175–198.

Holland, T. J. B. & Powell, R. 1998. An internally-consistent thermodynamic data set for phases of petrologic interest. *Journal of Metamorphic Geology*, **16**, 309-343.

Holland, T. J. B. & Powell, R. 2001. Calculations of phases relations involving haplogranitic melt using an internally consistent thermodynamic dataset. *Journal of Petrology*, **42**, 673–683.

Holland, T. J. B. & Powell, R. 2003. Activity-composition relations for phases in petrological calculations: an asymmetric multicomponent formulation. *Contributions to Mineralogy and Petrology*, **145**, 492-501.

Hoskin, P. W. O. & Schaltegger, U. 2003. The composition of zircon and igneous and metamorphic petrogenesis. In: Hachar, J. M. & Hoskin, P. W. O. (eds) *Zircon*. Reviews in Mineralogy and Geochemistry, **53**. Mineralogical Society of America, Washington, pp. 27–62.

Innocent, C., Michard, A., Guerrot, C. & Hamelin, B. 2003. U–Pb zircon age of 548 Ma for the leptynites (high-grade felsic rocks) of the central part of the Maures massif. Geodynamic significance of the so-called leptyno-amphibolitic complexes of the Variscan belt of Europe. *Bulletin de la Société géologique de France*, **174**, 585–594.

Ireland, T. R. & Williams, I. S. 2003. Considerations in zircon geochronology by SIMS. In: Hanchar, J. M. & Hoskin, P. W. O. (eds) *Zircon*. Reviews in Mineralogy and Geochemistry, **53**. Mineralogical Society of America, Washington, pp. 215–241.

Johnson, T. E., White, R. & Powell, R. 2008. Partial melting of metagreywacke: a calculated mineral equilibria study. *Journal of Metamorphic Geology,* **26**, 837–853.

Johnston, S. T. & Gutiérrez-Alonso, G. 2010. The North Amercian Cordillera and West European Variscides: contrating interpretations of similar mountain systems. *Gondwana Research*, **17**, 516–525.

Julivert, M., Fonboté J. M., Ribeiro, A. & Conde, L. N. 1972. Mapa Tectónico de la Península Ibérica y Baleares. *Instituto Geológico y Minero de España*, scale 1:1,000,000.

Kempe, U., Gruner, T., Nasdala, L. & Wolf, D. 2000. Relevance of cathodoluminescence for the interpretation of U–Pb zircon ages, with an example of an application to a study of zircons from the Saxonian Granulite Complex, Germany. In: Pagel, M., Barbin, V., Blanc, P. & Ohnenstetter, D. (eds) *Cathodoluminescence* in Geosciences. Springer, Berlin, 425–455.

Korotev, R. L. 1996. A self-consistent compilation of elemental concentration data for 93 geochemical reference samples. *Geostandards Newsletter*, **20**, 217–245.

Kriegsman, L. M., Aerden, D. G. A. M., Bakker, R. J., den Brok, S. W. J. & Schutjens, P. M. T. M. 1989. Variscan tectonometamorphic evolution of the eastern Lys-Caillaouas massif, Central Pyrenees – evidence for late orogenic extension prior to peak metamorhism. *Geologie en Mijnbouw*, **68**, 323–333.

Kriegsman, L. M. 1989. Deformation and metamorphism in the Trois Seigneurs massif, Pyrenees – evidence against a rift setting for its Variscan. *Geologie en Mijnbouw*, **68**, 323–333.

Lago, M., Arranz, E., Pocovi, A., Gale, C. & Gil-Imaz, A. 2004. Permian magmatism and basin dynamics in the southern Pyrenees: A record of the transition from late Variscan transection to early Alpine extension, in Permo-Carboniferous Magmatism and Rifting in Europe. Ed. by M. Wilson *et al*., *Geological Society,* Special Publications*,* **223**, 439–464.

Liesa, M. & Carreras, J. 1989. On the structure and metamorphism of the Roc de Frausa Massif (eastern Pyrenees). *Geodinamica Acta*, **3**, 149–161.

Liesa, M. 1994. Relations of Hercynian metamorphism with magmatism and deformation in the Eastern Pyrenees. Implications for Hercynian evolution. *Geologie en Mijnbouw,* **72**, 295–304.

Ludwig, K. R. 2002. SQUID 1.02, a user's manual. *Berkeley Geochronology Center,* Special Publications, **2**, 17.

Ludwig, K. R. 2003. ISOPLOT/Ex, version 3, a geochronological toolkit for Microsoft Excel. *Berkeley Geochronology Center*, Special Publications, **4**, 71.

Mahar, E. M., Baker, J. M., Powell, R. Holland, T. J. B. & Howell, N. 1997. The effect of Mn on mineral stability in metapelites. *Journal of Metamorphic Geology*, **15**, 223–238.

Martínez, F. J., Reche, J. & Iriondo, A. 2008. U–Pb Shrimp-RG zircon ages of Variscan igneous rocks from the Guilleries Massif (NE Iberia pre-Mesozoic basament). Geological implications. *Comptes Rendus Geosciences*, **340**, 223–232.

Martínez Catalán, J. R. 1990. A non-cylindrical model for the northwest Iberian allochthonous terranes and their equivalents in the Hercynian belt of western Europe. *Tectonophysics*, **179**, 253–272.

Martínez Catalán, J. R., Arenas, R., Díaz García, F., González Cuadra, P., Gómez-Barreriro, J., Abati, J., Castiñeiras, P., Fernández-Suárez, J., Sánchez Martínez, S., Andonaegui, P., González Clavijo, E., Díez Montes, A., Rubio Pascual, F. J. & Valle Aguado, B. 2007. Space and time in the tectonic evolution of the northwestern Iberian Massif: Implications for the Variscan belt. *The Geological Society of Ameriaca,* **200**, 403–423.

Martínez Catalán, J. R. 2011. Are the oroclines of the Variscan belt related to late Variscan strike-slip tectonics?. *Terra Nova*, **23**. 241–247.

Matte, Ph., 1986. Tectonics and plate tectonics model for the Variscan Belt of Europe. *Tectonophysics*, **126**, 329-374.

Matte, Ph. & Mattauer, M. 1987. Hercynian orogeny in the Pyrenees was not a rifting event. *Nature*, **325**, 739 – 740.

Matte, Ph. 1991. Acretionary history and crustal evolution of the Variscan Belt in Western Europe. *Tectonophysics*, **196**, 309–337.

Matte, Ph. 2001. The Variscan collage and orogeny (480–290 Ma) and the tectonic definition of the Armorica microplate: a review. *Terra Nova*, **13**, 122–128.

Maurel, O. 2003. L'exhumation de la Zone Axiale des Pyrénées orientales: une approche thermo-chronologique multi-méthodes du rôle des failles. Ph.D. thesis, Université de Montpellier. 263 pp.

Maurel, O., Respaut, J. P., Monié, P., Arnaud, N. & Brunel, M. 2004. U–Pb emplacement and $Ar^{40}/Ar^{39}$ cooling ages of the eastern Mont-Louis granite massif (eastern Pyrenees, France). *Comptes Rendus Geosciences*, **336**, 1091–1098.

Mezger, J. E., Passchier, C. W. & Régnier, J. L. 2004. Metastable staurolite–cordierite assemblage of the Bossòst dome: Late Variscan decompression and polyphase metamorphism in the Axial Zone of the Central Pyrenees. *Comptes Rendus Academie Sciences de Paris*, **336**, 827–837.

Miyashiro, A. 1973. Metamorphism and Metamorphic Belts. Eds: George Allen & Unwin Ltd, London. 492 pp.

Montero, P., Bea, F., Zinger, T. F., Scarrow, J. H., Molina, J. F. & Whitehouse, M. 2004. 55 million years of continuous anatexis in Central Iberia: single-zircon dating of the Peña Negra complex. *Journal of Geological Society of London*, **161**, 255–263.

Olivier, Ph., Gleizes, G. & Paquette, J. L. 2004. Gneiss domes and granite emplacement in an obliquely convergent regime: New interpretation of the Variscan Agly Massif (eastern Pyrenees, France). *Geological Society of America*, Special Paper, **380**, 229–242.

Olivier, Ph., Gleizes, G., Paquette, J. L. & Muñoz-Sáez, C. 2008. Structure and U–Pb dating of the Saint-Arnac pluton and the Ansignan charnockite (Agly Massif): a cross-section from the upper to the middle crust of the Variscan eastern Pyrenees. *Journal of the Geological Society of London*, **165**, 141–152.

Orejana, D., Villaseca, C., Perez-Soba, C., López-García, J. A. & Billstrom, K. 2009. The Variscan gabbros from the Spanish Central System: A case for crustal recycling in the sub-continental lithosperic mantle?. *Lithos*, **110**, 262–276.

Overstreet, W. C. 1967. The geological occurrence of monazite. US Geological Survey Professional Paper 530.

Paquette, J. L., Gleizes, G., Leblanc, D. & Bouchez, J. L. 1997. Le granite de Bassiès (Pyrénées): un pluton syntectonique d'âge Westphalien. Géochronologie U–Pb sur zircons. *Comptes Rendus de l'Académie des Sciences,* **324**, 387–392.

Parrish, R. R. 1990. U–Pb dating of monazite and its application to geological problems. *Canadian Journal of Earth Sciences,* **27**, 1431–1450.

Passchier, C. W. & Trouw, R. A. J. 1996. *Microtectonics*. Springer-Verlag, 289 pp.

Pérez-Estaún, A. & Bea, F. 2004. Macizo Ibérico. In: Vera, J.A. (ed.) *Geología de España.* SGE-IGME, Madrid, 19–230.

Postaire, B. 1984. Systématique Pb commun et U–Pb sur zircons: Applications aux roches de haut grade métamorphique impliquées dans la chaîne hercynienne (Europe de l'ouest) et aux granulites de Laponie (Finlande). *Mémoires de la Société Géologique et Minéralogique de Bretagne,* **15**, 29–72.

Pouget, P. 1991. Hercynian tectonometamorphic evolution of the Bosost dome (French-Spanish central Pyrenees). *Journal of the Geological Society of London,* **148**, 299–314.

Powell, R. & Downes, J. 1990. Garnet porphyroblast-bearing leucosomes in metapelites: mechanisms and an example from Broken Hill, Australia. In: Ashworth, J. R. & Brown, M. (eds.) *High Temperature Metamorphism and Crustal Anatexis,* Unwin-Hyman, London, 105–123 pp.

Powell, R., Holland, T. J. B. & Worley, B. 1998. Calculating phase diagrams involving solid solutions via non-linear equations, with examples using THERMOCALC. *Journal of Metamorphic Geology*, **16**, 577–588.

Powell, R. & Holland, T. J. B. 2008. On thermobarometry. *Journal of Metamorphic Geology*, **26**, 155–179.

Respaut, J. P. & Lancelot, J. R. 1983. Datation de la mise en place synmétamorphe de la charnockite d'Ansignan (massif de l'Agly) par la méthode U/Pb sur zircons et monazites. *Neues Jahrbuch für Mineralogie*, **147**, 21–34

Riesco, M., Stüwe, K., Reche, J. & Martinez, F. J. 2004. Silica depleted melting of pelites. Petrogenetic grid and application to the Susqueda aureole, Spain. *Journal of Metamorphic Geology*, **22**, 475–494.

Roberts, M. P., Pin, C., Clemens, J. D. & Paquette, J. L. 2000. Petrogenesis of mafic to felsic plutonic rock associations: the calc-alkaline Quérigut complex, French Pyrenees. *Journal of Petrology,* **41**, 809–844.

Rolland, Y., Corsini, M. & Demoux, A. 2009. Metamorphic and structural evolution of the Maures-Tanneron massif (SE Variscan chain): evidence of doming along a transpressional margin. *Bulletin de la Société Géologique de France,* **180**, 17–230.

Román-Berdiel, T., Casas, A. M., Olivia-Urcia, B., Pueyo, E. L. & Rillo, C. 2004. The main Variscan deformation event in the Pyrenees: new data from the structural study of the Bielsa granite. *Journal of Structural Geology*, **26**, 659–677.

Romer, R. L. & Soler, A. 1995. U–Pb age and lead isotopic characterization of Au-bearing skarn related to the Andorra granite (central Pyrenees, Spain). *Mineralium Deposita*, **30**, 374–383.

Rubatto, D. 2002. Zircon trace element geochemistry: partitioning with garnet and the link between U–Pb ages and metamorphism. *Chemical Geology*, **184**, 123–138.

de Saint Blanquat, M., Lardeaux, J. M. & Brunel, M. 1990. Petrological arguments for high-temperature extensional deformation in the Pyrenean Variscan crust (St. Barthélémy massif, Ariège, France). *Tectonophysics*, **177**, 245–262.

Sambridge, M. S. & Compston, W. 1994. Mixture modeling of multi-component data sets with application to ion-probe zircon ages. *Earth and Planetary Science Letters*, **128**, 373–390.

Sandiford, M. & Powell, R., 1991. Some remarks on high-temperature–low-pressure metamorphism in convergent orogens. *Journal of Metamorphic Geology*, **9**, 333–340.

Sawyer, E. W., Dombrowski, C. & Collins, W. J. 1999. Movement of melt during synchronous regional deformation and granulites-facies anatexis, an example from the Wuluma Hills, central Australia. In: Castro, A. Fernández, C. & Vigneresse, J. L. (eds) *Understanding Granites: Intergrating New and Classical Techniques*, Geological Society, Special publication, **168**, 221–237.

Sawyer, E. W. 2008. Atlas of Migmatites. The Canadian Mineralogist, Special publication 9. NRC Research Press, Ottawa, Ontario, Canada. 371 pp.

Sawyer, E. W., Cesaere, B. & Brown, M. 2011. When the Continental Crust Melts. *Elements*, **7**, 229–234.

Smith, H. A. & Giletti, B. J. 1997. Lead diffusion in monazite. *Geochimica et Cosmochimica Acta*, **61**, 1074–1055.

Soula, J. C., Debat, P., Deramond, J., Gucherreau, J. Y., Lamouroux, Ch., Pouget, P. & Roux, L. 1986a. Evolution structurale des ensembles métamorphiques des gneiss et des granitoïdes dans les Pyrénées centrales. *Bulletin de la Société Géologique de France,* **8**, 79–93.

Soula, J. C., Debat, J., Deramond, J. & Pouget, O. 1986b. A dynamic model of the structural evolution of the Variscan Pyrenees. *Tectonophysics*, **129**, 29–51

Spear, F. S. & Pyle, J. M. 2002. Apatite, monazite and xenotime in metamorphic rocks. *Reviews in Mineralogy and Geochemistry*, **48**, 293–335.

Spry, A. 1969. Metamorphic textures. Pergamon Press, 350 pp.

Stacey, J. S. & Kramers, J. D. 1975. Approximation of terrestrial lead isotope evolution by a two-stage model. *Earth and Planetary Science Letters*, **26**, 207–221.

Ternet, Y., Majesté-Menjoulas, C., Canérot, J., Baudin, T., Cocherie, A., Guerrot, C. & Rossi, P. 2004. Notice Explicative, Carte géologique de la France (1/50000), feuille Laruns-Somport (1069). *Bulletin de la Société Géologique de France*, Orleans.

Turrillot, P., Augier, R. & Faure, M. 2009. The top-to-the –East Sarzeau Shear Zone and its place in the syn-orogenic extensional tectonics of Southern Armorica. *Bulletin de la Société Géologique de France*, **180**, 247-261.

Vernon, R. H. 1976. Metamorphisc processes. Reactions and microstructures development. London: Murby, George Allen & Unwin Ltd. 247 pp.

Vilà, M., Pin, C., Enrique, P. & Liesa, M. 2005. Telescoping of three distinct magmatic suites in an orogenic setting: Generation of Hercynian igneous rocks of the Albera Massif (eastern Pyrenees). *Lithos*, **83**, 97–127.

Vilà, M., Pin, C., Liesa, M. & Enrique, P. 2007. LPHT metamorphism in a late orogenic transpressional setting, Albera Massif, NE Iberia: implications for the geodynamic evolution of the Variscan Pyrenees. *Journal Metamorphic Geology,* **25**, 321–347.

Vissers, R. L. M. 1992. Variscan extension in the Pyrenees. *Tectonics*, **11**, 1396–1384.

Wendt, I. & Carl, C. 1991. The statistical distribution of the mean squared weighted deviation. *Chemical Geology*, **86**, 275–285.

White, R. W., Powell, R., Holland, T. J. B. & Worley, B. A. 2000. The effect of $TiO_2$ and $Fe_2O_3$ on metapelitic assemblages at greenschist and amphibolite facies conditions: mineral equilibria calculations in the system $K_2O$–FeO–MgO–$Al_2O_3$–$SiO_2$–$H_2O$–$TiO_2$–$Fe_2O_3$. *Journal of Metamorphic Geology,* **18**, 497–511.

White, R. W. & Powell, R. 2002. Melt loss and the preservation of granulite facies mineral assemblages. *Journal of Metamorphic Geology,* **20**, 621–632.

White, R. W., Powell, R. & Clarke, G. L. 2002. The interpretation of reaction textures in Fe-rich metapelitic granulites of the Musgrave Block, central Australia: constraints from mineral equilibria calculations in the system $K_2O$-FeO-MgO-$Al_2O_3$-$SiO_2$-$H_2O$-$TiO_2$-$Fe_2O_3$. *Journal of Metamorphic Geology*, **20**, 41–55.

White, R. W., Pomroy, N. E. & Powell, R. 2005. An in-situ metatexite-diatexite transition in upper amphibolite facies rocks from Broken Hill, Australia. *Journal of Metamorphic Geology*, **23**, 579–602.

White, R. W., Powell, R. & Holland, T. J. B. 2007. Progress relating to calculation of partial melting equilibria for metapelites. *Journal of Metamorphic Geology*, **25**, 511–527.

Wickham, S. M. & Oxburgh, E. R. 1986. A rifted tectonic setting for Hercynian high-thermal gradient metamorphism in the Pyrenees. *Tectonophysics*, **129**, 53–69.

Wickham, S. M. 1987. Low-pressure regional metamorphism: the Trois Seigneurs Massif, Pyrenees, France. *Journal Petrology*, **28**, 127–169.

Wickham, S. M. & Oxburgh, E. R., 1987. Low-pressure regional metamorphism in the Pyrenees and its implications for the thermal evolution of rifted continental

crust. *Philosophical Transactions of the Royal Society of London*. *Series A: Mathematical and Physical Sciences*, **321**, 219–242.

Williams, I. S. 1997. U-Th-Pb geochronology by ion microprobe: not just ages but histories. *Economic Geology*, **7**, 1–35.

Zwart, H. J. 1962. On the determination of polymetamorphic mineral association and its application to the Bossost area (central Pyrenees). *Geologische Rundschau*, **52**, 38–65.

Zwart, H. J. 1963. Some examples of the relations between deformation and metamorphism from the Central Pyrenees. *Geologie en Mijnbouw*, **42**, 143–154.

Zwart, H. J. 1968. The Palaeozoic crystalline rocks of the Pyrenees in their structural setting. *Kristallinikum*, **6**, 125–140.

Zwart, H. J. 1979. The geology of the central Pyrenees. *Leidse Geologische Mededelingen*, **50**, 1–74.

Zwart, H. J. 1986. The Variscan geology of the Pyrenees. *Tectonophysic*s, **129**, 9–27.

# APPENDIX: MINERAL CHEMISTRY

**Table A1.** Analyses of biotite and cordierite from an andalusite-sillimanite micaschist of the Upper series.

| Sample | 187 | | | | | | | | | | | | | |
|---|---|---|---|---|---|---|---|---|---|---|---|---|---|---|
| Mineral | biotite | | | | | | | cordierite | | | | | | |
| Analysis | 187-3-2-bi | 187-3-7-bi | 187-3-17-bi | 187-3-22-bi | 187-3-23-bi | 187-3-30-bi | 187-2-38-bi | 187-3-3-cd | 187-3-9-cd | 187-3-10-cd | 187-3-18-cd | 187-3-21-cd | 187-3-26-cd | 187-3-31-cd |
| Spot | #2 | #4 | #10 | #13 | #15 | #18 | #22 | #3 | #6 | #7 | #11 | #12 | #16 | #19 |
| (wt%) | | | | | | | | | | | | | | |
| $SiO_2$ | 34.11 | 34.95 | 34.71 | 33.71 | 35.90 | 34.32 | 34.29 | 47.24 | 47.60 | 47.41 | 47.64 | 47.88 | 47.38 | 47.95 |
| $TiO_2$ | 2.26 | 2.92 | 3.39 | 2.54 | 2.84 | 1.46 | 2.71 | 0.00 | 0.05 | 0.00 | 0.02 | 0.05 | 0.01 | 0.05 |
| $Al_2O_3$ | 20.40 | 19.92 | 19.53 | 19.20 | 19.84 | 21.08 | 19.14 | 32.83 | 32.64 | 32.71 | 32.61 | 32.70 | 32.83 | 32.99 |
| FeO | 19.97 | 19.78 | 20.46 | 20.31 | 19.70 | 19.86 | 20.79 | 9.72 | 9.78 | 9.78 | 10.07 | 9.38 | 9.91 | 9.58 |
| MnO | 0.21 | 0.05 | 0.09 | 0.07 | 0.11 | 0.14 | 0.14 | 0.24 | 0.32 | 0.27 | 0.32 | 0.30 | 0.33 | 0.26 |
| MgO | 8.92 | 8.01 | 7.56 | 9.53 | 8.29 | 8.67 | 8.06 | 7.38 | 7.37 | 7.46 | 7.59 | 7.51 | 7.49 | 7.49 |
| CaO | 0.00 | 0.01 | 0.00 | 0.01 | 0.03 | 0.00 | 0.00 | 0.01 | 0.03 | 0.01 | 0.02 | 0.01 | 0.01 | 0.02 |
| $Na_2O$ | 0.20 | 0.23 | 0.17 | 0.14 | 0.16 | 0.19 | 0.17 | 0.19 | 0.21 | 0.27 | 0.20 | 0.18 | 0.16 | 0.25 |
| $K_2O$ | 7.40 | 8.70 | 8.46 | 7.73 | 8.22 | 8.22 | 8.25 | 0.00 | 0.01 | 0.02 | 0.01 | 0.00 | 0.01 | 0.02 |
| Total | 93.47 | 94.57 | 94.37 | 93.24 | 95.09 | 93.94 | 93.55 | 97.61 | 98.01 | 97.93 | 98.48 | 98.01 | 98.13 | 98.61 |
| Oxygen | 11 | 11 | 11 | 11 | 11 | 11 | 11 | 18 | 18 | 18 | 18 | 18 | 18 | 18 |
| Si | 2.73 | 2.77 | 2.77 | 2.71 | 2.84 | 2.72 | 2.76 | 4.92 | 4.94 | 4.92 | 4.92 | 4.96 | 4.91 | 4.94 |
| Ti | 0.14 | 0.17 | 0.20 | 0.15 | 0.17 | 0.09 | 0.16 | 0.00 | 0.00 | 0.00 | 0.00 | 0.00 | 0.00 | 0.00 |
| Al | 1.93 | 1.86 | 1.84 | 1.82 | 1.85 | 1.97 | 1.82 | 4.03 | 3.99 | 4.00 | 3.97 | 3.99 | 4.01 | 4.01 |
| $Fe^{3+}$ | 0.00 | 0.00 | 0.00 | 0.00 | 0.00 | 0.00 | 0.00 | 0.17 | 0.16 | 0.22 | 0.23 | 0.11 | 0.20 | 0.16 |
| $Fe^{2+}$ | 1.34 | 1.31 | 1.37 | 1.36 | 1.30 | 1.32 | 1.40 | 0.67 | 0.68 | 0.62 | 0.64 | 0.71 | 0.66 | 0.66 |
| Mn | 0.01 | 0.00 | 0.01 | 0.00 | 0.01 | 0.01 | 0.01 | 0.02 | 0.03 | 0.02 | 0.03 | 0.03 | 0.03 | 0.02 |
| Mg | 1.06 | 0.95 | 0.90 | 1.14 | 0.98 | 1.03 | 0.97 | 1.15 | 1.14 | 1.15 | 1.17 | 1.16 | 1.16 | 1.15 |
| Ca | 0.00 | 0.00 | 0.00 | 0.00 | 0.00 | 0.00 | 0.00 | 0.00 | 0.00 | 0.00 | 0.00 | 0.00 | 0.00 | 0.00 |
| Na | 0.03 | 0.04 | 0.03 | 0.02 | 0.02 | 0.03 | 0.03 | 0.04 | 0.04 | 0.05 | 0.04 | 0.04 | 0.03 | 0.05 |
| K | 0.76 | 0.88 | 0.86 | 0.79 | 0.83 | 0.83 | 0.85 | 0.00 | 0.00 | 0.00 | 0.00 | 0.00 | 0.00 | 0.00 |
| cations | 8.00 | 8.00 | 8.00 | 8.00 | 8.00 | 8.00 | 8.00 | 11.00 | 11.00 | 11.00 | 11.00 | 11.00 | 11.00 | 11.00 |
| $X_{Fe}$ ($Fe^{2+}$) | 0.56 | 0.58 | 0.60 | 0.54 | 0.57 | 0.56 | 0.59 | 0.37 | 0.38 | 0.35 | 0.35 | 0.38 | 0.36 | 0.37 |
| $X_{Fe}$ (Fetot) | 0.56 | 0.58 | 0.60 | 0.54 | 0.57 | 0.56 | 0.59 | 0.42 | 0.43 | 0.42 | 0.43 | 0.41 | 0.43 | 0.42 |

**Table A2.** Chemical composition of biotite from a sillimanite schist of the Intermediate series.

| Sample | 4.12 | | | | | | | | | | | | | | | |
|---|---|---|---|---|---|---|---|---|---|---|---|---|---|---|---|---|
| Analysis | 4.12-bi2 | 4.12-bi3 | 4.12-bi4 | 4.12-bi6 | 4.12-ms4 | 4.12-bi7 | 4.12-bi9 | 4.12-bi10 | 4.12-bi11 | 4.12-bi12 | 4.12-bi13 | 4.12-bi14 | 4.12-bi16 | 4.12_bi8 | 4.12_bi9 | 4.12_bi10 |
| Spot | #34 | #37 | #38 | #41 | #50 | #52 | #59 | #60 | #64 | #65 | #68 | #71 | #78 | #9 | #10 | #11 |
| (wt%) | | | | | | | | | | | | | | | | |
| $SiO_2$ | 35.26 | 35.17 | 35.32 | 35.08 | 35.51 | 34.84 | 35.04 | 34.53 | 34.87 | 35.12 | 34.73 | 34.53 | 34.88 | 34.83 | 34.22 | 34.85 |
| $TiO_2$ | 0.20 | 0.81 | 0.03 | 0.30 | 0.00 | 0.03 | 1.26 | 2.19 | 1.66 | 0.43 | 1.57 | 1.36 | 1.77 | 1.69 | 1.11 | 1.11 |
| $Al_2O_3$ | 21.39 | 20.51 | 22.01 | 21.13 | 21.93 | 21.66 | 20.49 | 20.20 | 20.28 | 21.08 | 20.03 | 20.24 | 20.20 | 20.10 | 20.84 | 20.71 |
| FeO | 18.62 | 19.68 | 18.43 | 18.86 | 17.23 | 18.34 | 19.32 | 19.50 | 19.96 | 19.23 | 19.87 | 20.21 | 19.07 | 19.69 | 18.71 | 19.48 |
| MnO | 0.24 | 0.31 | 0.31 | 0.35 | 0.28 | 0.42 | 0.36 | 0.34 | 0.32 | 0.27 | 0.29 | 0.29 | 0.29 | 0.31 | 0.28 | 0.34 |
| MgO | 9.62 | 8.86 | 9.59 | 9.42 | 10.22 | 10.02 | 9.05 | 8.35 | 8.69 | 9.66 | 8.89 | 8.93 | 8.82 | 8.75 | 9.57 | 9.23 |
| CaO | 0.00 | 0.00 | 0.01 | 0.00 | 0.00 | 0.00 | 0.00 | 0.00 | 0.02 | 0.00 | 0.00 | 0.02 | 0.00 | 0.01 | 0.00 | 0.00 |
| $Na_2O$ | 0.27 | 0.21 | 0.29 | 0.36 | 0.25 | 0.20 | 0.22 | 0.28 | 0.28 | 0.29 | 0.22 | 0.21 | 0.24 | 0.25 | 0.24 | 0.28 |
| $K_2O$ | 9.09 | 9.10 | 8.88 | 9.06 | 9.30 | 9.21 | 9.18 | 9.23 | 9.07 | 9.18 | 9.14 | 8.63 | 9.18 | 9.44 | 9.20 | 9.72 |
| Total | 94.69 | 94.65 | 94.87 | 94.56 | 94.72 | 94.72 | 94.92 | 94.62 | 95.15 | 95.26 | 94.74 | 94.42 | 94.45 | 95.07 | 94.17 | 95.72 |
| Oxygen | 11 | 11 | 11 | 11 | 11 | 11 | 11 | 11 | 11 | 11 | 11 | 11 | 11 | 11 | 11 | 11 |
| Si | 2.74 | 2.76 | 2.74 | 2.74 | 2.74 | 2.70 | 2.74 | 2.73 | 2.73 | 2.72 | 2.73 | 2.73 | 2.75 | 2.73 | 2.68 | 2.70 |
| Ti | 0.01 | 0.05 | 0.00 | 0.02 | 0.00 | 0.00 | 0.07 | 0.13 | 0.10 | 0.03 | 0.09 | 0.08 | 0.10 | 0.10 | 0.07 | 0.06 |
| Al | 1.96 | 1.90 | 2.01 | 1.94 | 2.00 | 1.98 | 1.89 | 1.88 | 1.87 | 1.92 | 1.86 | 1.88 | 1.88 | 1.86 | 1.93 | 1.89 |
| $Fe^{3+}$ | 0.00 | 0.00 | 0.00 | 0.00 | 0.00 | 0.00 | 0.00 | 0.00 | 0.00 | 0.00 | 0.00 | 0.00 | 0.00 | 0.00 | 0.00 | 0.00 |
| $Fe^{2+}$ | 1.21 | 1.29 | 1.20 | 1.23 | 1.11 | 1.19 | 1.26 | 1.29 | 1.31 | 1.25 | 1.31 | 1.33 | 1.26 | 1.29 | 1.23 | 1.26 |
| Mn | 0.02 | 0.02 | 0.02 | 0.02 | 0.02 | 0.03 | 0.02 | 0.02 | 0.02 | 0.02 | 0.02 | 0.02 | 0.02 | 0.02 | 0.02 | 0.02 |
| Mg | 1.12 | 1.04 | 1.11 | 1.10 | 1.18 | 1.16 | 1.06 | 0.98 | 1.02 | 1.12 | 1.04 | 1.05 | 1.04 | 1.02 | 1.12 | 1.06 |
| Ca | 0.00 | 0.00 | 0.00 | 0.00 | 0.00 | 0.00 | 0.00 | 0.00 | 0.00 | 0.00 | 0.00 | 0.00 | 0.00 | 0.00 | 0.00 | 0.00 |
| Na | 0.04 | 0.03 | 0.04 | 0.05 | 0.04 | 0.03 | 0.03 | 0.04 | 0.04 | 0.04 | 0.03 | 0.03 | 0.04 | 0.04 | 0.04 | 0.04 |
| K | 0.90 | 0.91 | 0.88 | 0.90 | 0.92 | 0.91 | 0.92 | 0.93 | 0.91 | 0.91 | 0.92 | 0.87 | 0.92 | 0.94 | 0.92 | 0.96 |
| cations | 8.00 | 8.00 | 8.00 | 8.00 | 8.00 | 8.00 | 8.00 | 8.00 | 8.00 | 8.00 | 8.00 | 8.00 | 8.00 | 8.00 | 8.00 | 8.00 |
| $X_{Fe}$ ($Fe^{2+}$) | 0.52 | 0.55 | 0.52 | 0.53 | 0.49 | 0.51 | 0.54 | 0.57 | 0.56 | 0.53 | 0.56 | 0.56 | 0.55 | 0.56 | 0.52 | 0.54 |
| $X_{Fe}$ (Fetot) | 0.52 | 0.55 | 0.52 | 0.53 | 0.49 | 0.51 | 0.54 | 0.57 | 0.56 | 0.53 | 0.56 | 0.56 | 0.55 | 0.56 | 0.52 | 0.54 |

**Table A2.** (Continued)

| Sample | 4.12 | | | | | | | | | | | | | | |
|---|---|---|---|---|---|---|---|---|---|---|---|---|---|---|---|
| Analysis | 4.12_bi13 | 4.12_bi14 | 4.12_bi18 | 4.12_bi21 | 4.12_bi23 | 4.12_bi24 | 4.12_bi2 | 4.12_bi27 | 4.12_bi29 | 4.12_bi30 | 4.12_bi40 | 4.12_bi42 | 4.12_bi44 | 4.12_bi45 | 4.12_bi46 |
| Spot | #14 | #15 | #19 | #22 | #24 | #25 | #26 | #28 | #30 | #31 | #41 | #43 | #45 | #46 | #47 |
| (wt%) | | | | | | | | | | | | | | | |
| $SiO_2$ | 34.54 | 33.70 | 33.81 | 34.30 | 34.11 | 34.13 | 34.50 | 34.22 | 33.91 | 33.84 | 34.01 | 34.65 | 33.90 | 34.60 | 35.37 |
| $TiO_2$ | 1.56 | 2.87 | 3.23 | 2.63 | 3.13 | 3.17 | 3.10 | 2.99 | 1.41 | 2.52 | 1.22 | 2.97 | 2.51 | 2.25 | 2.87 |
| $Al_2O_3$ | 20.44 | 19.27 | 19.79 | 19.15 | 18.56 | 19.70 | 20.01 | 19.64 | 21.52 | 20.44 | 19.95 | 19.59 | 19.37 | 20.49 | 20.29 |
| FeO | 19.21 | 21.35 | 20.79 | 21.65 | 21.77 | 21.20 | 20.21 | 21.37 | 19.60 | 20.00 | 19.80 | 21.40 | 20.50 | 18.51 | 18.81 |
| MnO | 0.33 | 0.20 | 0.21 | 0.22 | 0.30 | 0.13 | 0.22 | 0.18 | 0.32 | 0.18 | 0.23 | 0.26 | 0.22 | 0.14 | 0.12 |
| MgO | 9.14 | 7.29 | 7.11 | 7.72 | 7.53 | 7.03 | 7.11 | 7.31 | 9.25 | 7.77 | 9.73 | 7.67 | 8.51 | 8.33 | 8.12 |
| CaO | 0.00 | 0.00 | 0.00 | 0.00 | 0.00 | 0.03 | 0.01 | 0.00 | 0.04 | 0.01 | 0.02 | 0.00 | 0.00 | 0.03 | 0.00 |
| $Na_2O$ | 0.18 | 0.20 | 0.24 | 0.21 | 0.20 | 0.10 | 0.14 | 0.22 | 0.30 | 0.22 | 0.20 | 0.13 | 0.24 | 0.25 | 0.19 |
| $K_2O$ | 9.50 | 9.43 | 9.32 | 9.48 | 9.36 | 9.37 | 9.45 | 9.43 | 8.64 | 9.00 | 8.90 | 9.24 | 9.25 | 9.41 | 9.65 |
| Total | 94.90 | 94.31 | 94.50 | 95.36 | 94.96 | 94.86 | 94.75 | 95.36 | 94.99 | 93.98 | 94.06 | 95.91 | 94.50 | 94.01 | 95.42 |
| Oxygen | 11 | 11 | 11 | 11 | 11 | 11 | 11 | 11 | 11 | 11 | 11 | 11 | 11 | 11 | 11 |
| Si | 2.70 | 2.70 | 2.70 | 2.71 | 2.72 | 2.72 | 2.75 | 2.71 | 2.65 | 2.70 | 2.68 | 2.73 | 2.69 | 2.74 | 2.77 |
| Ti | 0.09 | 0.17 | 0.19 | 0.16 | 0.19 | 0.19 | 0.19 | 0.18 | 0.08 | 0.15 | 0.07 | 0.18 | 0.15 | 0.13 | 0.17 |
| Al | 1.88 | 1.82 | 1.86 | 1.78 | 1.74 | 1.85 | 1.88 | 1.83 | 1.98 | 1.92 | 1.85 | 1.82 | 1.81 | 1.91 | 1.87 |
| $Fe^{3+}$ | 0.00 | 0.00 | 0.00 | 0.00 | 0.00 | 0.00 | 0.00 | 0.00 | 0.00 | 0.00 | 0.00 | 0.00 | 0.00 | 0.00 | 0.00 |
| $Fe^{2+}$ | 1.26 | 1.43 | 1.39 | 1.43 | 1.45 | 1.41 | 1.35 | 1.41 | 1.28 | 1.33 | 1.30 | 1.41 | 1.36 | 1.23 | 1.23 |
| Mn | 0.02 | 0.01 | 0.01 | 0.01 | 0.02 | 0.01 | 0.01 | 0.01 | 0.02 | 0.01 | 0.02 | 0.02 | 0.01 | 0.01 | 0.01 |
| Mg | 1.07 | 0.87 | 0.85 | 0.91 | 0.89 | 0.84 | 0.84 | 0.86 | 1.08 | 0.92 | 1.14 | 0.90 | 1.01 | 0.98 | 0.95 |
| Ca | 0.00 | 0.00 | 0.00 | 0.00 | 0.00 | 0.00 | 0.00 | 0.00 | 0.00 | 0.00 | 0.00 | 0.00 | 0.00 | 0.00 | 0.00 |
| Na | 0.03 | 0.03 | 0.04 | 0.03 | 0.03 | 0.02 | 0.02 | 0.03 | 0.05 | 0.03 | 0.03 | 0.02 | 0.04 | 0.04 | 0.03 |
| K | 0.95 | 0.96 | 0.95 | 0.96 | 0.95 | 0.95 | 0.96 | 0.95 | 0.86 | 0.92 | 0.89 | 0.93 | 0.94 | 0.95 | 0.96 |
| cations | 8.00 | 8.00 | 8.00 | 8.00 | 8.00 | 8.00 | 8.00 | 8.00 | 8.00 | 8.00 | 8.00 | 8.00 | 8.00 | 8.00 | 8.00 |
| $X_{Fe}$ ($Fe^{2+}$) | 0.54 | 0.62 | 0.62 | 0.61 | 0.62 | 0.63 | 0.61 | 0.62 | 0.54 | 0.59 | 0.53 | 0.61 | 0.57 | 0.55 | 0.57 |
| $X_{Fe}$ (Fetot) | 0.54 | 0.62 | 0.62 | 0.61 | 0.62 | 0.63 | 0.61 | 0.62 | 0.54 | 0.59 | 0.53 | 0.61 | 0.57 | 0.55 | 0.57 |

**Table A2.** (Continued)

| Sample | 4.12 | | | | | | | | |
|---|---|---|---|---|---|---|---|---|---|
| Analysis | 4.12_bi55 | 4.12_bi58 | 4.12_bi60 | 4.12_bi63 | 4.12_bi64 | 4.12_bi68 | 4.12_bi71 | 4.12_bi72 | 4.12_bi85 |
| Spot | #56 | #59 | #61 | #64 | #65 | #69 | #72 | #73 | #91 |
| (wt%) | | | | | | | | | |
| $SiO_2$ | 33.62 | 34.18 | 34.19 | 34.25 | 33.58 | 34.53 | 34.44 | 34.01 | 34.21 |
| $TiO_2$ | 1.96 | 1.53 | 1.63 | 2.89 | 1.41 | 2.22 | 2.46 | 2.76 | 2.18 |
| $Al_2O_3$ | 19.19 | 19.75 | 19.68 | 19.40 | 19.84 | 19.40 | 19.51 | 19.52 | 19.84 |
| FeO | 20.91 | 19.78 | 19.66 | 20.50 | 19.65 | 20.55 | 20.78 | 20.97 | 20.01 |
| MnO | 0.25 | 0.24 | 0.30 | 0.20 | 0.24 | 0.18 | 0.15 | 0.20 | 0.28 |
| MgO | 8.84 | 9.11 | 8.86 | 7.79 | 8.95 | 8.09 | 7.65 | 7.71 | 8.33 |
| CaO | 0.00 | 0.00 | 0.02 | 0.00 | 0.03 | 0.03 | 0.00 | 0.00 | 0.00 |
| $Na_2O$ | 0.18 | 0.12 | 0.22 | 0.09 | 0.12 | 0.25 | 0.30 | 0.18 | 0.26 |
| $K_2O$ | 9.37 | 9.31 | 9.14 | 9.44 | 8.73 | 9.27 | 9.33 | 9.18 | 9.50 |
| Total | 94.32 | 94.02 | 93.70 | 94.56 | 92.55 | 94.52 | 94.62 | 94.53 | 94.61 |
| Oxygen | 11 | 11 | 11 | 11 | 11 | 11 | 11 | 11 | 11 |
| Si | 2.66 | 2.71 | 2.72 | 2.73 | 2.70 | 2.74 | 2.74 | 2.71 | 2.70 |
| Ti | 0.12 | 0.09 | 0.10 | 0.17 | 0.09 | 0.13 | 0.15 | 0.17 | 0.13 |
| Al | 1.79 | 1.84 | 1.84 | 1.82 | 1.88 | 1.81 | 1.83 | 1.83 | 1.85 |
| $Fe^{3+}$ | 0.00 | 0.00 | 0.00 | 0.00 | 0.00 | 0.00 | 0.00 | 0.00 | 0.00 |
| $Fe^{2+}$ | 1.39 | 1.31 | 1.31 | 1.36 | 1.32 | 1.36 | 1.38 | 1.40 | 1.32 |
| Mn | 0.02 | 0.02 | 0.02 | 0.01 | 0.02 | 0.01 | 0.01 | 0.01 | 0.02 |
| Mg | 1.04 | 1.07 | 1.05 | 0.92 | 1.07 | 0.96 | 0.91 | 0.92 | 0.98 |
| Ca | 0.00 | 0.00 | 0.00 | 0.00 | 0.00 | 0.00 | 0.00 | 0.00 | 0.00 |
| Na | 0.03 | 0.02 | 0.03 | 0.01 | 0.02 | 0.04 | 0.05 | 0.03 | 0.04 |
| K | 0.95 | 0.94 | 0.93 | 0.96 | 0.90 | 0.94 | 0.95 | 0.93 | 0.96 |
| cations | 8.00 | 8.00 | 8.00 | 8.00 | 8.00 | 8.00 | 8.00 | 8.00 | 8.00 |
| $X_{Fe}$ ($Fe^{2+}$) | 0.57 | 0.55 | 0.55 | 0.60 | 0.55 | 0.59 | 0.60 | 0.60 | 0.57 |
| $X_{Fe}$ (Fetot) | 0.57 | 0.55 | 0.55 | 0.60 | 0.55 | 0.59 | 0.60 | 0.60 | 0.57 |

**Table A3.** Chemical composition of cordierite from a sillimanite schist of the Intermediate series.

| Sample | 4.12 | | | | | | | | | | | | | | | | |
|---|---|---|---|---|---|---|---|---|---|---|---|---|---|---|---|---|---|
| Analysis | 4.12-cd1 | 4.12-cd2 | 4.12-cd3 | 4.12-cd4 | 4.12-cd6 | 4.12-cd7 | 4.12-cd8 | 4.12-cd9 | 4.12-cd10 | 4.12-cd11 | 4.12-cd12 | 4.12-cd13 b | 4.12-cd14 | 4.12-cd15 | 4.12-cd16 | 4.12-cd17 | 4.12-cd18 |
| Spot | #31 | #32 | #33 | #35 | #39 | #42 | #44 | #49 | #51 | #53 | #55 | #58 | #66 | #67 | #70 | #72 | #73 |
| (wt%) | | | | | | | | | | | | | | | | | |
| $SiO_2$ | 47.90 | 47.45 | 47.74 | 48.06 | 47.57 | 47.78 | 47.54 | 47.70 | 47.40 | 47.77 | 47.66 | 47.08 | 47.38 | 47.97 | 47.51 | 47.46 | 47.82 |
| $TiO_2$ | 0.00 | 0.00 | 0.00 | 0.02 | 0.00 | 0.01 | 0.01 | 0.01 | 0.00 | 0.01 | 0.00 | 0.03 | 0.00 | 0.02 | 0.00 | 0.01 | 0.02 |
| $Al_2O_3$ | 32.52 | 32.31 | 32.56 | 32.43 | 32.53 | 32.42 | 32.10 | 32.52 | 32.44 | 32.28 | 32.36 | 32.25 | 32.20 | 32.50 | 32.58 | 32.90 | 32.62 |
| FeO | 8.45 | 9.11 | 9.11 | 9.51 | 9.60 | 9.86 | 10.15 | 9.46 | 10.04 | 10.34 | 9.78 | 10.25 | 9.86 | 9.59 | 9.32 | 8.97 | 9.02 |
| MnO | 0.87 | 0.82 | 0.89 | 0.83 | 0.79 | 0.71 | 0.56 | 0.75 | 0.49 | 0.51 | 0.46 | 0.55 | 0.62 | 0.60 | 0.75 | 0.73 | 0.90 |
| MgO | 7.25 | 7.07 | 7.15 | 7.05 | 6.89 | 6.95 | 6.70 | 6.72 | 6.75 | 6.63 | 6.28 | 6.87 | 6.60 | 6.68 | 6.93 | 6.75 | 7.09 |
| CaO | 0.01 | 0.02 | 0.01 | 0.02 | 0.01 | 0.03 | 0.02 | 0.04 | 0.00 | 0.03 | 0.00 | 0.01 | 0.05 | 0.00 | 0.01 | 0.00 | 0.02 |
| $Na_2O$ | 0.52 | 0.42 | 0.44 | 0.45 | 0.42 | 0.35 | 0.30 | 0.50 | 0.41 | 0.26 | 0.78 | 0.45 | 0.55 | 0.74 | 0.43 | 0.75 | 0.54 |
| $K_2O$ | 0.01 | 0.01 | 0.01 | 0.00 | 0.02 | 0.00 | 0.00 | 0.00 | 0.01 | 0.00 | 0.00 | 0.00 | 0.00 | 0.00 | 0.02 | 0.01 | 0.02 |
| Total | 97.53 | 97.21 | 97.91 | 98.37 | 97.83 | 98.11 | 97.38 | 97.70 | 97.54 | 97.83 | 97.32 | 97.49 | 97.26 | 98.10 | 97.55 | 97.58 | 98.05 |
| Oxygen | 18 | 18 | 18 | 18 | 18 | 18 | 18 | 18 | 18 | 18 | 18 | 18 | 18 | 18 | 18 | 18 | 18 |
| Si | 4.98 | 4.96 | 4.95 | 4.97 | 4.95 | 4.96 | 4.98 | 4.97 | 4.95 | 4.99 | 4.98 | 4.92 | 4.96 | 4.97 | 4.95 | 4.93 | 4.95 |
| Ti | 0.00 | 0.00 | 0.00 | 0.00 | 0.00 | 0.00 | 0.00 | 0.00 | 0.00 | 0.00 | 0.00 | 0.00 | 0.00 | 0.00 | 0.00 | 0.00 | 0.00 |
| Al | 3.98 | 3.98 | 3.98 | 3.95 | 3.99 | 3.97 | 3.97 | 3.99 | 3.99 | 3.97 | 3.99 | 3.97 | 3.97 | 3.97 | 4.00 | 4.03 | 3.98 |
| $Fe^{3+}$ | 0.17 | 0.19 | 0.20 | 0.19 | 0.20 | 0.18 | 0.13 | 0.17 | 0.19 | 0.10 | 0.21 | 0.28 | 0.22 | 0.24 | 0.18 | 0.26 | 0.23 |
| $Fe^{2+}$ | 0.56 | 0.61 | 0.59 | 0.63 | 0.64 | 0.68 | 0.76 | 0.65 | 0.69 | 0.80 | 0.65 | 0.62 | 0.65 | 0.59 | 0.63 | 0.52 | 0.56 |
| Mn | 0.08 | 0.07 | 0.08 | 0.07 | 0.07 | 0.06 | 0.05 | 0.07 | 0.04 | 0.05 | 0.04 | 0.05 | 0.05 | 0.05 | 0.07 | 0.06 | 0.08 |
| Mg | 1.12 | 1.10 | 1.11 | 1.09 | 1.07 | 1.08 | 1.05 | 1.04 | 1.05 | 1.03 | 0.98 | 1.07 | 1.03 | 1.03 | 1.08 | 1.05 | 1.09 |
| Ca | 0.00 | 0.00 | 0.00 | 0.00 | 0.00 | 0.00 | 0.00 | 0.00 | 0.00 | 0.00 | 0.00 | 0.00 | 0.01 | 0.00 | 0.00 | 0.00 | 0.00 |
| Na | 0.10 | 0.09 | 0.09 | 0.09 | 0.08 | 0.07 | 0.06 | 0.10 | 0.08 | 0.05 | 0.16 | 0.09 | 0.11 | 0.15 | 0.09 | 0.15 | 0.11 |
| K | 0.00 | 0.00 | 0.00 | 0.00 | 0.00 | 0.00 | 0.00 | 0.00 | 0.00 | 0.00 | 0.00 | 0.00 | 0.00 | 0.00 | 0.00 | 0.00 | 0.00 |
| cations | 11.00 | 11.00 | 11.00 | 11.00 | 11.00 | 11.00 | 11.00 | 11.00 | 11.00 | 11.00 | 11.00 | 11.00 | 11.00 | 11.00 | 11.00 | 11.00 | 11.00 |
| $X_{Fe}$ ($Fe^{2+}$) | 0.33 | 0.36 | 0.35 | 0.37 | 0.37 | 0.39 | 0.42 | 0.39 | 0.40 | 0.44 | 0.40 | 0.37 | 0.39 | 0.36 | 0.37 | 0.33 | 0.34 |
| $X_{Fe}$ (Fetot) | 0.40 | 0.42 | 0.42 | 0.43 | 0.44 | 0.44 | 0.46 | 0.44 | 0.45 | 0.47 | 0.47 | 0.46 | 0.46 | 0.45 | 0.43 | 0.43 | 0.42 |

**Table A3.** (Continued)

| Sample | 4.12 | | | | | | | | | | | | | | | | |
|---|---|---|---|---|---|---|---|---|---|---|---|---|---|---|---|---|---|
| Analysis | 4.12-cd19 | 4.12-cd20 | 4.12-cd22 | 4.12_cd69 | 4.12_cd70 | 4.12_cd71 | 4.12_cd72 | 4.12_cd73 | 4.12_cd74 | 4.12_cd75 | 4.12_cd81 | 4.12_cd83 | 4.12_cd84 | 4.12_cd91 | 4.12_cd94 | 4.12_cd96 | 4.12_cd97 |
| Spot | #76 | #77 | #82 | #75 | #76 | #77 | #78 | #79 | #80 | #81 | #87 | #89 | #90 | #97 | #100 | #102 | #103 |
| (wt%) | | | | | | | | | | | | | | | | | |
| $SiO_2$ | 47.75 | 47.60 | 47.13 | 46.15 | 46.82 | 46.69 | 46.76 | 46.74 | 46.79 | 47.09 | 46.26 | 46.98 | 46.51 | 46.17 | 46.85 | 47.26 | 46.75 |
| $TiO_2$ | 0.00 | 0.02 | 0.04 | 0.02 | 0.01 | 0.00 | 0.00 | 0.02 | 0.01 | 0.00 | 0.00 | 0.04 | 0.04 | 0.01 | 0.02 | 0.00 | 0.00 |
| $Al_2O_3$ | 32.71 | 32.34 | 31.99 | 31.92 | 31.94 | 32.51 | 32.11 | 32.72 | 32.08 | 32.54 | 32.26 | 32.20 | 32.25 | 32.22 | 32.33 | 32.09 | 32.22 |
| FeO | 8.84 | 9.52 | 9.78 | 8.84 | 9.58 | 9.53 | 9.89 | 9.81 | 9.47 | 9.26 | 9.13 | 9.66 | 9.20 | 10.15 | 8.47 | 8.60 | 8.91 |
| MnO | 0.80 | 0.73 | 0.62 | 0.61 | 0.49 | 0.45 | 0.48 | 0.45 | 0.61 | 0.53 | 0.74 | 0.68 | 0.70 | 0.58 | 0.82 | 0.73 | 0.69 |
| MgO | 6.73 | 7.06 | 6.58 | 6.51 | 6.25 | 6.34 | 6.45 | 6.46 | 6.80 | 6.47 | 6.52 | 6.55 | 6.75 | 6.72 | 6.71 | 6.54 | 6.98 |
| CaO | 0.02 | 0.00 | 0.00 | 0.04 | 0.02 | 0.04 | 0.02 | 0.00 | 0.00 | 0.02 | 0.02 | 0.00 | 0.02 | 0.03 | 0.02 | 0.01 | 0.03 |
| $Na_2O$ | 0.86 | 0.35 | 0.58 | 1.00 | 0.99 | 0.95 | 0.91 | 0.71 | 0.59 | 0.86 | 0.92 | 0.79 | 0.86 | 0.68 | 0.99 | 0.97 | 0.88 |
| $K_2O$ | 0.02 | 0.00 | 0.01 | 0.01 | 0.00 | 0.03 | 0.02 | 0.01 | 0.00 | 0.00 | 0.00 | 0.02 | 0.02 | 0.01 | 0.01 | 0.02 | 0.01 |
| Total | 97.73 | 97.62 | 96.73 | 95.10 | 96.10 | 96.54 | 96.64 | 96.92 | 96.35 | 96.77 | 95.85 | 96.92 | 96.35 | 96.57 | 96.22 | 96.22 | 96.47 |
| Oxygen | 18 | 18 | 18 | 18 | 18 | 18 | 18 | 18 | 18 | 18 | 18 | 18 | 18 | 18 | 18 | 18 | 18 |
| Si | 4.95 | 4.96 | 4.96 | 4.91 | 4.94 | 4.90 | 4.91 | 4.90 | 4.93 | 4.93 | 4.89 | 4.92 | 4.89 | 4.86 | 4.92 | 4.97 | 4.90 |
| Ti | 0.00 | 0.00 | 0.00 | 0.00 | 0.00 | 0.00 | 0.00 | 0.00 | 0.00 | 0.00 | 0.00 | 0.00 | 0.00 | 0.00 | 0.00 | 0.00 | 0.00 |
| Al | 4.00 | 3.97 | 3.97 | 4.00 | 3.98 | 4.02 | 3.98 | 4.04 | 3.99 | 4.02 | 4.02 | 3.98 | 4.00 | 4.00 | 4.00 | 3.98 | 3.98 |
| $Fe^{3+}$ | 0.28 | 0.17 | 0.22 | 0.38 | 0.34 | 0.37 | 0.39 | 0.30 | 0.27 | 0.29 | 0.39 | 0.33 | 0.39 | 0.42 | 0.35 | 0.28 | 0.40 |
| $Fe^{2+}$ | 0.49 | 0.66 | 0.64 | 0.40 | 0.51 | 0.47 | 0.48 | 0.56 | 0.57 | 0.52 | 0.42 | 0.52 | 0.41 | 0.47 | 0.39 | 0.48 | 0.39 |
| Mn | 0.07 | 0.06 | 0.06 | 0.05 | 0.04 | 0.04 | 0.04 | 0.04 | 0.05 | 0.05 | 0.07 | 0.06 | 0.06 | 0.05 | 0.07 | 0.07 | 0.06 |
| Mg | 1.04 | 1.10 | 1.03 | 1.03 | 0.98 | 0.99 | 1.01 | 1.01 | 1.07 | 1.01 | 1.03 | 1.02 | 1.06 | 1.05 | 1.05 | 1.03 | 1.09 |
| Ca | 0.00 | 0.00 | 0.00 | 0.00 | 0.00 | 0.00 | 0.00 | 0.00 | 0.00 | 0.00 | 0.00 | 0.00 | 0.00 | 0.00 | 0.00 | 0.00 | 0.00 |
| Na | 0.17 | 0.07 | 0.12 | 0.21 | 0.20 | 0.19 | 0.19 | 0.14 | 0.12 | 0.17 | 0.19 | 0.16 | 0.18 | 0.14 | 0.20 | 0.20 | 0.18 |
| K | 0.00 | 0.00 | 0.00 | 0.00 | 0.00 | 0.00 | 0.00 | 0.00 | 0.00 | 0.00 | 0.00 | 0.00 | 0.00 | 0.00 | 0.00 | 0.00 | 0.00 |
| cations | 11.00 | 11.00 | 11.00 | 11.00 | 11.00 | 11.00 | 11.00 | 11.00 | 11.00 | 11.00 | 11.00 | 11.00 | 11.00 | 11.00 | 11.00 | 11.00 | 11.00 |
| $X_{Fe}$ ($Fe^{2+}$) | 0.32 | 0.38 | 0.38 | 0.28 | 0.34 | 0.32 | 0.32 | 0.36 | 0.35 | 0.34 | 0.29 | 0.34 | 0.28 | 0.31 | 0.27 | 0.32 | 0.26 |
| $X_{Fe}$ (Fetot) | 0.42 | 0.43 | 0.45 | 0.43 | 0.46 | 0.46 | 0.46 | 0.46 | 0.44 | 0.45 | 0.44 | 0.45 | 0.43 | 0.46 | 0.41 | 0.42 | 0.42 |

**Table A4.** Chemical composition of biotite from the patch migmatites of the Intermediate series affected by the Ceret contact aureole.

| Sample | 482 | | | | | | | | | | 526 | | | |
|---|---|---|---|---|---|---|---|---|---|---|---|---|---|---|
| Analysis | 482C-1-bt | 482C-6-bt | 482C-8-bt | 482C-12-bt | 482C-16-bt | 482C-20-bt | 482C-24-bt | 482C-30-bt | 482C-37-bt | 482C-38-bt | 526L2-2-bt | 526L2-5-bt | 526L2-9-bt | 526L2-20bi |
| Spot | #141 | #146 | #148 | #152 | #156 | #160 | #164 | #170 | #187 | #188 | #92 | #95 | #99 | #110 |
| (wt%) | | | | | | | | | | | | | | |
| $SiO_2$ | 34.32 | 34.89 | 34.92 | 34.86 | 34.69 | 35.06 | 34.22 | 34.63 | 34.96 | 34.28 | 34.93 | 35.32 | 35.03 | 35.47 |
| $TiO_2$ | 4.13 | 3.43 | 3.49 | 4.18 | 3.72 | 4.49 | 4.98 | 3.47 | 3.60 | 4.64 | 2.26 | 3.92 | 4.36 | 4.30 |
| $Al_2O_3$ | 18.13 | 18.18 | 18.90 | 18.37 | 18.51 | 18.03 | 18.10 | 18.36 | 18.80 | 18.04 | 18.78 | 18.37 | 17.90 | 17.82 |
| FeO | 22.39 | 21.76 | 20.75 | 22.04 | 21.55 | 21.29 | 21.12 | 21.94 | 21.77 | 22.25 | 21.03 | 19.59 | 21.43 | 18.90 |
| MnO | 0.04 | 0.11 | 0.05 | 0.08 | 0.00 | 0.08 | 0.02 | 0.01 | 0.04 | 0.08 | 0.03 | 0.03 | 0.08 | 0.05 |
| MgO | 6.62 | 7.31 | 7.68 | 7.25 | 7.22 | 7.00 | 6.64 | 7.23 | 7.09 | 6.47 | 8.39 | 9.28 | 8.11 | 9.41 |
| CaO | 0.00 | 0.00 | 0.01 | 0.01 | 0.05 | 0.02 | 0.06 | 0.00 | 0.00 | 0.01 | 0.00 | 0.00 | 0.01 | 0.03 |
| $Na_2O$ | 0.13 | 0.15 | 0.20 | 0.14 | 0.19 | 0.14 | 0.09 | 0.19 | 0.15 | 0.20 | 0.19 | 0.26 | 0.13 | 0.26 |
| $K_2O$ | 10.03 | 9.83 | 9.99 | 10.04 | 9.69 | 9.90 | 9.98 | 9.88 | 9.87 | 9.70 | 9.90 | 9.83 | 9.71 | 9.49 |
| Total | 95.79 | 95.66 | 95.99 | 96.97 | 95.62 | 96.01 | 95.21 | 95.71 | 96.28 | 95.67 | 95.51 | 96.60 | 96.76 | 95.73 |
| Oxygen | 11 | 11 | 11 | 11 | 11 | 11 | 11 | 11 | 11 | 11 | 11 | 11 | 11 | 11 |
| Si | 2.73 | 2.77 | 2.74 | 2.73 | 2.75 | 2.78 | 2.74 | 2.74 | 2.76 | 2.74 | 2.74 | 2.74 | 2.74 | 2.78 |
| Ti | 0.25 | 0.20 | 0.21 | 0.25 | 0.22 | 0.27 | 0.30 | 0.21 | 0.21 | 0.28 | 0.13 | 0.23 | 0.26 | 0.25 |
| Al | 1.70 | 1.70 | 1.75 | 1.70 | 1.73 | 1.68 | 1.71 | 1.71 | 1.75 | 1.70 | 1.74 | 1.68 | 1.65 | 1.64 |
| $Fe^{3+}$ | 0.00 | 0.00 | 0.00 | 0.00 | 0.00 | 0.00 | 0.00 | 0.00 | 0.00 | 0.00 | 0.00 | 0.00 | 0.00 | 0.00 |
| $Fe^{2+}$ | 1.49 | 1.44 | 1.36 | 1.44 | 1.43 | 1.41 | 1.42 | 1.45 | 1.43 | 1.49 | 1.38 | 1.27 | 1.40 | 1.24 |
| Mn | 0.00 | 0.01 | 0.00 | 0.01 | 0.00 | 0.01 | 0.00 | 0.00 | 0.00 | 0.01 | 0.00 | 0.00 | 0.01 | 0.00 |
| Mg | 0.79 | 0.86 | 0.90 | 0.85 | 0.85 | 0.83 | 0.79 | 0.85 | 0.83 | 0.77 | 0.98 | 1.07 | 0.95 | 1.10 |
| Ca | 0.00 | 0.00 | 0.00 | 0.00 | 0.00 | 0.00 | 0.01 | 0.00 | 0.00 | 0.00 | 0.00 | 0.00 | 0.00 | 0.00 |
| Na | 0.02 | 0.02 | 0.03 | 0.02 | 0.03 | 0.02 | 0.01 | 0.03 | 0.02 | 0.03 | 0.03 | 0.04 | 0.02 | 0.04 |
| K | 1.02 | 0.99 | 1.00 | 1.00 | 0.98 | 1.00 | 1.02 | 1.00 | 0.99 | 0.99 | 0.99 | 0.97 | 0.97 | 0.95 |
| cations | 8.00 | 8.00 | 8.00 | 8.00 | 8.00 | 8.00 | 8.00 | 8.00 | 8.00 | 8.00 | 8.00 | 8.00 | 8.00 | 8.00 |
| $X_{Fe}$ ($Fe^{2+}$) | 0.65 | 0.63 | 0.60 | 0.63 | 0.63 | 0.63 | 0.64 | 0.63 | 0.63 | 0.66 | 0.58 | 0.54 | 0.60 | 0.53 |
| $X_{Fe}$ (Fetot) | 0.65 | 0.63 | 0.60 | 0.63 | 0.63 | 0.63 | 0.64 | 0.63 | 0.63 | 0.66 | 0.58 | 0.54 | 0.60 | 0.53 |

**Table A4.** (Continued)

| Sample | 526 | | | | | | |
|---|---|---|---|---|---|---|---|
| Analysis | 526L2-24bi | 526L2-33bi | 526L2-36 | 526L2-39-bt | 526L2-45-bt | 526L2-50-bt | 526N-54-bt |
| Spot | #114 | #123 | #126 | #129 | #135 | #140 | #175 |
| (wt%) | | | | | | | |
| $SiO_2$ | 34.53 | 34.24 | 34.16 | 35.30 | 34.75 | 34.37 | 36.26 |
| $TiO_2$ | 4.22 | 3.21 | 3.78 | 4.07 | 3.96 | 4.00 | 3.19 |
| $Al_2O_3$ | 17.74 | 18.46 | 18.38 | 18.07 | 18.08 | 18.43 | 18.72 |
| FeO | 20.36 | 22.49 | 21.77 | 21.55 | 21.81 | 22.43 | 18.93 |
| MnO | 0.02 | 0.01 | 0.07 | 0.03 | 0.06 | 0.07 | 0.04 |
| MgO | 8.11 | 8.30 | 7.20 | 6.60 | 7.47 | 7.31 | 8.56 |
| CaO | 0.00 | 0.03 | 0.02 | 0.08 | 0.00 | 0.00 | 0.01 |
| $Na_2O$ | 0.32 | 0.29 | 0.28 | 0.21 | 0.22 | 0.19 | 0.20 |
| $K_2O$ | 9.63 | 9.16 | 9.50 | 9.93 | 9.72 | 9.40 | 9.87 |
| Total | 94.93 | 96.19 | 95.16 | 95.84 | 96.07 | 96.20 | 95.78 |
| Oxygen | 11 | 11 | 11 | 11 | 11 | 11 | 11 |
| Si | 2.74 | 2.69 | 2.72 | 2.80 | 2.74 | 2.72 | 2.83 |
| Ti | 0.25 | 0.19 | 0.23 | 0.24 | 0.24 | 0.24 | 0.19 |
| Al | 1.66 | 1.71 | 1.73 | 1.69 | 1.68 | 1.72 | 1.73 |
| $Fe^{3+}$ | 0.00 | 0.00 | 0.00 | 0.00 | 0.00 | 0.00 | 0.00 |
| $Fe^{2+}$ | 1.35 | 1.48 | 1.45 | 1.43 | 1.44 | 1.48 | 1.24 |
| Mn | 0.00 | 0.00 | 0.00 | 0.00 | 0.00 | 0.00 | 0.00 |
| Mg | 0.96 | 0.97 | 0.86 | 0.78 | 0.88 | 0.86 | 1.00 |
| Ca | 0.00 | 0.00 | 0.00 | 0.01 | 0.00 | 0.00 | 0.00 |
| Na | 0.05 | 0.04 | 0.04 | 0.03 | 0.03 | 0.03 | 0.03 |
| K | 0.98 | 0.92 | 0.97 | 1.01 | 0.98 | 0.95 | 0.98 |
| cations | 8.00 | 8.00 | 8.00 | 8.00 | 8.00 | 8.00 | 8.00 |
| $X_{Fe}$ ($Fe^{2+}$) | 0.58 | 0.60 | 0.63 | 0.65 | 0.62 | 0.63 | 0.55 |
| $X_{Fe}$ (Fetot) | 0.58 | 0.60 | 0.63 | 0.65 | 0.62 | 0.63 | 0.55 |

**Table A5.** Chemical composition of cordierite from the patch migmatites of the Intermediate series affected by the Ceret contact aureole.

| Sample | 482 | | | | | | | | | | 526 | | | | | | | | | |
|---|---|---|---|---|---|---|---|---|---|---|---|---|---|---|---|---|---|---|---|---|
| Analysis | 482C-3-cd | 482C-7-cd | 482C-13-cd | 482C-14-cd | 482C-26-cd | 482C-29-cd | 482C-33- cd | 482C-36-cd | 482C-39-cd | 482C-15-kfs | 526L2-7-cd | 526L2-11-cd | 526L2-12-cd | 526L2-14-cd | 526L2-17-cd | 526L2-22cd | 526L2-29cd | 526L2-34cd | 526L2-35cd | 526L2-44-cd |
| Spot | #143 | #147 | #153 | #154 | #166 | #169 | #183 | #186 | #189 | #155 | #97 | #101 | #102 | #104 | #107 | #112 | #119 | #124 | #125 | #134 |
| (wt%) | | | | | | | | | | | | | | | | | | | | |
| $SiO_2$ | 47.68 | 48.18 | 48.14 | 47.83 | 47.31 | 47.72 | 47.27 | 47.67 | 47.73 | 47.98 | 48.89 | 48.10 | 47.60 | 48.28 | 47.11 | 47.82 | 47.98 | 47.75 | 48.03 | 47.59 |
| $TiO_2$ | 0.00 | 0.02 | 0.02 | 0.00 | 0.01 | 0.07 | 0.00 | 0.00 | 0.03 | 0.00 | 0.00 | 0.01 | 0.00 | 0.00 | 0.00 | 0.00 | 0.01 | 0.01 | 0.00 | 0.01 |
| $Al_2O_3$ | 31.54 | 31.61 | 31.81 | 31.57 | 31.56 | 31.61 | 31.10 | 31.32 | 31.37 | 31.36 | 31.94 | 31.71 | 31.56 | 31.91 | 31.53 | 30.93 | 31.58 | 31.70 | 31.79 | 31.70 |
| FeO | 10.52 | 10.44 | 10.33 | 10.63 | 10.06 | 10.28 | 10.82 | 11.06 | 10.64 | 10.64 | 8.98 | 9.89 | 10.06 | 10.01 | 9.74 | 9.35 | 8.83 | 9.87 | 10.25 | 10.38 |
| MnO | 0.10 | 0.18 | 0.16 | 0.13 | 0.18 | 0.17 | 0.12 | 0.12 | 0.18 | 0.24 | 0.07 | 0.10 | 0.09 | 0.14 | 0.04 | 0.03 | 0.10 | 0.04 | 0.13 | 0.20 |
| MgO | 6.69 | 6.86 | 6.87 | 6.74 | 6.84 | 7.08 | 6.77 | 6.76 | 6.66 | 6.78 | 8.17 | 7.30 | 7.30 | 7.26 | 7.51 | 7.73 | 8.12 | 7.40 | 7.27 | 6.92 |
| CaO | 0.00 | 0.01 | 0.02 | 0.02 | 0.04 | 0.01 | 0.00 | 0.03 | 0.00 | 0.02 | 0.00 | 0.01 | 0.02 | 0.01 | 0.01 | 0.01 | 0.01 | 0.00 | 0.00 | 0.04 |
| $Na_2O$ | 0.23 | 0.14 | 0.15 | 0.19 | 0.28 | 0.11 | 0.14 | 0.15 | 0.16 | 0.19 | 0.23 | 0.29 | 0.20 | 0.19 | 0.22 | 0.20 | 0.17 | 0.19 | 0.19 | 0.22 |
| $K_2O$ | 0.00 | 0.00 | 0.02 | 0.00 | 0.01 | 0.00 | 0.00 | 0.02 | 0.03 | 0.01 | 0.00 | 0.03 | 0.01 | 0.02 | 0.00 | 0.01 | 0.00 | 0.01 | 0.00 | 0.00 |
| Total | 96.76 | 97.44 | 97.52 | 97.11 | 96.29 | 97.05 | 96.22 | 97.13 | 96.80 | 97.22 | 98.28 | 97.44 | 96.84 | 97.82 | 96.16 | 96.08 | 96.80 | 96.97 | 97.66 | 97.06 |
| Oxygen | 18 | 18 | 18 | 18 | 18 | 18 | 18 | 18 | 18 | 18 | 18 | 18 | 18 | 18 | 18 | 18 | 18 | 18 | 18 | 18 |
| Si | 5.03 | 5.05 | 5.04 | 5.04 | 5.01 | 5.02 | 5.03 | 5.02 | 5.04 | 5.05 | 5.04 | 5.02 | 5.01 | 5.03 | 4.98 | 5.05 | 5.02 | 5.01 | 5.01 | 5.00 |
| Ti | 0.00 | 0.00 | 0.00 | 0.00 | 0.00 | 0.01 | 0.00 | 0.00 | 0.00 | 0.00 | 0.00 | 0.00 | 0.00 | 0.00 | 0.00 | 0.00 | 0.00 | 0.00 | 0.00 | 0.00 |
| Al | 3.93 | 3.91 | 3.93 | 3.92 | 3.94 | 3.92 | 3.90 | 3.89 | 3.91 | 3.89 | 3.88 | 3.90 | 3.91 | 3.92 | 3.93 | 3.85 | 3.90 | 3.92 | 3.91 | 3.93 |
| $Fe^{3+}$ | 0.05 | 0.01 | 0.02 | 0.05 | 0.10 | 0.05 | 0.08 | 0.09 | 0.03 | 0.05 | 0.09 | 0.11 | 0.12 | 0.07 | 0.16 | 0.08 | 0.10 | 0.09 | 0.10 | 0.10 |
| $Fe^{2+}$ | 0.88 | 0.91 | 0.89 | 0.89 | 0.79 | 0.85 | 0.89 | 0.88 | 0.91 | 0.88 | 0.69 | 0.75 | 0.77 | 0.81 | 0.70 | 0.75 | 0.68 | 0.77 | 0.79 | 0.81 |
| Mn | 0.01 | 0.02 | 0.01 | 0.01 | 0.02 | 0.02 | 0.01 | 0.01 | 0.02 | 0.02 | 0.01 | 0.01 | 0.01 | 0.01 | 0.00 | 0.00 | 0.01 | 0.00 | 0.01 | 0.02 |
| Mg | 1.05 | 1.07 | 1.07 | 1.06 | 1.08 | 1.11 | 1.07 | 1.06 | 1.05 | 1.06 | 1.25 | 1.14 | 1.14 | 1.13 | 1.18 | 1.22 | 1.27 | 1.16 | 1.13 | 1.08 |
| Ca | 0.00 | 0.00 | 0.00 | 0.00 | 0.00 | 0.00 | 0.00 | 0.00 | 0.00 | 0.00 | 0.00 | 0.00 | 0.00 | 0.00 | 0.00 | 0.00 | 0.00 | 0.00 | 0.00 | 0.00 |
| Na | 0.05 | 0.03 | 0.03 | 0.04 | 0.06 | 0.02 | 0.03 | 0.03 | 0.03 | 0.04 | 0.05 | 0.06 | 0.04 | 0.04 | 0.05 | 0.04 | 0.03 | 0.04 | 0.04 | 0.04 |
| K | 0.00 | 0.00 | 0.00 | 0.00 | 0.00 | 0.00 | 0.00 | 0.00 | 0.00 | 0.00 | 0.00 | 0.00 | 0.00 | 0.00 | 0.00 | 0.00 | 0.00 | 0.00 | 0.00 | 0.00 |
| cations | 11.00 | 11.00 | 11.00 | 11.00 | 11.00 | 11.00 | 11.00 | 11.00 | 11.00 | 11.00 | 11.00 | 11.00 | 11.00 | 11.00 | 11.00 | 11.00 | 11.00 | 11.00 | 11.00 | 11.00 |
| $X_{Fe}$ ($Fe^{2+}$) | 0.45 | 0.46 | 0.45 | 0.46 | 0.42 | 0.44 | 0.45 | 0.45 | 0.46 | 0.45 | 0.35 | 0.40 | 0.40 | 0.42 | 0.37 | 0.38 | 0.35 | 0.40 | 0.41 | 0.43 |
| $X_{Fe}$ (Fetot) | 0.47 | 0.46 | 0.46 | 0.47 | 0.45 | 0.45 | 0.47 | 0.48 | 0.47 | 0.47 | 0.38 | 0.43 | 0.44 | 0.44 | 0.42 | 0.40 | 0.38 | 0.43 | 0.44 | 0.46 |

**Table A6.** Chemical analyses of a garnet porphyroblast from a patch migmatites of the Intermediate series affected by the Ceret contact aureole.

| Sample | 526N2 | | | | | | | | | | | | | | | | |
|---|---|---|---|---|---|---|---|---|---|---|---|---|---|---|---|---|---|
| Analysis | A_1 | A_2 | A_4 | A_5 | A_6 | A_7 | A_8 | A_10 | A_11 | A_12 | A_13 | A_14 | A_15 | A_16 | A_17 | A_18 | A_20 |
| Spot | #291 | #292 | #294 | #295 | #296 | #297 | #298 | #300 | #301 | #302 | #303 | #304 | #305 | #306 | #307 | #308 | #310 |
| (wt%) | | | | | | | | | | | | | | | | | |
| $SiO_2$ | 36.56 | 37.15 | 37.09 | 37.24 | 37.21 | 37.15 | 37.70 | 37.23 | 37.26 | 37.27 | 37.10 | 37.30 | 36.88 | 37.01 | 37.24 | 37.05 | 37.41 |
| $TiO_2$ | 0.05 | 0.00 | 0.04 | 0.02 | 0.03 | 0.03 | 0.04 | 0.01 | 0.01 | 0.04 | 0.04 | 0.04 | 0.01 | 0.06 | 0.08 | 0.06 | 0.03 |
| $Al_2O_3$ | 21.20 | 21.10 | 21.37 | 21.43 | 21.23 | 21.27 | 21.26 | 21.07 | 21.22 | 21.33 | 21.16 | 21.19 | 21.20 | 21.42 | 20.97 | 21.41 | 21.07 |
| FeO | 37.82 | 36.75 | 35.89 | 35.86 | 36.54 | 35.22 | 35.89 | 35.20 | 35.33 | 35.49 | 35.44 | 35.95 | 35.50 | 35.83 | 35.97 | 35.91 | 35.47 |
| MnO | 1.74 | 1.39 | 1.57 | 1.55 | 1.63 | 1.70 | 1.55 | 1.70 | 1.66 | 1.82 | 1.74 | 1.62 | 1.62 | 1.65 | 1.54 | 1.45 | 1.54 |
| MgO | 2.02 | 3.59 | 3.75 | 3.85 | 3.96 | 3.92 | 3.93 | 3.78 | 4.07 | 4.11 | 4.08 | 4.07 | 4.00 | 3.92 | 3.64 | 3.68 | 3.91 |
| CaO | 1.48 | 1.45 | 1.54 | 1.58 | 1.55 | 1.54 | 1.60 | 1.48 | 1.52 | 1.49 | 1.43 | 1.45 | 1.50 | 1.47 | 1.45 | 1.40 | 1.52 |
| $Na_2O$ | 0.00 | 0.00 | 0.00 | 0.00 | 0.00 | 0.00 | 0.00 | 0.00 | 0.00 | 0.00 | 0.00 | 0.00 | 0.00 | 0.00 | 0.00 | 0.00 | 0.00 |
| $K_2O$ | 0.00 | 0.00 | 0.00 | 0.00 | 0.00 | 0.00 | 0.00 | 0.00 | 0.00 | 0.00 | 0.00 | 0.00 | 0.00 | 0.00 | 0.00 | 0.00 | 0.00 |
| Total | 100.87 | 101.43 | 101.25 | 101.53 | 102.15 | 100.83 | 101.97 | 100.47 | 101.07 | 101.55 | 100.99 | 101.62 | 100.71 | 101.36 | 100.89 | 100.96 | 100.95 |
| Oxygen | 12 | 12 | 12 | 12 | 12 | 12 | 12 | 12 | 12 | 12 | 12 | 12 | 12 | 12 | 12 | 12 | 12 |
| Si | 2.94 | 2.95 | 2.94 | 2.94 | 2.92 | 2.95 | 2.97 | 2.97 | 2.95 | 2.94 | 2.94 | 2.94 | 2.94 | 2.93 | 2.97 | 2.95 | 2.97 |
| Ti | 0.00 | 0.00 | 0.00 | 0.00 | 0.00 | 0.00 | 0.00 | 0.00 | 0.00 | 0.00 | 0.00 | 0.00 | 0.00 | 0.00 | 0.00 | 0.00 | 0.00 |
| Al | 2.01 | 1.97 | 2.00 | 2.00 | 1.97 | 1.99 | 1.97 | 1.98 | 1.98 | 1.98 | 1.98 | 1.97 | 1.99 | 2.00 | 1.97 | 2.01 | 1.97 |
| $Fe^{3+}$ | 0.09 | 0.13 | 0.12 | 0.12 | 0.18 | 0.10 | 0.09 | 0.07 | 0.11 | 0.13 | 0.13 | 0.14 | 0.14 | 0.14 | 0.08 | 0.09 | 0.08 |
| $Fe^{2+}$ | 2.46 | 2.31 | 2.26 | 2.25 | 2.22 | 2.24 | 2.27 | 2.28 | 2.23 | 2.21 | 2.23 | 2.24 | 2.22 | 2.23 | 2.31 | 2.30 | 2.28 |
| Mn | 0.12 | 0.09 | 0.11 | 0.10 | 0.11 | 0.11 | 0.10 | 0.11 | 0.11 | 0.12 | 0.12 | 0.11 | 0.11 | 0.11 | 0.10 | 0.10 | 0.10 |
| Mg | 0.24 | 0.42 | 0.44 | 0.45 | 0.46 | 0.46 | 0.46 | 0.45 | 0.48 | 0.48 | 0.48 | 0.48 | 0.47 | 0.46 | 0.43 | 0.44 | 0.46 |
| Ca | 0.13 | 0.12 | 0.13 | 0.13 | 0.13 | 0.13 | 0.13 | 0.13 | 0.13 | 0.13 | 0.12 | 0.12 | 0.13 | 0.12 | 0.12 | 0.12 | 0.13 |
| Na | 0.00 | 0.00 | 0.00 | 0.00 | 0.00 | 0.00 | 0.00 | 0.00 | 0.00 | 0.00 | 0.00 | 0.00 | 0.00 | 0.00 | 0.00 | 0.00 | 0.00 |
| K | 0.00 | 0.00 | 0.00 | 0.00 | 0.00 | 0.00 | 0.00 | 0.00 | 0.00 | 0.00 | 0.00 | 0.00 | 0.00 | 0.00 | 0.00 | 0.00 | 0.00 |
| cations | 8.00 | 8.00 | 8.00 | 8.00 | 8.00 | 8.00 | 8.00 | 8.00 | 8.00 | 8.00 | 8.00 | 8.00 | 8.00 | 8.00 | 8.00 | 8.00 | 8.00 |
| grs | 0.04 | 0.04 | 0.04 | 0.04 | 0.04 | 0.04 | 0.04 | 0.04 | 0.04 | 0.04 | 0.04 | 0.04 | 0.04 | 0.04 | 0.04 | 0.04 | 0.04 |
| alm | 0.84 | 0.79 | 0.78 | 0.77 | 0.77 | 0.77 | 0.77 | 0.77 | 0.76 | 0.76 | 0.77 | 0.77 | 0.77 | 0.77 | 0.78 | 0.79 | 0.77 |
| prp | 0.08 | 0.14 | 0.14 | 0.15 | 0.15 | 0.15 | 0.15 | 0.15 | 0.16 | 0.16 | 0.16 | 0.16 | 0.15 | 0.15 | 0.14 | 0.14 | 0.15 |
| sps | 0.04 | 0.03 | 0.03 | 0.03 | 0.03 | 0.04 | 0.03 | 0.04 | 0.04 | 0.04 | 0.04 | 0.04 | 0.04 | 0.04 | 0.03 | 0.03 | 0.03 |
| $X_{Fe}$ ($Fe^{2+}$) | 0.91 | 0.84 | 0.84 | 0.83 | 0.83 | 0.83 | 0.83 | 0.84 | 0.82 | 0.82 | 0.82 | 0.82 | 0.82 | 0.83 | 0.84 | 0.84 | 0.83 |
| $X_{Fe}$ (Fetot) | 0.91 | 0.85 | 0.84 | 0.84 | 0.84 | 0.83 | 0.84 | 0.84 | 0.83 | 0.83 | 0.83 | 0.83 | 0.83 | 0.84 | 0.85 | 0.85 | 0.84 |

**Table A6.** (Continued)

| Sample | 526N2 | | | | | | | | | | | | | | | | |
|---|---|---|---|---|---|---|---|---|---|---|---|---|---|---|---|---|---|
| Analysis | A_21 | A_22 | A_23 | A_24 | A_25 | A_26 | A_27 | A_28 | A_29 | A_30 | A_34 | A_35 | A_36 | A_37 | A_38 | A_39 | A_40 |
| Spot | #311 | #312 | #313 | #314 | #315 | #316 | #317 | #318 | #319 | #320 | #324 | #325 | #326 | #327 | #328 | #329 | #330 |
| (wt%) | | | | | | | | | | | | | | | | | |
| $SiO_2$ | 37.06 | 37.39 | 37.13 | 37.20 | 37.27 | 37.53 | 36.98 | 37.10 | 37.38 | 37.59 | 37.51 | 37.41 | 37.36 | 37.20 | 37.04 | 36.97 | 36.68 |
| $TiO_2$ | 0.06 | 0.02 | 0.04 | 0.02 | 0.03 | 0.02 | 0.02 | 0.04 | 0.06 | 0.02 | 0.05 | 0.02 | 0.02 | 0.04 | 0.03 | 0.02 | 0.02 |
| $Al_2O_3$ | 21.37 | 21.37 | 21.18 | 21.36 | 21.34 | 21.31 | 21.44 | 21.42 | 21.00 | 21.28 | 21.30 | 21.31 | 21.26 | 21.04 | 21.06 | 21.25 | 20.95 |
| FeO | 35.48 | 35.83 | 36.00 | 35.64 | 36.33 | 36.03 | 35.52 | 35.61 | 36.16 | 35.67 | 36.11 | 36.38 | 36.42 | 36.48 | 37.25 | 37.40 | 37.49 |
| MnO | 1.60 | 1.65 | 1.50 | 1.50 | 1.54 | 1.59 | 1.47 | 1.45 | 1.42 | 1.27 | 1.16 | 1.16 | 1.05 | 1.18 | 1.23 | 1.46 | 1.66 |
| MgO | 3.94 | 4.06 | 3.95 | 4.02 | 4.08 | 4.18 | 3.89 | 4.00 | 4.10 | 3.96 | 4.01 | 3.94 | 3.68 | 3.72 | 3.41 | 3.08 | 2.30 |
| CaO | 1.42 | 1.50 | 1.54 | 1.55 | 1.49 | 1.46 | 1.53 | 1.53 | 1.56 | 1.55 | 1.53 | 1.48 | 1.38 | 1.46 | 1.45 | 1.46 | 1.50 |
| $Na_2O$ | 0.00 | 0.00 | 0.00 | 0.00 | 0.00 | 0.00 | 0.00 | 0.00 | 0.00 | 0.00 | 0.00 | 0.00 | 0.00 | 0.00 | 0.00 | 0.00 | 0.00 |
| $K_2O$ | 0.00 | 0.00 | 0.00 | 0.00 | 0.00 | 0.00 | 0.00 | 0.00 | 0.00 | 0.00 | 0.00 | 0.00 | 0.00 | 0.00 | 0.00 | 0.00 | 0.00 |
| Total | 100.93 | 101.82 | 101.34 | 101.29 | 102.08 | 102.12 | 100.85 | 101.15 | 101.68 | 101.34 | 101.67 | 101.70 | 101.17 | 101.12 | 101.47 | 101.64 | 100.60 |
| Oxygen | 12 | 12 | 12 | 12 | 12 | 12 | 12 | 12 | 12 | 12 | 12 | 12 | 12 | 12 | 12 | 12 | 12 |
| Si | 2.94 | 2.94 | 2.94 | 2.94 | 2.93 | 2.95 | 2.94 | 2.94 | 2.95 | 2.97 | 2.96 | 2.95 | 2.97 | 2.96 | 2.94 | 2.94 | 2.96 |
| Ti | 0.00 | 0.00 | 0.00 | 0.00 | 0.00 | 0.00 | 0.00 | 0.00 | 0.00 | 0.00 | 0.00 | 0.00 | 0.00 | 0.00 | 0.00 | 0.00 | 0.00 |
| Al | 2.00 | 1.98 | 1.98 | 1.99 | 1.98 | 1.97 | 2.01 | 2.00 | 1.95 | 1.98 | 1.98 | 1.98 | 1.99 | 1.97 | 1.97 | 1.99 | 1.99 |
| $Fe^{3+}$ | 0.10 | 0.13 | 0.14 | 0.12 | 0.16 | 0.14 | 0.11 | 0.12 | 0.14 | 0.07 | 0.10 | 0.11 | 0.07 | 0.11 | 0.14 | 0.13 | 0.09 |
| $Fe^{2+}$ | 2.25 | 2.23 | 2.24 | 2.24 | 2.22 | 2.23 | 2.25 | 2.24 | 2.24 | 2.29 | 2.28 | 2.29 | 2.34 | 2.31 | 2.33 | 2.35 | 2.44 |
| Mn | 0.11 | 0.11 | 0.10 | 0.10 | 0.10 | 0.11 | 0.10 | 0.10 | 0.09 | 0.09 | 0.08 | 0.08 | 0.07 | 0.08 | 0.08 | 0.10 | 0.11 |
| Mg | 0.47 | 0.48 | 0.47 | 0.47 | 0.48 | 0.49 | 0.46 | 0.47 | 0.48 | 0.47 | 0.47 | 0.46 | 0.44 | 0.44 | 0.40 | 0.36 | 0.28 |
| Ca | 0.12 | 0.13 | 0.13 | 0.13 | 0.13 | 0.12 | 0.13 | 0.13 | 0.13 | 0.13 | 0.13 | 0.13 | 0.12 | 0.12 | 0.12 | 0.12 | 0.13 |
| Na | 0.00 | 0.00 | 0.00 | 0.00 | 0.00 | 0.00 | 0.00 | 0.00 | 0.00 | 0.00 | 0.00 | 0.00 | 0.00 | 0.00 | 0.00 | 0.00 | 0.00 |
| K | 0.00 | 0.00 | 0.00 | 0.00 | 0.00 | 0.00 | 0.00 | 0.00 | 0.00 | 0.00 | 0.00 | 0.00 | 0.00 | 0.00 | 0.00 | 0.00 | 0.00 |
| cations | 8.00 | 8.00 | 8.00 | 8.00 | 8.00 | 8.00 | 8.00 | 8.00 | 8.00 | 8.00 | 8.00 | 8.00 | 8.00 | 8.00 | 8.00 | 8.00 | 8.00 |
| grs | 0.04 | 0.04 | 0.04 | 0.04 | 0.04 | 0.04 | 0.04 | 0.04 | 0.04 | 0.04 | 0.04 | 0.04 | 0.04 | 0.04 | 0.04 | 0.04 | 0.04 |
| alm | 0.77 | 0.77 | 0.77 | 0.77 | 0.77 | 0.77 | 0.77 | 0.77 | 0.77 | 0.78 | 0.78 | 0.78 | 0.80 | 0.79 | 0.80 | 0.81 | 0.83 |
| prp | 0.15 | 0.16 | 0.15 | 0.15 | 0.15 | 0.16 | 0.15 | 0.15 | 0.16 | 0.15 | 0.15 | 0.15 | 0.14 | 0.14 | 0.13 | 0.12 | 0.09 |
| sps | 0.04 | 0.04 | 0.03 | 0.03 | 0.03 | 0.03 | 0.03 | 0.03 | 0.03 | 0.03 | 0.03 | 0.03 | 0.02 | 0.03 | 0.03 | 0.03 | 0.04 |
| $X_{Fe}$ ($Fe^{2+}$) | 0.83 | 0.82 | 0.83 | 0.83 | 0.82 | 0.82 | 0.83 | 0.83 | 0.82 | 0.83 | 0.83 | 0.83 | 0.84 | 0.84 | 0.85 | 0.87 | 0.90 |
| $X_{Fe}$ (Fetot) | 0.83 | 0.83 | 0.84 | 0.83 | 0.83 | 0.83 | 0.84 | 0.83 | 0.83 | 0.83 | 0.83 | 0.84 | 0.85 | 0.85 | 0.86 | 0.87 | 0.90 |

**Table A7.** Chemical composition of biotite from the stromatic migmatites of the Intermediate series affected by the Ceret contact aureole.

| Sample | 472B | | | | | | | | | | | | | | |
|---|---|---|---|---|---|---|---|---|---|---|---|---|---|---|---|
| Analysis | 472b-1-bt | 472b-5-bt | 472b-8-bt | 472b-10-bt | 472b-12-bt | 472b-15-bt | 472b-22-bt | 472b-24-bt | 472b-29-bt | 472b-31-bt | 472b-43-bt | 472b-44-bt | 472b-46-bt | 472b-48-bi | 472b-59bi |
| Spot | #1 | #5 | #8 | #10 | #12 | #15 | #22 | #24 | #29 | #31 | #43 | #44 | #46 | #48 | #59 |
| (wt%) | | | | | | | | | | | | | | | |
| $SiO_2$ | 38.99 | 35.89 | 35.93 | 36.48 | 34.89 | 35.34 | 36.00 | 35.59 | 38.51 | 36.52 | 36.59 | 35.75 | 35.87 | 35.72 | 35.93 |
| $TiO_2$ | 3.61 | 3.23 | 2.59 | 2.82 | 3.16 | 3.36 | 3.03 | 3.25 | 2.76 | 2.71 | 2.25 | 3.09 | 2.65 | 2.25 | 3.27 |
| $Al_2O_3$ | 19.00 | 17.79 | 17.96 | 18.16 | 17.65 | 17.82 | 18.42 | 18.09 | 19.70 | 19.33 | 18.77 | 18.65 | 18.59 | 19.11 | 18.47 |
| FeO | 12.92 | 17.06 | 17.31 | 17.40 | 17.29 | 17.11 | 17.47 | 17.43 | 17.07 | 16.23 | 16.53 | 15.75 | 16.10 | 16.05 | 17.00 |
| MnO | 0.09 | 0.14 | 0.15 | 0.10 | 0.12 | 0.17 | 0.18 | 0.18 | 0.19 | 0.06 | 0.06 | 0.00 | 0.07 | 0.08 | 0.04 |
| MgO | 9.33 | 11.17 | 11.25 | 11.21 | 11.07 | 10.98 | 11.74 | 10.68 | 11.97 | 11.30 | 11.33 | 10.95 | 10.88 | 11.57 | 8.51 |
| CaO | 0.00 | 0.00 | 0.02 | 0.02 | 0.00 | 0.00 | 0.02 | 0.03 | 0.03 | 0.00 | 0.00 | 0.08 | 0.04 | 0.07 | 0.02 |
| $Na_2O$ | 0.31 | 0.32 | 0.40 | 0.30 | 0.37 | 0.35 | 0.28 | 0.25 | 0.31 | 0.31 | 0.30 | 0.32 | 0.26 | 0.33 | 0.23 |
| $K_2O$ | 10.22 | 9.54 | 9.39 | 9.39 | 9.40 | 9.65 | 8.73 | 9.27 | 8.91 | 9.61 | 9.33 | 9.51 | 9.38 | 9.41 | 9.53 |
| Total | 94.47 | 95.14 | 95.00 | 95.88 | 93.95 | 94.78 | 95.87 | 94.77 | 99.45 | 96.07 | 95.16 | 94.10 | 93.84 | 94.59 | 93.00 |
| Oxygen | 11 | 11 | 11 | 11 | 11 | 11 | 11 | 11 | 11 | 11 | 11 | 11 | 11 | 11 | 11 |
| Si | 3.04 | 2.78 | 2.79 | 2.81 | 2.74 | 2.75 | 2.77 | 2.78 | 2.85 | 2.79 | 2.82 | 2.79 | 2.81 | 2.76 | 2.88 |
| Ti | 0.21 | 0.19 | 0.15 | 0.16 | 0.19 | 0.20 | 0.18 | 0.19 | 0.15 | 0.16 | 0.13 | 0.18 | 0.16 | 0.13 | 0.20 |
| Al | 1.75 | 1.63 | 1.64 | 1.65 | 1.63 | 1.64 | 1.67 | 1.67 | 1.72 | 1.74 | 1.71 | 1.72 | 1.72 | 1.74 | 1.75 |
| $Fe^{3+}$ | 0.00 | 0.00 | 0.00 | 0.00 | 0.00 | 0.00 | 0.00 | 0.00 | 0.00 | 0.00 | 0.00 | 0.00 | 0.00 | 0.00 | 0.00 |
| $Fe^{2+}$ | 0.84 | 1.11 | 1.12 | 1.12 | 1.14 | 1.11 | 1.12 | 1.14 | 1.06 | 1.04 | 1.07 | 1.03 | 1.06 | 1.04 | 1.14 |
| Mn | 0.01 | 0.01 | 0.01 | 0.01 | 0.01 | 0.01 | 0.01 | 0.01 | 0.01 | 0.00 | 0.00 | 0.00 | 0.00 | 0.01 | 0.00 |
| Mg | 1.09 | 1.29 | 1.30 | 1.29 | 1.30 | 1.28 | 1.35 | 1.24 | 1.32 | 1.29 | 1.30 | 1.28 | 1.27 | 1.33 | 1.02 |
| Ca | 0.00 | 0.00 | 0.00 | 0.00 | 0.00 | 0.00 | 0.00 | 0.00 | 0.00 | 0.00 | 0.00 | 0.01 | 0.00 | 0.01 | 0.00 |
| Na | 0.05 | 0.05 | 0.06 | 0.04 | 0.06 | 0.05 | 0.04 | 0.04 | 0.04 | 0.05 | 0.04 | 0.05 | 0.04 | 0.05 | 0.04 |
| K | 1.02 | 0.94 | 0.93 | 0.92 | 0.94 | 0.96 | 0.86 | 0.92 | 0.84 | 0.94 | 0.92 | 0.95 | 0.94 | 0.93 | 0.98 |
| cations | 8.00 | 8.00 | 8.00 | 8.00 | 8.00 | 8.00 | 8.00 | 8.00 | 8.00 | 8.00 | 8.00 | 8.00 | 8.00 | 8.00 | 8.00 |
| $X_{Fe}$ ($Fe^{2+}$) | 0.44 | 0.46 | 0.46 | 0.47 | 0.47 | 0.47 | 0.45 | 0.48 | 0.44 | 0.45 | 0.45 | 0.45 | 0.45 | 0.44 | 0.53 |
| $X_{Fe}$ (Fetot) | 0.44 | 0.46 | 0.46 | 0.47 | 0.47 | 0.47 | 0.45 | 0.48 | 0.44 | 0.45 | 0.45 | 0.45 | 0.45 | 0.44 | 0.53 |

**Table A7.** (Continued)

| Sample | 472B | | | | 529 | | |
|---|---|---|---|---|---|---|---|
| Analysis | 472b-61bi | 472b-63bi | 472b-87-bt | 472b-90-bt | 529a-1-51 bi | 529a-1-54-bi | 529a-1-68 bi |
| Spot | #61 | #63 | #87 | #90 | #26 | #27 | #29 |
| (wt%) | | | | | | | |
| $SiO_2$ | 35.43 | 34.82 | 36.25 | 36.93 | 35.93 | 36.35 | 35.40 |
| $TiO_2$ | 3.18 | 3.62 | 2.79 | 2.13 | 3.26 | 2.23 | 2.93 |
| $Al_2O_3$ | 18.81 | 17.00 | 18.01 | 18.99 | 17.67 | 18.59 | 17.87 |
| FeO | 16.81 | 17.75 | 16.54 | 15.93 | 17.69 | 16.48 | 17.56 |
| MnO | 0.08 | 0.08 | 0.06 | 0.07 | 0.07 | 0.09 | 0.07 |
| MgO | 10.60 | 10.81 | 10.68 | 11.98 | 11.34 | 11.85 | 10.97 |
| CaO | 0.03 | 0.02 | 0.02 | 0.02 | 0.00 | 0.02 | 0.00 |
| $Na_2O$ | 0.24 | 0.23 | 0.30 | 0.36 | 0.29 | 0.28 | 0.22 |
| $K_2O$ | 9.60 | 9.53 | 9.32 | 9.62 | 9.00 | 8.60 | 8.43 |
| Total | 94.78 | 93.86 | 93.97 | 96.03 | 95.25 | 94.49 | 93.45 |
| Oxygen | 11 | 11 | 11 | 11 | 11 | 11 | 11 |
| Si | 2.76 | 2.75 | 2.85 | 2.81 | 2.79 | 2.82 | 2.81 |
| Ti | 0.19 | 0.22 | 0.16 | 0.12 | 0.19 | 0.13 | 0.17 |
| Al | 1.73 | 1.58 | 1.67 | 1.70 | 1.62 | 1.70 | 1.67 |
| $Fe^{3+}$ | 0.00 | 0.00 | 0.00 | 0.00 | 0.00 | 0.00 | 0.00 |
| $Fe^{2+}$ | 1.10 | 1.17 | 1.09 | 1.01 | 1.15 | 1.07 | 1.16 |
| Mn | 0.01 | 0.01 | 0.00 | 0.00 | 0.00 | 0.01 | 0.00 |
| Mg | 1.23 | 1.27 | 1.25 | 1.36 | 1.31 | 1.37 | 1.30 |
| Ca | 0.00 | 0.00 | 0.00 | 0.00 | 0.00 | 0.00 | 0.00 |
| Na | 0.04 | 0.04 | 0.05 | 0.05 | 0.04 | 0.04 | 0.03 |
| K | 0.95 | 0.96 | 0.93 | 0.93 | 0.89 | 0.85 | 0.85 |
| cations | 8.00 | 8.00 | 8.00 | 8.00 | 8.00 | 8.00 | 8.00 |
| $X_{Fe}$ ($Fe^{2+}$) | 0.47 | 0.48 | 0.46 | 0.43 | 0.47 | 0.44 | 0.47 |
| $X_{Fe}$ (Fetot) | 0.47 | 0.48 | 0.46 | 0.43 | 0.47 | 0.44 | 0.47 |

**Table A8.** Chemical composition of cordierite from the stromatic migmatites of the Intermediate series affected by the Ceret contact aureole.

| Sample | 472B | | | | | | | | | | | | | | | | |
|---|---|---|---|---|---|---|---|---|---|---|---|---|---|---|---|---|---|
| Analysis | 472b-2-cd | 472b-3-cd | 472b-6-cd | 472b-7-cd | 472b-9-cd | 472b-11-cd | 472b-13-cd | 472b-16-cd | 472b-17-cd | 472b-18-cd | 472b-19-cd | 472b-20-cd | 472b-21-cd | 472b-26-cd | 472b-28-cd | 472b-30-cd | 472b-32-cd |
| Spot | #2 | #3 | #6 | #7 | #9 | #11 | #13 | #16 | #17 | #18 | #19 | #20 | #21 | #26 | #28 | #30 | #32 |
| (wt%) | | | | | | | | | | | | | | | | | |
| $SiO_2$ | 47.91 | 47.78 | 48.68 | 48.61 | 49.10 | 48.08 | 48.09 | 48.32 | 47.07 | 47.52 | 48.57 | 48.43 | 48.37 | 47.35 | 47.44 | 47.34 | 48.45 |
| $TiO_2$ | 0.01 | 0.01 | 0.01 | 0.01 | 0.00 | 0.06 | 0.01 | 0.02 | 0.01 | 0.01 | 0.00 | 0.01 | 0.05 | 0.02 | 0.02 | 0.00 | 0.02 |
| $Al_2O_3$ | 31.63 | 31.82 | 32.06 | 32.09 | 32.21 | 31.74 | 31.99 | 32.11 | 31.24 | 31.53 | 32.12 | 32.05 | 32.24 | 31.32 | 31.17 | 31.17 | 32.12 |
| FeO | 7.00 | 7.22 | 6.82 | 7.49 | 7.24 | 7.52 | 7.01 | 6.82 | 7.15 | 6.88 | 7.34 | 6.98 | 6.96 | 7.21 | 7.25 | 6.92 | 7.48 |
| MnO | 0.30 | 0.26 | 0.36 | 0.28 | 0.24 | 0.31 | 0.38 | 0.23 | 0.28 | 0.24 | 0.25 | 0.34 | 0.26 | 0.26 | 0.29 | 0.14 | 0.22 |
| MgO | 9.06 | 8.89 | 8.89 | 9.06 | 9.00 | 9.01 | 9.02 | 9.04 | 9.05 | 8.62 | 8.86 | 8.98 | 8.99 | 8.78 | 8.71 | 8.99 | 9.15 |
| CaO | 0.02 | 0.03 | 0.00 | 0.01 | 0.02 | 0.01 | 0.01 | 0.02 | 0.03 | 0.16 | 0.01 | 0.01 | 0.02 | 0.14 | 0.00 | 0.05 | 0.04 |
| $Na_2O$ | 0.25 | 0.27 | 0.27 | 0.24 | 0.16 | 0.22 | 0.21 | 0.25 | 0.18 | 0.33 | 0.38 | 0.22 | 0.30 | 0.37 | 0.47 | 0.20 | 0.24 |
| $K_2O$ | 0.01 | 0.02 | 0.03 | 0.01 | 0.00 | 0.01 | 0.00 | 0.02 | 0.02 | 0.08 | 0.00 | 0.00 | 0.00 | 0.02 | 0.00 | 0.01 | 0.01 |
| Total | 96.19 | 96.30 | 97.12 | 97.80 | 97.97 | 96.96 | 96.72 | 96.83 | 95.03 | 95.37 | 97.53 | 97.02 | 97.19 | 95.47 | 95.35 | 94.82 | 97.73 |
| Oxygen | 18 | 18 | 18 | 18 | 18 | 18 | 18 | 18 | 18 | 18 | 18 | 18 | 18 | 18 | 18 | 18 | 18 |
| Si | 5.00 | 4.99 | 5.04 | 5.00 | 5.04 | 4.99 | 5.00 | 5.01 | 4.98 | 5.01 | 5.01 | 5.02 | 5.00 | 4.98 | 5.00 | 5.01 | 4.98 |
| Ti | 0.00 | 0.00 | 0.00 | 0.00 | 0.00 | 0.00 | 0.00 | 0.00 | 0.00 | 0.00 | 0.00 | 0.00 | 0.00 | 0.00 | 0.00 | 0.00 | 0.00 |
| Al | 3.89 | 3.91 | 3.91 | 3.89 | 3.90 | 3.88 | 3.92 | 3.92 | 3.89 | 3.91 | 3.90 | 3.91 | 3.93 | 3.89 | 3.87 | 3.89 | 3.89 |
| $Fe^{3+}$ | 0.15 | 0.17 | 0.07 | 0.16 | 0.04 | 0.17 | 0.13 | 0.11 | 0.19 | 0.15 | 0.16 | 0.09 | 0.13 | 0.22 | 0.22 | 0.12 | 0.18 |
| $Fe^{2+}$ | 0.46 | 0.46 | 0.52 | 0.49 | 0.58 | 0.48 | 0.48 | 0.49 | 0.44 | 0.46 | 0.47 | 0.51 | 0.47 | 0.41 | 0.41 | 0.49 | 0.46 |
| Mn | 0.03 | 0.02 | 0.03 | 0.02 | 0.02 | 0.03 | 0.03 | 0.02 | 0.03 | 0.02 | 0.02 | 0.03 | 0.02 | 0.02 | 0.03 | 0.01 | 0.02 |
| Mg | 1.41 | 1.38 | 1.37 | 1.39 | 1.38 | 1.39 | 1.40 | 1.40 | 1.43 | 1.35 | 1.36 | 1.39 | 1.38 | 1.38 | 1.37 | 1.42 | 1.40 |
| Ca | 0.00 | 0.00 | 0.00 | 0.00 | 0.00 | 0.00 | 0.00 | 0.00 | 0.00 | 0.02 | 0.00 | 0.00 | 0.00 | 0.02 | 0.00 | 0.01 | 0.00 |
| Na | 0.05 | 0.05 | 0.05 | 0.05 | 0.03 | 0.04 | 0.04 | 0.05 | 0.04 | 0.07 | 0.08 | 0.04 | 0.06 | 0.08 | 0.10 | 0.04 | 0.05 |
| K | 0.00 | 0.00 | 0.00 | 0.00 | 0.00 | 0.00 | 0.00 | 0.00 | 0.00 | 0.01 | 0.00 | 0.00 | 0.00 | 0.00 | 0.00 | 0.00 | 0.00 |
| cations | 11.00 | 11.00 | 11.00 | 11.00 | 11.00 | 11.00 | 11.00 | 11.00 | 11.00 | 11.00 | 11.00 | 11.00 | 11.00 | 11.00 | 11.00 | 11.00 | 11.00 |
| $X_{Fe}$ ($Fe^{2+}$) | 0.25 | 0.25 | 0.27 | 0.26 | 0.30 | 0.26 | 0.26 | 0.26 | 0.24 | 0.25 | 0.26 | 0.27 | 0.25 | 0.23 | 0.23 | 0.26 | 0.25 |
| $X_{Fe}$ (Fetot) | 0.30 | 0.31 | 0.30 | 0.32 | 0.31 | 0.32 | 0.30 | 0.30 | 0.31 | 0.31 | 0.32 | 0.30 | 0.30 | 0.32 | 0.32 | 0.30 | 0.31 |

**Table A8.** (Continued)

| Sample | 472B | | | | | | | | 529 | | | | | | |
|---|---|---|---|---|---|---|---|---|---|---|---|---|---|---|---|
| Analysis | 472b-35-cd | 472b-40-cd | 472b-42-cd | 472b-57cd | 472b-81-cd | 472b-84-cd | 472b-86-cd | 472b-89-cd | 529a-1-40cd | 529a-1-49 cd | 529a-1-50 cd | 529a-1-55 cd | 529a-1-69 cd | 529a-1-70 cd | 529a-1-71 cd |
| Spot | #35 | #40 | #42 | #57 | #81 | #84 | #86 | #89 | #23 | #24 | #25 | #28 | #30 | #31 | #32 |
| (wt%) | | | | | | | | | | | | | | | |
| $SiO_2$ | 49.73 | 49.13 | 48.38 | 47.49 | 48.61 | 48.58 | 48.26 | 48.82 | 47.89 | 47.80 | 47.97 | 48.54 | 48.29 | 48.37 | 48.62 |
| $TiO_2$ | 0.03 | 0.00 | 0.00 | 0.01 | 0.02 | 0.01 | 0.01 | 0.06 | 0.00 | 0.02 | 0.00 | 0.07 | 0.05 | 0.01 | 0.00 |
| $Al_2O_3$ | 32.90 | 32.15 | 31.73 | 31.41 | 31.71 | 32.15 | 31.64 | 31.91 | 33.02 | 32.62 | 32.97 | 33.12 | 32.63 | 32.98 | 32.97 |
| FeO | 6.69 | 6.57 | 6.86 | 6.91 | 7.28 | 6.75 | 6.79 | 6.85 | 7.23 | 7.31 | 7.27 | 6.69 | 7.20 | 7.24 | 7.11 |
| MnO | 0.22 | 0.21 | 0.27 | 0.14 | 0.14 | 0.27 | 0.19 | 0.25 | 0.25 | 0.22 | 0.21 | 0.30 | 0.22 | 0.20 | 0.28 |
| MgO | 9.38 | 9.16 | 8.79 | 8.87 | 9.03 | 9.15 | 8.98 | 9.22 | 9.02 | 8.88 | 8.92 | 9.07 | 8.83 | 8.96 | 9.14 |
| CaO | 0.04 | 0.02 | 0.02 | 0.02 | 0.03 | 0.04 | 0.03 | 0.01 | 0.00 | 0.02 | 0.01 | 0.05 | 0.00 | 0.02 | 0.03 |
| $Na_2O$ | 0.52 | 0.45 | 0.33 | 0.38 | 0.33 | 0.24 | 0.29 | 0.40 | 0.32 | 0.43 | 0.40 | 0.40 | 0.38 | 0.30 | 0.24 |
| $K_2O$ | 0.02 | 0.00 | 0.00 | 0.02 | 0.00 | 0.00 | 0.02 | 0.00 | 0.00 | 0.00 | 0.00 | 0.01 | 0.00 | 0.10 | 0.00 |
| Total | 99.53 | 97.69 | 96.38 | 95.25 | 97.15 | 97.19 | 96.21 | 97.52 | 97.73 | 97.30 | 97.75 | 98.25 | 97.60 | 98.18 | 98.39 |
| Oxygen | 18 | 18 | 18 | 18 | 18 | 18 | 18 | 18 | 18 | 18 | 18 | 18 | 18 | 18 | 18 |
| Si | 5.00 | 5.04 | 5.04 | 5.00 | 5.03 | 5.02 | 5.04 | 5.02 | 4.92 | 4.93 | 4.92 | 4.95 | 4.97 | 4.95 | 4.96 |
| Ti | 0.00 | 0.00 | 0.00 | 0.00 | 0.00 | 0.00 | 0.00 | 0.00 | 0.00 | 0.00 | 0.00 | 0.01 | 0.00 | 0.00 | 0.00 |
| Al | 3.90 | 3.89 | 3.90 | 3.90 | 3.87 | 3.91 | 3.89 | 3.87 | 4.00 | 3.97 | 3.99 | 3.98 | 3.96 | 3.97 | 3.97 |
| $Fe^{3+}$ | 0.20 | 0.12 | 0.08 | 0.17 | 0.14 | 0.10 | 0.10 | 0.16 | 0.23 | 0.26 | 0.24 | 0.19 | 0.17 | 0.20 | 0.16 |
| $Fe^{2+}$ | 0.37 | 0.44 | 0.52 | 0.43 | 0.49 | 0.48 | 0.50 | 0.43 | 0.39 | 0.37 | 0.38 | 0.39 | 0.45 | 0.42 | 0.45 |
| Mn | 0.02 | 0.02 | 0.02 | 0.01 | 0.01 | 0.02 | 0.02 | 0.02 | 0.02 | 0.02 | 0.02 | 0.03 | 0.02 | 0.02 | 0.02 |
| Mg | 1.41 | 1.40 | 1.37 | 1.39 | 1.39 | 1.41 | 1.40 | 1.41 | 1.38 | 1.36 | 1.36 | 1.38 | 1.35 | 1.37 | 1.39 |
| Ca | 0.00 | 0.00 | 0.00 | 0.00 | 0.00 | 0.00 | 0.00 | 0.00 | 0.00 | 0.00 | 0.00 | 0.01 | 0.00 | 0.00 | 0.00 |
| Na | 0.10 | 0.09 | 0.07 | 0.08 | 0.07 | 0.05 | 0.06 | 0.08 | 0.06 | 0.09 | 0.08 | 0.08 | 0.08 | 0.06 | 0.05 |
| K | 0.00 | 0.00 | 0.00 | 0.00 | 0.00 | 0.00 | 0.00 | 0.00 | 0.00 | 0.00 | 0.00 | 0.00 | 0.00 | 0.01 | 0.00 |
| cations | 11.00 | 11.00 | 11.00 | 11.00 | 11.00 | 11.00 | 11.00 | 11.00 | 11.00 | 11.00 | 11.00 | 11.00 | 11.00 | 11.00 | 11.00 |
| $X_{Fe}$ ($Fe^{2+}$) | 0.21 | 0.24 | 0.28 | 0.24 | 0.26 | 0.26 | 0.26 | 0.23 | 0.22 | 0.21 | 0.22 | 0.22 | 0.25 | 0.23 | 0.24 |
| $X_{Fe}$ (Fetot) | 0.29 | 0.29 | 0.30 | 0.30 | 0.31 | 0.29 | 0.30 | 0.29 | 0.31 | 0.32 | 0.31 | 0.29 | 0.31 | 0.31 | 0.30 |

**Table A9.** Chemical analyses of a garnet porphyroblast from a patch migmatites of the Intermediate series affected by the Ceret contact aureole.

| Sample | 529B | | | | | | | | | | | | | | |
|---|---|---|---|---|---|---|---|---|---|---|---|---|---|---|---|
| Analysis | g2_perfilA_1 | g2_perfilA_2 | g2_perfilA_3 | g2_perfilA_4 | g2_perfilA_5 | g2_perfilA_6 | g2_perfilA_7 | g2_perfilA_9 | g2_perfilA_10 | g2_perfilA_11 | g2_perfilA_12 | g2_perfilA_13 | g2_perfilA_14 | g2_perfilA_15 | g2_perfilA_16 |
| Spot | #175 | #176 | #177 | #178 | #179 | #180 | #181 | #183 | #184 | #185 | #186 | #187 | #188 | #189 | #190 |
| (wt%) | | | | | | | | | | | | | | | |
| $SiO_2$ | 38.13 | 37.87 | 38.00 | 37.37 | 37.85 | 38.23 | 37.55 | 38.20 | 38.53 | 38.32 | 38.06 | 38.03 | 37.74 | 38.03 | 37.91 |
| $TiO_2$ | 0.02 | 0.03 | 0.00 | 0.06 | 0.04 | 0.06 | 0.05 | 0.06 | 0.04 | 0.02 | 0.05 | 0.06 | 0.05 | 0.07 | 0.05 |
| $Al_2O_3$ | 21.51 | 21.68 | 21.63 | 21.21 | 21.75 | 21.56 | 21.63 | 21.67 | 21.62 | 21.68 | 21.47 | 21.73 | 21.82 | 21.66 | 21.57 |
| FeO | 34.30 | 32.91 | 32.19 | 32.74 | 31.51 | 31.06 | 31.67 | 30.90 | 31.08 | 31.05 | 30.92 | 31.19 | 31.32 | 30.61 | 30.46 |
| MnO | 3.14 | 2.09 | 1.92 | 2.21 | 2.01 | 1.90 | 1.96 | 1.92 | 1.95 | 1.80 | 1.92 | 1.90 | 1.92 | 1.98 | 1.87 |
| MgO | 3.54 | 5.54 | 6.10 | 5.86 | 6.59 | 6.69 | 6.88 | 6.63 | 6.82 | 6.74 | 6.88 | 7.26 | 6.98 | 6.72 | 7.01 |
| CaO | 1.26 | 1.23 | 1.27 | 1.24 | 1.29 | 1.28 | 1.26 | 1.30 | 1.32 | 1.34 | 1.35 | 1.31 | 1.35 | 1.36 | 1.30 |
| $Na_2O$ | 0.00 | 0.00 | 0.00 | 0.00 | 0.00 | 0.00 | 0.00 | 0.00 | 0.00 | 0.00 | 0.00 | 0.00 | 0.00 | 0.00 | 0.00 |
| $K_2O$ | 0.00 | 0.00 | 0.00 | 0.00 | 0.00 | 0.00 | 0.00 | 0.00 | 0.00 | 0.00 | 0.00 | 0.00 | 0.00 | 0.00 | 0.00 |
| Total | 101.90 | 101.35 | 101.11 | 100.69 | 101.04 | 100.78 | 101.00 | 100.68 | 101.36 | 100.95 | 100.65 | 101.48 | 101.18 | 100.43 | 100.17 |
| Oxygen | 12 | 12 | 12 | 12 | 12 | 12 | 12 | 12 | 12 | 12 | 12 | 12 | 12 | 12 | 12 |
| Si | 3.01 | 2.96 | 2.96 | 2.94 | 2.95 | 2.98 | 2.92 | 2.98 | 2.98 | 2.98 | 2.97 | 2.94 | 2.93 | 2.97 | 2.96 |
| Ti | 0.00 | 0.00 | 0.00 | 0.00 | 0.00 | 0.00 | 0.00 | 0.00 | 0.00 | 0.00 | 0.00 | 0.00 | 0.00 | 0.00 | 0.00 |
| Al | 2.00 | 2.00 | 1.99 | 1.97 | 1.99 | 1.98 | 1.98 | 1.99 | 1.97 | 1.99 | 1.97 | 1.98 | 1.99 | 1.99 | 1.99 |
| $Fe^{3+}$ | 0.00 | 0.08 | 0.08 | 0.15 | 0.11 | 0.05 | 0.17 | 0.04 | 0.05 | 0.05 | 0.08 | 0.14 | 0.15 | 0.05 | 0.07 |
| $Fe^{2+}$ | 2.26 | 2.08 | 2.02 | 2.00 | 1.94 | 1.97 | 1.89 | 1.98 | 1.96 | 1.97 | 1.93 | 1.87 | 1.88 | 1.95 | 1.92 |
| Mn | 0.21 | 0.14 | 0.13 | 0.15 | 0.13 | 0.13 | 0.13 | 0.13 | 0.13 | 0.12 | 0.13 | 0.12 | 0.13 | 0.13 | 0.12 |
| Mg | 0.42 | 0.65 | 0.71 | 0.69 | 0.76 | 0.78 | 0.80 | 0.77 | 0.79 | 0.78 | 0.80 | 0.84 | 0.81 | 0.78 | 0.82 |
| Ca | 0.11 | 0.10 | 0.11 | 0.10 | 0.11 | 0.11 | 0.10 | 0.11 | 0.11 | 0.11 | 0.11 | 0.11 | 0.11 | 0.11 | 0.11 |
| Na | 0.00 | 0.00 | 0.00 | 0.00 | 0.00 | 0.00 | 0.00 | 0.00 | 0.00 | 0.00 | 0.00 | 0.00 | 0.00 | 0.00 | 0.00 |
| K | 0.00 | 0.00 | 0.00 | 0.00 | 0.00 | 0.00 | 0.00 | 0.00 | 0.00 | 0.00 | 0.00 | 0.00 | 0.00 | 0.00 | 0.00 |
| cations | 8.00 | 8.00 | 8.00 | 8.00 | 8.00 | 8.00 | 8.00 | 8.00 | 8.00 | 8.00 | 8.00 | 8.00 | 8.00 | 8.00 | 8.00 |
| grs | 0.04 | 0.03 | 0.03 | 0.03 | 0.04 | 0.04 | 0.03 | 0.04 | 0.04 | 0.04 | 0.04 | 0.04 | 0.04 | 0.04 | 0.04 |
| alm | 0.76 | 0.71 | 0.69 | 0.70 | 0.67 | 0.67 | 0.67 | 0.67 | 0.66 | 0.67 | 0.66 | 0.65 | 0.66 | 0.66 | 0.65 |
| prp | 0.14 | 0.21 | 0.23 | 0.22 | 0.25 | 0.26 | 0.26 | 0.26 | 0.26 | 0.26 | 0.26 | 0.27 | 0.26 | 0.26 | 0.27 |
| sps | 0.07 | 0.05 | 0.04 | 0.05 | 0.04 | 0.04 | 0.04 | 0.04 | 0.04 | 0.04 | 0.04 | 0.04 | 0.04 | 0.04 | 0.04 |
| $X_{Fe}$ ($Fe^{2+}$) | 0.84 | 0.76 | 0.74 | 0.74 | 0.72 | 0.72 | 0.70 | 0.72 | 0.71 | 0.72 | 0.71 | 0.69 | 0.70 | 0.71 | 0.70 |
| $X_{Fe}$ (Fetot) | 0.84 | 0.77 | 0.75 | 0.76 | 0.73 | 0.72 | 0.72 | 0.72 | 0.72 | 0.72 | 0.72 | 0.71 | 0.72 | 0.72 | 0.71 |

**Table A9.** (Continued)

| Sample | 529B | | | | | | | | | | | | | | |
|---|---|---|---|---|---|---|---|---|---|---|---|---|---|---|---|
| Analysis | g2_perfilA_19 | g2_perfilA_20 | g2_perfilA_22 | g2_perfilA_23 | g2_perfilA_26 | g2_perfilA_28 | g2_perfilA_31 | g2_perfilA_32 | g2_perfilA_33 | g2_perfilA_34 | g2_perfilA_39 | g2_perfilA_40 | g2_perfilA_42 | g2_perfilA_44 | g2_perfilA_45 |
| Spot | #193 | #194 | #196 | #197 | #200 | #202 | #205 | #206 | #207 | #208 | #213 | #214 | #216 | #218 | #219 |
| (wt%) | | | | | | | | | | | | | | | |
| $SiO_2$ | 38.26 | 37.64 | 38.37 | 37.58 | 38.45 | 37.02 | 37.83 | 37.42 | 37.13 | 38.06 | 37.45 | 36.87 | 36.56 | 36.93 | 38.01 |
| $TiO_2$ | 0.07 | 0.06 | 0.06 | 0.06 | 0.05 | 0.08 | 0.05 | 0.06 | 0.07 | 0.05 | 0.08 | 0.05 | 0.05 | 0.06 | 0.07 |
| $Al_2O_3$ | 21.70 | 21.61 | 21.75 | 21.56 | 21.75 | 21.20 | 21.37 | 21.59 | 21.95 | 22.48 | 21.65 | 21.53 | 21.12 | 21.27 | 22.04 |
| FeO | 31.42 | 30.92 | 30.84 | 31.37 | 30.51 | 32.06 | 31.18 | 30.66 | 31.31 | 30.76 | 32.83 | 31.87 | 31.41 | 30.97 | 30.54 |
| MnO | 1.84 | 1.88 | 1.80 | 1.88 | 1.87 | 2.05 | 1.80 | 1.89 | 1.69 | 1.82 | 2.09 | 2.22 | 2.00 | 1.93 | 1.78 |
| MgO | 6.81 | 6.84 | 6.83 | 6.66 | 6.77 | 6.07 | 6.90 | 7.28 | 6.86 | 6.44 | 5.71 | 6.18 | 6.46 | 6.76 | 6.36 |
| CaO | 1.30 | 1.28 | 1.30 | 1.24 | 1.32 | 1.27 | 1.29 | 1.30 | 1.27 | 1.25 | 1.25 | 1.33 | 1.23 | 1.26 | 1.20 |
| $Na_2O$ | 0.00 | 0.00 | 0.00 | 0.00 | 0.00 | 0.00 | 0.00 | 0.00 | 0.00 | 0.00 | 0.00 | 0.00 | 0.00 | 0.00 | 0.00 |
| $K_2O$ | 0.00 | 0.00 | 0.00 | 0.00 | 0.00 | 0.00 | 0.00 | 0.00 | 0.00 | 0.00 | 0.00 | 0.00 | 0.00 | 0.00 | 0.00 |
| Total | 101.40 | 100.23 | 100.95 | 100.35 | 100.72 | 99.75 | 100.42 | 100.20 | 100.28 | 100.86 | 101.06 | 100.05 | 98.83 | 99.18 | 100.00 |
| Oxygen | 12 | 12 | 12 | 12 | 12 | 12 | 12 | 12 | 12 | 12 | 12 | 12 | 12 | 12 | 12 |
| Si | 2.96 | 2.95 | 2.98 | 2.94 | 2.99 | 2.93 | 2.96 | 2.92 | 2.90 | 2.96 | 2.93 | 2.91 | 2.91 | 2.92 | 2.98 |
| Ti | 0.00 | 0.00 | 0.00 | 0.00 | 0.00 | 0.00 | 0.00 | 0.00 | 0.00 | 0.00 | 0.00 | 0.00 | 0.00 | 0.00 | 0.00 |
| Al | 1.98 | 1.99 | 1.99 | 1.99 | 2.00 | 1.98 | 1.97 | 1.99 | 2.02 | 2.06 | 2.00 | 2.00 | 1.98 | 1.98 | 2.04 |
| $Fe^{3+}$ | 0.08 | 0.10 | 0.04 | 0.11 | 0.01 | 0.15 | 0.11 | 0.16 | 0.16 | 0.01 | 0.12 | 0.18 | 0.18 | 0.16 | 0.00 |
| $Fe^{2+}$ | 1.95 | 1.92 | 1.97 | 1.94 | 1.98 | 1.97 | 1.93 | 1.84 | 1.89 | 1.99 | 2.03 | 1.92 | 1.91 | 1.89 | 2.00 |
| Mn | 0.12 | 0.12 | 0.12 | 0.12 | 0.12 | 0.14 | 0.12 | 0.13 | 0.11 | 0.12 | 0.14 | 0.15 | 0.13 | 0.13 | 0.12 |
| Mg | 0.79 | 0.80 | 0.79 | 0.78 | 0.79 | 0.72 | 0.80 | 0.85 | 0.80 | 0.75 | 0.67 | 0.73 | 0.77 | 0.80 | 0.74 |
| Ca | 0.11 | 0.11 | 0.11 | 0.10 | 0.11 | 0.11 | 0.11 | 0.11 | 0.11 | 0.10 | 0.10 | 0.11 | 0.10 | 0.11 | 0.10 |
| Na | 0.00 | 0.00 | 0.00 | 0.00 | 0.00 | 0.00 | 0.00 | 0.00 | 0.00 | 0.00 | 0.00 | 0.00 | 0.00 | 0.00 | 0.00 |
| K | 0.00 | 0.00 | 0.00 | 0.00 | 0.00 | 0.00 | 0.00 | 0.00 | 0.00 | 0.00 | 0.00 | 0.00 | 0.00 | 0.00 | 0.00 |
| cations | 8.00 | 8.00 | 8.00 | 8.00 | 8.00 | 8.00 | 8.00 | 8.00 | 8.00 | 8.00 | 8.00 | 8.00 | 8.00 | 8.00 | 8.00 |
| grs | 0.04 | 0.04 | 0.04 | 0.03 | 0.04 | 0.03 | 0.04 | 0.04 | 0.03 | 0.04 | 0.03 | 0.04 | 0.03 | 0.03 | 0.03 |
| alm | 0.67 | 0.66 | 0.66 | 0.67 | 0.66 | 0.69 | 0.66 | 0.65 | 0.67 | 0.67 | 0.70 | 0.68 | 0.68 | 0.66 | 0.68 |
| prp | 0.26 | 0.26 | 0.26 | 0.25 | 0.26 | 0.23 | 0.26 | 0.27 | 0.26 | 0.25 | 0.22 | 0.24 | 0.25 | 0.26 | 0.25 |
| sps | 0.04 | 0.04 | 0.04 | 0.04 | 0.04 | 0.04 | 0.04 | 0.04 | 0.04 | 0.04 | 0.05 | 0.05 | 0.04 | 0.04 | 0.04 |
| $X_{Fe}$ ($Fe^{2+}$) | 0.71 | 0.71 | 0.71 | 0.71 | 0.72 | 0.73 | 0.71 | 0.69 | 0.70 | 0.73 | 0.75 | 0.73 | 0.71 | 0.70 | 0.73 |
| $X_{Fe}$ (Fetot) | 0.72 | 0.72 | 0.72 | 0.73 | 0.72 | 0.75 | 0.72 | 0.70 | 0.72 | 0.73 | 0.76 | 0.74 | 0.73 | 0.72 | 0.73 |

**Table A9.** (Continued)

| Sample | 529B | | | | | | |
|---|---|---|---|---|---|---|---|
| Analysis | g2_perfilA_49 | g2_perfilA_50 | g2_perfilA_51 | g2_perfilA_53 | g2_perfilA_54 | g2_perfilA_56 | g2_perfilA_57 |
| Spot | #223 | #224 | #225 | #227 | #228 | #230 | #231 |
| (wt%) | | | | | | | |
| $SiO_2$ | 36.46 | 36.19 | 36.26 | 37.04 | 35.75 | 35.50 | 35.82 |
| $TiO_2$ | 0.09 | 0.04 | 0.03 | 0.07 | 0.05 | 0.05 | 0.04 |
| $Al_2O_3$ | 21.56 | 21.35 | 21.25 | 21.80 | 20.71 | 21.16 | 21.05 |
| FeO | 31.31 | 31.53 | 31.97 | 32.87 | 33.28 | 33.01 | 33.27 |
| MnO | 2.00 | 2.01 | 1.98 | 2.20 | 2.25 | 2.32 | 2.47 |
| MgO | 6.64 | 6.38 | 6.18 | 5.46 | 5.26 | 5.30 | 4.97 |
| CaO | 1.27 | 1.23 | 1.32 | 1.22 | 1.22 | 1.18 | 1.24 |
| $Na_2O$ | 0.00 | 0.00 | 0.00 | 0.00 | 0.00 | 0.00 | 0.00 |
| $K_2O$ | 0.00 | 0.00 | 0.00 | 0.00 | 0.00 | 0.00 | 0.00 |
| Total | 99.33 | 98.73 | 98.99 | 100.66 | 98.52 | 98.52 | 98.86 |
| Oxygen | 12 | 12 | 12 | 12 | 12 | 12 | 12 |
| Si | 2.89 | 2.89 | 2.89 | 2.92 | 2.89 | 2.86 | 2.88 |
| Ti | 0.01 | 0.00 | 0.00 | 0.00 | 0.00 | 0.00 | 0.00 |
| Al | 2.01 | 2.01 | 2.00 | 2.02 | 1.97 | 2.01 | 2.00 |
| $Fe^{3+}$ | 0.21 | 0.21 | 0.22 | 0.13 | 0.25 | 0.26 | 0.23 |
| $Fe^{2+}$ | 1.87 | 1.89 | 1.91 | 2.03 | 2.00 | 1.97 | 2.01 |
| Mn | 0.13 | 0.14 | 0.13 | 0.15 | 0.15 | 0.16 | 0.17 |
| Mg | 0.78 | 0.76 | 0.73 | 0.64 | 0.63 | 0.64 | 0.60 |
| Ca | 0.11 | 0.11 | 0.11 | 0.10 | 0.11 | 0.10 | 0.11 |
| Na | 0.00 | 0.00 | 0.00 | 0.00 | 0.00 | 0.00 | 0.00 |
| K | 0.00 | 0.00 | 0.00 | 0.00 | 0.00 | 0.00 | 0.00 |
| cations | 8.00 | 8.00 | 8.00 | 8.00 | 8.00 | 8.00 | 8.00 |
| grs | 0.03 | 0.03 | 0.04 | 0.03 | 0.03 | 0.03 | 0.03 |
| alm | 0.67 | 0.68 | 0.68 | 0.71 | 0.72 | 0.71 | 0.72 |
| prp | 0.25 | 0.24 | 0.24 | 0.21 | 0.20 | 0.20 | 0.19 |
| sps | 0.04 | 0.04 | 0.04 | 0.05 | 0.05 | 0.05 | 0.05 |
| $X_{Fe}$ ($Fe^{2+}$) | 0.70 | 0.71 | 0.72 | 0.76 | 0.76 | 0.76 | 0.77 |
| $X_{Fe}$ (Fetot) | 0.73 | 0.73 | 0.74 | 0.77 | 0.78 | 0.78 | 0.79 |

**Table A10.** Chemical composition of biotite from a schollen migmatite of the Intermediate series affected by the Ceret contact aureole.

| Sample | 459 | | | | | | | | | | | | | | | | | | | |
|---|---|---|---|---|---|---|---|---|---|---|---|---|---|---|---|---|---|---|---|---|
| Analysis | 459L | 459L | 459L | 459L | 459L | 459L | 459L | 459L | 459L | 459L | 459L | 459L | 459L | 459L | 459L | 459L | 459L | 459L | 459L | 459L |
| Spot | 1 | 4 | 8 | 9 | 15 | 22 | 23 | 31 | 34 | 43 | 44 | 45 | 48 | 51 | 56 | 57 | 61 | 63 | 67 | 73 |
| (wt%) | | | | | | | | | | | | | | | | | | | | |
| $SiO_2$ | 35.26 | 35.36 | 34.72 | 34.65 | 34.41 | 34.54 | 36.13 | 35.33 | 34.95 | 35.78 | 34.92 | 34.25 | 35.15 | 35.15 | 34.98 | 34.98 | 35.01 | 34.82 | 34.90 | 35.27 |
| $TiO_2$ | 2.66 | 2.32 | 2.43 | 2.33 | 2.02 | 2.16 | 2.24 | 2.17 | 2.22 | 3.26 | 3.23 | 3.09 | 3.02 | 2.58 | 2.41 | 2.64 | 2.56 | 2.61 | 2.25 | 2.45 |
| $Al_2O_3$ | 20.19 | 20.80 | 20.04 | 20.25 | 19.99 | 19.72 | 19.98 | 19.89 | 20.11 | 19.92 | 18.83 | 19.07 | 19.55 | 19.26 | 19.66 | 19.30 | 20.33 | 20.17 | 20.00 | 20.51 |
| FeO | 18.97 | 18.33 | 18.56 | 19.34 | 19.29 | 19.22 | 18.52 | 18.44 | 18.41 | 19.15 | 19.12 | 20.61 | 18.62 | 20.13 | 20.97 | 19.83 | 20.01 | 17.83 | 19.34 | 18.49 |
| MnO | 0.08 | 0.09 | 0.02 | 0.05 | 0.06 | 0.04 | 0.00 | 0.15 | 0.00 | 0.08 | 0.06 | 0.15 | 0.10 | 0.17 | 0.06 | 0.09 | 0.08 | 0.05 | 0.17 | 0.12 |
| MgO | 9.13 | 9.39 | 9.42 | 9.35 | 10.90 | 10.00 | 9.54 | 10.03 | 9.34 | 8.88 | 8.77 | 8.09 | 9.10 | 8.97 | 8.45 | 8.94 | 8.65 | 9.36 | 9.15 | 9.38 |
| CaO | 0.00 | 0.00 | 0.00 | 0.01 | 0.04 | 0.03 | 0.01 | 0.02 | 0.02 | 0.02 | 0.09 | 0.06 | 0.11 | 0.00 | 0.02 | 0.00 | 0.04 | 0.00 | 0.00 | 0.02 |
| $Na_2O$ | 0.34 | 0.37 | 0.36 | 0.38 | 0.38 | 0.51 | 0.34 | 0.37 | 0.35 | 0.37 | 0.18 | 0.25 | 0.36 | 0.22 | 0.32 | 0.34 | 0.49 | 0.26 | 0.37 | 0.25 |
| $K_2O$ | 9.49 | 9.15 | 9.06 | 8.85 | 8.42 | 8.82 | 9.41 | 9.07 | 8.84 | 9.70 | 9.44 | 9.34 | 9.57 | 9.43 | 9.39 | 9.48 | 9.32 | 9.64 | 9.74 | 9.35 |
| Total | 96.14 | 95.81 | 94.60 | 95.21 | 95.52 | 95.03 | 96.16 | 95.46 | 94.25 | 97.16 | 94.64 | 94.90 | 95.58 | 95.93 | 96.25 | 95.60 | 96.49 | 94.74 | 95.92 | 95.83 |
| Oxygen | 11 | 11 | 11 | 11 | 11 | 11 | 11 | 11 | 11 | 11 | 11 | 11 | 11 | 11 | 11 | 11 | 11 | 11 | 11 | 11 |
| Si | 2.73 | 2.74 | 2.72 | 2.71 | 2.66 | 2.69 | 2.79 | 2.74 | 2.75 | 2.75 | 2.76 | 2.72 | 2.74 | 2.74 | 2.72 | 2.73 | 2.71 | 2.72 | 2.70 | 2.73 |
| Ti | 0.15 | 0.13 | 0.14 | 0.14 | 0.12 | 0.13 | 0.13 | 0.13 | 0.13 | 0.19 | 0.19 | 0.18 | 0.18 | 0.15 | 0.14 | 0.15 | 0.15 | 0.15 | 0.13 | 0.14 |
| Al | 1.84 | 1.90 | 1.85 | 1.86 | 1.82 | 1.81 | 1.82 | 1.82 | 1.87 | 1.80 | 1.76 | 1.78 | 1.80 | 1.77 | 1.80 | 1.78 | 1.85 | 1.86 | 1.83 | 1.87 |
| $Fe^{3+}$ | 0.00 | 0.00 | 0.00 | 0.00 | 0.00 | 0.00 | 0.00 | 0.00 | 0.00 | 0.00 | 0.00 | 0.00 | 0.00 | 0.00 | 0.00 | 0.00 | 0.00 | 0.00 | 0.00 | 0.00 |
| $Fe^{2+}$ | 1.23 | 1.19 | 1.22 | 1.26 | 1.25 | 1.25 | 1.19 | 1.20 | 1.21 | 1.23 | 1.26 | 1.37 | 1.21 | 1.31 | 1.37 | 1.29 | 1.29 | 1.17 | 1.25 | 1.20 |
| Mn | 0.01 | 0.01 | 0.00 | 0.00 | 0.00 | 0.00 | 0.00 | 0.01 | 0.00 | 0.01 | 0.00 | 0.01 | 0.01 | 0.01 | 0.00 | 0.01 | 0.01 | 0.00 | 0.01 | 0.01 |
| Mg | 1.05 | 1.08 | 1.10 | 1.09 | 1.26 | 1.16 | 1.10 | 1.16 | 1.10 | 1.02 | 1.03 | 0.96 | 1.06 | 1.04 | 0.98 | 1.04 | 1.00 | 1.09 | 1.06 | 1.08 |
| Ca | 0.00 | 0.00 | 0.00 | 0.00 | 0.00 | 0.00 | 0.00 | 0.00 | 0.00 | 0.00 | 0.01 | 0.00 | 0.01 | 0.00 | 0.00 | 0.00 | 0.00 | 0.00 | 0.00 | 0.00 |
| Na | 0.05 | 0.05 | 0.05 | 0.06 | 0.06 | 0.08 | 0.05 | 0.05 | 0.05 | 0.05 | 0.03 | 0.04 | 0.05 | 0.03 | 0.05 | 0.05 | 0.07 | 0.04 | 0.06 | 0.04 |
| K | 0.94 | 0.90 | 0.91 | 0.88 | 0.83 | 0.88 | 0.93 | 0.90 | 0.89 | 0.95 | 0.95 | 0.94 | 0.95 | 0.94 | 0.93 | 0.94 | 0.92 | 0.96 | 0.96 | 0.92 |
| cations | 8.00 | 8.00 | 8.00 | 8.00 | 8.00 | 8.00 | 8.00 | 8.00 | 8.00 | 8.00 | 8.00 | 8.00 | 8.00 | 8.00 | 8.00 | 8.00 | 8.00 | 8.00 | 8.00 | 8.00 |
| $X_{Fe}$ ($Fe^{2+}$) | 0.54 | 0.52 | 0.53 | 0.54 | 0.50 | 0.52 | 0.52 | 0.51 | 0.53 | 0.55 | 0.55 | 0.59 | 0.53 | 0.56 | 0.58 | 0.55 | 0.56 | 0.52 | 0.54 | 0.53 |
| $X_{Fe}$ (Fetot) | 0.54 | 0.52 | 0.53 | 0.54 | 0.50 | 0.52 | 0.52 | 0.51 | 0.53 | 0.55 | 0.55 | 0.59 | 0.53 | 0.56 | 0.58 | 0.55 | 0.56 | 0.52 | 0.54 | 0.53 |

**Table A10.** (Continued)

| Sample | 459 | | | | | | | | | | | | | | | | | | | |
|---|---|---|---|---|---|---|---|---|---|---|---|---|---|---|---|---|---|---|---|---|
| Analysis | 459L | 459L | 459L | 459L | 459L | 459L | 459L | 459L | 459L | 459L | 459L | 459L | 459L | 459L | 459L | 459L | 459L | 459L | 459L | 459L |
| Spot | 76 | 78 | 84 | 85 | 87 | 89 | 96 | 101 | 103 | 110 | 114 | 115 | 120 | 123 | 126 | 128 | 130 | 133 | 134 | 141 |
| (wt%) | | | | | | | | | | | | | | | | | | | | |
| $SiO_2$ | 33.69 | 35.38 | 34.33 | 34.72 | 35.59 | 35.26 | 34.75 | 34.75 | 35.43 | 34.99 | 35.39 | 35.31 | 35.72 | 34.65 | 35.37 | 35.04 | 35.34 | 35.61 | 34.65 | 35.31 |
| $TiO_2$ | 2.00 | 2.58 | 1.86 | 1.78 | 1.79 | 2.18 | 2.01 | 2.03 | 2.19 | 2.90 | 2.35 | 2.77 | 2.77 | 2.46 | 2.58 | 2.63 | 2.66 | 2.09 | 1.84 | 3.02 |
| $Al_2O_3$ | 20.05 | 20.36 | 20.47 | 19.82 | 21.62 | 20.57 | 20.41 | 20.00 | 20.28 | 19.44 | 20.29 | 19.53 | 19.73 | 19.57 | 19.72 | 20.12 | 20.03 | 19.94 | 22.25 | 19.48 |
| FeO | 20.61 | 18.90 | 20.73 | 20.11 | 19.29 | 19.51 | 19.86 | 20.66 | 19.64 | 18.32 | 18.99 | 18.92 | 18.73 | 19.85 | 18.72 | 19.12 | 18.17 | 17.71 | 18.69 | 20.85 |
| MnO | 0.14 | 0.10 | 0.04 | 0.08 | 0.00 | 0.09 | 0.09 | 0.08 | 0.11 | 0.16 | 0.10 | 0.10 | 0.18 | 0.04 | 0.15 | 0.10 | 0.06 | 0.15 | 0.10 | 0.18 |
| MgO | 9.64 | 8.98 | 9.47 | 9.65 | 9.20 | 9.25 | 9.52 | 8.39 | 8.75 | 9.37 | 9.12 | 9.34 | 9.54 | 9.50 | 9.54 | 9.91 | 9.11 | 10.11 | 8.90 | 8.25 |
| CaO | 0.00 | 0.00 | 0.00 | 0.11 | 0.12 | 0.00 | 0.09 | 0.08 | 0.04 | 0.01 | 0.02 | 0.00 | 0.00 | 0.07 | 0.00 | 0.01 | 0.06 | 0.03 | 0.05 | 0.07 |
| $Na_2O$ | 0.22 | 0.34 | 0.42 | 0.25 | 0.28 | 0.35 | 0.38 | 0.29 | 0.36 | 0.39 | 0.48 | 0.31 | 0.35 | 0.35 | 0.36 | 0.44 | 0.31 | 0.38 | 0.45 | 0.41 |
| $K_2O$ | 8.23 | 9.53 | 8.36 | 8.79 | 8.59 | 8.87 | 8.63 | 9.04 | 9.50 | 9.31 | 8.79 | 9.39 | 9.11 | 8.79 | 9.42 | 9.05 | 9.34 | 9.03 | 9.04 | 9.46 |
| Total | 94.58 | 96.17 | 95.68 | 95.31 | 96.47 | 96.09 | 95.74 | 95.31 | 96.29 | 94.88 | 95.54 | 95.68 | 96.13 | 95.27 | 95.86 | 96.41 | 95.07 | 95.04 | 95.97 | 97.03 |
| Oxygen | 11 | 11 | 11 | 11 | 11 | 11 | 11 | 11 | 11 | 11 | 11 | 11 | 11 | 11 | 11 | 11 | 11 | 11 | 11 | 11 |
| Si | 2.66 | 2.74 | 2.67 | 2.71 | 2.74 | 2.73 | 2.70 | 2.73 | 2.74 | 2.74 | 2.75 | 2.75 | 2.76 | 2.71 | 2.74 | 2.70 | 2.76 | 2.77 | 2.67 | 2.73 |
| Ti | 0.12 | 0.15 | 0.11 | 0.10 | 0.10 | 0.13 | 0.12 | 0.12 | 0.13 | 0.17 | 0.14 | 0.16 | 0.16 | 0.14 | 0.15 | 0.15 | 0.16 | 0.12 | 0.11 | 0.18 |
| Al | 1.86 | 1.86 | 1.88 | 1.82 | 1.96 | 1.88 | 1.87 | 1.85 | 1.85 | 1.79 | 1.86 | 1.79 | 1.80 | 1.80 | 1.80 | 1.82 | 1.85 | 1.83 | 2.02 | 1.78 |
| $Fe^{3+}$ | 0.00 | 0.00 | 0.00 | 0.00 | 0.00 | 0.00 | 0.00 | 0.00 | 0.00 | 0.00 | 0.00 | 0.00 | 0.00 | 0.00 | 0.00 | 0.00 | 0.00 | 0.00 | 0.00 | 0.00 |
| $Fe^{2+}$ | 1.36 | 1.22 | 1.35 | 1.31 | 1.24 | 1.26 | 1.29 | 1.36 | 1.27 | 1.20 | 1.24 | 1.23 | 1.21 | 1.30 | 1.21 | 1.23 | 1.19 | 1.15 | 1.21 | 1.35 |
| Mn | 0.01 | 0.01 | 0.00 | 0.01 | 0.00 | 0.01 | 0.01 | 0.01 | 0.01 | 0.01 | 0.01 | 0.01 | 0.01 | 0.00 | 0.01 | 0.01 | 0.00 | 0.01 | 0.01 | 0.01 |
| Mg | 1.13 | 1.03 | 1.10 | 1.12 | 1.06 | 1.07 | 1.10 | 0.98 | 1.01 | 1.09 | 1.06 | 1.08 | 1.10 | 1.11 | 1.10 | 1.14 | 1.06 | 1.17 | 1.02 | 0.95 |
| Ca | 0.00 | 0.00 | 0.00 | 0.01 | 0.01 | 0.00 | 0.01 | 0.01 | 0.00 | 0.00 | 0.00 | 0.00 | 0.00 | 0.01 | 0.00 | 0.00 | 0.00 | 0.00 | 0.00 | 0.01 |
| Na | 0.03 | 0.05 | 0.06 | 0.04 | 0.04 | 0.05 | 0.06 | 0.04 | 0.05 | 0.06 | 0.07 | 0.05 | 0.05 | 0.05 | 0.05 | 0.06 | 0.05 | 0.06 | 0.07 | 0.06 |
| K | 0.83 | 0.94 | 0.83 | 0.88 | 0.84 | 0.88 | 0.85 | 0.91 | 0.94 | 0.93 | 0.87 | 0.93 | 0.90 | 0.88 | 0.93 | 0.89 | 0.93 | 0.89 | 0.89 | 0.93 |
| cations | 8.00 | 8.00 | 8.00 | 8.00 | 8.00 | 8.00 | 8.00 | 8.00 | 8.00 | 8.00 | 8.00 | 8.00 | 8.00 | 8.00 | 8.00 | 8.00 | 8.00 | 8.00 | 8.00 | 8.00 |
| $X_{Fe}$ ($Fe^{2+}$) | 0.55 | 0.54 | 0.55 | 0.54 | 0.54 | 0.54 | 0.54 | 0.58 | 0.56 | 0.52 | 0.54 | 0.53 | 0.52 | 0.54 | 0.52 | 0.52 | 0.53 | 0.50 | 0.54 | 0.59 |
| $X_{Fe}$ (Fetot) | 0.55 | 0.54 | 0.55 | 0.54 | 0.54 | 0.54 | 0.54 | 0.58 | 0.56 | 0.52 | 0.54 | 0.53 | 0.52 | 0.54 | 0.52 | 0.52 | 0.53 | 0.50 | 0.54 | 0.59 |

**Table A10.** (Continued)

| Sample | 459 | | | | | | | | | | | | | | | | | | | |
|---|---|---|---|---|---|---|---|---|---|---|---|---|---|---|---|---|---|---|---|---|
| Analysis | 459L | 459L | 459L | 459L | 459L | 459L | 459L | 459L | 459L | 459L | 459L | 459L | 459L | 459L | 459L | 459L | 459L | 459L | 459L | 459L |
| Spot | 142 | 144 | 149 | 151 | 158 | 164 | 169 | 170 | 175 | 179 | 183 | 186 | 187 | 190 | 263 | 274 | 276 | 278 | 280 | 282 |
| (wt%) | | | | | | | | | | | | | | | | | | | | |
| $SiO_2$ | 35.24 | 35.05 | 35.91 | 35.31 | 34.82 | 34.59 | 34.95 | 34.50 | 34.95 | 34.21 | 34.80 | 34.93 | 35.36 | 35.38 | 35.14 | 35.05 | 35.07 | 34.44 | 34.75 | 34.39 |
| $TiO_2$ | 3.01 | 3.43 | 3.06 | 3.31 | 2.41 | 3.33 | 4.48 | 3.30 | 3.35 | 3.22 | 2.40 | 2.71 | 2.45 | 1.79 | 2.93 | 3.26 | 3.40 | 3.39 | 3.49 | 3.37 |
| $Al_2O_3$ | 19.35 | 19.09 | 20.63 | 19.75 | 20.17 | 19.09 | 18.46 | 18.73 | 19.61 | 18.65 | 19.94 | 20.19 | 20.56 | 20.85 | 20.47 | 19.26 | 19.39 | 18.89 | 19.56 | 18.43 |
| FeO | 20.31 | 20.55 | 18.06 | 19.57 | 20.06 | 19.95 | 20.61 | 20.53 | 19.51 | 21.36 | 19.17 | 19.00 | 18.83 | 18.95 | 18.82 | 20.56 | 20.18 | 19.59 | 18.41 | 20.16 |
| MnO | 0.14 | 0.19 | 0.18 | 0.09 | 0.00 | 0.21 | 0.09 | 0.11 | 0.08 | 0.09 | 0.07 | 0.07 | 0.17 | 0.02 | 0.13 | 0.12 | 0.06 | 0.06 | 0.02 | 0.02 |
| MgO | 8.73 | 8.10 | 7.95 | 8.34 | 8.57 | 8.12 | 7.92 | 8.66 | 8.31 | 8.47 | 9.06 | 8.62 | 9.42 | 9.97 | 8.01 | 8.67 | 8.03 | 8.43 | 9.14 | 8.53 |
| CaO | 0.04 | 0.05 | 0.18 | 0.00 | 0.00 | 0.00 | 0.02 | 0.03 | 0.07 | 0.00 | 0.09 | 0.02 | 0.01 | 0.00 | 0.02 | 0.04 | 0.03 | 0.00 | 0.04 | 0.00 |
| $Na_2O$ | 0.35 | 0.40 | 0.35 | 0.48 | 0.31 | 0.30 | 0.29 | 0.36 | 0.19 | 0.42 | 0.37 | 0.36 | 0.38 | 0.49 | 0.41 | 0.33 | 0.26 | 0.31 | 0.30 | 0.29 |
| $K_2O$ | 9.45 | 9.22 | 8.87 | 9.43 | 9.54 | 9.49 | 9.90 | 9.44 | 9.49 | 8.99 | 9.05 | 9.34 | 9.46 | 9.24 | 9.60 | 9.54 | 9.41 | 9.67 | 9.83 | 9.61 |
| Total | 96.63 | 96.07 | 95.19 | 96.28 | 95.88 | 95.08 | 96.71 | 95.66 | 95.55 | 95.41 | 94.96 | 95.25 | 96.64 | 96.68 | 95.53 | 96.83 | 95.84 | 94.78 | 95.54 | 94.79 |
| Oxygen | 11 | 11 | 11 | 11 | 11 | 11 | 11 | 11 | 11 | 11 | 11 | 11 | 11 | 11 | 11 | 11 | 11 | 11 | 11 | 11 |
| Si | 2.73 | 2.75 | 2.82 | 2.74 | 2.71 | 2.73 | 2.73 | 2.71 | 2.74 | 2.70 | 2.73 | 2.73 | 2.72 | 2.70 | 2.75 | 2.72 | 2.75 | 2.72 | 2.71 | 2.72 |
| Ti | 0.18 | 0.20 | 0.18 | 0.19 | 0.14 | 0.20 | 0.26 | 0.19 | 0.20 | 0.19 | 0.14 | 0.16 | 0.14 | 0.10 | 0.17 | 0.19 | 0.20 | 0.20 | 0.20 | 0.20 |
| Al | 1.77 | 1.76 | 1.91 | 1.81 | 1.85 | 1.78 | 1.70 | 1.73 | 1.81 | 1.73 | 1.84 | 1.86 | 1.86 | 1.88 | 1.89 | 1.76 | 1.79 | 1.76 | 1.80 | 1.72 |
| $Fe^{3+}$ | 0.00 | 0.00 | 0.00 | 0.00 | 0.00 | 0.00 | 0.00 | 0.00 | 0.00 | 0.00 | 0.00 | 0.00 | 0.00 | 0.00 | 0.00 | 0.00 | 0.00 | 0.00 | 0.00 | 0.00 |
| $Fe^{2+}$ | 1.32 | 1.35 | 1.19 | 1.27 | 1.31 | 1.32 | 1.35 | 1.35 | 1.28 | 1.41 | 1.26 | 1.24 | 1.21 | 1.21 | 1.23 | 1.33 | 1.32 | 1.29 | 1.20 | 1.33 |
| Mn | 0.01 | 0.01 | 0.01 | 0.01 | 0.00 | 0.01 | 0.01 | 0.01 | 0.01 | 0.01 | 0.00 | 0.00 | 0.01 | 0.00 | 0.01 | 0.01 | 0.00 | 0.00 | 0.00 | 0.00 |
| Mg | 1.01 | 0.95 | 0.93 | 0.97 | 0.99 | 0.96 | 0.92 | 1.01 | 0.97 | 1.00 | 1.06 | 1.01 | 1.08 | 1.14 | 0.93 | 1.00 | 0.94 | 0.99 | 1.06 | 1.01 |
| Ca | 0.00 | 0.00 | 0.02 | 0.00 | 0.00 | 0.00 | 0.00 | 0.00 | 0.01 | 0.00 | 0.01 | 0.00 | 0.00 | 0.00 | 0.00 | 0.00 | 0.00 | 0.00 | 0.00 | 0.00 |
| Na | 0.05 | 0.06 | 0.05 | 0.07 | 0.05 | 0.05 | 0.04 | 0.06 | 0.03 | 0.06 | 0.06 | 0.05 | 0.06 | 0.07 | 0.06 | 0.05 | 0.04 | 0.05 | 0.04 | 0.04 |
| K | 0.93 | 0.92 | 0.89 | 0.94 | 0.95 | 0.96 | 0.99 | 0.94 | 0.95 | 0.90 | 0.90 | 0.93 | 0.93 | 0.90 | 0.96 | 0.94 | 0.94 | 0.98 | 0.98 | 0.97 |
| cations | 8.00 | 8.00 | 8.00 | 8.00 | 8.00 | 8.00 | 8.00 | 8.00 | 8.00 | 8.00 | 8.00 | 8.00 | 8.00 | 8.00 | 8.00 | 8.00 | 8.00 | 8.00 | 8.00 | 8.00 |
| $X_{Fe}$ ($Fe^{2+}$) | 0.57 | 0.59 | 0.56 | 0.57 | 0.57 | 0.58 | 0.59 | 0.57 | 0.57 | 0.59 | 0.54 | 0.55 | 0.53 | 0.52 | 0.57 | 0.57 | 0.59 | 0.57 | 0.53 | 0.57 |
| $X_{Fe}$ (Fetot) | 0.57 | 0.59 | 0.56 | 0.57 | 0.57 | 0.58 | 0.59 | 0.57 | 0.57 | 0.59 | 0.54 | 0.55 | 0.53 | 0.52 | 0.57 | 0.57 | 0.59 | 0.57 | 0.53 | 0.57 |

**Table A11.** Chemical composition of cordierite from a schollen migmatite of the Intermediate series affected by the Ceret contact aureole.

| Sample | 459 | | | | | | | | | | | | | | |
|---|---|---|---|---|---|---|---|---|---|---|---|---|---|---|---|
| Analysis | 459L | 459L | 459L | 459L | 459L | 459L | 459L | 459L | 459L | 459L | 459L | 459L | 459L | 459L | 459L |
| Spot | 5 | 6 | 17 | 18 | 20 | 21 | 24 | 29 | 33 | 111 | 112 | 113 | 116 | 117 | 119 |
| (wt%) | | | | | | | | | | | | | | | |
| $SiO_2$ | 47.45 | 48.23 | 48.27 | 47.97 | 47.87 | 48.38 | 48.74 | 47.76 | 47.73 | 47.45 | 48.63 | 47.73 | 47.94 | 48.02 | 48.53 |
| $TiO_2$ | 0.00 | 0.03 | 0.00 | 0.00 | 0.04 | 0.00 | 0.00 | 0.05 | 0.04 | 0.00 | 0.00 | 0.00 | 0.00 | 0.14 | 0.00 |
| $Al_2O_3$ | 32.55 | 33.31 | 33.13 | 32.99 | 32.92 | 33.31 | 33.10 | 33.03 | 32.67 | 32.99 | 33.28 | 33.05 | 33.07 | 32.93 | 33.46 |
| FeO | 9.47 | 9.32 | 9.14 | 9.07 | 9.40 | 8.72 | 8.85 | 7.97 | 8.32 | 9.14 | 8.90 | 8.21 | 9.16 | 8.79 | 8.12 |
| MnO | 0.28 | 0.33 | 0.22 | 0.31 | 0.27 | 0.36 | 0.32 | 0.39 | 0.27 | 0.30 | 0.24 | 0.47 | 0.21 | 0.45 | 0.46 |
| MgO | 7.29 | 7.79 | 7.62 | 7.64 | 7.72 | 7.87 | 7.85 | 8.19 | 7.75 | 7.99 | 7.96 | 7.81 | 7.93 | 7.84 | 8.10 |
| CaO | 0.04 | 0.04 | 0.04 | 0.07 | 0.03 | 0.00 | 0.02 | 0.00 | 0.03 | 0.03 | 0.04 | 0.04 | 0.02 | 0.01 | 0.07 |
| $Na_2O$ | 0.38 | 0.37 | 0.37 | 0.34 | 0.38 | 0.27 | 0.34 | 0.38 | 0.24 | 0.49 | 0.38 | 0.35 | 0.37 | 0.51 | 0.48 |
| $K_2O$ | 0.11 | 0.00 | 0.00 | 0.00 | 0.03 | 0.00 | 0.00 | 0.08 | 0.05 | 0.09 | 0.00 | 0.23 | 0.00 | 0.05 | 0.05 |
| Total | 97.57 | 99.42 | 98.80 | 98.39 | 98.66 | 98.90 | 99.20 | 97.85 | 97.10 | 98.48 | 99.44 | 97.88 | 98.69 | 98.74 | 99.26 |
| Oxygen | 18 | 18 | 18 | 18 | 18 | 18 | 18 | 18 | 18 | 18 | 18 | 18 | 18 | 18 | 18 |
| Si | 4.93 | 4.91 | 4.95 | 4.94 | 4.92 | 4.95 | 4.97 | 4.92 | 4.97 | 4.87 | 4.95 | 4.92 | 4.91 | 4.92 | 4.93 |
| Ti | 0.00 | 0.00 | 0.00 | 0.00 | 0.00 | 0.00 | 0.00 | 0.00 | 0.00 | 0.00 | 0.00 | 0.00 | 0.00 | 0.01 | 0.00 |
| Al | 3.99 | 4.00 | 4.00 | 4.00 | 3.98 | 4.02 | 3.98 | 4.01 | 4.01 | 3.99 | 3.99 | 4.02 | 4.00 | 3.97 | 4.01 |
| $Fe^{3+}$ | 0.23 | 0.24 | 0.17 | 0.19 | 0.25 | 0.13 | 0.14 | 0.23 | 0.09 | 0.38 | 0.19 | 0.23 | 0.25 | 0.28 | 0.23 |
| $Fe^{2+}$ | 0.59 | 0.56 | 0.61 | 0.60 | 0.55 | 0.61 | 0.62 | 0.46 | 0.64 | 0.40 | 0.56 | 0.48 | 0.53 | 0.48 | 0.46 |
| Mn | 0.03 | 0.03 | 0.02 | 0.03 | 0.02 | 0.03 | 0.03 | 0.03 | 0.02 | 0.03 | 0.02 | 0.04 | 0.02 | 0.04 | 0.04 |
| Mg | 1.13 | 1.18 | 1.16 | 1.17 | 1.18 | 1.20 | 1.19 | 1.26 | 1.20 | 1.22 | 1.21 | 1.20 | 1.21 | 1.20 | 1.23 |
| Ca | 0.00 | 0.00 | 0.00 | 0.01 | 0.00 | 0.00 | 0.00 | 0.00 | 0.00 | 0.00 | 0.00 | 0.00 | 0.00 | 0.00 | 0.01 |
| Na | 0.08 | 0.07 | 0.07 | 0.07 | 0.08 | 0.05 | 0.07 | 0.08 | 0.05 | 0.10 | 0.08 | 0.07 | 0.07 | 0.10 | 0.09 |
| K | 0.01 | 0.00 | 0.00 | 0.00 | 0.00 | 0.00 | 0.00 | 0.01 | 0.01 | 0.01 | 0.00 | 0.03 | 0.00 | 0.01 | 0.01 |
| cations | 11.00 | 11.00 | 11.00 | 11.00 | 11.00 | 11.00 | 11.00 | 11.00 | 11.00 | 11.00 | 11.00 | 11.00 | 11.00 | 11.00 | 11.00 |
| $X_{Fe}$ ($Fe^{2+}$) | 0.34 | 0.32 | 0.35 | 0.34 | 0.32 | 0.34 | 0.34 | 0.27 | 0.35 | 0.25 | 0.32 | 0.28 | 0.31 | 0.28 | 0.27 |
| $X_{Fe}$ (Fetot) | 0.42 | 0.40 | 0.40 | 0.40 | 0.41 | 0.38 | 0.39 | 0.35 | 0.38 | 0.39 | 0.39 | 0.37 | 0.39 | 0.39 | 0.36 |

**Table A11.** (Continued)

| Sample | 459 | | | | | | | | | | | |
|---|---|---|---|---|---|---|---|---|---|---|---|---|
| Analysis | 459L | 459L | 459L | 459L | 459L | 459L | 459L | 459L | 459L | 459L | 459L | 459L |
| Spot | 122 | 124 | 125 | 129 | 132 | 135 | 181 | 184 | 185 | 188 | 191 | 194 |
| (wt%) | | | | | | | | | | | | |
| $SiO_2$ | 48.51 | 48.26 | 48.26 | 48.39 | 48.01 | 48.42 | 48.10 | 48.46 | 48.64 | 48.10 | 48.18 | 48.40 |
| $TiO_2$ | 0.09 | 0.00 | 0.00 | 0.00 | 0.04 | 0.01 | 0.04 | 0.01 | 0.06 | 0.00 | 0.04 | 0.06 |
| $Al_2O_3$ | 33.82 | 33.21 | 33.40 | 33.21 | 33.28 | 33.16 | 32.98 | 33.27 | 33.20 | 33.02 | 33.22 | 33.44 |
| FeO | 9.11 | 8.41 | 8.59 | 8.99 | 9.09 | 9.00 | 9.03 | 9.06 | 9.83 | 9.27 | 9.23 | 9.45 |
| MnO | 0.29 | 0.21 | 0.39 | 0.24 | 0.36 | 0.31 | 0.13 | 0.20 | 0.18 | 0.35 | 0.23 | 0.08 |
| MgO | 7.84 | 8.07 | 8.06 | 8.02 | 7.72 | 7.96 | 7.80 | 7.99 | 7.81 | 7.89 | 7.74 | 7.85 |
| CaO | 0.06 | 0.09 | 0.00 | 0.04 | 0.07 | 0.00 | 0.06 | 0.00 | 0.02 | 0.03 | 0.00 | 0.10 |
| $Na_2O$ | 0.40 | 0.40 | 0.40 | 0.36 | 0.41 | 0.46 | 0.47 | 0.50 | 0.46 | 0.40 | 0.57 | 0.47 |
| $K_2O$ | 0.00 | 0.04 | 0.00 | 0.00 | 0.02 | 0.03 | 0.00 | 0.00 | 0.01 | 0.00 | 0.03 | 0.00 |
| Total | 100.12 | 98.70 | 99.11 | 99.26 | 99.00 | 99.36 | 98.61 | 99.49 | 100.21 | 99.05 | 99.26 | 99.86 |
| Oxygen | 18 | 18 | 18 | 18 | 18 | 18 | 18 | 18 | 18 | 18 | 18 | 18 |
| Si | 4.90 | 4.93 | 4.92 | 4.93 | 4.91 | 4.93 | 4.93 | 4.92 | 4.92 | 4.92 | 4.91 | 4.90 |
| Ti | 0.01 | 0.00 | 0.00 | 0.00 | 0.00 | 0.00 | 0.00 | 0.00 | 0.00 | 0.00 | 0.00 | 0.00 |
| Al | 4.03 | 4.00 | 4.01 | 3.99 | 4.01 | 3.98 | 3.99 | 3.98 | 3.96 | 3.98 | 3.99 | 3.99 |
| $Fe^{3+}$ | 0.23 | 0.21 | 0.23 | 0.22 | 0.25 | 0.26 | 0.23 | 0.27 | 0.28 | 0.27 | 0.30 | 0.28 |
| $Fe^{2+}$ | 0.54 | 0.51 | 0.50 | 0.54 | 0.53 | 0.50 | 0.54 | 0.50 | 0.55 | 0.52 | 0.48 | 0.52 |
| Mn | 0.03 | 0.02 | 0.03 | 0.02 | 0.03 | 0.03 | 0.01 | 0.02 | 0.02 | 0.03 | 0.02 | 0.01 |
| Mg | 1.18 | 1.23 | 1.22 | 1.22 | 1.18 | 1.21 | 1.19 | 1.21 | 1.18 | 1.20 | 1.18 | 1.19 |
| Ca | 0.01 | 0.01 | 0.00 | 0.00 | 0.01 | 0.00 | 0.01 | 0.00 | 0.00 | 0.00 | 0.00 | 0.01 |
| Na | 0.08 | 0.08 | 0.08 | 0.07 | 0.08 | 0.09 | 0.09 | 0.10 | 0.09 | 0.08 | 0.11 | 0.09 |
| K | 0.00 | 0.01 | 0.00 | 0.00 | 0.00 | 0.00 | 0.00 | 0.00 | 0.00 | 0.00 | 0.00 | 0.00 |
| cations | 11.00 | 11.00 | 11.00 | 11.00 | 11.00 | 11.00 | 11.00 | 11.00 | 11.00 | 11.00 | 11.00 | 11.00 |
| $X_{Fe}$ ($Fe^{2+}$) | 0.31 | 0.29 | 0.29 | 0.31 | 0.31 | 0.29 | 0.31 | 0.29 | 0.32 | 0.30 | 0.29 | 0.31 |
| $X_{Fe}$ (Fetot) | 0.39 | 0.37 | 0.37 | 0.39 | 0.40 | 0.39 | 0.39 | 0.39 | 0.41 | 0.40 | 0.40 | 0.40 |

**Table A12.** Chemical analyses of a garnet porphyroblast from a schollen migmatite of the Intermediate series affected by the Ceret contact aureole.

| Sample | 459h | | | | | | | | | | | | | | | | |
|---|---|---|---|---|---|---|---|---|---|---|---|---|---|---|---|---|---|
| Analysis | A_1 | A_4 | A_5 | A_6 | A_7 | A_8 | A_9 | A_10 | A_11 | A_12 | A_13 | A_15 | A_16 | A_18 | A_19 | A_21 | A_22 |
| Spot | #151 | #154 | #155 | #156 | #157 | #158 | #159 | #160 | #161 | #162 | #163 | #165 | #166 | #168 | #169 | #171 | #172 |
| (wt%) | | | | | | | | | | | | | | | | | |
| $SiO_2$ | 35.25 | 36.23 | 35.92 | 36.17 | 36.57 | 36.26 | 36.44 | 36.14 | 36.18 | 36.23 | 36.55 | 36.17 | 36.31 | 36.49 | 36.09 | 35.97 | 36.39 |
| $TiO_2$ | 0.07 | 0.17 | 0.22 | 0.23 | 0.21 | 0.23 | 0.19 | 0.19 | 0.15 | 0.06 | 0.06 | 0.08 | 0.20 | 0.12 | 0.24 | 0.12 | 0.25 |
| $Al_2O_3$ | 20.47 | 20.75 | 20.52 | 20.99 | 20.59 | 20.84 | 20.90 | 20.92 | 20.98 | 20.91 | 20.69 | 20.41 | 20.87 | 20.93 | 20.61 | 20.44 | 20.90 |
| FeO | 36.13 | 35.04 | 35.49 | 35.65 | 35.84 | 35.57 | 36.00 | 35.86 | 35.51 | 35.99 | 35.62 | 35.67 | 36.20 | 36.33 | 35.99 | 36.02 | 36.07 |
| MnO | 3.67 | 1.54 | 1.71 | 1.64 | 1.71 | 1.77 | 1.72 | 1.76 | 1.60 | 1.82 | 1.65 | 1.52 | 1.58 | 1.49 | 1.43 | 1.75 | 1.90 |
| MgO | 2.42 | 3.13 | 2.98 | 2.84 | 2.93 | 2.83 | 2.79 | 2.82 | 2.81 | 2.95 | 2.87 | 3.03 | 3.09 | 3.03 | 3.05 | 2.99 | 2.62 |
| CaO | 1.29 | 2.51 | 2.56 | 2.55 | 2.55 | 2.55 | 2.57 | 2.58 | 2.63 | 2.68 | 2.88 | 2.75 | 2.55 | 2.36 | 2.39 | 2.19 | 2.47 |
| $Na_2O$ | 0.00 | 0.00 | 0.00 | 0.00 | 0.00 | 0.00 | 0.00 | 0.00 | 0.00 | 0.00 | 0.00 | 0.00 | 0.00 | 0.00 | 0.00 | 0.00 | 0.00 |
| $K_2O$ | 0.00 | 0.00 | 0.00 | 0.00 | 0.00 | 0.00 | 0.00 | 0.00 | 0.00 | 0.00 | 0.00 | 0.00 | 0.00 | 0.00 | 0.00 | 0.00 | 0.00 |
| Total | 99.30 | 99.37 | 99.40 | 100.07 | 100.40 | 100.05 | 100.61 | 100.27 | 99.86 | 100.64 | 100.32 | 99.63 | 100.80 | 100.75 | 99.80 | 99.48 | 100.60 |
| Oxygen | 12 | 12 | 12 | 12 | 12 | 12 | 12 | 12 | 12 | 12 | 12 | 12 | 12 | 12 | 12 | 12 | 12 |
| Si | 2.88 | 2.93 | 2.91 | 2.91 | 2.94 | 2.92 | 2.92 | 2.91 | 2.92 | 2.90 | 2.94 | 2.93 | 2.90 | 2.92 | 2.92 | 2.92 | 2.92 |
| Ti | 0.00 | 0.01 | 0.01 | 0.01 | 0.01 | 0.01 | 0.01 | 0.01 | 0.01 | 0.00 | 0.00 | 0.00 | 0.01 | 0.01 | 0.01 | 0.01 | 0.02 |
| Al | 1.97 | 1.98 | 1.96 | 1.99 | 1.95 | 1.98 | 1.98 | 1.98 | 2.00 | 1.98 | 1.96 | 1.95 | 1.97 | 1.97 | 1.96 | 1.96 | 1.98 |
| $Fe^{3+}$ | 0.25 | 0.13 | 0.18 | 0.15 | 0.14 | 0.14 | 0.15 | 0.17 | 0.14 | 0.21 | 0.16 | 0.19 | 0.20 | 0.17 | 0.17 | 0.19 | 0.14 |
| $Fe^{2+}$ | 2.23 | 2.24 | 2.23 | 2.26 | 2.27 | 2.26 | 2.26 | 2.24 | 2.25 | 2.20 | 2.24 | 2.22 | 2.22 | 2.26 | 2.26 | 2.25 | 2.28 |
| Mn | 0.25 | 0.11 | 0.12 | 0.11 | 0.12 | 0.12 | 0.12 | 0.12 | 0.11 | 0.12 | 0.11 | 0.10 | 0.11 | 0.10 | 0.10 | 0.12 | 0.13 |
| Mg | 0.30 | 0.38 | 0.36 | 0.34 | 0.35 | 0.34 | 0.33 | 0.34 | 0.34 | 0.35 | 0.34 | 0.37 | 0.37 | 0.36 | 0.37 | 0.36 | 0.31 |
| Ca | 0.11 | 0.22 | 0.22 | 0.22 | 0.22 | 0.22 | 0.22 | 0.22 | 0.23 | 0.23 | 0.25 | 0.24 | 0.22 | 0.20 | 0.21 | 0.19 | 0.21 |
| Na | 0.00 | 0.00 | 0.00 | 0.00 | 0.00 | 0.00 | 0.00 | 0.00 | 0.00 | 0.00 | 0.00 | 0.00 | 0.00 | 0.00 | 0.00 | 0.00 | 0.00 |
| K | 0.00 | 0.00 | 0.00 | 0.00 | 0.00 | 0.00 | 0.00 | 0.00 | 0.00 | 0.00 | 0.00 | 0.00 | 0.00 | 0.00 | 0.00 | 0.00 | 0.00 |
| cations | 8.00 | 8.00 | 8.00 | 8.00 | 8.00 | 8.00 | 8.00 | 8.00 | 8.00 | 8.00 | 8.00 | 8.00 | 8.00 | 8.00 | 8.00 | 8.00 | 8.00 |
| grs | 0.04 | 0.07 | 0.07 | 0.07 | 0.07 | 0.07 | 0.07 | 0.07 | 0.07 | 0.07 | 0.08 | 0.08 | 0.07 | 0.07 | 0.07 | 0.06 | 0.07 |
| alm | 0.79 | 0.77 | 0.77 | 0.78 | 0.78 | 0.78 | 0.78 | 0.78 | 0.78 | 0.77 | 0.77 | 0.77 | 0.78 | 0.79 | 0.78 | 0.78 | 0.79 |
| prp | 0.09 | 0.12 | 0.12 | 0.11 | 0.11 | 0.11 | 0.11 | 0.11 | 0.11 | 0.11 | 0.11 | 0.12 | 0.12 | 0.12 | 0.12 | 0.12 | 0.10 |
| sps | 0.08 | 0.03 | 0.04 | 0.04 | 0.04 | 0.04 | 0.04 | 0.04 | 0.04 | 0.04 | 0.04 | 0.03 | 0.03 | 0.03 | 0.03 | 0.04 | 0.04 |
| $X_{Fe}$ ($Fe^{2+}$) | 0.88 | 0.86 | 0.86 | 0.87 | 0.87 | 0.87 | 0.87 | 0.87 | 0.87 | 0.86 | 0.87 | 0.86 | 0.86 | 0.86 | 0.86 | 0.86 | 0.88 |
| $X_{Fe}$ (Fetot) | 0.89 | 0.86 | 0.87 | 0.88 | 0.87 | 0.88 | 0.88 | 0.88 | 0.88 | 0.87 | 0.87 | 0.87 | 0.87 | 0.87 | 0.87 | 0.87 | 0.89 |

**Table A12.** (Continued)

| Sample | 459h | | | | | | | | | | | | | | | | |
|---|---|---|---|---|---|---|---|---|---|---|---|---|---|---|---|---|---|
| Analysis | A_24 | A_25 | A_26 | A_34 | A_36 | A_37 | A_38 | A2_1 | A2_4 | A2_5 | A2_6 | A2_7 | A2_8 | A2_9 | A2_10 | A2_11 | A2_12 |
| Spot | #174 | #175 | #176 | #184 | #186 | #187 | #188 | #189 | #192 | #193 | #194 | #195 | #196 | #197 | #198 | #199 | #200 |
| (wt%) | | | | | | | | | | | | | | | | | |
| $SiO_2$ | 35.82 | 35.68 | 36.35 | 35.75 | 35.48 | 35.83 | 36.08 | 35.12 | 35.57 | 35.38 | 35.00 | 35.35 | 35.21 | 35.31 | 35.23 | 37.03 | 34.92 |
| $TiO_2$ | 0.30 | 0.30 | 0.28 | 0.19 | 0.15 | 0.17 | 0.21 | 0.36 | 0.39 | 0.34 | 0.28 | 0.18 | 0.11 | 0.27 | 0.13 | 0.18 | 0.13 |
| $Al_2O_3$ | 20.61 | 20.39 | 20.88 | 20.50 | 20.52 | 20.54 | 21.03 | 20.00 | 20.31 | 20.32 | 20.31 | 20.44 | 20.40 | 20.17 | 20.57 | 21.00 | 20.14 |
| FeO | 35.85 | 35.72 | 36.22 | 36.30 | 36.87 | 36.69 | 36.99 | 36.74 | 36.98 | 36.75 | 37.15 | 36.83 | 36.43 | 37.48 | 36.80 | 36.58 | 36.86 |
| MnO | 1.70 | 1.85 | 1.56 | 1.69 | 1.72 | 1.79 | 1.79 | 1.61 | 1.66 | 1.76 | 1.75 | 1.82 | 1.71 | 1.76 | 1.81 | 1.67 | 1.74 |
| MgO | 2.91 | 2.86 | 2.82 | 2.31 | 2.12 | 2.07 | 1.98 | 1.94 | 2.01 | 2.12 | 2.18 | 2.24 | 2.25 | 2.27 | 2.32 | 2.28 | 2.45 |
| CaO | 2.45 | 2.49 | 2.56 | 2.41 | 2.40 | 2.38 | 2.39 | 2.51 | 2.58 | 2.45 | 2.47 | 2.39 | 2.31 | 2.42 | 2.33 | 2.43 | 2.30 |
| $Na_2O$ | 0.00 | 0.00 | 0.00 | 0.00 | 0.00 | 0.00 | 0.00 | 0.00 | 0.00 | 0.00 | 0.00 | 0.00 | 0.00 | 0.00 | 0.00 | 0.00 | 0.00 |
| $K_2O$ | 0.00 | 0.00 | 0.00 | 0.00 | 0.00 | 0.00 | 0.00 | 0.00 | 0.00 | 0.00 | 0.00 | 0.00 | 0.00 | 0.00 | 0.00 | 0.00 | 0.00 |
| Total | 99.64 | 99.29 | 100.67 | 99.15 | 99.26 | 99.47 | 100.47 | 98.28 | 99.50 | 99.12 | 99.14 | 99.25 | 98.42 | 99.68 | 99.19 | 101.17 | 98.54 |
| Oxygen | 12 | 12 | 12 | 12 | 12 | 12 | 12 | 12 | 12 | 12 | 12 | 12 | 12 | 12 | 12 | 12 | 12 |
| Si | 2.90 | 2.90 | 2.92 | 2.92 | 2.90 | 2.92 | 2.92 | 2.91 | 2.91 | 2.90 | 2.87 | 2.89 | 2.90 | 2.88 | 2.88 | 2.96 | 2.87 |
| Ti | 0.02 | 0.02 | 0.02 | 0.01 | 0.01 | 0.01 | 0.01 | 0.02 | 0.02 | 0.02 | 0.02 | 0.01 | 0.01 | 0.02 | 0.01 | 0.01 | 0.01 |
| Al | 1.97 | 1.96 | 1.97 | 1.97 | 1.98 | 1.98 | 2.00 | 1.95 | 1.96 | 1.96 | 1.96 | 1.97 | 1.98 | 1.94 | 1.98 | 1.98 | 1.95 |
| $Fe^{3+}$ | 0.19 | 0.20 | 0.16 | 0.16 | 0.20 | 0.15 | 0.14 | 0.19 | 0.18 | 0.19 | 0.26 | 0.23 | 0.20 | 0.27 | 0.24 | 0.07 | 0.28 |
| $Fe^{2+}$ | 2.24 | 2.23 | 2.27 | 2.32 | 2.32 | 2.35 | 2.36 | 2.35 | 2.34 | 2.32 | 2.28 | 2.29 | 2.31 | 2.29 | 2.28 | 2.38 | 2.26 |
| Mn | 0.12 | 0.13 | 0.11 | 0.12 | 0.12 | 0.12 | 0.12 | 0.11 | 0.11 | 0.12 | 0.12 | 0.13 | 0.12 | 0.12 | 0.13 | 0.11 | 0.12 |
| Mg | 0.35 | 0.35 | 0.34 | 0.28 | 0.26 | 0.25 | 0.24 | 0.24 | 0.24 | 0.26 | 0.27 | 0.27 | 0.28 | 0.28 | 0.28 | 0.27 | 0.30 |
| Ca | 0.21 | 0.22 | 0.22 | 0.21 | 0.21 | 0.21 | 0.21 | 0.22 | 0.23 | 0.22 | 0.22 | 0.21 | 0.20 | 0.21 | 0.20 | 0.21 | 0.20 |
| Na | 0.00 | 0.00 | 0.00 | 0.00 | 0.00 | 0.00 | 0.00 | 0.00 | 0.00 | 0.00 | 0.00 | 0.00 | 0.00 | 0.00 | 0.00 | 0.00 | 0.00 |
| K | 0.00 | 0.00 | 0.00 | 0.00 | 0.00 | 0.00 | 0.00 | 0.00 | 0.00 | 0.00 | 0.00 | 0.00 | 0.00 | 0.00 | 0.00 | 0.00 | 0.00 |
| cations | 8.00 | 8.00 | 8.00 | 8.00 | 8.00 | 8.00 | 8.00 | 8.00 | 8.00 | 8.00 | 8.00 | 8.00 | 8.00 | 8.00 | 8.00 | 8.00 | 8.00 |
| grs | 0.07 | 0.07 | 0.07 | 0.07 | 0.07 | 0.07 | 0.07 | 0.07 | 0.07 | 0.07 | 0.07 | 0.07 | 0.07 | 0.07 | 0.07 | 0.07 | 0.06 |
| alm | 0.78 | 0.78 | 0.79 | 0.80 | 0.81 | 0.81 | 0.81 | 0.82 | 0.81 | 0.81 | 0.81 | 0.81 | 0.81 | 0.81 | 0.80 | 0.80 | 0.80 |
| prp | 0.11 | 0.11 | 0.11 | 0.09 | 0.08 | 0.08 | 0.08 | 0.08 | 0.08 | 0.08 | 0.08 | 0.09 | 0.09 | 0.09 | 0.09 | 0.09 | 0.10 |
| sps | 0.04 | 0.04 | 0.03 | 0.04 | 0.04 | 0.04 | 0.04 | 0.04 | 0.04 | 0.04 | 0.04 | 0.04 | 0.04 | 0.04 | 0.04 | 0.04 | 0.04 |
| $X_{Fe}$ ($Fe^{2+}$) | 0.86 | 0.87 | 0.87 | 0.89 | 0.90 | 0.90 | 0.91 | 0.91 | 0.91 | 0.90 | 0.90 | 0.89 | 0.89 | 0.89 | 0.89 | 0.90 | 0.88 |
| $X_{Fe}$ (Fetot) | 0.87 | 0.88 | 0.88 | 0.90 | 0.91 | 0.91 | 0.91 | 0.91 | 0.91 | 0.91 | 0.91 | 0.90 | 0.90 | 0.90 | 0.90 | 0.90 | 0.89 |

**Table A12.** (Continued)

| Sample | 459h | | | | | | | | | | | | | | |
|---|---|---|---|---|---|---|---|---|---|---|---|---|---|---|---|
| Analysis | A2_15 | A2_17 | A2_19 | A2_20 | A2_22 | A2_27 | A2_29 | A2_30 | A2_31 | A2_32 | A2_34 | A2_35 | A2_36 | A2_37 | A2_38 |
| Spot | #203 | #205 | #207 | #208 | #210 | #215 | #217 | #218 | #219 | #220 | #222 | #223 | #224 | #225 | #226 |
| (wt%) | | | | | | | | | | | | | | | |
| $SiO_2$ | 36.09 | 36.57 | 36.13 | 35.90 | 36.25 | 36.28 | 36.47 | 36.01 | 36.22 | 36.93 | 37.43 | 36.20 | 36.65 | 36.59 | 37.11 |
| $TiO_2$ | 0.16 | 0.13 | 0.16 | 0.18 | 0.06 | 0.06 | 0.05 | 0.06 | 0.05 | 0.10 | 0.08 | 0.09 | 0.08 | 0.08 | 0.03 |
| $Al_2O_3$ | 20.90 | 20.89 | 20.50 | 20.67 | 20.69 | 20.65 | 20.62 | 20.96 | 20.60 | 21.28 | 21.54 | 21.06 | 21.14 | 21.22 | 21.59 |
| FeO | 36.82 | 36.41 | 36.39 | 36.56 | 37.50 | 36.80 | 36.19 | 36.06 | 35.79 | 36.42 | 35.71 | 36.22 | 35.87 | 35.91 | 36.67 |
| MnO | 1.68 | 1.51 | 1.61 | 1.61 | 1.77 | 1.71 | 1.74 | 1.75 | 1.66 | 1.72 | 1.60 | 1.69 | 2.04 | 2.36 | 3.03 |
| MgO | 2.53 | 2.75 | 2.87 | 2.94 | 2.01 | 2.64 | 3.00 | 2.96 | 2.98 | 2.98 | 3.32 | 3.58 | 3.38 | 3.19 | 2.29 |
| CaO | 2.46 | 2.32 | 2.36 | 2.33 | 1.47 | 1.98 | 2.10 | 2.40 | 2.46 | 2.50 | 1.99 | 1.55 | 1.39 | 1.25 | 1.23 |
| $Na_2O$ | 0.00 | 0.00 | 0.00 | 0.00 | 0.00 | 0.00 | 0.00 | 0.00 | 0.00 | 0.00 | 0.00 | 0.00 | 0.00 | 0.00 | 0.00 |
| $K_2O$ | 0.00 | 0.00 | 0.00 | 0.00 | 0.00 | 0.00 | 0.00 | 0.00 | 0.00 | 0.00 | 0.00 | 0.00 | 0.00 | 0.00 | 0.00 |
| Total | 100.64 | 100.58 | 100.02 | 100.19 | 99.75 | 100.12 | 100.17 | 100.20 | 99.76 | 101.93 | 101.67 | 100.39 | 100.55 | 100.60 | 101.95 |
| Oxygen | 12 | 12 | 12 | 12 | 12 | 12 | 12 | 12 | 12 | 12 | 12 | 12 | 12 | 12 | 12 |
| Si | 2.90 | 2.94 | 2.92 | 2.89 | 2.96 | 2.93 | 2.94 | 2.90 | 2.93 | 2.92 | 2.96 | 2.90 | 2.93 | 2.93 | 2.95 |
| Ti | 0.01 | 0.01 | 0.01 | 0.01 | 0.00 | 0.00 | 0.00 | 0.00 | 0.00 | 0.01 | 0.00 | 0.01 | 0.00 | 0.00 | 0.00 |
| Al | 1.98 | 1.98 | 1.95 | 1.96 | 1.99 | 1.97 | 1.96 | 1.99 | 1.96 | 1.98 | 2.01 | 1.99 | 2.00 | 2.01 | 2.02 |
| $Fe^{3+}$ | 0.19 | 0.13 | 0.19 | 0.22 | 0.09 | 0.16 | 0.16 | 0.21 | 0.17 | 0.16 | 0.06 | 0.20 | 0.12 | 0.12 | 0.07 |
| $Fe^{2+}$ | 2.28 | 2.31 | 2.27 | 2.24 | 2.46 | 2.33 | 2.28 | 2.22 | 2.25 | 2.25 | 2.30 | 2.23 | 2.28 | 2.29 | 2.37 |
| Mn | 0.11 | 0.10 | 0.11 | 0.11 | 0.12 | 0.12 | 0.12 | 0.12 | 0.11 | 0.12 | 0.11 | 0.11 | 0.14 | 0.16 | 0.20 |
| Mg | 0.30 | 0.33 | 0.35 | 0.35 | 0.24 | 0.32 | 0.36 | 0.36 | 0.36 | 0.35 | 0.39 | 0.43 | 0.40 | 0.38 | 0.27 |
| Ca | 0.21 | 0.20 | 0.20 | 0.20 | 0.13 | 0.17 | 0.18 | 0.21 | 0.21 | 0.21 | 0.17 | 0.13 | 0.12 | 0.11 | 0.10 |
| Na | 0.00 | 0.00 | 0.00 | 0.00 | 0.00 | 0.00 | 0.00 | 0.00 | 0.00 | 0.00 | 0.00 | 0.00 | 0.00 | 0.00 | 0.00 |
| K | 0.00 | 0.00 | 0.00 | 0.00 | 0.00 | 0.00 | 0.00 | 0.00 | 0.00 | 0.00 | 0.00 | 0.00 | 0.00 | 0.00 | 0.00 |
| cations | 8.00 | 8.00 | 8.00 | 8.00 | 8.00 | 8.00 | 8.00 | 8.00 | 8.00 | 8.00 | 8.00 | 8.00 | 8.00 | 8.00 | 8.00 |
| grs | 0.07 | 0.06 | 0.07 | 0.06 | 0.04 | 0.06 | 0.06 | 0.07 | 0.07 | 0.07 | 0.06 | 0.04 | 0.04 | 0.04 | 0.03 |
| alm | 0.80 | 0.79 | 0.79 | 0.79 | 0.84 | 0.80 | 0.79 | 0.78 | 0.78 | 0.78 | 0.78 | 0.78 | 0.78 | 0.79 | 0.81 |
| prp | 0.10 | 0.11 | 0.11 | 0.11 | 0.08 | 0.10 | 0.12 | 0.11 | 0.12 | 0.11 | 0.13 | 0.14 | 0.13 | 0.12 | 0.09 |
| sps | 0.04 | 0.03 | 0.04 | 0.04 | 0.04 | 0.04 | 0.04 | 0.04 | 0.04 | 0.04 | 0.04 | 0.04 | 0.05 | 0.05 | 0.07 |
| $X_{Fe}$ ($Fe^{2+}$) | 0.88 | 0.88 | 0.87 | 0.86 | 0.91 | 0.88 | 0.86 | 0.86 | 0.86 | 0.86 | 0.85 | 0.84 | 0.85 | 0.86 | 0.90 |
| $X_{Fe}$ (Fetot) | 0.89 | 0.88 | 0.88 | 0.87 | 0.91 | 0.89 | 0.87 | 0.87 | 0.87 | 0.87 | 0.86 | 0.85 | 0.86 | 0.86 | 0.90 |

**Table A13.** Chemical composition of biotite from a residuum melanosome of the Intermediate series affected by the Ceret contact aureole.

| Sample | 462 | | | | | | | | | | | | | | | |
|---|---|---|---|---|---|---|---|---|---|---|---|---|---|---|---|---|
| Analysis | 462g | 462g | 462g | 462g | 462g | 462g | 462g | 462g | 462g | 462g | 462g | 462g | 462g | 462g | 462g | 462g |
| Spot | 536 | 538 | 545 | 547 | 549 | 555 | 557 | 561 | 565 | 567 | 568 | 571 | 573 | 580 | 587 | 588 |
| (wt%) | | | | | | | | | | | | | | | | |
| $SiO_2$ | 31.98 | 32.83 | 33.66 | 34.25 | 32.89 | 37.29 | 33.81 | 33.29 | 35.31 | 31.68 | 34.19 | 35.84 | 35.39 | 37.79 | 34.48 | 30.82 |
| $TiO_2$ | 3.13 | 2.49 | 2.38 | 3.63 | 3.08 | 3.39 | 3.22 | 3.37 | 3.33 | 3.64 | 3.35 | 3.29 | 3.02 | 2.24 | 2.47 | 2.74 |
| $Al_2O_3$ | 17.40 | 20.00 | 18.96 | 19.12 | 19.59 | 18.82 | 19.79 | 19.66 | 19.37 | 18.79 | 19.37 | 20.18 | 20.46 | 21.16 | 19.57 | 20.15 |
| FeO | 16.56 | 19.91 | 17.80 | 17.73 | 18.22 | 17.05 | 18.54 | 18.49 | 17.50 | 19.24 | 18.76 | 15.71 | 16.57 | 16.83 | 16.80 | 18.23 |
| MnO | 0.00 | 0.00 | 0.00 | 0.00 | 0.00 | 0.00 | 0.00 | 0.13 | 0.00 | 0.00 | 0.00 | 0.00 | 0.00 | 0.00 | 0.00 | 0.00 |
| MgO | 8.49 | 10.30 | 13.63 | 10.85 | 11.68 | 8.85 | 10.42 | 10.62 | 9.21 | 11.66 | 9.40 | 10.00 | 10.50 | 11.25 | 10.95 | 14.69 |
| CaO | 0.57 | 0.00 | 0.00 | 0.00 | 0.00 | 0.00 | 0.00 | 0.00 | 0.00 | 0.00 | 0.00 | 0.00 | 0.00 | 0.00 | 0.00 | 0.00 |
| $Na_2O$ | 0.00 | 0.23 | 0.14 | 0.30 | 0.00 | 0.25 | 0.20 | 0.30 | 0.26 | 0.13 | 0.23 | 0.36 | 0.29 | 0.25 | 0.24 | 0.20 |
| $K_2O$ | 4.48 | 3.86 | 4.34 | 6.47 | 5.31 | 6.17 | 6.55 | 6.04 | 8.49 | 2.96 | 7.55 | 8.23 | 7.87 | 3.30 | 6.97 | 3.20 |
| Total | 82.60 | 89.61 | 90.91 | 92.34 | 90.77 | 91.81 | 92.53 | 91.90 | 93.48 | 88.10 | 92.86 | 93.61 | 94.10 | 92.82 | 91.49 | 90.02 |
| Oxygen | 11 | 11 | 11 | 11 | 11 | 11 | 11 | 11 | 11 | 11 | 11 | 11 | 11 | 11 | 11 | 11 |
| Si | 2.90 | 2.74 | 2.72 | 2.76 | 2.69 | 3.04 | 2.71 | 2.69 | 2.80 | 2.67 | 2.74 | 2.82 | 2.77 | 3.01 | 2.77 | 2.50 |
| Ti | 0.21 | 0.16 | 0.14 | 0.22 | 0.19 | 0.21 | 0.19 | 0.20 | 0.20 | 0.23 | 0.20 | 0.19 | 0.18 | 0.13 | 0.15 | 0.17 |
| Al | 1.86 | 1.97 | 1.81 | 1.82 | 1.89 | 1.81 | 1.87 | 1.87 | 1.81 | 1.87 | 1.83 | 1.87 | 1.89 | 1.99 | 1.85 | 1.93 |
| $Fe^{3+}$ | 0.00 | 0.00 | 0.00 | 0.00 | 0.00 | 0.00 | 0.00 | 0.00 | 0.00 | 0.00 | 0.00 | 0.00 | 0.00 | 0.00 | 0.00 | 0.00 |
| $Fe^{2+}$ | 1.26 | 1.39 | 1.20 | 1.19 | 1.25 | 1.16 | 1.24 | 1.25 | 1.16 | 1.36 | 1.26 | 1.03 | 1.08 | 1.12 | 1.13 | 1.24 |
| Mn | 0.00 | 0.00 | 0.00 | 0.00 | 0.00 | 0.00 | 0.00 | 0.01 | 0.00 | 0.00 | 0.00 | 0.00 | 0.00 | 0.00 | 0.00 | 0.00 |
| Mg | 1.15 | 1.28 | 1.64 | 1.30 | 1.42 | 1.07 | 1.25 | 1.28 | 1.09 | 1.47 | 1.12 | 1.17 | 1.23 | 1.34 | 1.31 | 1.78 |
| Ca | 0.06 | 0.00 | 0.00 | 0.00 | 0.00 | 0.00 | 0.00 | 0.00 | 0.00 | 0.00 | 0.00 | 0.00 | 0.00 | 0.00 | 0.00 | 0.00 |
| Na | 0.00 | 0.04 | 0.02 | 0.05 | 0.00 | 0.04 | 0.03 | 0.05 | 0.04 | 0.02 | 0.04 | 0.05 | 0.04 | 0.04 | 0.04 | 0.03 |
| K | 0.52 | 0.41 | 0.45 | 0.66 | 0.55 | 0.64 | 0.67 | 0.62 | 0.86 | 0.32 | 0.77 | 0.83 | 0.79 | 0.34 | 0.71 | 0.33 |
| cations | 8.00 | 8.00 | 8.00 | 8.00 | 8.00 | 8.00 | 8.00 | 8.00 | 8.00 | 8.00 | 8.00 | 8.00 | 8.00 | 8.00 | 8.00 | 8.00 |
| $X_{Fe}$ ($Fe^{2+}$) | 0.52 | 0.52 | 0.42 | 0.48 | 0.47 | 0.52 | 0.50 | 0.49 | 0.52 | 0.48 | 0.53 | 0.47 | 0.47 | 0.46 | 0.46 | 0.41 |
| $X_{Fe}$ (Fetot) | 0.52 | 0.52 | 0.42 | 0.48 | 0.47 | 0.52 | 0.50 | 0.49 | 0.52 | 0.48 | 0.53 | 0.47 | 0.47 | 0.46 | 0.46 | 0.41 |

**Table A14.** Chemical composition of cordierite from a residuum melanosome of the Intermediate series affected by the Ceret contact aureole.

| Sample | 462 | | | | | | | | | | | | | | | | | |
|---|---|---|---|---|---|---|---|---|---|---|---|---|---|---|---|---|---|---|
| Analysis | 462g | 462g | 462g | 462g | 462g | 462g | 462g | 462g | 462g | 462g | 462g | 462g | 462g | 462g | 462g | 462g | 462g | 462g |
| Spot | 535 | 537 | 540 | 542 | 546 | 548 | 553 | 556 | 558 | 560 | 566 | 569 | 572 | 574 | 575 | 576 | 577 | 579 |
| (wt%) | | | | | | | | | | | | | | | | | | |
| $SiO_2$ | 47.80 | 48.77 | 48.45 | 47.20 | 48.33 | 48.69 | 48.00 | 48.38 | 48.56 | 48.22 | 48.27 | 48.19 | 48.31 | 48.32 | 48.70 | 48.33 | 48.66 | 48.67 |
| $TiO_2$ | 0.00 | 0.15 | 0.00 | 0.13 | 0.00 | 0.12 | 0.00 | 0.00 | 0.00 | 0.00 | 0.00 | 0.12 | 0.00 | 0.00 | 0.00 | 0.00 | 0.00 | 0.00 |
| $Al_2O_3$ | 33.05 | 33.41 | 33.46 | 31.97 | 33.30 | 33.09 | 32.72 | 33.41 | 33.18 | 33.14 | 33.39 | 33.43 | 33.25 | 33.11 | 33.51 | 33.22 | 33.51 | 33.21 |
| FeO | 7.10 | 7.55 | 7.89 | 7.26 | 7.63 | 8.13 | 7.79 | 7.70 | 8.02 | 8.14 | 7.89 | 7.65 | 7.76 | 7.81 | 8.26 | 8.13 | 8.06 | 8.22 |
| MnO | 0.00 | 0.27 | 0.00 | 0.00 | 0.00 | 0.00 | 0.14 | 0.00 | 0.00 | 0.12 | 0.14 | 0.00 | 0.11 | 0.11 | 0.00 | 0.15 | 0.19 | 0.00 |
| MgO | 7.91 | 8.74 | 8.86 | 8.16 | 8.82 | 8.65 | 8.51 | 8.65 | 8.50 | 8.60 | 8.66 | 8.86 | 9.01 | 8.46 | 8.76 | 8.76 | 8.89 | 8.65 |
| CaO | 0.00 | 0.00 | 0.00 | 0.17 | 0.00 | 0.00 | 0.00 | 0.00 | 0.00 | 0.00 | 0.00 | 0.00 | 0.00 | 0.00 | 0.00 | 0.00 | 0.00 | 0.00 |
| $Na_2O$ | 0.50 | 0.27 | 0.27 | 0.31 | 0.25 | 0.31 | 0.24 | 0.22 | 0.25 | 0.21 | 0.34 | 0.20 | 0.40 | 0.21 | 0.19 | 0.18 | 0.29 | 0.27 |
| $K_2O$ | 0.46 | 0.00 | 0.00 | 0.23 | 0.00 | 0.00 | 0.00 | 0.00 | 0.00 | 0.00 | 0.00 | 0.00 | 0.00 | 0.00 | 0.00 | 0.00 | 0.00 | 0.00 |
| Total | 96.81 | 99.16 | 98.93 | 95.42 | 98.34 | 99.00 | 97.40 | 98.36 | 98.51 | 98.44 | 98.69 | 98.45 | 98.83 | 98.02 | 99.41 | 98.77 | 99.60 | 99.02 |
| Oxygen | 18 | 18 | 18 | 18 | 18 | 18 | 18 | 18 | 18 | 18 | 18 | 18 | 18 | 18 | 18 | 18 | 18 | 18 |
| Si | 4.96 | 4.95 | 4.92 | 4.98 | 4.94 | 4.96 | 4.96 | 4.95 | 4.97 | 4.94 | 4.92 | 4.92 | 4.91 | 4.97 | 4.94 | 4.93 | 4.92 | 4.95 |
| Ti | 0.00 | 0.01 | 0.00 | 0.01 | 0.00 | 0.01 | 0.00 | 0.00 | 0.00 | 0.00 | 0.00 | 0.01 | 0.00 | 0.00 | 0.00 | 0.00 | 0.00 | 0.00 |
| Al | 4.04 | 4.00 | 4.01 | 3.97 | 4.01 | 3.97 | 3.99 | 4.03 | 4.00 | 4.00 | 4.01 | 4.02 | 3.98 | 4.01 | 4.00 | 3.99 | 3.99 | 3.98 |
| $Fe^{3+}$ | 0.20 | 0.13 | 0.20 | 0.14 | 0.16 | 0.16 | 0.13 | 0.11 | 0.11 | 0.17 | 0.21 | 0.15 | 0.28 | 0.09 | 0.16 | 0.18 | 0.23 | 0.16 |
| $Fe^{2+}$ | 0.42 | 0.51 | 0.47 | 0.50 | 0.50 | 0.53 | 0.55 | 0.55 | 0.57 | 0.53 | 0.46 | 0.50 | 0.38 | 0.58 | 0.54 | 0.51 | 0.45 | 0.53 |
| Mn | 0.00 | 0.02 | 0.00 | 0.00 | 0.00 | 0.00 | 0.01 | 0.00 | 0.00 | 0.01 | 0.01 | 0.00 | 0.01 | 0.01 | 0.00 | 0.01 | 0.02 | 0.00 |
| Mg | 1.22 | 1.32 | 1.34 | 1.28 | 1.34 | 1.31 | 1.31 | 1.32 | 1.30 | 1.31 | 1.32 | 1.35 | 1.36 | 1.30 | 1.32 | 1.33 | 1.34 | 1.31 |
| Ca | 0.00 | 0.00 | 0.00 | 0.02 | 0.00 | 0.00 | 0.00 | 0.00 | 0.00 | 0.00 | 0.00 | 0.00 | 0.00 | 0.00 | 0.00 | 0.00 | 0.00 | 0.00 |
| Na | 0.10 | 0.05 | 0.05 | 0.06 | 0.05 | 0.06 | 0.05 | 0.04 | 0.05 | 0.04 | 0.07 | 0.04 | 0.08 | 0.04 | 0.04 | 0.04 | 0.06 | 0.05 |
| K | 0.06 | 0.00 | 0.00 | 0.03 | 0.00 | 0.00 | 0.00 | 0.00 | 0.00 | 0.00 | 0.00 | 0.00 | 0.00 | 0.00 | 0.00 | 0.00 | 0.00 | 0.00 |
| cations | 11.00 | 11.00 | 11.00 | 11.00 | 11.00 | 11.00 | 11.00 | 11.00 | 11.00 | 11.00 | 11.00 | 11.00 | 11.00 | 11.00 | 11.00 | 11.00 | 11.00 | 11.00 |
| $X_{Fe}$ ($Fe^{2+}$) | 0.25 | 0.28 | 0.26 | 0.28 | 0.27 | 0.29 | 0.29 | 0.29 | 0.31 | 0.29 | 0.26 | 0.27 | 0.22 | 0.31 | 0.29 | 0.28 | 0.25 | 0.29 |
| $X_{Fe}$ (Fetot) | 0.34 | 0.33 | 0.33 | 0.33 | 0.33 | 0.35 | 0.34 | 0.33 | 0.35 | 0.35 | 0.34 | 0.33 | 0.33 | 0.34 | 0.35 | 0.34 | 0.34 | 0.35 |

**Table A15.** Chemical analyses of a garnet porphyroblast from a residuum melanosome of the Intermediate series affected by the Ceret contact aureole.

| Sample | 462q | | | | | | | | | | | | | | | | | |
|---|---|---|---|---|---|---|---|---|---|---|---|---|---|---|---|---|---|---|
| Analysis | A_1 | A_2 | A_3 | A_4 | A_5 | A_6 | A_7 | A_8 | A_11 | A_12 | A_13 | A_14 | A_15 | A_16 | A_18 | A_19 | A_20 | A_21 |
| Spot | #369 | #370 | #371 | #372 | #373 | #374 | #375 | #376 | #379 | #380 | #381 | #382 | #383 | #384 | #386 | #387 | #388 | #389 |
| (wt%) | | | | | | | | | | | | | | | | | | |
| $SiO_2$ | 36.42 | 37.97 | 37.95 | 37.67 | 37.48 | 37.59 | 36.90 | 37.79 | 36.78 | 37.07 | 37.43 | 37.42 | 37.73 | 37.16 | 36.93 | 37.42 | 38.04 | 37.26 |
| $TiO_2$ | 0.09 | 0.07 | 0.07 | 0.09 | 0.10 | 0.12 | 0.10 | 0.10 | 0.06 | 0.05 | 0.08 | 0.09 | 0.15 | 0.13 | 0.13 | 0.09 | 0.14 | 0.10 |
| $Al_2O_3$ | 21.04 | 21.77 | 21.69 | 21.68 | 21.53 | 21.63 | 21.31 | 21.45 | 21.58 | 21.65 | 21.31 | 21.61 | 21.70 | 21.51 | 21.39 | 21.49 | 21.63 | 21.51 |
| FeO | 36.78 | 32.73 | 32.44 | 32.19 | 32.02 | 32.11 | 31.52 | 32.34 | 32.57 | 32.87 | 32.98 | 32.75 | 32.79 | 32.51 | 32.99 | 32.67 | 33.16 | 33.41 |
| MnO | 1.45 | 0.60 | 0.74 | 0.68 | 0.77 | 0.76 | 0.69 | 0.77 | 0.92 | 0.87 | 0.88 | 0.92 | 0.97 | 0.92 | 0.91 | 0.93 | 1.04 | 0.96 |
| MgO | 3.08 | 6.56 | 6.94 | 7.01 | 6.94 | 6.90 | 5.70 | 6.07 | 5.99 | 6.28 | 6.49 | 6.24 | 6.22 | 6.34 | 6.05 | 6.15 | 6.03 | 5.97 |
| CaO | 1.21 | 1.17 | 1.19 | 1.22 | 1.24 | 1.12 | 1.17 | 1.21 | 1.19 | 1.13 | 1.17 | 1.08 | 1.17 | 1.09 | 1.16 | 1.13 | 1.09 | 1.10 |
| $Na_2O$ | 0.00 | 0.00 | 0.00 | 0.00 | 0.00 | 0.00 | 0.00 | 0.00 | 0.00 | 0.00 | 0.00 | 0.00 | 0.00 | 0.00 | 0.00 | 0.00 | 0.00 | 0.00 |
| $K_2O$ | 0.00 | 0.00 | 0.00 | 0.00 | 0.00 | 0.00 | 0.00 | 0.00 | 0.00 | 0.00 | 0.00 | 0.00 | 0.00 | 0.00 | 0.00 | 0.00 | 0.00 | 0.00 |
| Total | 100.07 | 100.87 | 101.02 | 100.54 | 100.08 | 100.23 | 97.39 | 99.73 | 99.09 | 99.92 | 100.34 | 100.11 | 100.73 | 99.66 | 99.56 | 99.88 | 101.13 | 100.31 |
| Oxygen | 12 | 12 | 12 | 12 | 12 | 12 | 12 | 12 | 12 | 12 | 12 | 12 | 12 | 12 | 12 | 12 | 12 | 12 |
| Si | 2.93 | 2.96 | 2.95 | 2.94 | 2.94 | 2.94 | 2.99 | 2.99 | 2.93 | 2.92 | 2.94 | 2.95 | 2.95 | 2.94 | 2.93 | 2.95 | 2.97 | 2.93 |
| Ti | 0.01 | 0.00 | 0.00 | 0.01 | 0.01 | 0.01 | 0.01 | 0.01 | 0.00 | 0.00 | 0.00 | 0.01 | 0.01 | 0.01 | 0.01 | 0.01 | 0.01 | 0.01 |
| Al | 2.00 | 2.00 | 1.98 | 1.99 | 1.99 | 2.00 | 2.03 | 2.00 | 2.02 | 2.01 | 1.97 | 2.01 | 2.00 | 2.00 | 2.00 | 2.00 | 1.99 | 2.00 |
| $Fe^{3+}$ | 0.11 | 0.07 | 0.11 | 0.12 | 0.12 | 0.10 | 0.00 | 0.01 | 0.11 | 0.13 | 0.14 | 0.09 | 0.07 | 0.10 | 0.13 | 0.08 | 0.05 | 0.12 |
| $Fe^{2+}$ | 2.37 | 2.06 | 2.00 | 1.98 | 1.98 | 2.00 | 2.13 | 2.12 | 2.06 | 2.03 | 2.03 | 2.07 | 2.07 | 2.04 | 2.06 | 2.08 | 2.12 | 2.08 |
| Mn | 0.10 | 0.04 | 0.05 | 0.04 | 0.05 | 0.05 | 0.05 | 0.05 | 0.06 | 0.06 | 0.06 | 0.06 | 0.06 | 0.06 | 0.06 | 0.06 | 0.07 | 0.06 |
| Mg | 0.37 | 0.76 | 0.80 | 0.81 | 0.81 | 0.80 | 0.69 | 0.72 | 0.71 | 0.74 | 0.76 | 0.73 | 0.73 | 0.75 | 0.71 | 0.72 | 0.70 | 0.70 |
| Ca | 0.10 | 0.10 | 0.10 | 0.10 | 0.10 | 0.09 | 0.10 | 0.10 | 0.10 | 0.10 | 0.10 | 0.09 | 0.10 | 0.09 | 0.10 | 0.10 | 0.09 | 0.09 |
| Na | 0.00 | 0.00 | 0.00 | 0.00 | 0.00 | 0.00 | 0.00 | 0.00 | 0.00 | 0.00 | 0.00 | 0.00 | 0.00 | 0.00 | 0.00 | 0.00 | 0.00 | 0.00 |
| K | 0.00 | 0.00 | 0.00 | 0.00 | 0.00 | 0.00 | 0.00 | 0.00 | 0.00 | 0.00 | 0.00 | 0.00 | 0.00 | 0.00 | 0.00 | 0.00 | 0.00 | 0.00 |
| cations | 8.00 | 8.00 | 8.00 | 8.00 | 8.00 | 8.00 | 8.00 | 8.00 | 8.00 | 8.00 | 8.00 | 8.00 | 8.00 | 8.00 | 8.00 | 8.00 | 8.00 | 8.00 |
| grs | 0.03 | 0.03 | 0.03 | 0.03 | 0.03 | 0.03 | 0.03 | 0.03 | 0.03 | 0.03 | 0.03 | 0.03 | 0.03 | 0.03 | 0.03 | 0.03 | 0.03 | 0.03 |
| alm | 0.81 | 0.70 | 0.69 | 0.69 | 0.68 | 0.69 | 0.72 | 0.71 | 0.71 | 0.71 | 0.70 | 0.71 | 0.71 | 0.70 | 0.71 | 0.71 | 0.72 | 0.72 |
| prp | 0.12 | 0.25 | 0.26 | 0.27 | 0.26 | 0.26 | 0.23 | 0.24 | 0.23 | 0.24 | 0.25 | 0.24 | 0.24 | 0.24 | 0.23 | 0.24 | 0.23 | 0.23 |
| sps | 0.03 | 0.01 | 0.02 | 0.01 | 0.02 | 0.02 | 0.02 | 0.02 | 0.02 | 0.02 | 0.02 | 0.02 | 0.02 | 0.02 | 0.02 | 0.02 | 0.02 | 0.02 |
| $X_{Fe}$ ($Fe^{2+}$) | 0.86 | 0.73 | 0.71 | 0.71 | 0.71 | 0.71 | 0.76 | 0.75 | 0.74 | 0.73 | 0.73 | 0.74 | 0.74 | 0.73 | 0.74 | 0.74 | 0.75 | 0.75 |
| $X_{Fe}$ (Fetot) | 0.87 | 0.74 | 0.72 | 0.72 | 0.72 | 0.72 | 0.76 | 0.75 | 0.75 | 0.75 | 0.74 | 0.75 | 0.75 | 0.74 | 0.75 | 0.75 | 0.76 | 0.76 |

**Table A15.** (Continued)

| Sample | 462q | | | | | | | | | | | | | | | | |
|---|---|---|---|---|---|---|---|---|---|---|---|---|---|---|---|---|---|
| Analysis | A_23 | A_24 | A_26 | A_27 | A_29 | A_30 | A_32 | A_33 | A_35 | A_36 | A_41 | A_42 | A_43 | A_45 | A_46 | A_47 | A_48 |
| Spot | #391 | #392 | #394 | #395 | #397 | #398 | #400 | #401 | #403 | #404 | #409 | #410 | #411 | #413 | #414 | #415 | #416 |
| (wt%) | | | | | | | | | | | | | | | | | |
| $SiO_2$ | 37.64 | 36.68 | 37.29 | 37.14 | 36.94 | 37.26 | 37.08 | 37.29 | 36.83 | 37.35 | 37.09 | 37.28 | 36.95 | 37.01 | 37.04 | 37.56 | 37.58 |
| $TiO_2$ | 0.06 | 0.04 | 0.12 | 0.05 | 0.05 | 0.11 | 0.15 | 0.18 | 0.09 | 0.08 | 0.15 | 0.08 | 0.15 | 0.11 | 0.16 | 0.10 | 0.13 |
| $Al_2O_3$ | 21.40 | 21.59 | 21.44 | 21.35 | 21.45 | 21.64 | 21.58 | 21.31 | 21.13 | 21.49 | 21.63 | 21.39 | 21.69 | 21.16 | 21.69 | 21.22 | 21.75 |
| FeO | 33.11 | 33.70 | 32.93 | 33.31 | 33.51 | 33.45 | 33.13 | 32.71 | 33.06 | 33.11 | 33.04 | 32.02 | 32.78 | 32.28 | 32.83 | 33.01 | 32.93 |
| MnO | 1.00 | 1.04 | 1.09 | 1.12 | 1.06 | 0.95 | 1.00 | 1.10 | 1.05 | 1.05 | 1.08 | 1.03 | 0.94 | 1.02 | 0.95 | 0.99 | 0.99 |
| MgO | 5.72 | 5.57 | 5.76 | 5.76 | 5.59 | 5.79 | 6.01 | 5.86 | 6.12 | 5.91 | 6.15 | 6.33 | 6.27 | 6.35 | 6.20 | 6.25 | 6.33 |
| CaO | 1.07 | 1.18 | 1.11 | 1.10 | 1.15 | 1.08 | 1.14 | 1.12 | 1.08 | 1.09 | 1.19 | 1.08 | 1.19 | 1.18 | 1.17 | 1.13 | 1.17 |
| $Na_2O$ | 0.00 | 0.00 | 0.00 | 0.00 | 0.00 | 0.00 | 0.00 | 0.00 | 0.00 | 0.00 | 0.00 | 0.00 | 0.00 | 0.00 | 0.00 | 0.00 | 0.00 |
| $K_2O$ | 0.00 | 0.00 | 0.00 | 0.00 | 0.00 | 0.00 | 0.00 | 0.00 | 0.00 | 0.00 | 0.00 | 0.00 | 0.00 | 0.00 | 0.00 | 0.00 | 0.00 |
| Total | 100.00 | 99.80 | 99.74 | 99.83 | 99.75 | 100.28 | 100.09 | 99.57 | 99.36 | 100.08 | 100.33 | 99.21 | 99.97 | 99.11 | 100.04 | 100.26 | 100.88 |
| Oxygen | 12 | 12 | 12 | 12 | 12 | 12 | 12 | 12 | 12 | 12 | 12 | 12 | 12 | 12 | 12 | 12 | 12 |
| Si | 2.98 | 2.91 | 2.96 | 2.94 | 2.93 | 2.94 | 2.93 | 2.96 | 2.93 | 2.95 | 2.92 | 2.96 | 2.91 | 2.94 | 2.92 | 2.96 | 2.94 |
| Ti | 0.00 | 0.00 | 0.01 | 0.00 | 0.00 | 0.01 | 0.01 | 0.01 | 0.01 | 0.00 | 0.01 | 0.00 | 0.01 | 0.01 | 0.01 | 0.01 | 0.01 |
| Al | 2.00 | 2.02 | 2.00 | 1.99 | 2.01 | 2.01 | 2.01 | 1.99 | 1.98 | 2.00 | 2.01 | 2.00 | 2.02 | 1.98 | 2.01 | 1.97 | 2.00 |
| $Fe^{3+}$ | 0.04 | 0.15 | 0.07 | 0.11 | 0.12 | 0.10 | 0.12 | 0.06 | 0.15 | 0.09 | 0.14 | 0.07 | 0.14 | 0.12 | 0.13 | 0.10 | 0.11 |
| $Fe^{2+}$ | 2.15 | 2.08 | 2.12 | 2.10 | 2.11 | 2.11 | 2.06 | 2.11 | 2.05 | 2.10 | 2.03 | 2.05 | 2.02 | 2.03 | 2.04 | 2.07 | 2.04 |
| Mn | 0.07 | 0.07 | 0.07 | 0.08 | 0.07 | 0.06 | 0.07 | 0.07 | 0.07 | 0.07 | 0.07 | 0.07 | 0.06 | 0.07 | 0.06 | 0.07 | 0.07 |
| Mg | 0.67 | 0.66 | 0.68 | 0.68 | 0.66 | 0.68 | 0.71 | 0.69 | 0.73 | 0.70 | 0.72 | 0.75 | 0.74 | 0.75 | 0.73 | 0.73 | 0.74 |
| Ca | 0.09 | 0.10 | 0.09 | 0.09 | 0.10 | 0.09 | 0.10 | 0.10 | 0.09 | 0.09 | 0.10 | 0.09 | 0.10 | 0.10 | 0.10 | 0.10 | 0.10 |
| Na | 0.00 | 0.00 | 0.00 | 0.00 | 0.00 | 0.00 | 0.00 | 0.00 | 0.00 | 0.00 | 0.00 | 0.00 | 0.00 | 0.00 | 0.00 | 0.00 | 0.00 |
| K | 0.00 | 0.00 | 0.00 | 0.00 | 0.00 | 0.00 | 0.00 | 0.00 | 0.00 | 0.00 | 0.00 | 0.00 | 0.00 | 0.00 | 0.00 | 0.00 | 0.00 |
| cations | 8.00 | 8.00 | 8.00 | 8.00 | 8.00 | 8.00 | 8.00 | 8.00 | 8.00 | 8.00 | 8.00 | 8.00 | 8.00 | 8.00 | 8.00 | 8.00 | 8.00 |
| grs | 0.03 | 0.03 | 0.03 | 0.03 | 0.03 | 0.03 | 0.03 | 0.03 | 0.03 | 0.03 | 0.03 | 0.03 | 0.03 | 0.03 | 0.03 | 0.03 | 0.03 |
| alm | 0.72 | 0.73 | 0.72 | 0.72 | 0.73 | 0.73 | 0.72 | 0.72 | 0.71 | 0.72 | 0.71 | 0.70 | 0.71 | 0.70 | 0.71 | 0.71 | 0.70 |
| prp | 0.22 | 0.21 | 0.22 | 0.22 | 0.22 | 0.22 | 0.23 | 0.23 | 0.24 | 0.23 | 0.24 | 0.25 | 0.24 | 0.25 | 0.24 | 0.24 | 0.24 |
| sps | 0.02 | 0.02 | 0.02 | 0.02 | 0.02 | 0.02 | 0.02 | 0.02 | 0.02 | 0.02 | 0.02 | 0.02 | 0.02 | 0.02 | 0.02 | 0.02 | 0.02 |
| $X_{Fe}$ ($Fe^{2+}$) | 0.76 | 0.76 | 0.76 | 0.76 | 0.76 | 0.76 | 0.74 | 0.75 | 0.74 | 0.75 | 0.74 | 0.73 | 0.73 | 0.73 | 0.74 | 0.74 | 0.73 |
| $X_{Fe}$ (Fetot) | 0.76 | 0.77 | 0.76 | 0.76 | 0.77 | 0.76 | 0.76 | 0.76 | 0.75 | 0.76 | 0.75 | 0.74 | 0.75 | 0.74 | 0.75 | 0.75 | 0.74 |

**Table A15.** (Continued)

| Sample | 462q | | | | | | | | | | | | | | | | |
|---|---|---|---|---|---|---|---|---|---|---|---|---|---|---|---|---|---|
| Analysis | A_49 | A_50 | A_54 | A_55 | A_56 | A_57 | A_58 | A_59 | A_60 | A_61 | A_62 | A_63 | A_64 | A_65 | A_66 | A_67 | A_69 |
| Spot | #417 | #418 | #422 | #423 | #424 | #425 | #426 | #427 | #428 | #429 | #430 | #431 | #432 | #433 | #434 | #435 | #437 |
| (wt%) | | | | | | | | | | | | | | | | | |
| $SiO_2$ | 37.33 | 36.92 | 37.34 | 37.30 | 36.93 | 36.79 | 37.19 | 37.50 | 37.57 | 37.38 | 37.33 | 37.12 | 37.28 | 36.76 | 37.30 | 37.56 | 36.18 |
| $TiO_2$ | 0.11 | 0.13 | 0.14 | 0.14 | 0.09 | 0.11 | 0.09 | 0.06 | 0.08 | 0.06 | 0.09 | 0.09 | 0.11 | 0.10 | 0.06 | 0.10 | 0.12 |
| $Al_2O_3$ | 21.52 | 21.60 | 21.39 | 21.56 | 21.50 | 21.53 | 21.71 | 21.75 | 21.45 | 21.36 | 21.55 | 21.63 | 21.31 | 21.20 | 21.47 | 21.44 | 20.64 |
| FeO | 32.96 | 32.75 | 32.54 | 32.40 | 32.73 | 32.38 | 32.74 | 32.74 | 32.50 | 33.19 | 32.67 | 32.77 | 32.78 | 32.58 | 32.63 | 32.36 | 36.59 |
| MnO | 1.00 | 0.91 | 0.89 | 0.98 | 0.95 | 1.03 | 1.00 | 0.98 | 1.02 | 0.93 | 0.84 | 1.00 | 0.85 | 0.87 | 0.78 | 0.80 | 1.39 |
| MgO | 6.32 | 6.06 | 6.28 | 6.07 | 6.23 | 6.20 | 6.20 | 6.27 | 6.27 | 6.15 | 6.26 | 6.20 | 6.39 | 6.39 | 6.72 | 6.74 | 3.02 |
| CaO | 1.05 | 1.02 | 1.16 | 1.13 | 1.16 | 1.15 | 1.19 | 1.15 | 1.17 | 1.09 | 1.13 | 1.14 | 1.11 | 1.14 | 1.18 | 1.18 | 1.17 |
| $Na_2O$ | 0.00 | 0.00 | 0.00 | 0.00 | 0.00 | 0.00 | 0.00 | 0.00 | 0.00 | 0.00 | 0.00 | 0.00 | 0.00 | 0.00 | 0.00 | 0.00 | 0.00 |
| $K_2O$ | 0.00 | 0.00 | 0.00 | 0.00 | 0.00 | 0.00 | 0.00 | 0.00 | 0.00 | 0.00 | 0.00 | 0.00 | 0.00 | 0.00 | 0.00 | 0.00 | 0.00 |
| Total | 100.29 | 99.39 | 99.74 | 99.58 | 99.59 | 99.19 | 100.12 | 100.45 | 100.06 | 100.16 | 99.87 | 99.95 | 99.83 | 99.04 | 100.14 | 100.18 | 99.11 |
| Oxygen | 12 | 12 | 12 | 12 | 12 | 12 | 12 | 12 | 12 | 12 | 12 | 12 | 12 | 12 | 12 | 12 | 12 |
| Si | 2.93 | 2.93 | 2.95 | 2.95 | 2.92 | 2.92 | 2.93 | 2.94 | 2.96 | 2.95 | 2.95 | 2.93 | 2.94 | 2.92 | 2.93 | 2.95 | 2.94 |
| Ti | 0.01 | 0.01 | 0.01 | 0.01 | 0.01 | 0.01 | 0.01 | 0.00 | 0.00 | 0.00 | 0.01 | 0.01 | 0.01 | 0.01 | 0.00 | 0.01 | 0.01 |
| Al | 1.99 | 2.02 | 1.99 | 2.01 | 2.01 | 2.02 | 2.01 | 2.01 | 1.99 | 1.98 | 2.00 | 2.01 | 1.98 | 1.99 | 1.99 | 1.98 | 1.98 |
| $Fe^{3+}$ | 0.12 | 0.10 | 0.09 | 0.06 | 0.14 | 0.12 | 0.12 | 0.10 | 0.08 | 0.11 | 0.09 | 0.12 | 0.12 | 0.15 | 0.15 | 0.11 | 0.10 |
| $Fe^{2+}$ | 2.05 | 2.07 | 2.06 | 2.08 | 2.03 | 2.03 | 2.04 | 2.05 | 2.06 | 2.07 | 2.06 | 2.04 | 2.05 | 2.02 | 1.99 | 2.01 | 2.39 |
| Mn | 0.07 | 0.06 | 0.06 | 0.07 | 0.06 | 0.07 | 0.07 | 0.07 | 0.07 | 0.06 | 0.06 | 0.07 | 0.06 | 0.06 | 0.05 | 0.05 | 0.10 |
| Mg | 0.74 | 0.72 | 0.74 | 0.72 | 0.73 | 0.73 | 0.73 | 0.73 | 0.74 | 0.72 | 0.74 | 0.73 | 0.75 | 0.76 | 0.79 | 0.79 | 0.37 |
| Ca | 0.09 | 0.09 | 0.10 | 0.10 | 0.10 | 0.10 | 0.10 | 0.10 | 0.10 | 0.09 | 0.10 | 0.10 | 0.09 | 0.10 | 0.10 | 0.10 | 0.10 |
| Na | 0.00 | 0.00 | 0.00 | 0.00 | 0.00 | 0.00 | 0.00 | 0.00 | 0.00 | 0.00 | 0.00 | 0.00 | 0.00 | 0.00 | 0.00 | 0.00 | 0.00 |
| K | 0.00 | 0.00 | 0.00 | 0.00 | 0.00 | 0.00 | 0.00 | 0.00 | 0.00 | 0.00 | 0.00 | 0.00 | 0.00 | 0.00 | 0.00 | 0.00 | 0.00 |
| cations | 8.00 | 8.00 | 8.00 | 8.00 | 8.00 | 8.00 | 8.00 | 8.00 | 8.00 | 8.00 | 8.00 | 8.00 | 8.00 | 8.00 | 8.00 | 8.00 | 8.00 |
| grs | 0.03 | 0.03 | 0.03 | 0.03 | 0.03 | 0.03 | 0.03 | 0.03 | 0.03 | 0.03 | 0.03 | 0.03 | 0.03 | 0.03 | 0.03 | 0.03 | 0.03 |
| alm | 0.71 | 0.72 | 0.71 | 0.71 | 0.71 | 0.70 | 0.71 | 0.71 | 0.70 | 0.71 | 0.71 | 0.71 | 0.71 | 0.70 | 0.70 | 0.69 | 0.82 |
| prp | 0.24 | 0.24 | 0.24 | 0.24 | 0.24 | 0.24 | 0.24 | 0.24 | 0.24 | 0.24 | 0.24 | 0.24 | 0.25 | 0.25 | 0.26 | 0.26 | 0.12 |
| sps | 0.02 | 0.02 | 0.02 | 0.02 | 0.02 | 0.02 | 0.02 | 0.02 | 0.02 | 0.02 | 0.02 | 0.02 | 0.02 | 0.02 | 0.02 | 0.02 | 0.03 |
| $X_{Fe}$ ($Fe^{2+}$) | 0.73 | 0.74 | 0.74 | 0.74 | 0.73 | 0.73 | 0.74 | 0.74 | 0.74 | 0.74 | 0.74 | 0.74 | 0.73 | 0.73 | 0.72 | 0.72 | 0.87 |
| $X_{Fe}$ (Fetot) | 0.75 | 0.75 | 0.74 | 0.75 | 0.75 | 0.75 | 0.75 | 0.75 | 0.74 | 0.75 | 0.75 | 0.75 | 0.74 | 0.74 | 0.73 | 0.73 | 0.87 |

**Table A16.** Chemical composition of biotite from a fold-structured migmatite of the Lower series.

| Sample | 515 | | | | | | | | | | | | | | |
|---|---|---|---|---|---|---|---|---|---|---|---|---|---|---|---|
| Analysis | 515a2-bi1 | 515a2-bi3 | 515a2-bi4 | 515a2-bi6 | 515a2-bi7 | 515a2-bi8 | 515a2-bi10 | 515a2-bi11 | 515a2_bi2 | 515a2_bi3 | 515a2_bi6 | 515a2_bi10 | 515a2_bi11 | 515a2p-bi1 | 515a2p-bi2 |
| Spot | #1 | #6 | #7 | #11 | #14 | #17 | #22 | #24 | #2 | #3 | #6 | #10 | #11 | #83 | #85 |
| (wt%) | | | | | | | | | | | | | | | |
| $SiO_2$ | 35.54 | 35.09 | 35.48 | 35.45 | 35.21 | 35.05 | 35.36 | 35.06 | 35.79 | 35.17 | 36.04 | 35.49 | 35.67 | 35.46 | 35.26 |
| $TiO_2$ | 2 | 2.46 | 2.61 | 1.76 | 2.04 | 3.04 | 3 | 3.1 | 1.82 | 1.65 | 1.7 | 1.9 | 1.66 | 2.02 | 2.06 |
| $Al_2O_3$ | 19.45 | 18.79 | 18.52 | 19.35 | 18.87 | 18.61 | 18.13 | 18.67 | 19.11 | 18.7 | 19.91 | 18.74 | 19.43 | 18.93 | 18.66 |
| FeO | 18.22 | 18.82 | 18.78 | 17.5 | 18.33 | 18.42 | 17.88 | 17.54 | 17.99 | 18.37 | 17.54 | 18.74 | 18.94 | 17.62 | 18.59 |
| MnO | 0.11 | 0.22 | 0.22 | 0.26 | 0.27 | 0.24 | 0.26 | 0.23 | 0.19 | 0.31 | 0.15 | 0.17 | 0.28 | 0.1 | 0.11 |
| MgO | 10.67 | 9.94 | 10 | 10.69 | 11.06 | 9.98 | 10.5 | 10.4 | 11.01 | 10.8 | 10.71 | 11.07 | 10.08 | 11.24 | 11.28 |
| CaO | 0 | 0.01 | 0.01 | 0.02 | 0 | 0 | 0 | 0.01 | 0.01 | 0.07 | 0.05 | 0.01 | 0.06 | 0 | 0 |
| $Na_2O$ | 0.39 | 0.24 | 0.38 | 0.34 | 0.41 | 0.36 | 0.37 | 0.39 | 0.26 | 0.26 | 0.29 | 0.27 | 0.35 | 0.45 | 0.24 |
| $K_2O$ | 8.61 | 8.74 | 8.93 | 9.1 | 8 | 8.64 | 8.58 | 8.64 | 9.05 | 8.75 | 9.12 | 9.14 | 8.5 | 8.43 | 8.05 |
| Total | 94.990 | 94.310 | 94.930 | 94.470 | 94.190 | 94.340 | 94.080 | 94.040 | 95.230 | 94.080 | 95.510 | 95.530 | 94.970 | 94.250 | 94.250 |
| Oxygen | 11 | 11 | 11 | 11 | 11 | 11 | 11 | 11 | 11 | 11 | 11 | 11 | 11 | 11 | 11 |
| Si | 2.76 | 2.77 | 2.78 | 2.76 | 2.76 | 2.76 | 2.79 | 2.76 | 2.77 | 2.76 | 2.78 | 2.74 | 2.78 | 2.77 | 2.77 |
| Ti | 0.12 | 0.15 | 0.15 | 0.10 | 0.12 | 0.18 | 0.18 | 0.18 | 0.11 | 0.10 | 0.10 | 0.11 | 0.10 | 0.12 | 0.12 |
| Al | 1.78 | 1.75 | 1.71 | 1.78 | 1.74 | 1.73 | 1.68 | 1.73 | 1.74 | 1.73 | 1.81 | 1.71 | 1.79 | 1.74 | 1.73 |
| $Fe^{3+}$ | 0.00 | 0.00 | 0.00 | 0.00 | 0.00 | 0.00 | 0.00 | 0.00 | 0.00 | 0.00 | 0.00 | 0.00 | 0.00 | 0.00 | 0.00 |
| $Fe^{2+}$ | 1.18 | 1.24 | 1.23 | 1.14 | 1.20 | 1.21 | 1.18 | 1.16 | 1.16 | 1.21 | 1.13 | 1.21 | 1.24 | 1.15 | 1.22 |
| Mn | 0.01 | 0.01 | 0.01 | 0.02 | 0.02 | 0.02 | 0.02 | 0.02 | 0.01 | 0.02 | 0.01 | 0.01 | 0.02 | 0.01 | 0.01 |
| Mg | 1.24 | 1.17 | 1.17 | 1.24 | 1.29 | 1.17 | 1.23 | 1.22 | 1.27 | 1.26 | 1.23 | 1.28 | 1.17 | 1.31 | 1.32 |
| Ca | 0.00 | 0.00 | 0.00 | 0.00 | 0.00 | 0.00 | 0.00 | 0.00 | 0.00 | 0.01 | 0.00 | 0.00 | 0.01 | 0.00 | 0.00 |
| Na | 0.06 | 0.04 | 0.06 | 0.05 | 0.06 | 0.06 | 0.06 | 0.06 | 0.04 | 0.04 | 0.04 | 0.04 | 0.05 | 0.07 | 0.04 |
| K | 0.85 | 0.88 | 0.89 | 0.90 | 0.80 | 0.87 | 0.86 | 0.87 | 0.89 | 0.88 | 0.90 | 0.90 | 0.85 | 0.84 | 0.81 |
| cations | 8.00 | 8.00 | 8.00 | 8.00 | 8.00 | 8.00 | 8.00 | 8.00 | 8.00 | 8.00 | 8.00 | 8.00 | 8.00 | 8.00 | 8.00 |
| $X_{Fe}$ ($Fe^{2+}$) | 0.49 | 0.52 | 0.51 | 0.48 | 0.48 | 0.51 | 0.49 | 0.49 | 0.48 | 0.49 | 0.48 | 0.49 | 0.51 | 0.47 | 0.48 |
| $X_{Fe}$ (Fetot) | 0.49 | 0.52 | 0.51 | 0.48 | 0.48 | 0.51 | 0.49 | 0.49 | 0.48 | 0.49 | 0.48 | 0.49 | 0.51 | 0.47 | 0.48 |

**Table A16.** (Continued)

| Sample | 515 | | | | | | | | | |
|---|---|---|---|---|---|---|---|---|---|---|
| Analysis | 515a2p-bi3 | 515a2p-bi4 | 515a2p-bi6 | 515a2p-bi7 | 515a2p-bi8 | 515a2p-bi10 | 515a2p-bi12 | 515a2p-bi15 | 515a2p-bi18 | 515a2p-bi20 |
| Spot | #1 | #89 | #94 | #97 | #98 | #115 | #118 | #121 | #132 | #140 |
| (wt%) | | | | | | | | | | |
| $SiO_2$ | 36.11 | 35.67 | 35.49 | 36.02 | 36.28 | 35.65 | 35.50 | 35.39 | 35.87 | 35.96 |
| $TiO_2$ | 2.39 | 2.29 | 2.36 | 2.43 | 2.26 | 2.68 | 2.46 | 2.55 | 2.20 | 2.62 |
| $Al_2O_3$ | 19.18 | 18.89 | 18.97 | 19.02 | 18.62 | 18.23 | 18.96 | 18.95 | 19.87 | 19.03 |
| FeO | 17.50 | 17.56 | 17.42 | 16.67 | 17.22 | 17.34 | 17.51 | 17.22 | 16.39 | 16.24 |
| MnO | 0.12 | 0.09 | 0.11 | 0.08 | 0.10 | 0.15 | 0.10 | 0.17 | 0.15 | 0.07 |
| MgO | 10.85 | 10.60 | 11.21 | 11.02 | 11.49 | 11.68 | 10.79 | 11.38 | 11.07 | 11.00 |
| CaO | 0.00 | 0.00 | 0.00 | 0.00 | 0.00 | 0.03 | 0.02 | 0.00 | 0.00 | 0.00 |
| $Na_2O$ | 0.36 | 0.42 | 0.37 | 0.34 | 0.29 | 0.34 | 0.22 | 0.36 | 0.14 | 0.26 |
| $K_2O$ | 8.61 | 8.81 | 8.43 | 8.58 | 8.62 | 8.94 | 8.44 | 8.42 | 8.53 | 8.83 |
| Total | 95.12 | 94.33 | 94.36 | 94.16 | 94.88 | 95.04 | 94.00 | 94.44 | 94.22 | 94.01 |
| Oxygen | 11 | 11 | 11 | 11 | 11 | 11 | 11 | 11 | 11 | 11 |
| Si | 2.80 | 2.79 | 2.77 | 2.82 | 2.82 | 2.76 | 2.79 | 2.76 | 2.80 | 2.82 |
| Ti | 0.14 | 0.13 | 0.14 | 0.14 | 0.13 | 0.16 | 0.15 | 0.15 | 0.13 | 0.15 |
| Al | 1.75 | 1.74 | 1.75 | 1.75 | 1.70 | 1.66 | 1.76 | 1.74 | 1.83 | 1.76 |
| $Fe^{3+}$ | 0.00 | 0.00 | 0.00 | 0.00 | 0.00 | 0.00 | 0.00 | 0.00 | 0.00 | 0.00 |
| $Fe^{2+}$ | 1.14 | 1.15 | 1.14 | 1.09 | 1.12 | 1.12 | 1.15 | 1.12 | 1.07 | 1.06 |
| Mn | 0.01 | 0.01 | 0.01 | 0.01 | 0.01 | 0.01 | 0.01 | 0.01 | 0.01 | 0.00 |
| Mg | 1.25 | 1.24 | 1.30 | 1.28 | 1.33 | 1.35 | 1.26 | 1.32 | 1.29 | 1.28 |
| Ca | 0.00 | 0.00 | 0.00 | 0.00 | 0.00 | 0.00 | 0.00 | 0.00 | 0.00 | 0.00 |
| Na | 0.05 | 0.06 | 0.06 | 0.05 | 0.04 | 0.05 | 0.03 | 0.05 | 0.02 | 0.04 |
| K | 0.85 | 0.88 | 0.84 | 0.86 | 0.85 | 0.88 | 0.85 | 0.84 | 0.85 | 0.88 |
| cations | 8.00 | 8.00 | 8.00 | 8.00 | 8.00 | 8.00 | 8.00 | 8.00 | 8.00 | 8.00 |
| $X_{Fe}$ ($Fe^{2+}$) | 0.48 | 0.48 | 0.47 | 0.46 | 0.46 | 0.45 | 0.48 | 0.46 | 0.45 | 0.45 |
| $X_{Fe}$ (Fetot) | 0.48 | 0.48 | 0.47 | 0.46 | 0.46 | 0.45 | 0.48 | 0.46 | 0.45 | 0.45 |

**Table A17.** Chemical composition of cordierite from a fold-structured migmatite of the Lower series.

| Sample | 515 | | | | | | | | | | | | | | |
|---|---|---|---|---|---|---|---|---|---|---|---|---|---|---|---|
| Analysis | 515a2-cd1 | 515a2-cd | 515a2-cd3 | 515a2-cd4 | 515a2-cd5 | 515a2-cd6 | 515a2-cd7 | 515a2-cd8 | 515a2-cd9 | 515a2-cd10 | 515a2-cd11 | 515a2-cd14 | 515a2p-cd1 | 515a2p-cd2 | 515a2p-cd3 |
| Spot | #2 | #3 | #4 | #12 | #13 | #15 | #16 | #18 | #19 | #21 | #23 | #27 | #84 | #86 | #87 |
| (wt%) | | | | | | | | | | | | | | | |
| $SiO_2$ | 47.91 | 47.77 | 48.21 | 47.71 | 47.85 | 47.93 | 48.05 | 47.81 | 47.42 | 47.54 | 47.86 | 48.14 | 48.21 | 47.93 | 48.16 |
| $TiO_2$ | 0.00 | 0.03 | 0.00 | 0.00 | 0.02 | 0.00 | 0.02 | 0.00 | 0.01 | 0.01 | 0.00 | 0.02 | 0.00 | 0.00 | 0.02 |
| $Al_2O_3$ | 32.64 | 32.52 | 32.62 | 32.48 | 32.83 | 32.51 | 32.79 | 32.68 | 32.45 | 32.66 | 32.63 | 32.88 | 32.70 | 33.11 | 33.06 |
| FeO | 7.86 | 7.54 | 7.33 | 7.46 | 7.30 | 7.53 | 7.40 | 7.59 | 7.57 | 7.71 | 7.63 | 7.92 | 7.45 | 7.20 | 7.19 |
| MnO | 0.45 | 0.50 | 0.53 | 0.50 | 0.32 | 0.43 | 0.48 | 0.50 | 0.41 | 0.42 | 0.38 | 0.55 | 0.21 | 0.24 | 0.30 |
| MgO | 8.30 | 8.46 | 7.88 | 8.39 | 8.03 | 8.31 | 8.53 | 8.26 | 8.33 | 8.26 | 8.21 | 8.29 | 8.58 | 8.92 | 8.82 |
| CaO | 0.03 | 0.03 | 0.09 | 0.01 | 0.03 | 0.00 | 0.00 | 0.01 | 0.03 | 0.02 | 0.04 | 0.03 | 0.00 | 0.00 | 0.00 |
| $Na_2O$ | 0.34 | 0.32 | 0.25 | 0.52 | 0.71 | 0.65 | 0.56 | 0.56 | 0.62 | 0.56 | 0.56 | 0.26 | 0.40 | 0.33 | 0.33 |
| $K_2O$ | 0.00 | 0.00 | 0.09 | 0.03 | 0.01 | 0.01 | 0.02 | 0.02 | 0.02 | 0.02 | 0.00 | 0.00 | 0.01 | 0.01 | 0.00 |
| Total | 97.53 | 97.17 | 97.00 | 97.10 | 97.10 | 97.37 | 97.85 | 97.43 | 96.86 | 97.20 | 97.31 | 98.09 | 97.56 | 97.74 | 97.88 |
| | | | | | | | | | | | | | | | |
| Oxygen | 18 | 18 | 18 | 18 | 18 | 18 | 18 | 18 | 18 | 18 | 18 | 18 | 18 | 18 | 18 |
| Si | 4.95 | 4.95 | 5.02 | 4.94 | 4.95 | 4.95 | 4.93 | 4.94 | 4.92 | 4.92 | 4.95 | 4.95 | 4.97 | 4.92 | 4.94 |
| Ti | 0.00 | 0.00 | 0.00 | 0.00 | 0.00 | 0.00 | 0.00 | 0.00 | 0.00 | 0.00 | 0.00 | 0.00 | 0.00 | 0.00 | 0.00 |
| Al | 3.98 | 3.97 | 4.00 | 3.96 | 4.00 | 3.96 | 3.97 | 3.98 | 3.97 | 3.98 | 3.98 | 3.99 | 3.97 | 4.01 | 4.00 |
| $Fe^{3+}$ | 0.18 | 0.18 | 0.02 | 0.26 | 0.24 | 0.28 | 0.28 | 0.26 | 0.32 | 0.29 | 0.24 | 0.15 | 0.17 | 0.22 | 0.18 |
| $Fe^{2+}$ | 0.50 | 0.47 | 0.61 | 0.38 | 0.39 | 0.37 | 0.36 | 0.39 | 0.34 | 0.38 | 0.42 | 0.53 | 0.47 | 0.40 | 0.44 |
| Mn | 0.04 | 0.04 | 0.05 | 0.04 | 0.03 | 0.04 | 0.04 | 0.04 | 0.04 | 0.04 | 0.03 | 0.05 | 0.02 | 0.02 | 0.03 |
| Mg | 1.28 | 1.31 | 1.22 | 1.30 | 1.24 | 1.28 | 1.31 | 1.27 | 1.29 | 1.27 | 1.27 | 1.27 | 1.32 | 1.37 | 1.35 |
| Ca | 0.00 | 0.00 | 0.01 | 0.00 | 0.00 | 0.00 | 0.00 | 0.00 | 0.00 | 0.00 | 0.00 | 0.00 | 0.00 | 0.00 | 0.00 |
| Na | 0.07 | 0.06 | 0.05 | 0.10 | 0.14 | 0.13 | 0.11 | 0.11 | 0.12 | 0.11 | 0.11 | 0.05 | 0.08 | 0.07 | 0.07 |
| K | 0.00 | 0.00 | 0.01 | 0.00 | 0.00 | 0.00 | 0.00 | 0.00 | 0.00 | 0.00 | 0.00 | 0.00 | 0.00 | 0.00 | 0.00 |
| cations | 11.00 | 11.00 | 11.00 | 11.00 | 11.00 | 11.00 | 11.00 | 11.00 | 11.00 | 11.00 | 11.00 | 11.00 | 11.00 | 11.00 | 11.00 |
| | | | | | | | | | | | | | | | |
| $X_{Fe}$ ($Fe^{2+}$) | 0.28 | 0.27 | 0.33 | 0.23 | 0.24 | 0.22 | 0.22 | 0.24 | 0.21 | 0.23 | 0.25 | 0.29 | 0.26 | 0.23 | 0.24 |
| $X_{Fe}$ (Fetot) | 0.35 | 0.33 | 0.34 | 0.33 | 0.34 | 0.34 | 0.33 | 0.34 | 0.34 | 0.34 | 0.34 | 0.35 | 0.33 | 0.31 | 0.31 |

**Table A17.** (Continued)

| Sample | 515 | | | | | | | | | | | | | | |
|---|---|---|---|---|---|---|---|---|---|---|---|---|---|---|---|
| Analysis | 515a2p-cd4 | 515a2p-cd5 | 515a2p-cd6 | 515a2p-cd7 | 515a2p-cd8 | 515a2p-cd9 | 515a2p-cd10 | 515a2p-cd11 | 515a2p-cd12 | 515a2p-cd13 | 515a2p-cd14 | 515a2p-cd15 | 515a2p-cd16 | 515a2p-cd17 | 515a2p-cd18 |
| Spot | #90 | #91 | #92 | #95 | #96 | #99 | #100 | #101 | #102 | #103 | #104 | #114 | #123 | #124 | #125 |
| (wt%) | | | | | | | | | | | | | | | |
| $SiO_2$ | 48.61 | 48.37 | 48.30 | 48.20 | 48.69 | 48.39 | 47.99 | 48.34 | 48.37 | 48.15 | 48.68 | 48.58 | 48.26 | 47.94 | 48.39 |
| $TiO_2$ | 0.03 | 0.00 | 0.03 | 0.01 | 0.00 | 0.03 | 0.00 | 0.00 | 0.01 | 0.00 | 0.03 | 0.00 | 0.00 | 0.00 | 0.02 |
| $Al_2O_3$ | 32.94 | 32.85 | 32.74 | 33.07 | 32.94 | 32.65 | 32.95 | 32.87 | 32.79 | 32.55 | 32.75 | 32.80 | 32.95 | 32.62 | 32.89 |
| FeO | 7.03 | 7.23 | 7.40 | 7.10 | 7.28 | 7.13 | 7.20 | 7.21 | 7.20 | 7.28 | 7.63 | 6.44 | 7.16 | 7.04 | 7.13 |
| MnO | 0.22 | 0.23 | 0.18 | 0.28 | 0.17 | 0.22 | 0.15 | 0.23 | 0.26 | 0.22 | 0.22 | 0.20 | 0.26 | 0.25 | 0.29 |
| MgO | 8.90 | 8.53 | 8.63 | 8.91 | 8.87 | 8.75 | 8.72 | 8.74 | 8.61 | 8.59 | 8.73 | 9.20 | 8.90 | 8.68 | 8.73 |
| CaO | 0.00 | 0.01 | 0.00 | 0.00 | 0.02 | 0.01 | 0.00 | 0.01 | 0.00 | 0.03 | 0.02 | 0.01 | 0.02 | 0.02 | 0.00 |
| $Na_2O$ | 0.25 | 0.32 | 0.30 | 0.40 | 0.44 | 0.39 | 0.39 | 0.42 | 0.45 | 0.37 | 0.17 | 0.25 | 0.40 | 0.44 | 0.57 |
| $K_2O$ | 0.00 | 0.00 | 0.01 | 0.01 | 0.01 | 0.00 | 0.02 | 0.02 | 0.00 | 0.00 | 0.00 | 0.00 | 0.00 | 0.00 | 0.00 |
| Total | 97.98 | 97.54 | 97.59 | 97.98 | 98.42 | 97.57 | 97.42 | 97.84 | 97.69 | 97.19 | 98.23 | 97.48 | 97.95 | 96.99 | 98.02 |
| | | | | | | | | | | | | | | | |
| Oxygen | 18 | 18 | 18 | 18 | 18 | 18 | 18 | 18 | 18 | 18 | 18 | 18 | 18 | 18 | 18 |
| Si | 4.98 | 4.99 | 4.98 | 4.94 | 4.97 | 4.98 | 4.94 | 4.96 | 4.97 | 4.98 | 4.99 | 4.99 | 4.94 | 4.96 | 4.95 |
| Ti | 0.00 | 0.00 | 0.00 | 0.00 | 0.00 | 0.00 | 0.00 | 0.00 | 0.00 | 0.00 | 0.00 | 0.00 | 0.00 | 0.00 | 0.00 |
| Al | 3.98 | 3.99 | 3.98 | 3.99 | 3.96 | 3.96 | 4.00 | 3.98 | 3.97 | 3.97 | 3.96 | 3.97 | 3.98 | 3.98 | 3.97 |
| $Fe^{3+}$ | 0.09 | 0.10 | 0.12 | 0.22 | 0.20 | 0.15 | 0.19 | 0.19 | 0.17 | 0.14 | 0.08 | 0.09 | 0.21 | 0.19 | 0.24 |
| $Fe^{2+}$ | 0.51 | 0.53 | 0.52 | 0.39 | 0.42 | 0.47 | 0.43 | 0.43 | 0.45 | 0.49 | 0.57 | 0.47 | 0.40 | 0.42 | 0.37 |
| Mn | 0.02 | 0.02 | 0.02 | 0.02 | 0.01 | 0.02 | 0.01 | 0.02 | 0.02 | 0.02 | 0.02 | 0.02 | 0.02 | 0.02 | 0.03 |
| Mg | 1.36 | 1.31 | 1.33 | 1.36 | 1.35 | 1.34 | 1.34 | 1.34 | 1.32 | 1.32 | 1.33 | 1.41 | 1.36 | 1.34 | 1.33 |
| Ca | 0.00 | 0.00 | 0.00 | 0.00 | 0.00 | 0.00 | 0.00 | 0.00 | 0.00 | 0.00 | 0.00 | 0.00 | 0.00 | 0.00 | 0.00 |
| Na | 0.05 | 0.06 | 0.06 | 0.08 | 0.09 | 0.08 | 0.08 | 0.08 | 0.09 | 0.07 | 0.03 | 0.05 | 0.08 | 0.09 | 0.11 |
| K | 0.00 | 0.00 | 0.00 | 0.00 | 0.00 | 0.00 | 0.00 | 0.00 | 0.00 | 0.00 | 0.00 | 0.00 | 0.00 | 0.00 | 0.00 |
| cations | 11.00 | 11.00 | 11.00 | 11.00 | 11.00 | 11.00 | 11.00 | 11.00 | 11.00 | 11.00 | 11.00 | 11.00 | 11.00 | 11.00 | 11.00 |
| | | | | | | | | | | | | | | | |
| $X_{Fe}$ ($Fe^{2+}$) | 0.27 | 0.29 | 0.28 | 0.22 | 0.24 | 0.26 | 0.24 | 0.24 | 0.26 | 0.27 | 0.30 | 0.25 | 0.23 | 0.24 | 0.22 |
| $X_{Fe}$ (Fetot) | 0.31 | 0.32 | 0.32 | 0.31 | 0.32 | 0.31 | 0.32 | 0.32 | 0.32 | 0.32 | 0.33 | 0.28 | 0.31 | 0.31 | 0.31 |

**Table A17.** (Continued)

| Sample | 515 | | | | | | | |
|---|---|---|---|---|---|---|---|---|
| Analysis | 515a2p-cd19 | 515a2p-cd20 | 515a2p-cd21 | 515a2p-cd22 | 515a2p-cd23 | 515a2p-cd24 | 515a2p-cd25 | 515a2p-cd26 |
| Spot | #126 | #127 | #128 | #129 | #130 | #136 | #137 | #141 |
| (wt%) | | | | | | | | |
| $SiO_2$ | 48.30 | 48.37 | 48.41 | 48.30 | 48.46 | 48.52 | 48.71 | 48.23 |
| $TiO_2$ | 0.02 | 0.02 | 0.00 | 0.01 | 0.01 | 0.01 | 0.01 | 0.00 |
| $Al_2O_3$ | 32.81 | 33.23 | 33.03 | 33.06 | 32.68 | 33.03 | 32.95 | 32.66 |
| FeO | 6.59 | 6.92 | 6.73 | 6.76 | 6.61 | 6.81 | 6.32 | 7.26 |
| MnO | 0.30 | 0.24 | 0.26 | 0.34 | 0.33 | 0.20 | 0.30 | 0.26 |
| MgO | 8.70 | 8.85 | 8.81 | 9.00 | 8.80 | 8.62 | 9.02 | 8.78 |
| CaO | 0.00 | 0.00 | 0.00 | 0.04 | 0.05 | 0.00 | 0.00 | 0.02 |
| $Na_2O$ | 0.41 | 0.37 | 0.31 | 0.33 | 0.30 | 0.67 | 0.43 | 0.36 |
| $K_2O$ | 0.01 | 0.00 | 0.00 | 0.02 | 0.01 | 0.00 | 0.00 | 0.00 |
| Total | 97.14 | 98.00 | 97.55 | 97.86 | 97.25 | 97.86 | 97.74 | 97.57 |
| | | | | | | | | |
| Oxygen | 18 | 18 | 18 | 18 | 18 | 18 | 18 | 18 |
| Si | 4.99 | 4.95 | 4.98 | 4.95 | 5.00 | 4.97 | 4.99 | 4.97 |
| Ti | 0.00 | 0.00 | 0.00 | 0.00 | 0.00 | 0.00 | 0.00 | 0.00 |
| Al | 3.99 | 4.01 | 4.01 | 3.99 | 3.98 | 3.98 | 3.98 | 3.96 |
| $Fe^{3+}$ | 0.11 | 0.16 | 0.10 | 0.17 | 0.08 | 0.21 | 0.12 | 0.18 |
| $Fe^{2+}$ | 0.46 | 0.44 | 0.48 | 0.41 | 0.49 | 0.37 | 0.42 | 0.45 |
| Mn | 0.03 | 0.02 | 0.02 | 0.03 | 0.03 | 0.02 | 0.03 | 0.02 |
| Mg | 1.34 | 1.35 | 1.35 | 1.37 | 1.35 | 1.31 | 1.38 | 1.35 |
| Ca | 0.00 | 0.00 | 0.00 | 0.00 | 0.01 | 0.00 | 0.00 | 0.00 |
| Na | 0.08 | 0.07 | 0.06 | 0.07 | 0.06 | 0.13 | 0.09 | 0.07 |
| K | 0.00 | 0.00 | 0.00 | 0.00 | 0.00 | 0.00 | 0.00 | 0.00 |
| cations | 11.00 | 11.00 | 11.00 | 11.00 | 11.00 | 11.00 | 11.00 | 11.00 |
| | | | | | | | | |
| $X_{Fe}$ ($Fe^{2+}$) | 0.25 | 0.24 | 0.26 | 0.23 | 0.27 | 0.22 | 0.23 | 0.25 |
| $X_{Fe}$ (Fetot) | 0.30 | 0.30 | 0.30 | 0.30 | 0.30 | 0.31 | 0.28 | 0.32 |

**Table A18.** Chemical analyses of garnet from a fold-structured migmatite of the Lower series.

| Sample | 515 | | | | | | | | | |
|---|---|---|---|---|---|---|---|---|---|---|
| Analysis | 515a2_3gB_1 | 515a2_3gB_2 | 515a2_3gB_3 | 515a2_3gB_4 | 515a2_3gB_5 | 515a2_3gB_6 | 515a2_3gB_7 | 515a2_3gB_8 | 515a2_3gB_9 | 515a2_3gB_10 |
| Spot | #303 | #304 | #305 | #306 | #307 | #308 | #309 | #310 | #311 | #312 |
| (wt%) | | | | | | | | | | |
| $SiO_2$ | 37.07 | 37.10 | 37.25 | 37.06 | 37.14 | 37.38 | 36.85 | 37.23 | 37.24 | 36.92 |
| $TiO_2$ | 0.00 | 0.00 | 0.03 | 0.03 | 0.00 | 0.02 | 0.02 | 0.00 | 0.03 | 0.02 |
| $Al_2O_3$ | 20.51 | 20.59 | 20.90 | 20.92 | 20.68 | 20.90 | 20.72 | 20.92 | 20.97 | 20.97 |
| FeO | 30.33 | 31.37 | 30.85 | 31.18 | 31.84 | 31.45 | 31.65 | 31.06 | 31.09 | 31.25 |
| MnO | 8.40 | 7.31 | 6.90 | 6.94 | 7.04 | 7.12 | 7.18 | 7.17 | 7.10 | 8.07 |
| MgO | 2.34 | 3.00 | 3.19 | 3.47 | 3.31 | 3.21 | 3.19 | 3.30 | 3.07 | 2.42 |
| CaO | 1.17 | 1.24 | 1.30 | 1.38 | 1.14 | 1.16 | 1.15 | 1.32 | 1.49 | 1.25 |
| $Na_2O$ | 0.00 | 0.00 | 0.00 | 0.00 | 0.00 | 0.00 | 0.00 | 0.00 | 0.00 | 0.00 |
| $K_2O$ | 0.00 | 0.00 | 0.00 | 0.00 | 0.00 | 0.00 | 0.00 | 0.00 | 0.00 | 0.00 |
| Total | 99.82 | 100.61 | 100.42 | 100.98 | 101.15 | 101.24 | 100.76 | 101.00 | 100.99 | 100.90 |
| Oxygen | 12 | 12 | 12 | 12 | 12 | 12 | 12 | 12 | 12 | 12 |
| Si | 3.01 | 2.98 | 2.99 | 2.95 | 2.96 | 2.98 | 2.95 | 2.97 | 2.97 | 2.97 |
| Ti | 0.00 | 0.00 | 0.00 | 0.00 | 0.00 | 0.00 | 0.00 | 0.00 | 0.00 | 0.00 |
| Al | 1.96 | 1.95 | 1.98 | 1.97 | 1.94 | 1.96 | 1.96 | 1.97 | 1.97 | 1.99 |
| $Fe^{3+}$ | 0.01 | 0.09 | 0.04 | 0.12 | 0.13 | 0.08 | 0.13 | 0.09 | 0.07 | 0.08 |
| $Fe^{2+}$ | 2.05 | 2.02 | 2.03 | 1.96 | 2.00 | 2.02 | 1.99 | 1.98 | 2.00 | 2.02 |
| Mn | 0.58 | 0.50 | 0.47 | 0.47 | 0.48 | 0.48 | 0.49 | 0.48 | 0.48 | 0.55 |
| Mg | 0.28 | 0.36 | 0.38 | 0.41 | 0.39 | 0.38 | 0.38 | 0.39 | 0.37 | 0.29 |
| Ca | 0.10 | 0.11 | 0.11 | 0.12 | 0.10 | 0.10 | 0.10 | 0.11 | 0.13 | 0.11 |
| Na | 0.00 | 0.00 | 0.00 | 0.00 | 0.00 | 0.00 | 0.00 | 0.00 | 0.00 | 0.00 |
| K | 0.00 | 0.00 | 0.00 | 0.00 | 0.00 | 0.00 | 0.00 | 0.00 | 0.00 | 0.00 |
| cations | 8.00 | 8.00 | 8.00 | 8.00 | 8.00 | 8.00 | 8.00 | 8.00 | 8.00 | 8.00 |
| grs | 0.03 | 0.03 | 0.04 | 0.04 | 0.03 | 0.03 | 0.03 | 0.04 | 0.04 | 0.04 |
| alm | 0.68 | 0.69 | 0.68 | 0.68 | 0.69 | 0.69 | 0.69 | 0.68 | 0.68 | 0.69 |
| prp | 0.09 | 0.12 | 0.13 | 0.13 | 0.13 | 0.12 | 0.12 | 0.13 | 0.12 | 0.10 |
| sps | 0.19 | 0.16 | 0.15 | 0.15 | 0.15 | 0.16 | 0.16 | 0.16 | 0.16 | 0.18 |
| $X_{Fe}$ ($Fe^{2+}$) | 0.88 | 0.85 | 0.84 | 0.83 | 0.84 | 0.84 | 0.84 | 0.83 | 0.85 | 0.87 |
| $X_{Fe}$ (Fetot) | 0.88 | 0.85 | 0.84 | 0.83 | 0.84 | 0.85 | 0.85 | 0.84 | 0.85 | 0.88 |

# LIST OF FIGURE CAPTIONS

## CHAPTER 1

**Figure 1.1.** Geological map of the Axial Pyrenean Zone and North Pyrenean Zone with the location of granulite facies rocks (the area studied is outlined). The upper right inset displays the general location of the Pyrenees within the European Variscides.....9

## CHAPTER 2

**Figure 2.1.** Geological sketch map of the Roc de Frausa Massif and Sant Llorenç–La Jonquera plutonic complex, modified from Liesa (1994).....14

**Figure 2.2.** Synthetic stratigraphic column of Roc de Frausa Massif indicating the intrusion level of the Sant Llorenç–La Jonquera plutonic complex and the Ceret gabbro-diorite, modified from Liesa (1994). New U-Pb zircon dating obtained by Aguilar *et al.* (in review) in bold.....16

## CHAPTER 3

**Figure 3.1.** Geological sketch map of the Roc de Frausa Massif and Sant Llorenç–La Jonquera plutonic complex, modified from Liesa (1994). Location of field photographs and the position of the structural profile are indicated.....18

**Figure 3.2.** Structural relationships of the Roc de Frausa: (a) subvertical folded relics of S0 in andalusite–sillimanite micaschists exhibiting S1 cleavage; (b) folded relics of S0 in sillimanite schists from the Intermediate series; (c) stromatic migmatites around the Ceret gabbro-diorite contact aureole parallel to S2; (d) D2 folds of leucosomes and S2 axial-plane cleavage in migmatites from the Lower series; (e) S2 foliation in the Ceret gabbro-diorite and migmatitic enclaves (highlighted by a dotted black line); and (f) open D3 folds in the Roc de Frausa gneisses affecting S1 foliation. Location in figure 3.1.....20

**Figure 3.3.** Cross-sections and lower hemispheric stereoplots showing the main structural relationships between the different rock units (legend as in figure 3.1 and location of the cross-sections in figure 3.1. L*: fold axes of the corresponding deformation events. Sm: milonitic foliation. Modified from Liesa & Carreras (1989) .....22

## CHAPTER 4

**Figure 4.1.** Geological sketch map of the Roc de Frausa Massif and Sant Llorenç–La Jonquera plutonic complex with the location of representative samples used in this thesis. Modified from Liesa (1994). ..... 25

**Figure 4.2.** Microstructural relationshisps of the Upper series (a–b) and the Intermediate series not affected by the Ceret contact aureole (c–d). (a) Andalusite porphyroblasts wrapped by S1 foliation, defined by muscovite, biotite and sillimanite with well-developed S1 pressure shadows; (b) poikiloblastic cordierite (outlined by white dashed lines) including a straight S1 internal foliation without pressure shadow; (c) S0 folded relics within S1 intrafoliation; and (d) cordierite poikiloblast (outlined by white dashed lines) contains straight trails of muscovite, biotite and sillimanite, continuous with external S1 foliation. No pressure shadows are formed around cordierite. ..... 27

**Figure 4.3.** Schematic blastesis-deformation relationships of metapelites and migmatites from the different crustal levels of the Roc de Frausa Massif. ..... 28

**Figure 4.4.** Macro- to microstructural relationships in patch migmatites from the Intermediate series affected by the Ceret gabbro-diorite contact aureole: (a) coarse-grained lenses of leucosome embedded by sillimanite and biotite-rich paleosome; (b) biotite and sillimanite parallel to S1 foliation folded by the D2 event and patches of K-feldspar-rich leucosome parallel to axial plane of F2 fold; (c) detail of the garnet rim from picture d including sillimanite and biotite parallel to S1 foliation; (d) biotite, sillimanite and garnet parallel to S1 foliation folded by the D2 event; and (e) cordierite poikiloblats including folded S1 foliation and S2 oriented biotite. ..... 30

**Figure 4.5.** Macro- to microstructural relationships in stromatic migmatites from the Intermediate series affected by the Ceret gabbro-diorite contact aureole: (a) alternating fine-grained melanosome layers with coarse-grained leucosomes parallel to S2 foliation; (b) garnet porphyroblasts in the boundary of leucosome and melanosome; (c) layer of Leucosome (quartz+plagioclase+garnet) hosted by a sillimanite-poor and cordierite-rich melanosome; (d) cordierite poikiloblasts mostly enclose biotite; and (e) detail of spinel included by cordierite from picture c. ..... 32

**Figure 4.6.** Macro- to microstructural relationships in schollen migmatites from the Intermediate series affected by the Ceret gabbro-diorite contact aureole: (a, b) biotite and sillimanite-rich paleosome embedded in a coarse-grained leucosome; (c) S1 foliation defined by sillimanite and biotite-rich paleosome is folded by the D2 event; (d) detail of the F2 fold: the limb are defined by S1 which is an axial plane foliation of a former one mimicking S0 and by fibrolitic sillimanite; (e) prismatic sillimanite in the leucosome with inclusions trails of biotite, ilmenite and locally, green spinel parallel to S1 fabric; and (f) cordierite corona around a garnet porphyroblast in the leucosome.....34

**Figure 4.7.** Macro- to microstructural relationships in residuum melanosomes from the Intermediate series affected by the Ceret gabbro-diorite contact aureole: (a) Massive residuum melanosome with granoblastic texture; (b) garnet porphyroblasts, biotite, ilmenite and brown spinel embedded in a cordierite-rich matrix; (c) idiomorphic cordierite with cyclic twinning; (d) idiomorphic to xenomorphic plagioclases together with biotite plates around garnet; (e) interstitial quartz between cordierite; and (f) brown spinel included in cordierite. .....35

**Figure 4.8.** Sketch of the deformation events registered in the different types of migmatites from contact metamorphism around the Ceret gabbro-diorite. .....36

**Figure 4.9.** Macro- to microstructural relationships in migmatitic rocks from the Lower series: (a) tightly folded lithological banding and leucosome parallel to S1 foliation; (b) detail of the S1 folds with biotite crystallizing parallel to the axial plane of F2 folds in the paleosomes and quartz-feldspar bands in the leucosome; (c) corroded isolated garnet in contact with plagioclases and biotite; and (d) poikiloblastic cordierite including S1 oriented biotite.....38

**Figure 4.10.** Meso- and microscopic photographs of Variscan igneous rocks: (a) Sant Llorenç–La Jonquera tonalite whit magmatic foliation defined by idiomorphic plagioclase and mafic minerals (biotite and hornblende) and oriented NE–SW in the photograph; (b) biotite and hornblende crystallizing in clusters in the tonalite; (c) plagioclase-rich gabbro from the Ceret stock (same outcrop as sample 420) whit slightly bigger black crystals of clinopyroxene; and (d) Clinopyroxene is almost completely surrounded by hornblende and biotite. Pyroxene includes idiomorphic plagioclase forming an ophitic texture. .....39

**Figure 4.11.** Chemical zoning profile exhibited by garnet for the different types of migmatites from the Intermediate series affected by the Ceret gabbro-diorite contact aureole. See text for details. ..... 44

**Figure 4.12.** Chemical zoning profile exhibited by garnet for fold-structure migmatites from the Lower series (sample 515). See text for details. ..... 45

**Figure 4.13.** Biotite-cordierite $X_{Fe}$ composition relationships for the metapelites and migmatites from the different crustal levels of the Roc de Frausa Massif. ..... 47

**Figure 4.14.** $Al_2O_3$–FeO–MgO compositional diagram for different types of migmatites from the Intermediate series affected by the Ceret contact aureole. Mineral compositions (mol.%) and whole-rock analyses (mol.%) plot at progressively lower $X_{Fe}$ values for the different types. ..... 48

**Figure 4.15.** Harker diagram showing the correlation between SiO2 and other major elements (in mol.% adjusted to 100%) for metasedimentary rocks and migmatites from the different crustal levels of the Roc de Frausa Massif. See text for explanation. ..... 50

**Figure 4.16.** $SiO_2$–$Al_2O_3$–FeO+MgO+$TiO_2$ and $SiO_2$–$Al_2O_3$–$K_2O$+$Na_2O$ ternary plots for metasedimentary rocks and migmatites from the different crustal levels of the Roc de Frausa Massif. Mineral vectors correspond to the mean composition of the analyzed garnet, cordierite and plagioclase. See text for details. ..... 52

## CHAPTER 5

**Figure 5.1.** Geological sketch map and synthetic stratigraphic column of the Roc de Frausa Massif with the location of the four representative samples used in calculating P–T conditions. Modified from Liesa & Carreras (1989) ..... 55

**Figure 5.2.** MnNCKFMASTHO *P*–*T* pseudosection calculated for the whole-rock composition of a representative andalusite–sillimanite micaschist from the Upper series (in moles adjusted to 100%). The *P*–*T* path is derived by comparing the modeled assemblages and isopleths with the assemblages, chemistry and zoning of minerals observed in the studied sample (187). See text for details. (b–d) Enlarged and simplified parts of the pseudosection with calculated isopleths of mineral composition for the areas of interest. The solidus is underlined by a dark-dashed line. . 57

**Figure 5.3.** MnNCKFMASTHO *P*–*T* pseudosection calculated for the whole-rock composition of a representative sillimanite schist from the Intermediate series not affected by the Ceret contact aureole (in moles adjusted to 100%). The *P*–*T* path is derived by comparing the modeled assemblages and isopleths with the assemblages, chemistry and zoning of minerals observed in the studied sample (4.12b). See text for details. (b–d) Enlarged and simplified parts of the pseudosection with calculated isopleths of mineral composition for the areas of interest. The solidus is underlined by a dark-dashed line. ..... 59

**Figure 5.4.** $H_2O$ undersaturated MnNCKFMASTHO *P*–*T* pseudosection calculated for the whole-rock composition from the Intermediate series affected by the Ceret gabbro-diorite contact aureole (in moles adjusted to 100%). The sample (459) corresponds to a migmatite of the inner contact aureole. The *P*–*T* path is derived by comparing the modeled assemblages and isopleths with the assemblages, chemistry and zoning of minerals observed in the studied sample. See text for details. (b–g) Enlarged and simplified parts of the pseudosection with calculated isopleths of mineral composition and molar proportions for the areas of interest. The solidus is underlined by a dark-dashed line. ..... 61

**Figure 5.5.** $H_2O$ undersaturated MnNCKFMASTHO *P*–*T* pseudosection calculated for the whole-rock composition of a fold-structured migmatite from the Lower series (in moles adjusted to 100%). The *P*–*T* path is derived by comparing the modeled assemblages and isopleths with the assemblages, chemistry and zoning of minerals observed in the studied sample (515). See text for details. (b–f) Enlarged and simplified parts of the pseudosection with calculated isopleths of mineral composition for the areas of interest. The solidus is underlined by a dark-dashed line. . 63

## CHAPTER 6

**Figure 6.1.** *T*–*M*($H_2O$) pseudosection calculated for a patch migmatite showing the minimum range of water (blue shaded area) required to a minimum melting temperature. The code for the first appearance of a mineral is indicated above the diagram. The solidus is traced by a red line. ..... 67

**Figure 6.2.** Geological sketch map of the Roc de Frausa Massif with the location of four characteristic migmatitic rocks used in this study. Modified from Liesa & Carreras (1989). ..... 69

**Figure 6.3.** NCKFMASHTO *P–T* pseudosection calculated for the whole-rock composition of a patch migmatite formed at the Ceret gabbro-diorite contact aureole (in moles adjusted to 100%). The *P–T* path is derived by comparing the modeled assemblages and isopleths with the assemblages and mineral chemistry observed in the studied sample (526). See text for details. (b–d) Enlarged and simplified parts of the pseudosection with calculated isopleths of mineral composition for the areas of interest. The solidus is underlined by a dashed line. ..... 70

**Figure 6.4.** *P–T* pseudosection of the patch migmatite (sample 526) with calculated isopleths of the molar proportions of liquid, sillimanite, garnet and cordierite for the areas of interest. The solidus is underlined by a dashed line. ..... 71

**Figure 6.5.** NCKFMASHTO *P–T* pseudosection calculated for the whole-rock composition of a stromatic migmatite affected by the Ceret gabbro-diorite contact aureole (in moles adjusted to 100%). The *P–T* path is derived by comparing the modeled assemblages and isopleths with assemblages and mineral chemistry observed in the studied sample (529). See text for details. (b–d) Enlarged and simplified parts of the pseudosection with calculated isopleths of mineral composition for the areas of interest. The solidus is underlined by a dashed line. ..... 72

**Figure 6.6.** *P–T* pseudosection of the stromatic migmatite (sample 529) with calculated isopleths of the molar proportions of liquid, garnet, cordierite and spinel for the areas of interest. The solidus is underlined by a dashed line. ..... 73

**Figure 6.7.** NCKFMASHTO *P–T* pseudosection calculated for the whole-rock composition of a schollen migmatite affected by the Ceret gabbro-diorite contact aureole (in moles adjusted to 100%). The *P–T* path is derived by comparing the modeled assemblages and isopleths with assemblages and mineral chemistry observed in the studied sample (459). See text for details. (b–d) Enlarged and simplified parts of the pseudosection with calculated isopleths of mineral composition for the areas of interest. The solidus is underlined by a dashed line. ..... 75

**Figure 6.8.** *P*–*T* pseudosection of the schollen migmatite (sample 459) with calculated isopleths of the molar proportions of liquid, sillimanite, garnet and cordierite for the areas of interest. The solidus is underlined by a dashed line. .....76

**Figure 6.9.** NCKFMASHTO *P*–*T* pseudosection calculated for the whole-rock composition of a residuum melanosome located as a xenolith within the Ceret gabbro-diorite contact aureole (in moles adjusted to 100%). The *P*–*T* path is derived by comparing the modeled assemblages and isopleths with assemblages and mineral chemistry observed in the studied sample (462). See text for details. (b–d) Enlarged and simplified parts of the pseudosection with calculated isopleths of mineral composition for the areas of interest. The solidus is underlined by a dashed line. .....77

**Figure 6.10.** *P*–*T* pseudosection of the residuum melanosome (sample 462) with calculated isopleths of the molar proportions of liquid, garnet, cordierite and spinel for the areas of interest. The solidus is underlined by a dashed line. .....79

**Figure 6.11.** *P*–*T* diagram showing the different paths of migmatitic rocks affected by the Ceret contact aureole. The solidus for the different samples is underlined by a dashed line. .....81

**Figure 6.12.** *T*–*M*($H_2O$) pseudosection calculated for the whole-rock composition of a hypothetical protolith (in moles adjusted to 100%) at 5.5 kbar and contoured for the molar proportions of liquid. *M*($H_2O$) is the molar content of water in mol. %. The four-color cooling and fluid infiltration paths are discussed in the text. Black stippled field indicates partial preservation of granulite facies assemblages. The solidus is underlined by a dashed red line. .....84

**Figure 6.13.** Sketch ilustrating the five episodes of melt loss alternating with four fluid infiltration events at 5.5 Kbar and 790 °C. .....86

**Figure 6.14.** Calculated *T*–$X_{\text{melt loss}}$ pseudosection at 5.5 kbar showing the effect of multiples partial melt loss–fluid infiltration events. $X_{\text{melt loss}}$ is the proportion of melt removed from the protolith composition at 790 °C in mol. %. The five black horizontal arrows are discussed in the text. Stippled fields indicate the partial preservation of granulite facies assemblages. The solidus is underlined by a dashed red line. .....88

**Figure 6.15.** Diagram showing the mineral proportions for the different melting episodes calculated by THERMOCALC.....90

**Figure 6.16.** $SiO_2$–$Al_2O_3$–($FeO$+$MgO$+$TiO_2$) and $SiO_2$–$Al_2O_3$–($K_2O$+$Na_2O$) ternary plots representing the composition of the hypotethical protolith, the different types of migmatites, the representative igneous rocks and the compositions calculated by THERMOCALC for residues 1–5 and for the anatectic melt at the solidus. See text and Table 6.1 for further information. ..... 93

## CHAPTER 7

**Figure 7.1.** Geological sketch map of the Roc de Frausa Massif and Sant Llorenç–La Jonquera plutonic complex with the location of representative samples used in this study. Modified from Liesa (1994)..... 98

**Figure 7.2.** Cathodoluminescence images of the analyzed zircon rims from migmatites of the Lower series (samples 349 and 524) with the location of the SHRIMP spots ..... 99

**Figure 7.3.** Cathodoluminescence images of the analyzed zircons from a Sant Llorenç–La Jonquera tonalite (sample 530) and a Ceret stock gabbro (sample 420) with the location of the SHRIMP spots. ..... 100

**Figure 7.4.** Tera-Wasserburg diagrams of SHRIMP U–Pb zircon ages from the fold-structured migmatites of the Lower series: (a) sample 349 and (b) sample 524. The grey solid ellipses represent the data used to obtain the weighted mean age (inset), whereas the white ellipses were discarded. Inherited ages are not shown for clarity. Error ellipses are ± 2σ. ..... 102

**Figure 7.5.** Tera-Wasserburg diagrams of zircon U–Pb ages from Variscan igneous rocks: (a) Sant Llorenç–La Jonquera tonalite (sample 530) and (b) Ceret stock gabbro (sample 420). Error crosses are ± 2σ..... 105

**Figure 7.6.** Compositional diagrams for zircon from the migmatites of the Lower series (samples 349 and 524): (a) U versus Th, (b) Hf versus Eu/Eu* and (c) Yb/Gd versus Ce/Sm. The marked analyses are those not used to get the mean age. ..... 109

**Figure 7.7.** Chondrite-normalized rare earth (REE) patterns for the migmatites from the Lower series: sample 349 (a) and sample 524 (b). Chondrite normalization according to Anders & Grevesse (1989), modified by Korotev (1996)..... 110

**Figure 7.8.** Compositional diagrams for zircon from the Sant Llorenç–La Jonquera tonalite (sample 530): (a) Th/U versus Yb/Gd plot, (b) Yb/Gd versus Ce/Sm plot and (c) chondrite normalized REE patterns. Chondrite normalization as in Fig. 7.7. .....112

**Figure 7.9.** Compositional diagrams for zircon from the Ceret stock gabbro (sample 420): (a) Hf versus Eu/Eu* plot, (b) ∑REE versus Hf plot and (c) Yb/Gd versus Ce/Sm plot.....113

## CHAPTER 8

**Figure 8.1.** *P–T* paths and sketches of the petrological successions for representative samples from the different levels of the Roc de Frausa Massif. See text for discussion.....120

**Figure 8.2.** Sketch of the Variscan zonation in NE Iberia and S France, modified from Druguet (2001), with the available ages of the migmatites and intrusive rocks. *NPF*: North-Pyrenean Fault. .....129

**Figure 8.3.** Sketch of the Variscan belt, modified from Martínez Catalán (2011), showing the widespread location of the Middle Carboniferous partial melting event. ....133

**Figure 8.4.** Geodynamic model for the tectonic evolution of the last stages of Variscan orogeny in the Roc de Frausa Massif and summary of *P–T* paths (Fig. 8.1). Idealized position of the studied samples is indicated by circles. (a) The D1 deformation event took place during the compressive phase at 320–315 Ma. (b) The Sant Llorenç–La Jonquera pluton intruded interkinematically during 314–311 Ma at the upper crustal level. (c) The emplacement of Ceret gabbro-diorite stock and the D2 deformation event occur during the tectonic exhumation at 312–307 Ma.....137

# LIST OF TABLE CAPTIONS

**Table 4.1.** Representative mineral analyses of an andalusite–sillimanite micaschist from the Upper series (sample 187) and a sillimanite schist from the Intermediate series (sample 4.12b). ..... 41

**Table 4.2.** Representative mineral analyses of the different types of migmatites from the Intermediate series affected by the Ceret contact aureole. ..... 43

**Table 4.3.** Representative mineral analyses of a fold-structured migmatite from the Lower series (sample 515). ..... 46

**Table 4.4.** Representative X-Ray fluorescence (XRF) whole rock analyses of metapelites and migmatites from the different crustal levels of the Roc de Frausa Massif. ..... 51

**Table 6.1.** Residue and anatectic melt bulk compositions calculated by THERMOCALC in mol.%. The residues are calculated for each melting episode and anatectic melt compositions at the solidus for a patch migmatite (sample 526), a stromatic migmatite (sample 529), a schollen migmatite (sample 459) and a residuum melanosome (sample 462). ..... 91

**Table 6.2.** Representative whole-rock compositions of the late-Variscan igneous rocks from Sant Llorenç–La Jonquera pluton (tonalite to leucogranite) and from Ceret gabbro-diorite stock. ..... 92

**Table 7.1.** U-Th-Pb SHRIMP-RG analytical data for zircons from the fold-structured migmatites of the Lower series (samples 349 and 524). ..... 103

**Table 7.2.** U-Th-Pb SHRIMP-RG analytical data for zircons from the Sant Llorenç–La Jonquera tonalite (samples 530) and the Ceret stock gabbro (sample 420). ..... 106

**Table 7.3.** U-Th-Pb SHRIMP-RG analytical data for zircons from the migmatites from the Ceret stock contact aureole (sample 529). ..... 108

**Table 7.4.** U, Th, Hf and trace element (REE) composition of zircon for the fold-structured migmatites from the Lower series (samples 349 and 524). Concentrations are given ppm. ..... 111

**Table 7.5.** U, Th, Hf and trace element (REE) composition of zircon for the Sant Llorenç–La Jonquera tonalite (samples 530) and the Ceret stock gabbro (sample 420). Concentrations are given ppm. ..... 114

**Table 8.1.** Available ages for migmatites and intrusive rocks of the Variscan Belt at the Pyrenees, the Catalan Coastal Ranges and Montagne Noire. ..... 131